A Modeling Assessment of Using Optical Fiber Devices For Electric Field Measurements

David Alumbaugh[1], Evan Um[1], Michael T. V. Wylie[2] and Bjorn Paulsson[2]
[1]Lawrence Berkeley National Laboratory, One Cyclotron Road, Berkeley, CA 94720
[2]Paulsson, Inc, 16543 Arminta Street, Van Nuys, CA 91406-1745

SUMMARY

In this paper, we describe numerical studies that have been undertaken to investigate the plausibility of using fiber-optic sensing technologies for the measurement of electric fields in geophysical applications. An initial study simulating a single fiber wrapped with a piezoelectric polymer (polyvinylidene fluoride or PVDF) showed too low a sensitivity for geophysical applications except in very specialized down-hole monitoring situations. This led to a second study whereby we simulated fiber being wound around cores composed of lead zirconate titanate (PZT), a ceramic with high piezoelectric properties, using two different 'polling' and winding configurations. After a brief introduction to the possible advantages of measuring electric fields using fiber optics, we will discuss the numerical modeling results and present conclusions on the way forward with this measurement technology.

Keywords: electric field, piezoelectric, fiber optic sensing

INTRODUCTION

In the last 10 years we've seen a rapid increase in the deployment of fiber optic sensors for geophysical sensing. As described in Hartog (2017), measuring small changes in travel-time in pulses of laser light within glass fibers due to the stretching or contraction in the fiber allows for novel deployments in well completions and surface installations of Distributed Acoustic Sensing (DAS), Distributed Strain Sensing (DSS), and Distributed Temperature Sensing (DTS) measurements. In addition to the relatively inexpensive sensor installation and the fact that the fiber provides nearly continuous – high spatial resolution measurements along its length, a principal attraction of these type of measurements for permanent installations is that there are no buried or downhole electronics. That is, only the fiber is subsurface and all the electronics are contained in the interrogator which is housed on the surface and can be easily accessed. This provides an advantage over traditional permanent subsurface installations where electronics are buried and often serve as a point of failure.

Due to the advantages of not having downhole electronics, Alumbaugh et al. (2022) numerically investigated the plausibility of a downhole completion that would enable electric field measurements along either the outside or inside of a well completion. As shown in Figure 1, the model assumed a fiber wrapped with polyvinylidene fluoride (PVDF), which is a flexible polymer that has relatively high piezoelectric constants (d_{33} and d_{13}) that transduce electrical to mechanical energy (and vice-versa) for a non-ceramic material. Note that 'poling' the material such that the produced mechanical strain is in the same direction as the electric field of interest is given by the d_{33} value, while poling the material to produce a d_{13} value indicates a strain will be produced perpendicular to the electric field of interest.

Though PVDF has piezoelectric constants that are smaller than those of high-piezoelectric ceramics such as lead zirconate titanate (PZT), the polymer was chosen as the material due to its flexibility as it was assumed that ceramic materials would fracture and break during common fiber installation practices for subsurface well completions. Thus, the work of Alumbaugh et al. (2022) assumed that the PVDF was poled to produce d_{13} values between 4 and 23 ($x10^{-12}$ m/V) which would cause the fiber to stretch along a well casing due to electric fields perpendicular to the casing. The numerical study indicated that this type of fiber measurement was far too insensitive to most electric field measurements of geophysical interest (i.e. the noise level was estimated to be 10's of mV/m). However, it was noted that if an electric source could be placed downhole, optical measurements in the vicinity of the source could be used to define the oil/water mixture as well as identify water wet versus oil wet fracture zones post fracking operations.

Though the initial study strongly suggested that a single fiber with a piezoelectric coating would not provide the electric field sensitivity required for most geophysical applications, it did suggest that layers of fiber wound around a PZT may produce high enough sensitivity to warrant long-term deployment in downhole or sea floor environments to provide monitoring of carbon-sequestration operations. Therefore, LBNL recently

partnered with Paulsson, Inc., a small company with experience in building high sensitivity fiber-based acoustic and acceleration sensors, to submit a successful Phase 1 proposal to the US Department of Energy's (DOE's) Small-Business Innovative Research (SBIR) program (DE-SC0023609). In the remainder of this paper we first describe the sensor configurations that were simulated using a modified version of the SIMPEG2D code described in Heagy and Oldenburg (2019), and then describe the workflow used to convert calculated electric fields to mechanical strain in the fiber which allows us to estimate the electric field noise floor per layer of fiber wound around piezoelectric cores. Ultimately these theoretical noise floor estimates will be compared to lab measurements of sensors that are currently being assembled in Paulsson, Inc.'s Van Nuys, CA facilities.

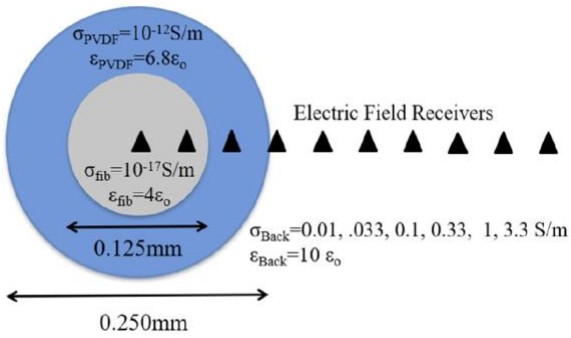

Figure 1: Electromagnetic properties of the model used to simulate the electromagnetic response of a PVDF-coated glass fiber in an otherwise homogeneous medium as simulated by Alumbaugh et al. (2022).

ELECTROMAGNETIC MODELS AND SIMULATIONS

For the lab measurements that will be undertaken in Phase 1 of this SBIR project, we are working with APC International, Ltd (https://www.americanpiezo.com/) to manufacture and supply the piezoelectric materials necessary to build the transducer. To build the electromagnetic property models as well as estimate the strain the cores will place on the fiber, we used electromagnetic material and piezoelectric values for two different PZT materials from a book published by the company (APC International Ltd.,2011) which are given in Table 1. Note that the PZ840 and PZ855 represent end members of the PZT offerings from APC in terms of the loss tangent values that were used to determine the conductivities and dielectric constants, as well as the piezoelectric constants. In addition to providing a theoretical analysis for these two different materials, we also tested two different core and winding configurations as shown in Figure 2; a core that uses end-to-end windings to make use of d_{33}-generated strain produced along the length of the core in the same direction as that of the electric field being measured, as well as a 'solenoidal' type of winding that makes use of d_{31}-generated strain in the direction radially perpendicular to that of the electric field being 'measured'. Note that the core for the latter is a hollow cylinder which is necessary to property 'pole' the material with a d_{31} piezoelectric constant and the fiber for the former will be wound around caps on the top and bottom such that the minimum bending radius of the fiber is maintained.

Material	σ(S/m)	ε(F/m)	d_{33}(m/V)x10^{-12}	d_{31}(m/V)x10^{-12}
PZ840	$2.7x10^{-7}$	$1.1x10^{-8}$	$2.9x10^{2}$	$1.25x10^{2}$
PZ855	$6.1x10^{-6}$	$3.6x10^{-8}$	$6.3x10^{2}$	$2.76x10^{2}$

Table 1: Electromagnetic and piezoelectric properties of two different lead-zirconate compounds examined in this study. From APC International Ltd. (2011).

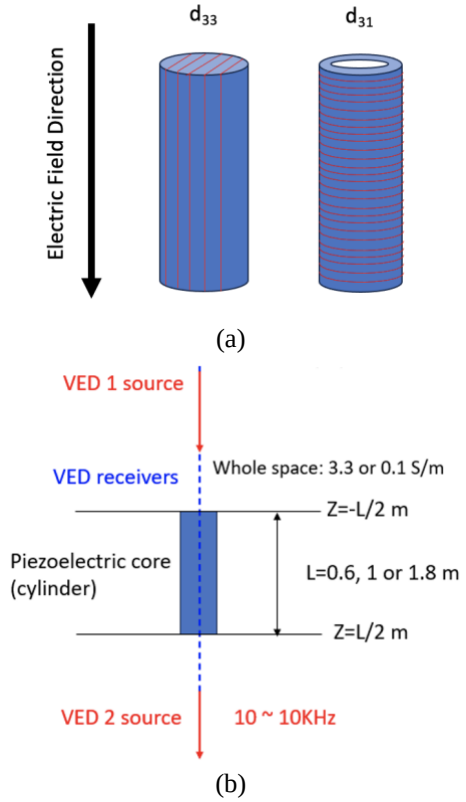

Figure 2: (a) Two different core and optical winding configurations simulated in this study. The red lines represent the optical fiber winding directions for the two cases, while the blue solids represent the shape of the piezoelectric core material. In the left most wind the transducer will have caps that ensure the minimum bending radius of the fiber is maintained. (b) A vertical cross-section through the solid cylinder model showing how the model was set up. Note that the diameter of the core is 5cm.

The numerical algorithm used is a version of SIMPEG2D (Heagy and Oldenburg, 2019) that has been modified to account for the dielectric constant values shown in Table 1 via the inclusion of a complex conductivity term. A

vertical cross section through the solid cylinder model with dimensions and resistivity values outside of the core are shown in Figure 2b. In order to produce a fairly uniform vertical electric field across the region of interest, two electric dipoles were used with one located 4m off each end of the core as shown in Figure 2b. Calculations of the electric fields were made at different locations within the core as well as just outside of it at 10Hz, 100Hz, 1kHz, and 10kHz. Note that for geophysical applications we want to go to lower frequencies; however, the numerical solution became less stable below 10Hz. Thus, for initial testing, we limited the calculations to 10-10,000 Hz. In terms of background resistivities we used two; 0.1S/m and 3.3S/m to represent 'average' earth and sea-water conductivity values.

Examples of the electric field calculations for the solid PZ855 core embedded in sea-water are shown in Figure 3 with 3a depicting the 100 Hz results and 3b depicting the 10 kHz solution. Here E_Z represents the 'vertical' electric field we are trying to measure with the piezoelectric device, and E_X the radial or horizontal component. Note that; 1) the electric field amplitudes are 'amplified' across the core boundary due to the much higher resistivity of the core material compared to that of the background; 2) the vertical electric field is fairly uniform in amplitude along the length of the core as well as with radial position; 3) the vertical electric fields are at least one order of magnitude higher than the strongest horizontal fields; and 4) the horizontal field amplitude goes to zero at the center of the core which is caused by the orientation of the two electric dipoles. Because we are only interested in 'measuring' the vertical field, which is much stronger than the horizontal, we don't need to worry about the behavior of the horizontal field.

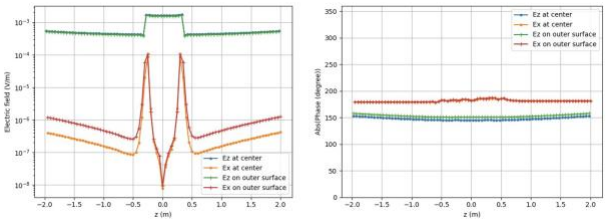

(a)

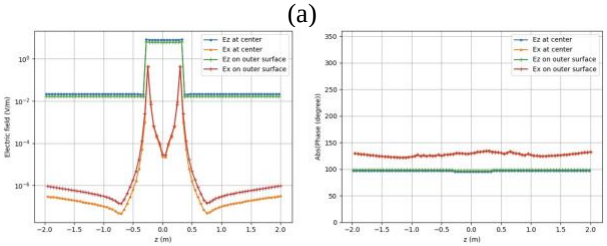

(b)

Figure 3: Electric field calculations for the solid PZ855 core located in seawater at (a) 100 Hz and (b) 10 kHz. Here E_Z represents the electric field which we are interested in measuring and E_X the horizontal or radial field. The two sets of calculations are for the center of the model and for just inside the edge of the core. The left-hand figure is amplitude and the right-hand is phase. Note that the phase calculations are not used in the subsequent piezoelectric transducer noise calculations.

PIEZOELECTRIC SENSOR NOISE-FLOOR ESTIMATES

To estimate electric field noise floor estimates we used the following workflow for the two optical fiber winding configurations.

1. Calculate number of turns of fiber per core for 105μm diameter fiber (up-buffered polyimide coating):
   a. Hollow cylinder with solenoidal windings: 5442 turns.
   b. Solid cylinder assuming 2cm square plates with end-to-end windings: 459 turns.
2. Calculate length of stretchable fiber for a single winding layer of core assuming number of turns given above:
   a. Hollow cylinder with solenoidal windings: 391m.
   b. Solid cylinder with end-to-end windings: 466m.
3. Use the calculated vertical electric fields from the modeling described in the previous section:
   a. Inside core:
      i. Hollow cylinder: just inside outer edge.
      ii. Solid cylinder: in center of core.
   b. Outside core.
4. Multiply Piezoelectric Charge Constant in Table 1 by electric field inside core to determine the piezoelectrically generated strain produced on the fiber.
5. Multiply calculated strain by stretchable length of fiber determined in 2) to get amount of fiber-stretch per layer of optical fiber windings.
6. Divide the amount of fiber stretch by the interrogator noise floor (7.4E-11m) and multiply the electric field outside of the core in the homogenous medium by this ratio. This provides the estimated electric field noise floor or conversely, the sensitivity of the sensor.

The optical noise floor is derived from commercial optical sensing systems utilizing interferometric sensing configurations. The estimated noise floor as a function of frequency that are estimated by applying this workflow for the two different core and winding geometries in Figure 1 are given in Figure 4a for the solenoidal winding geometry and Figure 4b for the end-to-end winding configuration. The four curves in each plot represent results for different core materials and background resistivities. Note that the core material has a much bigger effect on the noise floor than the background resistivity. The higher sensitivity/lower noise floor provided by the PZ840 material is likely due to it having over an order of magnitude lower resistivity than PZ855, even though the PZ840m also has a lower piezoelectric charge constant. Also note that the end-to-end winding produces better noise-floors than the solenoidal winding for the same size

core. This can be expected due to the larger d_{33} values shown in Table 1 when compared to d_{31}. Lastly, note that the noise floor increases (i.e. sensitivity decreases) as the frequency gets lower. This most likely is due to the ratio of E_Z inside the core to outside the core decreasing with decreasing frequency as shown when comparing Figure 3a to 3b.

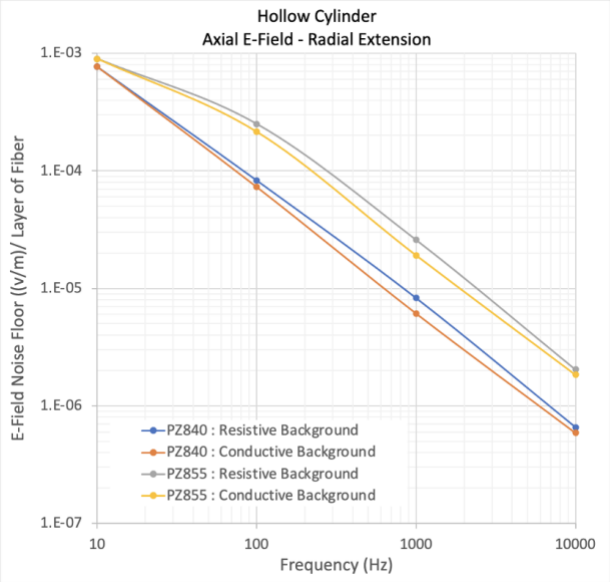

(a)

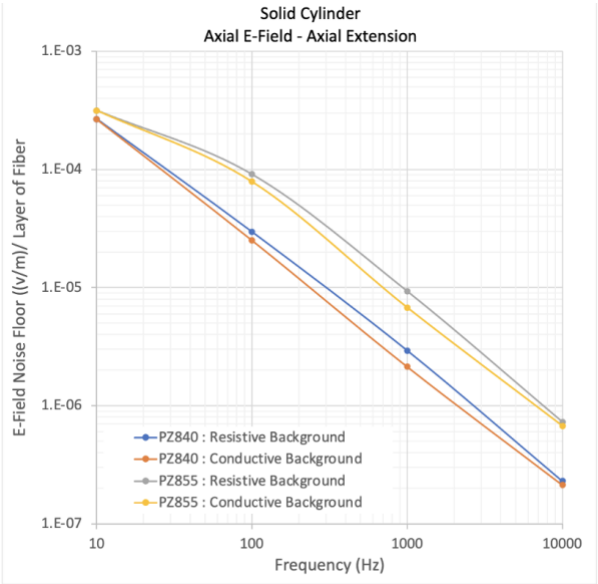

(b)

Figure 4: Electric field noise floors as a function of frequency estimated for the a) solenoidal-hollow cylinder core configuration shown in Figure 1, and the (b) solid core – end-to-end winding sensor configuration. The blue and red curves represent estimates for the PZ840 material embedded in the two different background resistivities, and the yellow and grey curves for the PZ855 PZT.

DISCUSSION

The numerical results for optical fiber sensing of electric fields that we have presented makes assumptions that may result in inaccurate predictions. Most notable of these is that the conductivities and dielectric permitivities given in Table 1 that were used in the modeling effort were derived from the book provided by the manufacturer (APC International Ltd.,2011). Independent internet searches have shown reported conductivities of PZT to be much lower; however, modeling of these lower conductivity materials imply a high contrast between the background and core material which can result in numerical instabilities. A second factor that we have not included here is the possibility that other electric field components (i.e. E_X and E_Y) could also cause a response in the piezoelectric material which could contaminate the response. On the other hand, the noise floor calculations assume a single layer of fiber on 0.6 m long cores. More wraps of fiber as well as longer cores will only improve the sensitivity. In any event, the next step in this project is to build prototypes of the sensors simulated in this paper and measure the frequency response in a small water filled tank. This will allow us not only to determine the accuracy of our calculations, but also determine if further studies of this type of sensor is warranted.

CONCLUSION

In this paper we have presented a numerical study to examine the possibility of making electric field measurements using optical fiber wound around different PZT materials. Though the results look promising, the estimated electric field sensitivities (~0.1mV at 10Hz to 0.1 μV/m at 10kHz) still look less than the 1pV/m to 1nV/m noise floors provide by connecting two electrodes up in a dipole configuration. Thus, the next phase of this project will involve making measurements on prototype sensors in the lab. After these measurements are made we will look at methods to enhance the sensitivity to determine if this type of electric field sensor is worth pursuing.

ACKNOWLEDGMENTS

Work for this project has been funded via the DOE's Small Business Innovative Research (SBIUR) program under grant DE-SC0023609. The authors would also like to thank Professor Lindsey Heagy from the University of British Columbia and the rest of the SIMPEG group for providing the modifications to the SIMPEG2D code that were necessary to make these calculations.

REFERENCES

Alumbaugh, D. L., Um, E. S., Hoversten, G. M., and Key, K., 2021, Distributed electric field sensing using fibre optics in borehole environments; Geophysical Prospecting, **70**(1), 210-221.

APC International, LTD, 2011, Piezoelectric Ceramics: Principles and Applications, APC International.

Hartog, A. H., 2017, An Introduction to Distributed Optical Fibre Sensors; CRC Press, https://doi.org/10.201/9781315119014.

Heagy, L.J. and Oldenburg, D.W., 2019. Modeling electromagnetics on cylindrical meshes with applications to steel-cased wells. *Computers & Geosciences*, *125*, pp.115-130.

7th International Symposium on Three-Dimensional Electromagnetics
Vancouver, BC, Canada, November 13–15, 2023

Resolving bottlenecks of 3D controlled-source electromagnetic Gauss-Newton inversion.

Anna Avdeeva[1], Rune Mittet[1] and Ole Martin Pedersen[1]
[1]Allton AS

Summary

We propose a new approach to Gauss-Newton optimization to solve the three-dimensional VTI-anisotropic controlled-source electromagnetic inverse problem. The main two bottlenecks of the Gauss-Newton implementation are computation and storage of the large Jacobian matrix, and large memory and time required for the solution to the system of normal equations. To overcome the first issue, the simulation and optimization meshes are decoupled with the use of node-based basis functions. This significantly reduces the number of optimization parameters and hence the memory requirements. The second issue is solved by using a new preconditioner in Conjugate-Gradient solver. Our preconditioner is based on a limited-memory quasi-Newton approximation to the inverse of the Hessian matrix and reduces number of Conjugate-Gradient iterations. This preconditioner is much more efficient than the commonly used Jacobi preconditioner. To further reduce the computational time the code is parallelized in a hybrid manner using MPI and openMP. The method is validated with an off-shore controlled-source electromagnetic dataset acquired at the slow spreading Mohns ridge located east of Greenland and southwest of Svalbard.

Keywords: CSEM, 3D, inversion

Introduction

The solution to a geophysical inverse problem is commonly sought through minimization of an objective function. To find such a minimum in the large-scale 3D case, the gradient-based or Gauss-Newton (GN) optimization methods are employed. While gradient-based methods are less demanding in terms of computer resources, Nguyen et al. (2016) showed that GN method can lead to a much better inversion results.

The GN method relies on the computation of the Jacobian matrix that contains information about the derivatives of the simulated data with respect to conductivity. Storage of the Jacobian matrix requires a huge amount of memory, especially in the 3D case. Moreover, due to the dense structure of the Jacobian matrix, the matrix-vector multiplications needed for solving the GN system of normal equations can become very expensive.

Many researchers proposed strategies to make 3D GN inversions feasible (see, for example, Li et al., 2011; Grayver et al., 2013; Amaya et al., 2016; Mittet & Avdeeva, 2023). Some straightforward solutions are to use a subset of the measured data or coarse inversion grids, but the choice of the subset or the coarsening is subjective and relies on the geophysicist's experience, and may lead to a loss of important information. A more advanced approach by Amaya et al. (2016) combines several source positions for simultaneous-source simulations. The resulting Hessian matrix can be described as a low-rank approximation to the GN Hessian.

To reduce the memory usage and the computation time while preserving the quality of the inversion results, Li et al. (2011) proposes a compressed implicit Jacobian scheme. It is therefore not necessary to store the large Jacobian matrix in memory, but this scheme comes at the price of some computational overhead. In this scheme the Jacobian matrix multiplication with a vector is converted to a matrix-vector operation of the field matrices with this vector. To further mitigate the computational overhead they apply the adaptive cross approximation method to compress one of the field matrices.

We propose an alternative solution to the problem. To reduce memory required by the Jacobian we use node-based basis functions to decouple simulation and optimization meshes. This strategy is discussed in detail in Mittet & Avdeeva (2023), where it is successfuly verified for a 2.5D case. In this abstract we focus on bottlenecks of the numerical implementation and give recepies on how to overcome these bottlenecks. We present a solution that can be applied to a large 3D data sets, with relatively modest compu-

tational resources. In addition, to speed up the solution of the system of normal equations a new preconditioner for Conjugate-Gradient (CG) solver is suggested. We validate the inversion on both 2.5D and 3D marine controlled-source electromagnetic (CSEM) datasets.

3D CSEM GN inversion methodology

The goal of a VTI-anisotropic CSEM inversion is to find the distribution of the model parameters $\mathbf{m}$, for example the electrical conductivity $\boldsymbol{\sigma} = (\boldsymbol{\sigma}_h, \boldsymbol{\sigma}_v)$, in the volume of interest V from observations of electric and magnetic fields excited by sources $\mathbf{x}_s$ at receivers $\mathbf{x}_r$. This is sought through minimization of an objective functional:

$$\varphi = \varphi_d + \lambda\varphi_s \rightarrow \min_{\lambda,\mathbf{m}}, \tag{1}$$

where φ_d and φ_s are the data misfit and regularization terms. The data misfit is a weighted difference betweed predicted and observed data

$$\varphi_d(\mathbf{m}) = \frac{\mathbf{1}}{\mathbf{2}}\|\mathbf{f(m)} - \mathbf{d^{obs}}\|^{\mathbf{2}}_{\mathbf{W_d^T W_d}}, \tag{2}$$

and the regularization term is a standard stabilizing functional based on the gradients of the model, that steer the solution towards a smooth model. Matrix $\mathbf{W}_d$ is a diagonal matrix with the data weights.

After second-order Taylor expansion of equation 1, we obtain the GN system of normal equations

$$\begin{aligned}\left[\Re\left\{\mathbf{J_m^H W_d^T W_d J_m}\right\} + \lambda\nabla^2_{\mathbf{m}}\varphi_s(\mathbf{m}) + \alpha\mathbf{I}\right]\mathbf{p} = \\ -\Re\left\{\mathbf{J_m^H W_d^T W_d}\left[\mathbf{f(m)} - \mathbf{d^{obs}}\right]\right\} - \lambda\nabla_{\mathbf{m}}\varphi_s(\mathbf{m}),\end{aligned} \tag{3}$$

here $\mathbf{p}$ is the search direction vector, and $\mathbf{J_m} \in \mathbf{C^{N_d \times N_m}}$ is the Jacobian matrix, consisting of partial derivatives of the data with respect to model parameters $\mathbf{m}$. N_d and N_m are the number of data and model parameters, respectively. The sought after model update vector $\delta\mathbf{m}$ is found by a line search along the direction $\mathbf{p}$. The vector $\boldsymbol{\sigma}$ is obtained from $\mathbf{m}$ by a set of parameter transformations.

To improve the condition number of the system the matrix on the left of the eq. 3, a small damping term $\alpha\mathbf{I}$ is added. In the beginning of the optimization process, $\alpha = 0.01 * \mathrm{diag}\left[\Re\left\{\mathbf{J_m^H W_d^T W_d J_m}\right\} + \lambda\nabla^2_{\mathbf{m}}\varphi_s(\mathbf{m})\right]$.

For the realistic size VTI 3D inverse problem and in case $\mathbf{m} = \boldsymbol{\sigma}$, the Jacobian matrix $\mathbf{J}_{\boldsymbol{\sigma}}$ can be in the order of hundreds of TB (see Table 2 for a few examples). Such matrices are difficult to store and manipulate even on modern computer architectures. To reduce the memory requirements we propose to decouple the simulation and the optimization domains by a set of parameter transformations which are discussed in the next section. After the transformations the memory requirements for one Jacobian could be reduced from hundreds of TB to tens of TB, or even less depending on the user's choice. This memory requirements can still be large and therefore we propose a hybrid MPI/OpenMP implementation to split the problem between compute nodes and cores of a cluster in a scallable manner. After Jacobian is computed and can be stored in memory, the system of normal eqs. 3 is solved with the Conjugate-Gradient (CG) solver. To improve the convergence of the solver, a new preconditioner is suggested below.

Overcoming bottlenecks

Parameter transformations

In this section we introduce a set of parameter transformations that significantly reduces memory requirements needed for computation and storage of the Jacobian matrix. In total we perform three transformations of parameters:

- from conductivity $\boldsymbol{\sigma} \in \mathbb{R}_{2\times n_x \times n_y \times n_z}$ to unbounded parameters $\boldsymbol{\chi} \in \mathbb{R}_{2\times n_x \times n_y \times n_z}$, here n_x, n_y, n_z are number of nodes in simulation mesh along three orthogonal directions;
- from $\boldsymbol{\chi} \in \mathbb{R}_{2\times n_x \times n_y \times n_z}$ to flat seabed parameters $\tilde{\boldsymbol{\chi}} \in \mathbb{R}_{2\times n_x \times n_y \times m_z}$. Note that the number of the vertical nodes $m_z < n_z$, and the size of parameter vector is reduced, mostly due to the fact that the water is not anymore part of the domain;
- from $\tilde{\boldsymbol{\chi}} \in \mathbb{R}_{2\times n_x \times n_y \times m_z}$ to a coarser inversion parameterization $\mathbf{m} \in \mathbb{R}_{2\times n^o_x \times n^o_y \times n^o_z}$. This transformation is based on node-based basis functions. Superscript o denotes optimization mesh.

These transformations are discussed in detail in Mittet & Avdeeva (2023), here we only focus on the last one, since straightforward implementation of this transform can lead to large memory requirements and significant computational time.

To make the explanations simple we resort to a 1D case for now. As mentioned in Mittet & Avdeeva (2023), the parameter $\tilde{\chi}(x)$ can be considered continuous, if on the interval $[0, x_{max}]$

$$\tilde{\chi}(x) = \sum_n \tilde{\chi}_n \phi_n(x), \tag{4}$$

where $\tilde{\chi}_n$ and $\phi_n(x)$ are node values and sinc basis funtions centered at nodes x_n, respectively. The sampling interval is the same as in a simulation grid.

Alternative representation of $\tilde{\chi}(x)$ with a new set of basis functions ψ_ν and node values m_ν is

$$\tilde{\chi}(x) = \sum_\nu m_\nu \psi_\nu(x). \tag{5}$$

In this representation the sampling interval is 2 to 5 times coarser than in the simulation domain. The coefficients m_ν are the unknowns in the optimization problem.

In the 1D case, to perform the transformations from $\tilde{\boldsymbol{\chi}}$ to $\mathbf{m}$ and back, we form three transformation matrices

$$\begin{aligned} A^{(x)}_{ln} &= \int_0^{x_{max}} \phi_n(x)\phi_l(x)dx, \\ B^{(x)}_{\gamma n} &= \int_0^{x_{max}} \psi_\gamma(x)\phi_n(x)dx, \\ C^{(x)}_{\nu\gamma} &= \int_0^{x_{max}} \psi_\nu(x)\psi_\gamma(x)dx. \end{aligned} \tag{6}$$

For the 3D case, much larger matrices $\mathbf{C}$, $\mathbf{B}$ and $\mathbf{A}$ are computed. For example,

$$C_{\Gamma\Lambda} = C^{(x)}_{\nu\gamma} C^{(y)}_{\alpha\beta} C^{(z)}_{\lambda\kappa}. \tag{7}$$

Matrices $\mathbf{A}$, $\mathbf{B}$ are formed similarly.

With these matrices the parameter transforms are given as

$$\mathbf{A}\tilde{\boldsymbol{\chi}} = \mathbf{B}^T\mathbf{m}, \tag{8a}$$

$$\mathbf{C}\mathbf{m} = \mathbf{B}\tilde{\boldsymbol{\chi}}. \tag{8b}$$

The sizes of the transform matrices depend on the number of elements in the parameter vectors $\tilde{\boldsymbol{\chi}}$ and $\mathbf{m}$, respectively, and can become large. However, due to the use of nodal basis functions $\mathbf{A}, \mathbf{B}$ and $\mathbf{C}$ are sparse. Examples of the memory requirements for these matrices are shown in Table 1.

In the 1D and 2.5D cases, it is possible to perform and store their factorizations once, before the initial inversion iteration, and use direct solvers, such as MUMPS, to perform the necessary transformations. In the 3D case, the matrices are large, especially matrix $\mathbf{A}$, and factorization and direct solvers are not anymore a suitable choice. In the 3D case, a CG solver with the Jacobi preconditioner is used. Since both matrices $\mathbf{A}$ and $\mathbf{C}$ are diagonal-dominant the Jacobi preconditioner gives good convergency, normally with less than 10 iterations to achieve relative residual error of 10^{-5}. We employ a CG solver from the Eigen C++ library (see Guennebaud et al., 2010).

During the inversion we need to compute the Jacobian with respect to the parameters $\mathbf{m}$. In this case, we need to solve the following system of equations

$$\mathbf{A}\mathbf{J}_\mathbf{m} = \mathbf{B}^T\mathbf{J}_{\tilde{\boldsymbol{\chi}}}. \tag{9}$$

Due to the large size of the matrix $\mathbf{J}_{\tilde{\boldsymbol{\chi}}}$ the CG solution of the system 9 would be computationally very expensive. Therefore, instead we use the following approximation

$$\mathbf{J}_\mathbf{m} \approx \mathrm{diag}^{-1}(\mathbf{A})\,\mathbf{B}^T\mathbf{J}_{\tilde{\boldsymbol{\chi}}}. \tag{10}$$

Our tests showed that this approximation is sufficiently good.

Note that we do not need to compute the whole matrix $\mathbf{J}_{\tilde{\boldsymbol{\chi}}}$, but depending on the available memory we can compute only a small number of rows, that we transform using equation 10 to form a part of matrix $\mathbf{J}_\mathbf{m}$, and then continue with the next portion of rows. We will discuss this below in section on the hybrid MPI and openMP implemetation.

Preconditioning CG solver

After the $\mathbf{J}_\mathbf{m}$ is computed, the system of normal equations 3 can be solved with CG solver. We do not compute or store the system matrix of eq. 3, instead the action of $\mathbf{J}_\mathbf{m}$ and $\mathbf{J}^H_\mathbf{m}$ on a vector are implemented. To speed up the computations we keep both matrices $\mathbf{J}_\mathbf{m}$ and $\mathbf{J}^H_\mathbf{m}$ in memory.

It is well known that the number of CG iterations could be greatly reduced by finding a good preconditioner. Normally in 3D CSEM inversion the diagonal Jacobi preconditioner is used.

We propose a preconditioner based on a limited-memory quasi-Newton approximation to the inverse of the Hessian matrix. At each GN iteration k, we use the L-BFGS two loop recursion algorithm from Nocedal & Wright (1999), to construct the preconditioner. In the two loop recursion, we choose the diagonal matrix $\mathbf{H}^0_k$ to contain the inverse of the diagonal of system matrix on its diagonal. The computation of the diagonal of the system matrix is not very expensive and is computed anyway, to decide on the damping factor α (see eq. 3).

To make sure that this preconditioner is successful we propose a damped version of L-BFGS, in which vectors $\mathbf{s}_k = \mathbf{m}_{k+1} - \mathbf{m}_k$ are modified as follows:

$$\tilde{\mathbf{s}}_k = \theta_k \mathbf{s}_k + (1-\theta_k)\mathbf{H}_k\mathbf{y}_k, \tag{11}$$

here the scalar θ_k is defined as

$$\theta_k = \begin{cases} 1, & \text{if } \tau_k \geq 0.2 \\ 0.8/(1-\tau_k), & \text{otherwise} \end{cases}, \tag{12}$$

with $\tau_k = \frac{\mathbf{s}_k^T \mathbf{y}_k}{\mathbf{y}_k^T \mathbf{H}_k \mathbf{y}_k}$, $\mathbf{y}_k = \mathbf{g}_{k+1} - \mathbf{g}_k$, $\mathbf{g}_k = \left(\frac{\partial \varphi}{\partial \mathbf{m}}\right)_k$ and $\mathbf{H}_k$ is L-BFGS approximation to the inverse of the Hessian matrix.

Similar approach was proposed in Nocedal & Wright (1999), but there it was formulated for the Hessian approximation $\mathbf{B}_{k+1}$, while we are interested in the update to the inverse of the Hessian $\mathbf{H}_{k+1}$.

The change to vectors $\mathbf{s}_k$ ensures positive definiteness of our preconditioner $\mathbf{H}_{k+1}$. Note that $\theta_k = 0$ gives $\mathbf{H}_{k+1} = \mathbf{H}_k$, and $\theta_k = 1$ gives the $\mathbf{H}_{k+1}$ matrix according to the unmodified L-BFGS method, so the values of θ_k between 0 and 1 gives a matrix that interpolates between these two cases. In Figure 1 we show the comparison of three 2.5D GN inversion runs in terms of the number of CG iterations per GN iteration. From the figure we see that solving the system without a preconditioner is very inefficient (black curve). The new preconditioner (red curve) for the most of the GN iterations performs at least 2 times better than the Jacobi preconditioner (blue curve). This approach was also tested on inversion of various 3D datasets and most of the time the number of CG iterations stays below 300.

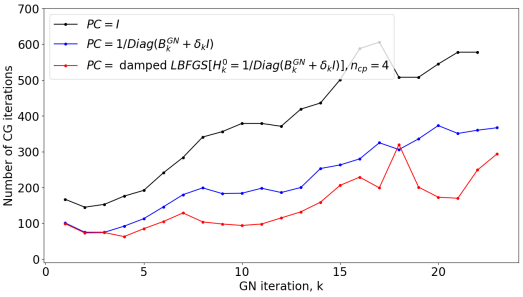

Figure 1: Effect of CG preconditioner on a number of CG iterations. Number of CG iterations is plotted for each GN iteration. Here Atlab3 dataset along central profile is inverted with 2.5D inversion.

Parallel implementation

To further speed up the computations we parallelize our solution. For the forward simulations the parallel implementation is straightforward, the responses from various sources are computed simalteneously on different cores. The parallel implemetation for Jacobian computation and CG solution to the system of normal equations is a bit more complicated.

The Jacobian is distributed by rows to various compute nodes. Depending on the available memory only a small number of rows of $\mathbf{J}_{\boldsymbol{\sigma}}$ is computed on the nodes at the same time. Then all three parameter transformations are performed, which fills some portion of rows of a distributed matrix $\mathbf{J}_{\mathbf{m}}$. This process is repeated until the whole matrix $\mathbf{J}_{\mathbf{m}}$ is filled. We use the PETSc library (Balay et al., 2023) to distribute and manipulate the matrix $\mathbf{J}_{\mathbf{m}}$. This library uses the message-passing model for parallel programming and employs MPI for all interprocessor communication.

The transformations of the Jacobian computed on each node are also parallelized by the use of openMP. The first two transformations of the Jacobian are straightforward. For the last one, every node has to have access to matrix $\mathbf{B}_{\mathbf{J}} = \mathrm{diag}^{-1}(\mathbf{A})\mathbf{B}^T$ (see eq. 10). To reduce the memory requirements and also to speed up the sparse-dense matrix multiplications $\mathbf{B}_{\mathbf{J}}\mathbf{J}_{\tilde{\mathbf{X}}}$, in the matrix $\mathbf{B}$ we set elements B_{ij} to zero when $B_{ij} < \varepsilon * \max_{ij}(B_{ij})$. While for the parameter transformations 8 we use $\varepsilon = 10^{-5}$, for the Jacobian transformation 10 the coefficient $\varepsilon = 10^{-2}$. Multiple synthetic tests demonstrate that there is no quality degradation when using these values of ε.

We use openMP to speed-up all matrix-vector multiplications, required at each CG iteration. To solve the system of eq. 3 we utilize the CG solver provided within the PETSc library.

GN Inversion Applications

Application to Atlab-3 CSEM data

In this section we apply our inversion scheme to a dataset acquired at Mohns ridge by the ATLAB consortium. The consortium was formed by NTNU in 2016 with the aim to utilize a wide variety of geophysical data, in order to investigate the nature, dynamics, diversities and resources at mid-ocean ridges and oceanic plates. Since 2016 data was collected at the Mohns and Knipovich ridges, including CSEM, MT, seismic, chemical and biological data.

Johansen et al. (2019) presented the first CSEM inversion results from the Mohns ridge. They invert Atlab-1 data (green dots on Figure 2). Mittet & Avdeeva (2023) improved resolution and expanded the 2.5D CSEM inversion results, by inverting both Atlab-1 and Atlab-3 (blue and red dots on Figure 2) datasets. In this abstract we invert Atlab-3(2) data acquired in 2022 at the Mohns ridge (red dots). The data are measured along three profiles perpendicular to the Atlab-1 line, which facilitates 3D interpretation.

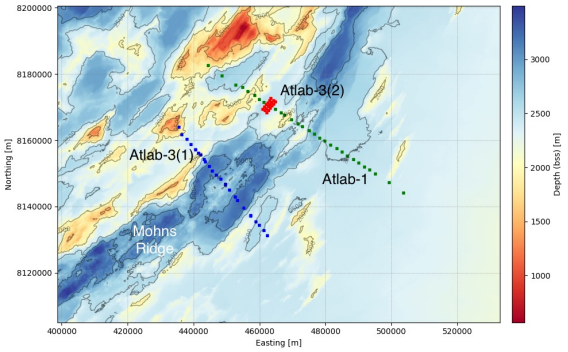

Figure 2: Locations of Atlab-1 and Atlab-3 datasets.

Each profile consists of 80 transmitters and 6 receivers separated by approximately 100 m and 800 m, respectively. The data at 1.6, 4.8, 8 and 11.2 Hz are inverted. The water depth in the area is approximately 2450 m and the bathymetry is relatively flat. The information on mesh sizes and memory requirements for the transformation and Jacobian matrices are shown in the first and third rows of Tables 1 and 2 for 2.5D and 3D inversions, respectively. The minimum total memory required for the inversion runs is 0.8 GB and 1.4 TB for 2.5D and 3D inversions, respectively.

Figure 3 compares vertical resistivity images obtained by the 3D and 2.5D inversions along the central Atlab-3(2) profile. The results are very similar and fit the data to an RMS of 1.1. Both images compare well with the overlayed seismic cross-section. The resistive layer obtained by 3D inversion has slightly more structure and the change in depth to the top of this layer below the 4th receiver is more obvious.

Conclusions

We propose a new algorithm for 3D VTI-anisotropic CSEM inversion, based on the Gauss-Newton optimization. To reduce the memory requirements of the Gauss-Newton method we suggest to decouple the simulation and optimization domains, using node-based basis functions. We show that, in the 3D case, the memory required by the Jacobian can be reduced from hundreds to tens of TB. To speed up the CG solution of the GN system of normal equations the new preconditioner is suggested. This preconditioner is at least two times more efficient than the commonly used Jacobi preconditioner. With this new GN scheme a large datasets can be inverted in 3D with modest computer resources. The algorithm is succesfully validated on 2.5D and 3D marine CSEM datasets acquired at Mohns ridge.

Acknowledgments

We thank the ATLAB consortium for allowing us to present the results of inversion of Atlab-3 dataset. ATLAB consortium has received funding from Norwegian governmental institutions and industry. The reprocessed seismic data was provided by ShearWater.

REFERENCES

Amaya, M., Morten, J. P., & Boman, L. (2016). A low-rank approximation for large-scale 3D controlled-source electromagnetic Gauss-Newton inversion. *Geophysics*, *81*(3), E211–E225.

Balay, S., Abhyankar, S., Adams, M. F., Benson, S., Brown, J., Brune, P., et al. (2023). *PETSc/TAO users manual* (Tech. Rep. No. ANL-21/39 - Revision 3.20). Argonne National Laboratory.

Grayver, A. V., Streich, R., & Ritter, O. (2013). Three-dimensional parallel distributed inversion of CSEM data using a direct forward solver. *Geophysical Journal International*, *193*, 1432–1446.

Guennebaud, G., Jacob, B., et al. (2010). *Eigen v3.* http://eigen.tuxfamily.org.

Johansen, S. E., Panzner, M., Mittet, R., Amundsen, H. E. F., Lim, E. V., Landrø, M., et al. (2019). Deep electrical imaging of the ultraslow-spreading Mohns Ridge. *Nature*, *567*, 379–383.

Li, M., Abubakar, A., Liu, J., Pan, G., & Habashy, T. M. (2011). A compressed implicit Jacobian scheme for 3D electromagnetic data inversion. *Geophysics*, *76*(3), F173–F183.

Mittet, R., & Avdeeva, A. (2023). Gauss-Newton inversion with node-based basis functions: Application to imaging of seabed minerals in an area with rough bathymetry. *Geophysics*, accepted.

Nguyen, A. K., Nordskag, J. I., Wiik, T., Bjørke, A. K., Boman, L., Pedersen, O. M., et al. (2016). Comparing large-scale 3D Gauss-Newton and BFGS CSEM inversions. In *Seg expanded abstracts 2016* (pp. 872–877). SEG.

Nocedal, J., & Wright, S. J. (1999). *Numerical optimization.* New York: Springer-Verlag.

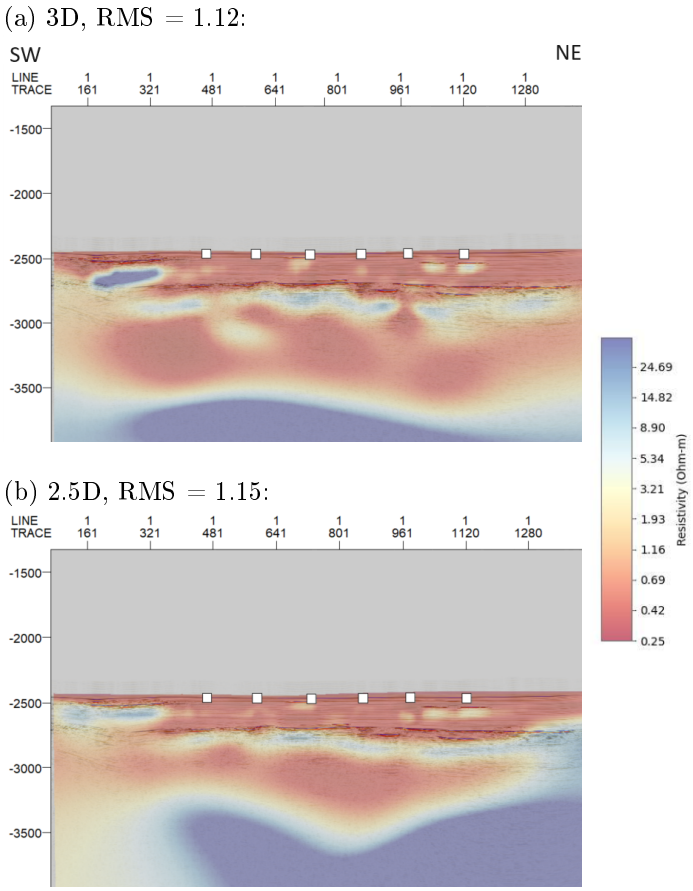

Figure 3: Comparison of 3D (top) and 2.5D (bottom) inversion results. The vertical resistivity images along central Atlab3 profile are shown. The seismic cross-section is plotted on top of the resistivity images for comparison.

problem size	$n_x \times n_y \times n_z$	$n_x^o \times n_y^o \times n_z^o$	**A** (GB)	**B** (GB)	**C** (GB)	$\mathbf{B_J}$ (GB)
2.5D, Atlab-3(2)	$415 \times 1 \times 167$	$157 \times 1 \times 43$	0.75	0.32	0.77	0.003
3D, small	$94 \times 169 \times 77$	$26 \times 53 \times 23$	5.2	6.5	0.007	0.06
3D, medium, Atlab-3(2)	$228 \times 214 \times 167$	$104 \times 97 \times 66$	40.6	45.7	0.15	0.57
3D, large	$622 \times 514 \times 101$	$199 \times 161 \times 18$	313	233	0.13	1.1

Table 1: Examples of memory requirements of the transformation matrices.

problem size	N_s	N_r	N_{tr}	N_{fr}	$n_x \times n_y \times n_z$	$\mathbf{J_\sigma}$ (GB)	$n_x^o \times n_y^o \times n_z^o$	$\mathbf{J_m}$ (GB)
2.5D, Atlab-3(2)	80	6	480	4	$415 \times 1 \times 167$	3.98	$157 \times 1 \times 43$	0.39
3D, small	57	12	467	3	$94 \times 169 \times 77$	102	$26 \times 53 \times 23$	2.6
3D, medium, Atlab-3(2)	240	18	4320	4	$228 \times 214 \times 167$	8392	$104 \times 97 \times 66$	685
3D, large	700	139	54813	5	$622 \times 514 \times 101$	527483	$199 \times 161 \times 18$	9421

Table 2: Examples of reductions of memory required by the Jacobian matrix. Here we assume that we invert fields $(\mathbf{E_x}, \mathbf{E_y}, \mathbf{H_x}, \mathbf{H_y})$ and $(\mathbf{E_x}, \mathbf{H_y})$ in 3D and in 2.5D cases, respectively.

7th International Symposium on Three-Dimensional Electromagnetics
Vancouver, BC, Canada, November 13–15, 2023

AEM Surveys Applied for Iron Formation Mapping: A Proxy for Iron Ore Exploration

Marco Antonio Couto Junior[1], Dionisio Uendro Carlos[1] and Raphael Fernandes Prieto[1]
[1]VALE S.A. (Ferrous Exploration Team)

Summary

The use of Airborne Electromagnetic data in iron ore exploration is yet not a standard approach to map mineralized iron formations and their relations with the host rocks. However, initial results conducted by VALE's ferrous geophysics team have been demonstrating promising on the potential use of such methodology. Both time and frequency domain data demonstrated a clear spatial correlation of strong resistors with the position of known mineralized iron formation layers in the Serra Sul region, Carajás Mineral Province, Brazil. This paper presents the first results and discusses the future challenges regarding the use of this type of data.

Keywords: AEM, Mineral Exploration, Iron Ore

Introduction

In mineral exploration, the Airborne Electromagnetic Methods (AEM) have become the benchmark in the geophysicist's utility belt to map highly conductive targets related to base metals mineralization. The variable set of AEM methods has demonstrated its effectiveness in mapping conductive massive sulfides related to all sorts of deposit styles for base metals, like porphyries, volcanogenic-hosted-massive sulfides (VHMS), orogenic gold, iron-oxide-copper-gold (IOCG), among others, for more than five decades - Okada (2022) and Ley-Cooper & Viezzoli (2017). However, concerning the exploration of iron ore with supergene alteration genesis, the method is still not a standard approach, with very scarce literature related to it, limiting it to a few case studies in the Hamersley Basin in Australia, as presented by Neroni et al. (2016) and Flis et al. (1998), although it demonstrated its significant value in mapping mineralized iron formations.

VALE's ferrous geophysics team in Brazil has been conducting a set of experiments regarding the use of AEM data to delineate the mineralized iron formation layers in the Carajás Mineral Province (CMP) and in the Iron Quadrangle Mineral Province (IQMP), Northern and Southeast Brazil, respectively. The early experiments started in 2020, with the execution of more than 18,000 km of RESOLVE surveys, a frequency domain electromagnetic (FDEM) airborne system. Most of these surveys focused on geotechnical and hydrogeological studies, but a few blocks were conducted over mineralized iron formation in both CMP and IQMP. These surveys demonstrated important resistive anomalies related to the iron ore formations.

Particularly, in the CMP, these resistive anomalies clearly present a strong spatial correlation with known mineralized iron formation in the Serra Sul iron mine. The comparison of these results with historical GEOTEM surveys, a transient electromagnetic (TEM) airborne system, showed a strong correlation of known mineralized iron formation with resistive zones on the district scale, supported by petrophysical data in key lithotypes related to the mineralization. These results supported and encouraged the execution of more than 7,000 km of Helitem surveys in the CMP, focusing on key iron ore targets, with promising results to offer more detailed resistivity mapping compared to the historical data and a significant complement to the standard approach in iron ore mapping, i.e., Airborne Gravity Gradiometry (AGG) and Airborne Magnetics (AMAG). This paper presents the Serra Sul results of these experiments conducted by the VALE ferrous team so far and points out future directions in AEM research for iron ore mapping.

Area of study

The study area is in the Serra Sul region in the CMP, Pará State, Brazil, particularly in the S11D mine and the S16 target (Figure 1a). In this area, the iron formation is composed by compact jaspelites layers from the Carajás Formation at the botton of the sequence, followed by friable hematite towards to the top of the layer, due to the supergene alteration process - Silva & Costa (2020). On the top of it, iron crust occurs as the product of the foremost supergene alteration process within the iron formation. The host rocks for the iron formation are composed by metabasalts from the Igarapé-Cigarra and Parauapebas Formations to the North and South, respectively (Figure 2b).

Material and Methods

The AEM Surveys

The AEM surveys studied in this work are composed of GEOTEM, Helitem, and RESOLVE data. The basic system information and flight specs are presented in Tables 1 and 2 for the airborne TEM and FDEM systems, respectively. All surveys present the magnetic data acquired jointly, but only the AEM data will be discussed here.

Specification	GEOTEM	Helitem
Base Freq. (Hz)	90	30
Waveform Type	Half-sine	Rectangular
Pulse Width (ms)	2.08	8.89
Dipole Moment (NIA)	418,000	461,000
No. of Channels	20	25
Terrain Clearence (m)	120	50-60
Line Spacing (m)	250	100
Line Direction	N-S	N-S

Table 1: Specifications for the airborne TEM systems: GEOTEM and Helitem.

Dip. Moment (Am2)	Coil Orient.	Freq.
359	HCP	400 Hz
187	HCP	1.8 kHz
150	VCA	3.3 kHz
72	HCP	8.2 kHz
49	HCP	40 kHz
17	HCP	140 kHz

Table 2: Specifications for the RESOLVE system. HCP: horizontal coplanar and VCA: vertical coaxial coil orientations. The survey was conducted with 50 m line spacing, 63 m terrain clearence and N-S orientation. For futher details about the RESOLVE system, check Geosci.xyz documentation.

Data Processing and Modeling Approach

The modeling approach was based on different commercial inversion solutions for each type of AEM data: FDEM and TEM.

The RESOLVE data were processed by the contractor, which focused on the removal of any anthropogenic and/or coupling effects within the data. No additional processing was applied. The inversion was conducted using the 1D VOXI-EM suite available in Seequent Oasis Montaj software, which solves for the electrical conductivity using the approach from Ellis (1999) and minimizes the objective function using the Tikhonov minimum gradient regularizer. We followed all the recommendations presented in the VOXI-EM Seequent's documentation, running unconstrained inversions. The mesh was defined with regular cells with 1/4 line spacing horizontal dimensions and a 5 m vertical dimension. The estimated error was defined as the data relative error noise floor for each RESOLVE's frequency, based on the noise level measured during the altitude flights (we used 5% or 10% depending on the frequency).

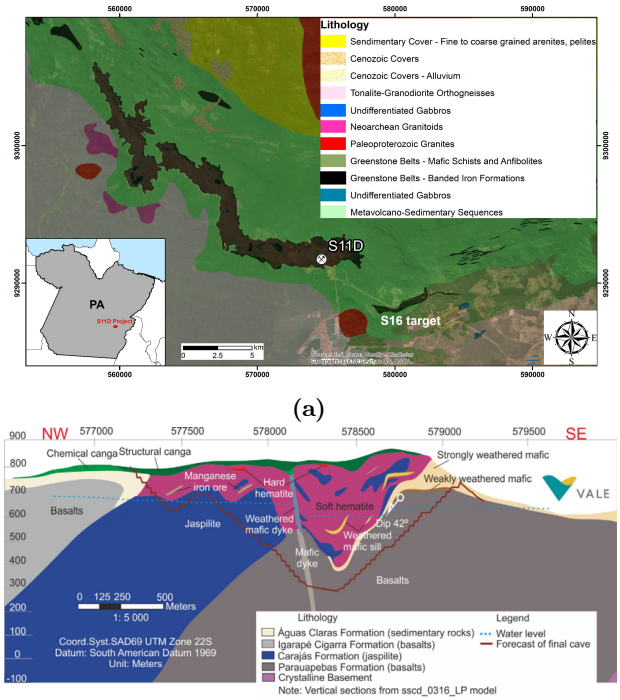

Figure 1: (a) Serra Sul region in the CMP. The S11D mine and S16 target are indicated. (b) NE-SW schematic section in the S11D region - figure from Silva & Costa (2020).

The GEOTEM data were not processed or modeled due to the incompleteness of information regarding this historical data; they were only used for dB/dt and apparent conductance maps for interpretation. Nevertheless, the Helitem data were processed using the AGS Workbench suite, with the application of automatic processing and further manual/visual refinement, following a similar approach presented in Auken et al. (2009). The automatic processing focused on running moving averages for each time regime (narrow and wide time windows for early and late times, respectively) and on removing steep decays to cull out any induced polarization (IP) effects present in the data. Additionally, the noise floor estimation was conducted based on the data standard deviation, and it was considered to remove noisy data in the late times.

The Helitem data were finally inverted using the Spatial-Constrained-Inversion (SCI) technique - Viezzoli et al. (2008), based on the AarhusInv code workflow presented in

Auken et al. (2015), implemented in the AGS Workbench, which applies a modified Marquardt optimization process. This technique is based on a 1D inversion approach, but with spatial constraints along and between the flight lines, aiming to recover a quasi-3D model. In this work, the 1D models were smoothly discretized into 25 layers, with a 5 m thickness for the first layer, logarithmically increasing downwards until a 500 m depth. The smooth model assumes that the layer resistivities can vary freely through the model with fixed thicknesses. The starting resistivity model considered a 500 $\Omega{\cdot}m$ semi-space, constrained with a factor of 1.3, meaning that 30% variations from the initial model were allowed.

Results

The analysis started in the S11D mine with the RESOLVE survey data in this area (Figure 2c). The RESOLVE inversion recovered a strong resistive body (conductivity values smaller than 10^{-5} mS/m) with a clear spatial association with the position of known iron formation layers in the D body in the S11D mine, as shown in Figure 2a, suggesting its continuation into the C body (the contact zone is indicated in Figure 2a). In fact, the strong resistive anomaly spatially agrees quite well in depth with the known undivided iron formation (which includes all types of iron bodies, mainly: jaspelite, friable hematites, and iron crust). The petrophysical data from the borehole geophysics in the S11D mine (not shown in this paper) confirmed this resistivity contrast between the undivided iron formation (resistivity values greater than 1000 $\Omega{\cdot}m$) from the Carajás Formation and their host rocks composed by the weathered altered mafic units from the Parauapebas and Igarapé-Cigarra Formations (resistivity values smaller than 500 $\Omega{\cdot}m$).

Regionally, the GEOTEM apparent conductance demonstrated this continuity to the whole S11 body, towards NW (Figure 2c), with conductance values around zero.

As mentioned earlier, these results motivated the execution of newer Helitem surveys in the Serra Sul region. Although these surveys did not cover the same area as the RESOLVE survey, they covered the S16 target, a key mineralization for the Serra Sul exploration program. The processed and modeled data using the SCI approach are presented in Figure 4. The raw data showed a strong resistive domain over the plateau of the iron formation (an amplitude drop in the dB/dt data), and the suggestion of a strong IP effect in the region of the mafic units to the southern portion of the area, indicated by the late times negative values. The IP effect was not addressed in this work yet, as the real resistivity parameterization was used. The SCI model indicates the continuity of the resistive anomaly related to the mineralized iron formation layer to the Northern region of the plateau, as indicated by the lithological borehole information in Figure 3b.

Spatially, the Helitem data present a strong resistor (values greater than 1000 $\Omega{\cdot}m$) associated with the iron formation plateau in the S16 target region, suggesting its continuity towards the Eastern portion of the area. In comparison with the conductance information recovered from the regional GEOTEM data in the same area, a significant improvement in the resistivity model spatial resolution can be noted.

Discussion and Next Steps

The AEM data in the Serra Sul area proved to be useful in mapping the strong resistor associated with known mineralized iron formation layers. These resistors are also strongly correlated with AGG and AMAG data (not shown in this paper), which are the standard geophysical approaches for iron ore exploration in VALE's deposits in Brazil. Although this is not discussed in this paper, the AEM data provided greater spatial resolution in comparison to these other two methodologies, becoming an additional geophysical tool for iron ore exploration.

However, a set of challenges still remains regarding the optimal use of AEM data. The first is properly addressing data distortion due to natural effects related to the EM fields and their relationship with subsurface mineral content, such as the IP and the superparamagnetic effects. The Helitem and RESOLVE data clearly highlight the significance of these distortions in the iron ore context, showing negative late-time transients and negative signals at the lower frequencies (for the FDEM data, not shown in this paper), respectively. Properly addressing these effects will allow to recover more reliable resistivity models and achieve better geological interpretation.

The second challenge concerns the best way to integrate the AEM with AGG and AMAG data seeking to improve their interpretation, specially for non-geophysicists fellow colleagues. VALE's ferrous geophysics team is currently addressing this topic in collaboration with MIRA Geoscience, developing an AEM processing suite based on Auken et al. (2009) and joint 3D inversions of all these three methodologies. The project is ongoing and the first results applying the cross-gradient approach for joint inversions demonstrated promising results to improve each methodology inversion. Our team is also currently exploring Artificial Intelligence approaches, working on the creation of Machine Learning models as lithological predictors, seeking to improve the use of geophysical data for the geological framework modeling, a key step in the resource estimation. The initial results (not presented in this paper) are very promising and they should be improved with better data processing and modeling.

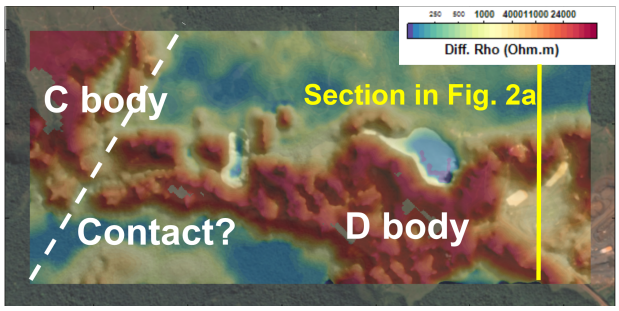

(a)

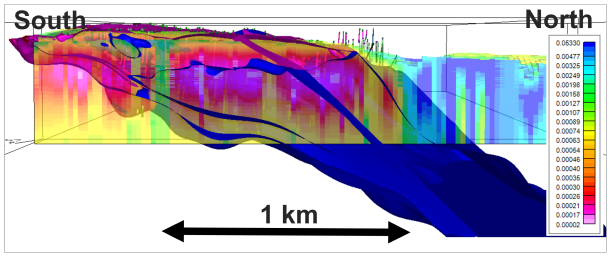

(b)

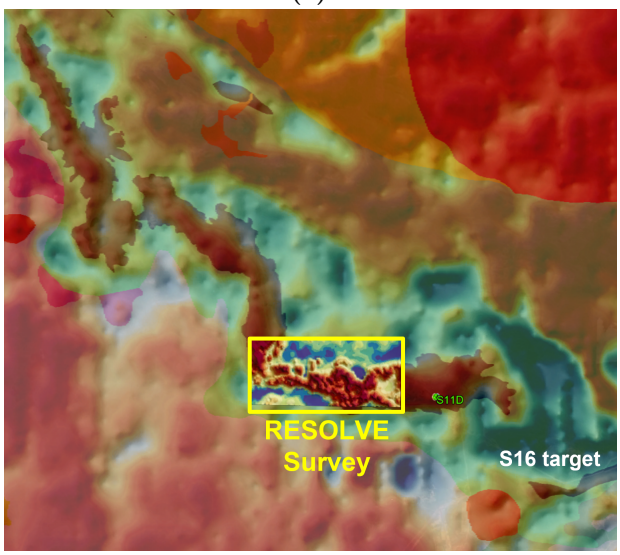

(c)

Figure 2: (a) RESOLVE survey area in S11D mine, with the indication of mineralized bodies C and D over the resistivity map for this area. (b) RESOLVE conductivity model (in mS/m) for the profile indicated in Figure 2a. (c) GEOTEM apparent conductance map over the geological map (50% transparency) in the Serra Sul area, including all mineralized bodies in the S11 deposit and the S16 target, and the RESOLVE survey area. Red and blue colors mean lower and higher conductance domains.

Conclusion

The Serra Sul case demonstrated that the AEM data is an useful tool in the geophysicist's options to be applied in iron ore exploration. The mineralized iron formations clearly present an important spatial correlation with strong resistors in this geological environment, allowing to define their contact within the mafic host rocks. However, proper data processing and modeling routines, along with optimal data integration with other geophysical methodologies are the current challenges on the use of this data. VALE'geophysics team already started to investigate these problems, bringing exciting discussion in the near future.

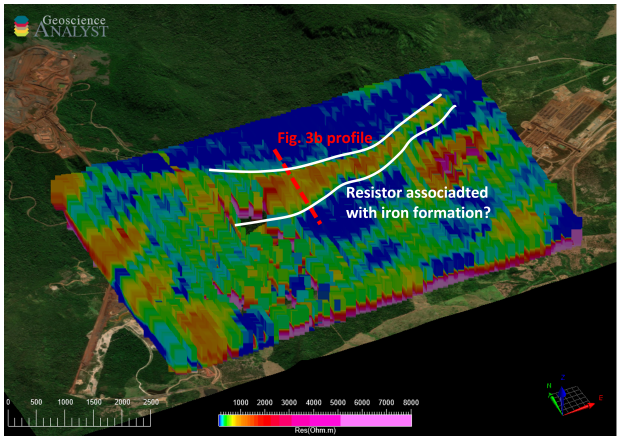

(a)

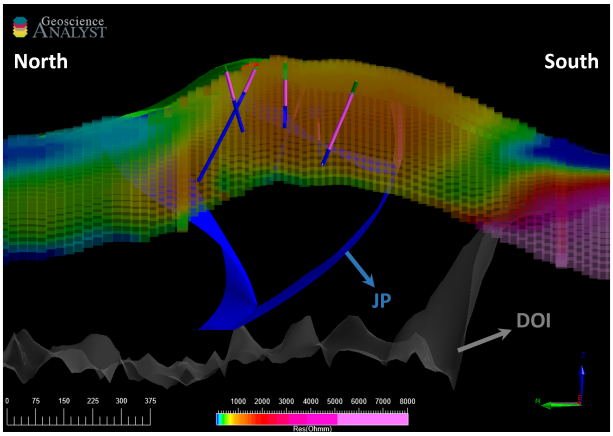

(b)

Figure 3: (a) Helitem SCI model (resistivity) over the S16 target. (b) SCI section indicated in Figure 3a. The lithological borehole data and the geological models are presented in the section. The lithological color code follows the one in Figure 2b.

Acknowledgments

The authors would like to thank VALE S.A. for the permission of this publication. They also thank Seequent and AGS for the Workbench trial license used to process and run the inversions of the Helitem data.

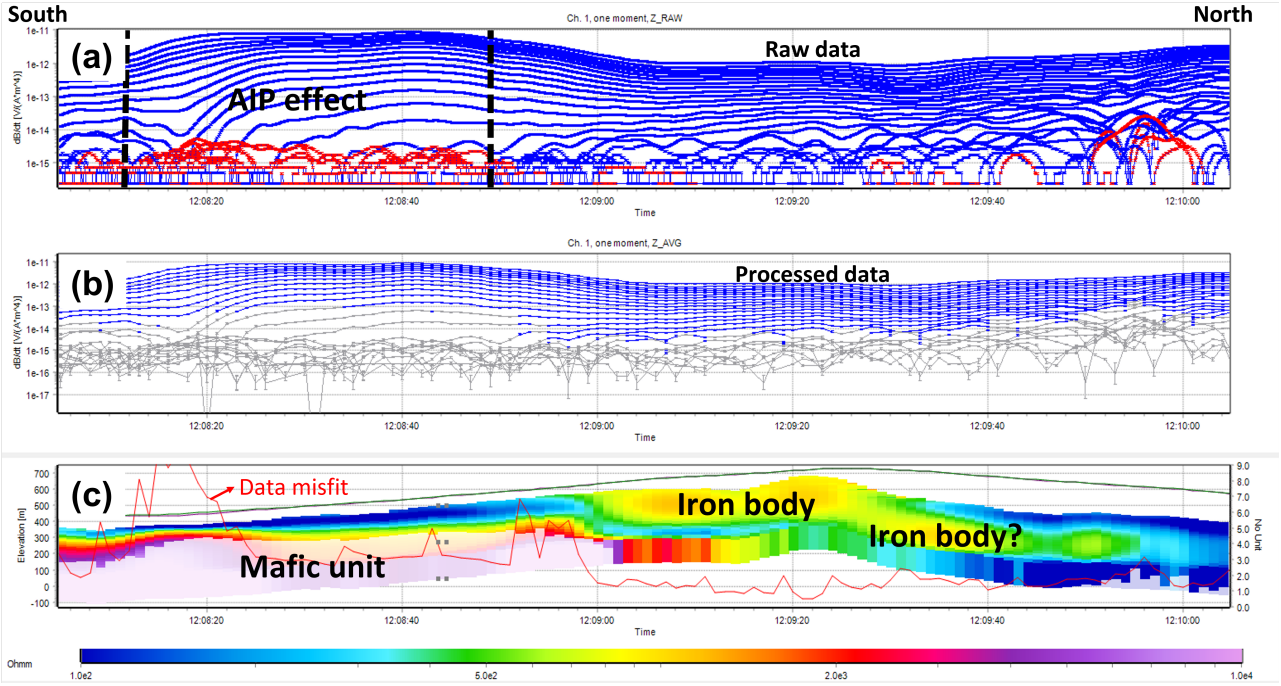

Figure 4: Helitem processing and SCI model over the S16 target with geological interpreted. (a) Raw data. (b) Processed data. (c) SCI resistivity section. This section refers to the one indicated in Figure 3a.

REFERENCES

Auken, E., Christiansen, A. V., Kirkegaard, C., Fiandaca, G., Schamper, C., Behroozmand, A. A., et al. (2015). An overview of a highly versatile forward and stable inverse algorithm for airborne, ground-based and borehole electromagnetic and electric data. *Exploration Geophysics*, *46*(3), 223-235.

Auken, E., Christiansen, A. V., Westergaard, J. H., Kirkegaard, C., Foged, N., & Viezzoli, A. (2009). An integrated processing scheme for high-resolution airborne electromagnetic surveys, the SkyTEM system. *Exploration Geophysics*, *40*(2), 184-192.

Ellis, R. G. (1999). Smooth 3D inversion of airborne transient electro-magnetic data using the TFQMR-FFT fast integral equation method. In *Proceedings of the Second International Symposium on Three-Dimensional Electromagnetics*. The University of Utah.

Flis, M., Hawke, P., & McMillan, A. (1998). The application of multifrequency airborne electromagnetics to iron ore exploration. *Exploration Geophysics*, *29*(1-2), 254-258.

Ley-Cooper, A., & Viezzoli, A. (2017). Airborne EM: An Important Exploration Method for Revealing Geological Insights into the Subsurface. In Y. Berbers & W. Zwaenepoel (Eds.), *Proceedings of Exploration 17: Sixth Decennial International Conference on Mineral Exploration.* Decennial Minerals Exploration Conferences.

Neroni, R., Murray, R., & Kepert, D. (2016). Application of the airborne electromagnetic method for Banded Iron-Formation mapping in the Hamersley Province, Western Australia. *ASEG Extended Abstracts*, *2016*(1), 1-8.

Okada, K. (2022). Breakthrough technologies for mineral exploration. *Mineral Economics*, *35*, 429-454.

Silva, A. C. S., & Costa, M. L. (2020). Genesis of the 'soft' iron ore at S11D Deposit, in Carajás, Amazon Region, Brazil. *Brazilian Journal of Geology*, *50*(1).

Viezzoli, A., Christiansen, A. V., Auken, E., & Sørensen, K. (2008). Quasi-3D modeling of airborne TEM data by spatially constrained inversion. *Geophysics*, *73*(3), F105-F113.

Airborne Natural Source Electromagnetics Using an Arbitrary Base Station

Devin C. Cowan[1], Lindsey J. Heagy[2] and Douglas W. Oldenburg[3]
University of British Columbia

SUMMARY

The expensive and time-consuming nature of magnetotelluric (MT) surveys has motivated the development of airborne natural source EM (NSEM) systems, which includes Z-axis Tipper EM (ZTEM), quantum audio magnetotellurics (QAMT) and MobileMT. These systems compute transfer functions from airborne magnetic data, and horizontal field measurements at a base station located on the Earth's surface. Available literature offering in-depth analysis of the factors that influence airborne NSEM data and inversion results remains sparse; especially for systems that measure electric fields at the base station. In our work, we characterize the nature of QAMT data, and by extension MobileMT data. We demonstrate the impact of the conductivity at the base station on ZTEM and QAMT anomalies. And we investigate the impact of the starting and reference model on ZTEM and QAMT inversion results when the conductivity at the base station differs significantly from the host conductivity within the survey region. Our analysis determined that QAMT data are directly sensitive to the conductivity at the base station, and that QAMT anomalies are produced by anomalous magnetic fields arising from 3D structures within the survey region. Like ZTEM, models recovered through QAMT inversion depend significantly on the choice in starting and reference models. When the conductivity near the base station differs significantly from the background conductivity within the survey region, target structures are likely recovered erroneously. When the true host conductivity within the survey region is used as the starting and reference models, both ZTEM and QAMT inversions recover conductive and resistive structures appropriately regardless of base station conductivity. However, structures are also recovered near the base station. And these structures likely assist in fitting signatures produced by targets within the survey region, thus reducing our confidence in the recovered model.

Keywords: QAMT, ZTEM, inversion, airborne natural source EM

INTRODUCTION

Natural source electromagnetic (NSEM) methods have long been used to characterize the distribution of subsurface electrical conductivities (Tikhonov, 1950, Cagniard, 1953; Ward 1959; others). NSEM data are generated by computing the transfer functions that relate directional components of the Earth's natural magnetic (and electric) fields. Ground-based magnetotelluric (MT) data extract the most comprehensive information from the Earth's NSEM fields and are directly sensitive to subsurface conductivities (Cagniard, 1953). However, the expensive and time-consuming nature of MT surveys has motivated the development of airborne NSEM systems.

Airborne NSEM systems compute transfer functions from airborne magnetic data, and horizontal field measurements at a base station located on the Earth's surface. Z-axis Tipper EM (ZTEM) computes transfer functions from z-component airborne magnetic data and horizontal magnetic fields at a base station (Lo and Zang, 2008). Although much more economic than MT surveys, ZTEM data are collected within a relatively narrow frequency band (30 Hz - 720 Hz) and are only sensitive to contrasts in electrical conductivity across vertical interfaces. To economically collect MT-like impedance data, the quantum audio magnetotellurics (QAMT) system was developed. This system measures horizontal airborne magnetic fields and horizontal electric fields at the base station (Larnier et al., 2021). MobileMT (MobileMT) measures comparable fields to QAMT and outputs the data as apparent conductivities via internally computing the determinant of the admittance tensor (Sattel et al., 2019).

Available literature offering analysis of the factors that influence airborne NSEM data and inversion results remains sparse. This is especially true for systems that measure electric fields at the base station; e.g. a fundamental analysis of the differences between MT and QAMT impedances. We do know from several studies (Sattel et al., 2019; Holtham, 2012; others) that both ZTEM and MobileMT inversion results are significantly impacted by the choice in starting model. However, because the signals contained with airborne NSEM data are unique to each system, it would be worthwhile to compare inversion results across multiple systems for the same set of inversion parameters.

Our work starts by characterizing the signals present in airborne NSEM data for a base station that measures electric fields; for similar analysis of ZTEM data, see (Lo and Zang, 2008; Holtham, 2012). We discuss the nature of QAMT impedance data before simulating and

comparing MT and QAMT data over a conductor and a resistor. Numerical simulation is then used to characterize the impact of the conductivity at the base station on 3D ZTEM and QAMT anomalies. Unconstrained inversion is used to demonstrate how ZTEM and QAMT inversion results are influenced when the conductivity at the base station differs significantly from the host conductivity within the survey region. Inversion is performed using the conductivity at the base station as the starting and reference models. Then the true host conductivity within the survey region is used as the starting and reference models.

NATURE OF QAMT IMPEDANCES

Defining the QAMT impedance tensor

Starting from the 2x2 impedance tensor that defines MT data (Holtham, 2012), we derive an expression for the 2x2 impedance tensor defining QAMT data. For MT, the impedance tensor is defined as:

$$\begin{bmatrix} Z_{xx} & Z_{xy} \\ Z_{yx} & Z_{yy} \end{bmatrix} = \begin{bmatrix} E_x^{(x)} & E_x^{(y)} \\ E_y^{(x)} & E_y^{(y)} \end{bmatrix} \begin{bmatrix} H_x^{(x)} & H_x^{(y)} \\ H_y^{(x)} & H_y^{(y)} \end{bmatrix}^{-1} \quad (1)$$

where impedances Z_{ij} define the relationships between horizontal electric and magnetic fields for 2 incident planewave polarizations; denoted by superscripts (x) and (y). Expression (1) implies that anomalies observed in the MT impedance data depend on spatial variations in both electric and magnetic field measurements throughout the survey area. Let us now restate expression (1) more concisely as:

$$\boldsymbol{Z = E_{rx} H_{rx}^{-1}} \quad (2)$$

where the subscript rx refers to a non-stationary receiver location. When collecting QAMT data, the electric fields used to compute the impedances are measured at a base station (Larnier, et al., 2021). We therefore define the 2x2 impedance tensor for QAMT as:

$$\boldsymbol{Q = E_b H_{rx}^{-1}} \quad (3)$$

where subscript b refers to fields measured at the base station. We let Q_{ij} denote the QAMT impedances within the tensor. Using expression (2) and (3), we obtain:

$$\boldsymbol{Q = E_b E_{rx}^{-1} E_{rx} H_{rx}^{-1} = E_b E_{rx}^{-1} Z} \quad (4)$$

According to expression (4), QAMT impedances are equivalent to removing the direct influence of spatial variation in the electric field from MT impedances and normalizing the quantity by the electric fields measured at the base station. We therefore expect the shape and location of anomalies within QAMT impedance data to be primarily driven by anomalous magnetic fields within the survey area. And electric fields act as more of a scaling factor for QAMT anomalies.

Numerical Simulation for a Synthetic Model

To better understand expression (4), we use SimPEG (Heagy, et al., 2017) to simulate the NSEM fields and impedances for a model consisting of a conductor (0.01 S/m) and a resistor (0.0001 S/m) within a halfspace (0.001 S/m); see Figure 1. We quantify the change in amplitude and phase experienced by the NSEM fields due to the conductor and resistor for an incident planewave polarization along the x-direction, relative to the fields for a 0.001 S/m halfspace. We then examine MT and QAMT anomalies to determine whether they are driven by anomalous electric or magnetic fields.

Electric and magnetic fields are simulated at the Earth's surface for both the block and halfspace models. Both the conductor and resistor are buried at a depth of 300 m, and have dimensions 2000 m x 600 m x 500 m. The simulated fields are then used to compute Z_{xy} and Q_{xy} impedances. In this paper, all fields and impedances are simulated using a $-i\omega t$ Fourier convention with X = Northing, Y = Easting and Z +ve downward.

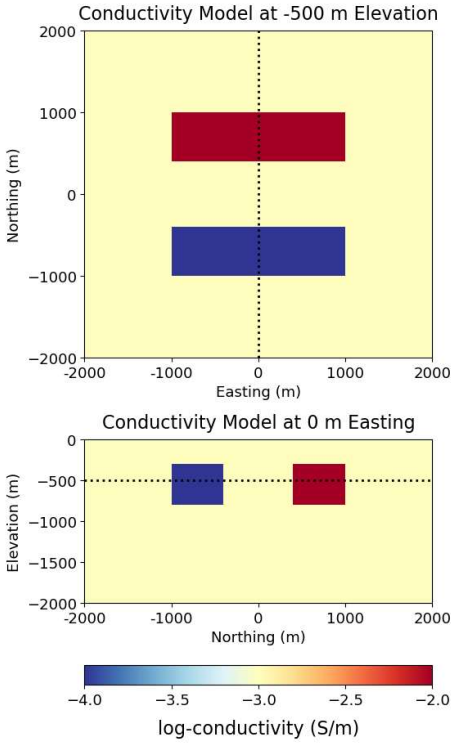

Figure 1. Conductivity model.

For our analysis, we consider fields $E_x^{(x)}$ and $H_y^{(x)}$, as defined in expression (1), and impedances Z_{xy} and Q_{xy}. To characterize the impact of the conductor and resistor on the amplitudes, we compute the percent amplitude difference. I.e.:

$$\%\ \text{ampl. diff.} = 100\% \times \left(\frac{|f(\sigma_{block})| - |f(\sigma_{hs})|}{|f(\sigma_{hs})|} \right) \quad (5)$$

And for the phase, we compute the difference in amplitude. I.e.

$$\text{Phase diff} = |\varphi(\sigma_{block})| - |\varphi(\sigma_{hs})| \quad (6)$$

In Figure 2, we illustrate the impact of the conductor and resistor on the amplitudes of $E_x^{(x)}$ and $H_y^{(x)}$, Z_{xy} and Q_{xy} at 360 Hz. And in Figure 3, we illustrate the impact on the phase at 360 Hz. Comparing Figures 2a and 3a to Figures 2b and 3b, we see that anomalous electric fields produce much stronger and more compact signatures than anomalous magnetic fields in both amplitude and phase. Therefore, natural source electric fields are much more impacted by confined structures than magnetic fields. When examining the size and location of the signatures in Figures 2c and 3c, we see that signatures in Z_{xy} are highly correlated with those in $E_x^{(x)}$ (Figures 2a and 3a) and effectively uncorrelated with those in $H_y^{(x)}$ (Figures 2b and 3b); implying anomalous electric fields are almost entirely responsible for anomalous signatures in MT impedance data. However, when examining the size and location of signatures in Figures 2d and 3d, we see that signatures in Q_{xy} are highly correlated with those in $H_y^{(x)}$ (Figures 2b and 3b) and uncorrelated with those in $E_x^{(x)}$ (Figures 2a and 3a). This supports our assertion following expression (4) that the shape and amplitude of QAMT impedance anomalies are primarily driven by anomalous magnetic fields within the survey region.

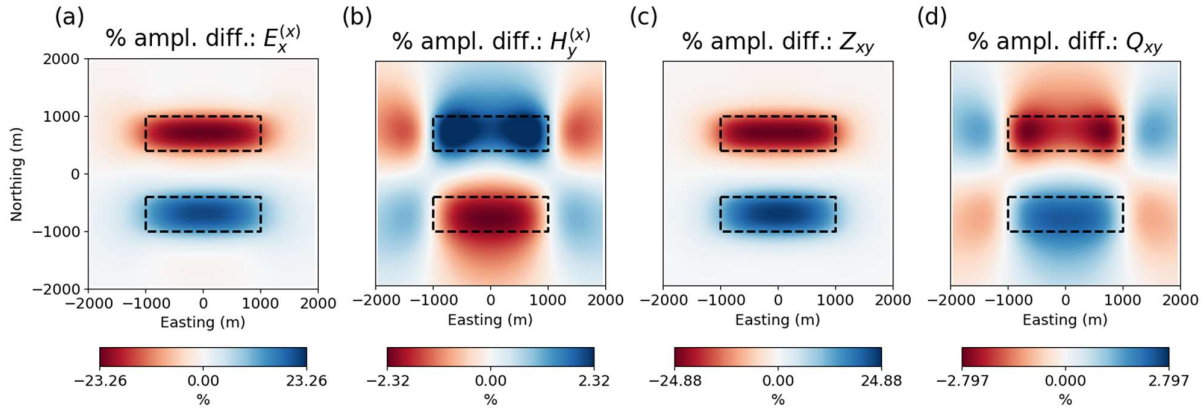

Figure 2. % amplitude difference at 360 Hz for (a) $E_x^{(x)}$, (b) $H_y^{(x)}$, (c) Z_{xy} and (d) Q_{xy}.

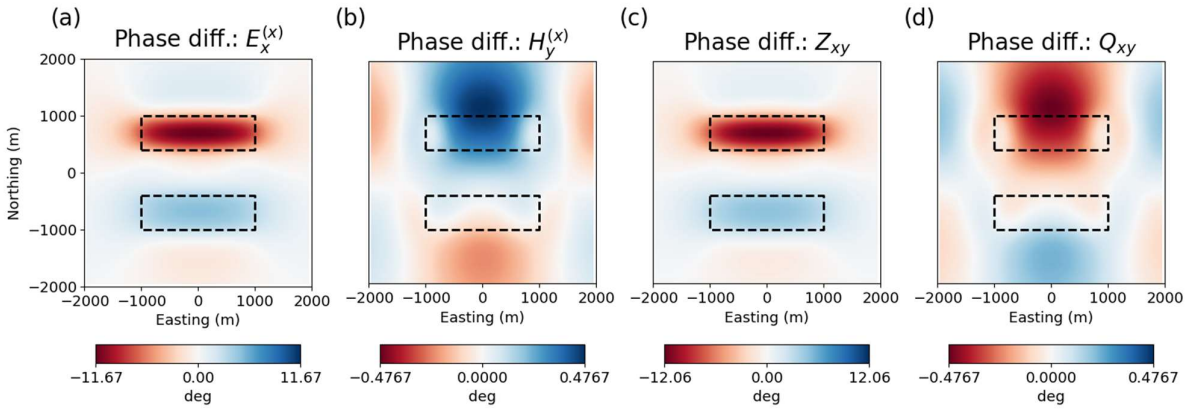

Figure 3. Phase difference at 360 Hz for (a) $E_x^{(x)}$, (b) $H_y^{(x)}$, (c) Z_{xy} and (d) Q_{xy}.

INFLUENCE OF BASE STATION CONDUCTIVITY ON AIRBORNE NSEM ANOMALIES

Base station conductivity defines the conductivity within the region that influences field measurements at the base station. Here, we characterize the influence of the base station conductivity on ZTEM and QAMT anomalies due to 3D structures within the survey region. Magnetic fields are simulated for the block model illustrated in Figure 1; wherein a conductor (0.01 S/m) and a resistor (0.0001 S/m) are buried within a 0.001 S/m host. Assuming the base station is sufficiently far away from the survey region, and that the NSEM fields at the base station can be characterized by a local halfspace, we simulate the horizontal electric and magnetic fields for halfspace conductivities of 0.0001 S/m, 0.001 S/m and 0.01 S/m. From the simulated fields, QAMT impedances are computed according to expression (4) and ZTEM data are computed according to (Holtham, 2013):

$$\begin{bmatrix} \mathrm{T_{zx}} \\ \mathrm{T_{zy}} \end{bmatrix} = \begin{bmatrix} H_x^{(x)} & H_x^{(y)} \\ H_y^{(x)} & H_y^{(y)} \end{bmatrix}_{\mathrm{b}}^{-1} \begin{bmatrix} H_{\mathrm{z}}^{(x)} \\ H_{\mathrm{z}}^{(y)} \end{bmatrix}_{\mathrm{rx}} \tag{7}$$

In Figure 4, we show the real and imaginary components of T_{zy} at 360 Hz for base station conductivities of 0.0001 S/m, 0.001 S/m and 0.01 S/m. We see the shape and amplitude of the anomalies in the tipper plots is consistent regardless of the base station conductivity. Thus in the absence of 3D structure at the base station, ZTEM data provide information solely about structures within the survey region.

In Figure 5, we show the real and imaginary components of Q_{xy} impedance data at 360 Hz for base station conductivities of 0.0001 S/m, 0.001 S/m and 0.01 S/m. Each time the base station conductivity is increased by a factor of 10, both the real and imaginary components of Q_{xy} are decreased by roughly a factor of $\sqrt{10}$, implying the amplitudes of QAMT impedances are proportional to the inverse square-root of the base station conductivity.

INVERSION USING BASE STATION CONDUCTIVITY

Here, we examine how ZTEM and QAMT inversion results are impacted when the base station conductivity differs significantly from the host conductivity within the survey region. Synthetic data are generated and inverted using the UBC-GIF E3DMT v2 code (Shekhtman, et al., 2023). The code uses a weighted least-squares approach (Li and Oldenburg, 1996), which minimizes an objective function of the form:

$$\varphi(m) = \varphi_{\mathrm{d}}(m) + \beta\varphi_{\mathrm{m}}(m) \tag{8}$$

The data misfit φ_{d} is 2-norm the weighted residual between observed and predicted data for a model m. And

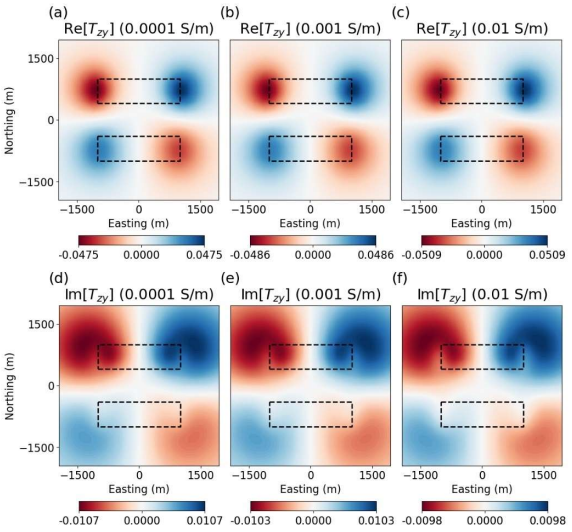

Figure 4. Real and imaginary components of Tzy at 360 Hz for base station conductivities of 0.0001 S/m, 0.001 S/m and 0.01 S/m.

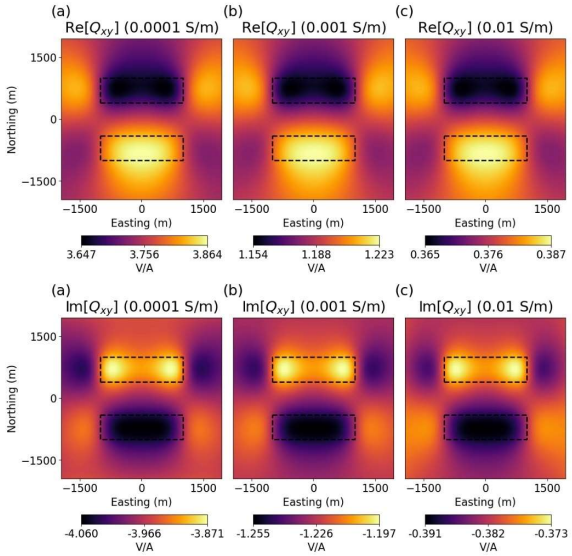

Figure 5. Real and imaginary components of Qxy at 360 Hz for base station conductivities of 0.0001 S/m, 0.001 S/m and 0.01 S/m.

β is the trade-off parameter that balances the data misfit and regularization given by:

$$\varphi_{\mathrm{m}}(m) = \alpha_s \int w_{\mathrm{s}} \, |m\text{-}\mathrm{m_{ref}}|^2 dv + \sum_{\mathrm{x,y,z}} \alpha_{\mathrm{i}} \int w_{\mathrm{i}} \left| \frac{\partial \mathrm{m}}{\partial \gamma_{\mathrm{i}}} \right|^2 dv \tag{9}$$

Constants α_{i} weight the relative contributions of the smallness and smoothness terms, $\mathrm{m_{ref}}$ is the reference model, and $\mathrm{w_i}$ are user-defined weighting functions.

For this exercise, we assume that the base station conductivity is known and is used to set the starting and reference models for the inversion. And to reduce the impact of the reference model, we set $\alpha_s = 10^{-10}$ and $\alpha_x = \alpha_y = \alpha_z = 1$.

The model we intend to recover within the survey region was illustrated in Figure 1 and consists of a conductor (0.01 S/m) and a resistor (0.0001 S/m) buried within a 0.001 host. Synthetic QAMT data are generated at frequencies of 45 Hz, 90 Hz, 270 Hz, 720 Hz and 2160 Hz. Synthetic ZTEM data are generated for the first 4 frequencies. The base station used to generate both QAMT and ZTEM data is located at (-30000, 0, 0). Synthetic QAMT and ZTEM data are generated for base station conductivities of 0.0001 S/m, 0.001 S/m and 0.01 S/m; wherein these conductivities are assigned to all cells within 2 skin depths of the base station at the lowest frequency.

In Figure 6, we show the recovered models from ZTEM inversion due to different base station conductivities. These cases represent the outcomes when the base station conductivity is known and assumed to be equal to the host conductivity. When the base station conductivity is equal to the host conductivity (Figure 6b), ZTEM inversion recovers the conductor and resistor appropriately. For a base station conductivity of 0.0001 S/m (Figure 6a), the conductor and the top of the resister are recovered at much larger depths. And the recovered background conductivity is approximately equal to the base station conductivity. For a base station conductivity of 0.01 S/m (Figure 6c), the conductor and resister are recovered at the surface. And the recovered background conductivity is approximately equal to the base station conductivity.

In Figure 7, we show the recovered models from QAMT inversion due to different base station conductivities. These cases represent the outcome when apparent conductivities computed from QAMT impedances are directly used to choose starting and reference models. When the base station conductivity is equal to the host conductivity (Figure 7b), QAMT inversion recovers the conductor and resistor at appropriately. For a base station conductivity of 0.0001 S/m (Figure 7a), the conductor and the top of the resister are recovered at much larger depth. And the recovered background conductivity is approximately equal to the base station conductivity. For a base station conductivity of 0.01 S/m (Figure 7c), the conductor and resister are recovered at the surface. And the recovered background conductivity is approximately equal to the base station conductivity.

This exercise shows that despite collecting MT-like impedances, QAMT inversion suffers from the same challenges as ZTEM inversion; i.e. that over/underestimation of the starting and reference

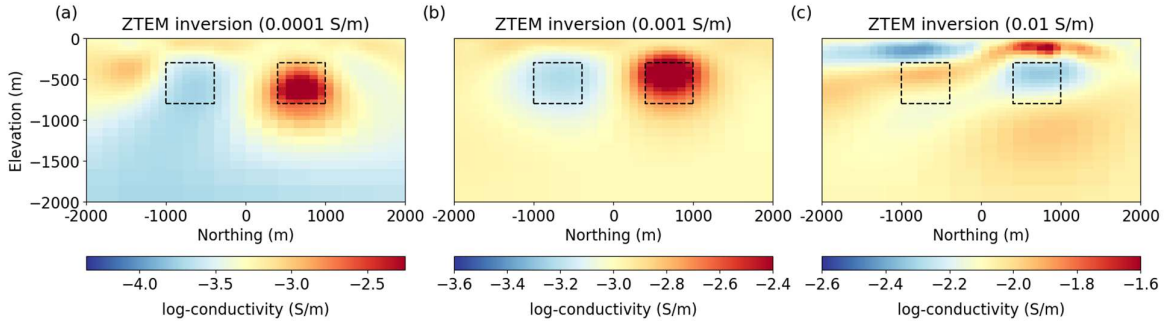

Figure 6. Models from ZTEM inversion where the base station conductivity is used as the starting and reference models: (a) 0.0001 S/m, (b) 0.0001 S/m and (c) 0.01 S/m.

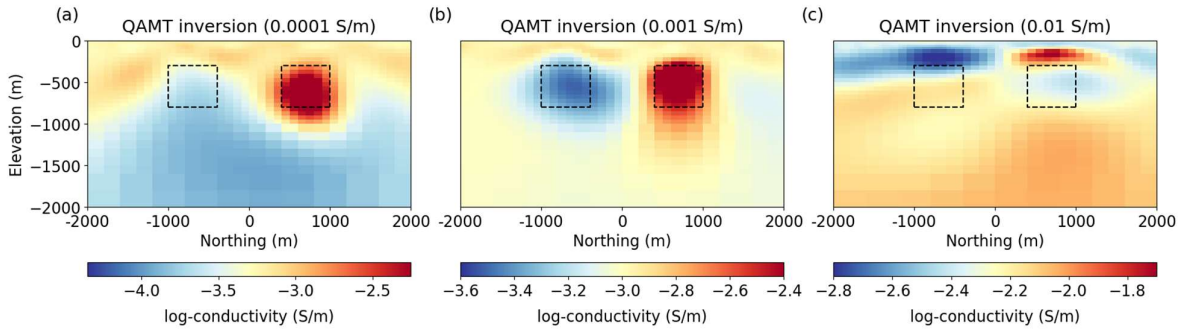

Figure 7. Models from QAMT inversion where the base station conductivity is used as the starting and reference models: (a) 0.0001 S/m, (b) 0.0001 S/m and (c) 0.01 S/m.

models will lead to the recovery of conductors and resistors at erroneous depths. And that choosing a starting and/or reference model directly from apparent conductivities, which are directly sensitivity to the base station conductivity, may not be advisable for QAMT inversion.

INVERSION USING HOST CONDUCTIVITY

Here, we illustrate the ZTEM and QAMT inversion results for different base station conductivities when the true host conductivity within the survey region is known and is used as the starting and reference models.

In Figure 8, we show the recovered models from ZTEM inversion within the survey region due to different base station conductivities. Regardless of the base station conductivity, structures are recovered consistently and at the appropriate depths when the true host conductivity is used as the starting and reference models. Furthermore, the recovered background conductivity is approximately equal to the true host conductivity of 0.001 S/m. Similar results are observed in Figure 9, where we show the recovered models from QAMT inversion within the survey region due to different base station conductivities. Compared ZTEM, QAMT inversion results show a higher contrast in conductivity between recovered structures and the host. However, there also appears to be a little more variation in the recovered models.

In Figure 10, we show the recovered models from ZTEM inversion near the base station. Here, the inversion appears to recover smooth 3D resistive structures, regardless of the true base station conductivity. In Figure 11, we show the recovered models from QAMT inversion near the base station. When the base station conductivity and host conductivity within the survey region are equal, there is no structure recovered at the base station. However when the base station conductivity and host conductivity differ significantly, the inversion recovers significant structure near the base station.

DISCUSSION

Our work started by characterizing the signals present in airborne NSEM data for a base station that measures electric fields. Like ZTEM, QAMT anomalies were shown to result from anomalous magnetic fields produced by 3D structures within the survey region, which are then scaled by field measurements at the base station. And compared to MT impedance anomalies, QAMT impedance anomalies are smaller in amplitude. Assuming the fields at the base station are characterized by a conductive halfspace, we showed that the amplitudes of QAMT impedances are inversely proportional to the square-root of the base station conductivity. We however expect the relationship between QAMT anomalies and the base station conductivity to be more complicated in the presence of 3D structures near the base station.

Recovered models from weighted least-squares inversion of ZTEM and QAMT data are both highly dependent on the starting and reference models. We showed that when the base conductivity differs from the host conductivity and is used as the starting and reference models, structures recovered from airborne NSEM inversion are placed at erroneous depths. However when the true host conductivity is used as the starting and reference models, the inversion of airborne NSEM data recovers consistent structures within the survey region at appropriate depths.

Because EM data are sensitive to cells in proximity of receivers, airborne NSEM inversion is likely to recover structure near the base station. These structures influence the predicted magnetic and electric fields measured at the base station, and thus play a significant role in fitting the data. If structures recovered near the base station play a sufficient role in fitting the shape and amplitudes of airborne NSEM anomalies, we may have reduced confidence in the structures that are recovered within the survey region. Further investigation is needed to characterize the impact of structures recovered near the base station on our interpretation of the inversion result.

CONCLUSION

Airborne NSEM data are effective at identifying 3D conductors and resistors within the survey area by the anomalous magnetic fields they produce. However, these methods are not directly sensitive to the subsurface conductivity within the survey region. When a-priori knowledge of the host conductivity within the survey region is known, both QAMT and ZTEM inversion are effective at recovering conductive and resistive structures within the region of interest. However, unconstrained QAMT and ZTEM inversion is likely to recover structures near the base station that play a significant role in fitting the observed data. This in turn decreases our confidence in the structures recovered within the survey region. All things considered, airborne NSEM methods are much more economical that MT methods and show great promise in being used for a wide range of geophysical applications. And it would be worthwhile to research improvements to inversion methodologies and survey design that includes the collection of airborne NSEM data.

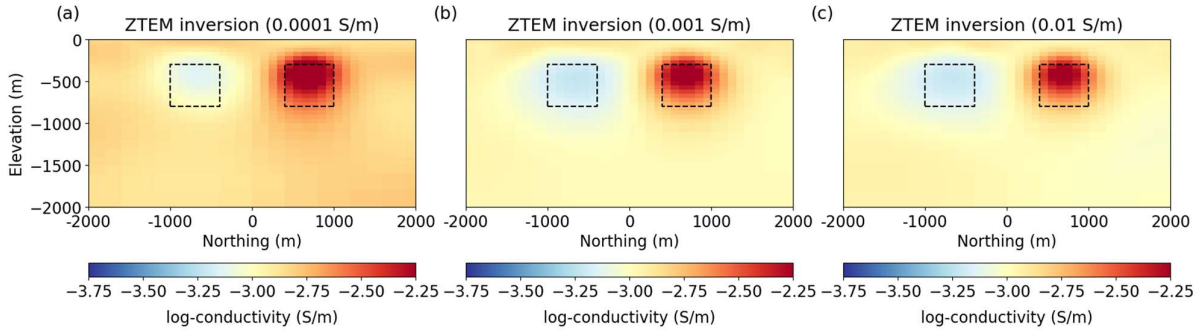

Figure 8. Models from ZTEM inversion within the survey region when the host conductivity is used as the starting and reference models. Base station conductivities of (a) 0.0001 S/m, (b) 0.0001 S/m and (c) 0.01 S/m.

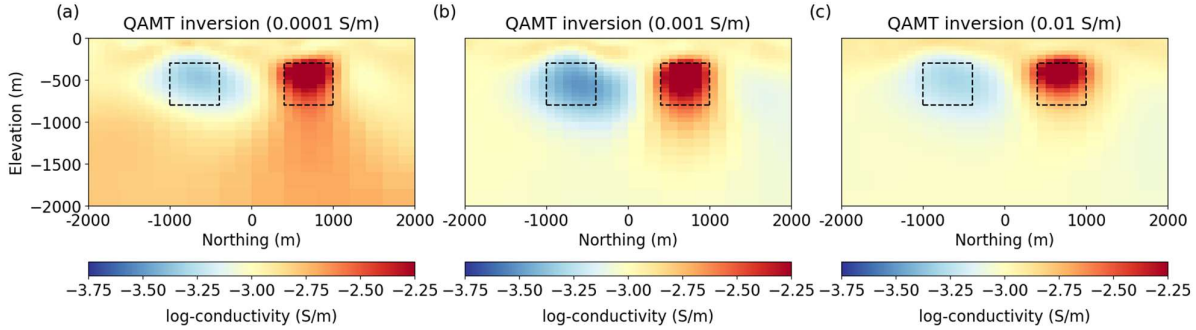

Figure 9. Models from QAMT inversion within the survey region when the host conductivity is used as the starting and reference models. Base station conductivities of (a) 0.0001 S/m, (b) 0.0001 S/m and (c) 0.01 S/m.

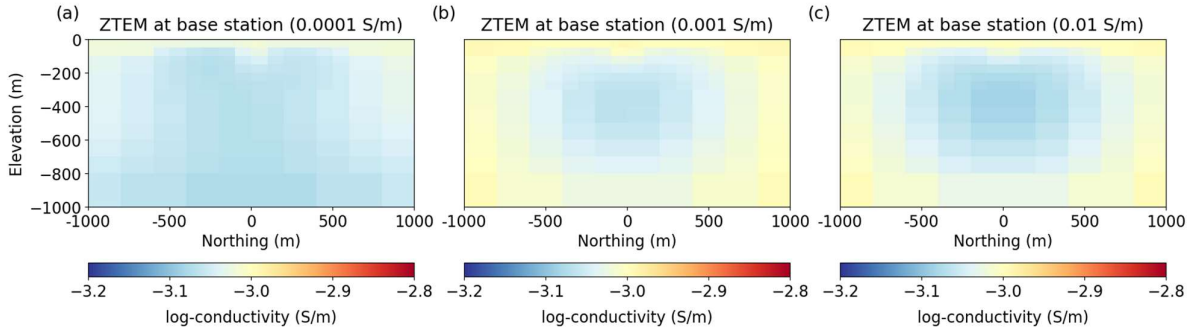

Figure 10. Models from ZTEM inversion near the base station (Easting = -30,000 m) when the host conductivity is used as the starting and reference models. Base station conductivities of (a) 0.0001 S/m, (b) 0.0001 S/m and (c) 0.01 S/m.

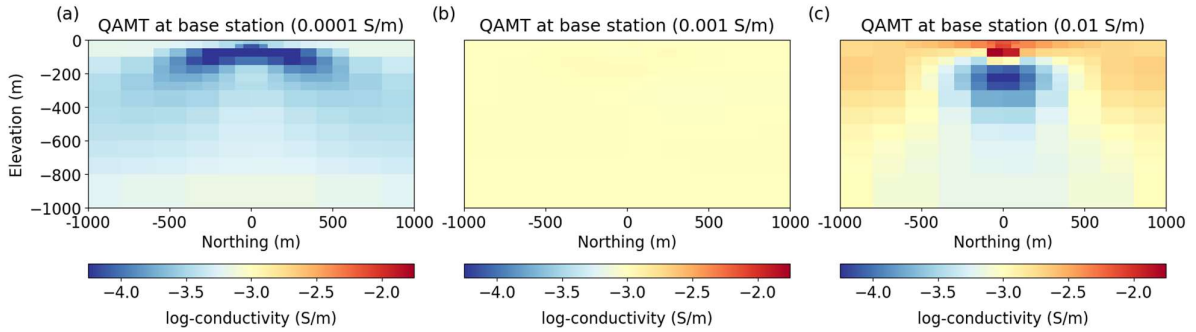

Figure 11. Models from QAMT inversion near the base station (Easting = -30,000 m) when the host conductivity is used as the starting and reference models. Base station conductivities of (a) 0.0001 S/m, (b) 0.0001 S/m and (c) 0.01 S/m.

REFERENCES

Cagniard, L. (1953). Basic Theory of the Magneto-Telluric Method of Geophysical Prospecting. In *Geophysics,* Volume 18, 605–635.

Heagy, L. J., Cockett, R., Kang, S., Rosenkjaer, G. K., and Oldenburg, D. W. (2017). A framework for simulation and inversion in electromagnetics, *Computers & Geosciences*, Volume 107, 1-19, ISSN 0098-3004, http://dx.doi.org/10.1016/j.cageo.2017.06.018.

Holtham, E. (2013). Inversion of Natural Source Electromagnetic Data, *PhD dissertation*, University of British Columbia.

Larnier, H., Chubak, G., Schneider, M., Schiffler, M., and Stolz, R. (2021). Three component SQUID-based system for airborne natural field electromagnetics, *SEG Technical Program Expanded Abstracts*, 1290-1294.

Li, Yaoguo & Oldenburg, D. W. (1996). 3-D inversion of magnetic data. *Geophysics*, Volume 61, 394-408.

Lo, B., and M. Zang (2008). Numerical modeling of Z-TEM (airborne AFMAG) responses to guide exploration strategies, *SEG Technical Program Expanded Abstracts*, Volume 27, 1098–1102.

Sattel, D., Witherly, K. and Kaminski, V. (2019). A brief analysis of MobileMT data, *SEG Technical Program Expanded Abstracts*, 2138-2142.

Tikhonov, A. N. (1950). The determination of the electrical properties of deep layers of the earth's crust, *Doklady. Academii Nauk, SSR,* Volume 73, 295–297.

Shekhtman, R., Oldenburg, D.W., and Haber, E. (2023) E3DMT v2; A Program Library for Forward Modelling and Inversion of Natural Source Electromagnetic Data over 3D Structures. Developed under the consortium research project *Inversion Research Consortium II*, UBC-Geophysical Inversion Facility, Department of Earth and Ocean Sciences, University of British Columbia, Vancouver, British Columbia.

Ward, S. H. (1959). AFMAG – Airborne and ground, *Geophysics*, Volume 24, 761-789.

Rapid 3D finite-difference modelling for magnetotellurics based on Reduced Basis Method

Hao Dong[1,2] and Yijie Cui[1]

[1] China University of Geosciences, Beijing, 100083, China
[2] Key Laboratory of Intraplate Volcanoes and Earthquakes, Ministry of Education, Beijing 100083, China

SUMMARY

Despite the fast development of the computer hardware and numerical simulation methods, the limited efficiency to solve the large-scale partial differential equations (PDE) in forward modelling is still the major obstacle to fast, real-time electromagnetic geophysical inversions. To address this issue, we introduce a reduced basis method to rapidly solve the PDE problem arise from the finite-difference discretization of curl-curl equations. The reduced basis method aims to project the full solution space of a PDE problem to its lower dimensional subspace, with a series of transformation basis. The reduced solution space can therefore be rapidly calculated by the spanning of a series of basis functions from the orthonormalization of a number of full solutions. The result from comparisons between the new method against its conventional counterpart with COMMEMI-3D synthetic test shows a promising speed-up of more than 100x. This may provide a new method to deal with challenges from near real-time simulations in industrial applications, or Bayesian inversions that requires millions of forward calculations.

Keywords: Reduced Basis, Electromagnetics, Forward Modelling, Finite Difference, Curl-Curl Equations

INTRODUCTION

In PDE based optimization problems, the speed of the forward modelling has always been the key to efficiently deal with large-scale problems, as with geophysical inversions. The rapid development of 3D modelling methods in the past decades have made it possible to perform complex large scale 3D EM inversions, which allow us to better understand the Earth. Recently, increasing applications of EM monitoring methods have emerged, like the fracturing monitoring in the oil/gas industry, or the groundwater monitoring in environmental engineering. All of these applications require repeated near real-time inversion results, which in turn calls for forward simulations with extremely high efficiency. However, even for modern clusters, conventional methods may still take hundreds to thousands seconds to solve the PDE problems, which fails to satisfy the requirement of the near real-time applications. Here we introduce a new reduced basis method (RBM) to rapidly solve the PDE problem arise from the finite-difference discretization of time-harmonic Maxwell equations, which are the foundation of most frequency domain EM problems. We show that our RBM can efficiently project the full solution space of a PDE problem to its lower dimensional subspace (Manassero et al., 2020), which drastically reduces the computational cost, while maintaining acceptable accuracy level.

METHODS

For most frequency-domain EM problems, the time-harmonic Maxwell's equations can be expressed as:

$$\begin{aligned} \nabla \times E &= -i\omega\mu H \\ \nabla \times H &= i\omega\varepsilon E + J + J^{ext}, \end{aligned} \tag{1}$$

where E and H are the electric and magnetic fields, ω is angular frequency, ε is the electric permittivity of the model domain, μ is the permeability, while $J = \sigma E$ denotes the electric conduction currents in the domain and J^{ext} stands for the external current forcing.
For quasi-static approximation (displacement currents are negligible) Equations (1) can be reduced to a second-order Curl-Curl problem based on electric fields. Without loss of generality, we can merge the internal and external current terms:

$$\nabla \times \nabla \times E + i\omega\mu\sigma E = J, \tag{2}$$

The equations (2) are often discretized (using e.g. finite element or finite difference methods) as linear equations of dimension N:

$$\mathrm{A}(\mu)\mathrm{x}(\mu) = \mathrm{b}(\mu), \tag{3}$$

where $\mathrm{A} \in \mathbb{R}^{\mathrm{N}\times\mathrm{N}}$, b and $\mathrm{x} \in \mathbb{R}^{\mathrm{N}}$. Note that for a given forward modelling problem, the system matrix A and the right-hand side b should both be functions of the model parameter $\boldsymbol{\mu}$ (in terms of physical and geometric property for a given parameter domain P). All the solutions x, which naturally also depend on the model parameter $\boldsymbol{\mu}$, form a Hilbert space (or solution space) V. Here we define the original PDE problem as the "full order" (FO) system, with which we define the residual as:

$$\mathrm{r}(\mathrm{x};\mu) = \mathrm{b}(\mu) - \mathrm{A}(\mu)\mathrm{x}, \quad \forall\, \mathrm{x} \in \mathbb{R}^{\mathrm{N}}, \tag{4}$$

The reduced basis method

For large scale 3D EM problems, solving the above FO system may entail significant computational costs, as the dimension of the problem (N) can be forbiddingly large to solve. Consider a "reduced order" (RO) system of dimension N_R that approximates (3):

$$\mathrm{A_R}(\mu)\mathrm{x_R}(\mu) = \mathrm{b_R}(\mu), \tag{5}$$

where $\mathrm{A_R}(\mu) \in \mathbb{R}^{\mathrm{N_R}\times\mathrm{N_R}}$, $\mathrm{b_R}(\mu)$ and $\mathrm{x_R}(\mu) \in \mathbb{R}^{\mathrm{N_R}}$. The problem can be greatly simplified, if we can find a projection, with which any $\mathrm{x}(\mu)$ in V can be approximated well enough (Quarteroni et al., 2016). By a linear combination of the RO solutions, the FO solution can be expressed in the form of:

$$\mathrm{x}(\mu) = \mathbb{V}\mathrm{x_R}(\mu), \tag{6}$$

where $\mathbb{V} \in \mathbb{R}^{\mathrm{N}\times\mathrm{N_R}}$, is a $\mu-$independent projection matrix, which maps the reduced solution space to the original solution space ($V_R \to V$). In other words, eq. (6) can be considered as the algebraic form of a Galerkin method over a subspace of dimension N_R from the N dimension space. The solution $\mathrm{x_R}$ of (5), can be determined by enforcing a suitable orthogonality criterion on the residual of the solution. We therefore have a FO residual estimation of:

$$\mathrm{r^R} = \mathrm{r}(\mathbb{V}\mathrm{x_R};\mu), \tag{7}$$

using the RO solution from (5). Now if we can enforce the condition that the orthogonal projection of residual (7) onto the reduced solution space V_R is zero:

$$\mathbb{V}^{\mathrm{T}}\big(\mathrm{b}(\mu) - \mathrm{A}(\mu)\mathbb{V}\mathrm{x_R}(\mu)\big) = 0, \tag{8}$$

we obtain the RO problem (5) from the FO system. Then through this projection, we can map the reduced system from the FO system by:

$$\begin{aligned} \mathrm{A_R}(\mu) &= \mathbb{V}^{\mathrm{T}}\mathrm{A}(\mu)\mathbb{V}, \\ \mathrm{b_R}(\mu) &= \mathbb{V}^{\mathrm{T}}\mathrm{b}(\mu), \end{aligned} \tag{9}$$

which effectively construct a reduced subspace of from the original space (dimension $N \to N_R$).

The assembly of the reduced basis functions

To evaluate the reduced system (5), we still need to assemble the projection matrix $\mathbb{V}$, sometimes called the reduced basis function (RBF) beforehand. To this end, we start from a set of FO solutions (a.k.a. snapshots):

$$\{\mathrm{x}(\mu^1),\ \mathrm{x}(\mu^2), \ldots,\ \mathrm{x}(\mu^{\mathrm{R}})\}, \tag{11}$$

with respect to a set of R model parameters. We can build a set of R functions (called "basis functions") by orthonormalize those snapshots

$$\{\nu^1,\ \nu^2, \dots,\ \nu^R\}, \tag{12}$$

regarding a suitable inner scaler product operation:

$$\left(\nu_j, \nu_k\right)_R = \delta_{jk}, where\ 1 \le j,k \le R \tag{13}$$

Then we can generate the reduced basis space by:

$$V_R = span\{\nu^1, \quad \nu^2, \dots, \quad \nu^R\}$$
$$= span\{x(\mu^1),\ x(\mu^2), \dots,\ x(\mu^R)\}, \tag{14}$$

which is nested (i.e., $V_{R-1} \subset V_R$). Since the reduced basis naturally also belongs to the original solution space V, we can expand the reduced basis function with respect to the original basis functions:

$$\nu_m = \sum_{i=1}^{N} v_m^{(i)}\, \varphi^i, 1 \le m \le N \tag{15}$$

where $\varphi = \{\varphi^1, \varphi^2, \dots, \varphi^N\}$ is the basis function of the original solution space V. Then the projection matrix can be assembled as:

$$(\mathbb{V})_{im} = v_m^{(i)}, 1 \le m \le N_R, 1 \le i \le N, \tag{16}$$

Exploiting the nested nature of V_R, we may use a greedy algorithm to recursively select a number of snapshots for the reduced basis space, by a certain optimal criterion. For example, we can add more snapshots, till the residual (7) satisfies the precision requirement.

In summary, the reduce basis method can be roughly divide into two stages:

1. the offline stage:

a) generate the original finite difference discretization of the curl-curl equations (3);

b) calculate a number of FO solution snapshots (11) using greed algorithm, and:

c) assemble the projection matrix (15) to build the reduced system;

2. the online stage:

a) build and solve the reduced system (5);

b) recover the approximate solution of the full system (6) and appraise the residual with (8);

SYNTHETIC EXAMPLES

To test the performance of our new RB method, we compare the modelling performance of the new method against that of its conventional finite difference counterpart, using the COMMEMI-3D synthetic model for magnetotellurics (Zhdanov et al., 1997; Fig. 1). The model domain is discretized into a 71 by 71 by 53 mesh, with a DoF of about 0.8 million. After the offline building stage of the reduced subspace (may take hours for personal computers), the DoFs of the approximate system can be reduced to merely a few hundred to thousand.

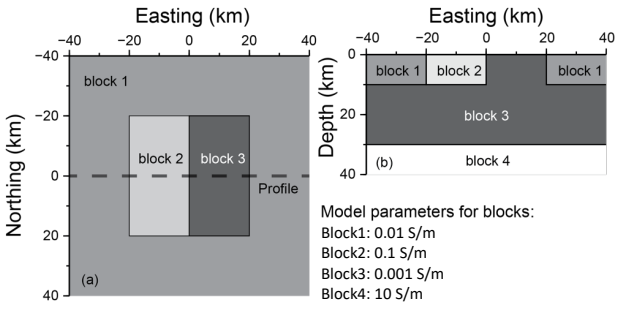

Figure 1: parameter setup of the COMMEMI-3D2 model (modified from Zhdanov et al., 1997)

To solve the full order linear system arises from the conventional FD method, we use an iterative QMR solver combined with divergence correction method.

As for the reduced system, we can use the direct method (Gaussian elimination with LU decomposition) as the DoF of the reduced system is small enough. As a result, the time for the forward problem reduces from about 105 s to less than 1s (Table 1) on a laptop computer with 8-core Apple M1 processor.

Table 1: efficiency comparison between the conventional full and reduced order systems

method	Mode	DoFs	Period	Walltime
Full Order	XY	826848	0.1s	103.20s
			100s	104.48 s
	YX	826848	0.1s	105.22 s
			100s	106.11 s
Reduced Order	XY	214	0.1s	0.93s
			100s	0.93s
	YX	228	0.1s	0.97s
			100s	0.98s

On the other hand, the computed electromagnetic fields from the RO system show almost identical results, when compared with its FO counterpart (Fig. 2), with acceptable precision with relative residual of < 10^{-5}.

CONCLUSIONS

We have developed a new reduced basis method to solve the time-harmonic Maxwell problem related to EM inversions. The efficiency of the new method allows us to rapidly perform approximate forward modelling calculations for moderate-scale 3D MT problems, which may provide a new way to improve the efficiency of electromagnetic inversions used with near real-time monitoring problems. It may also provide a rapid forward modelling method for Bayesian inversions, which may require millions of forward calculations in 3D cases.

ACKNOWLEDGMENTS

The research is supported by NFSC projects 4227040447 and 4212100033.

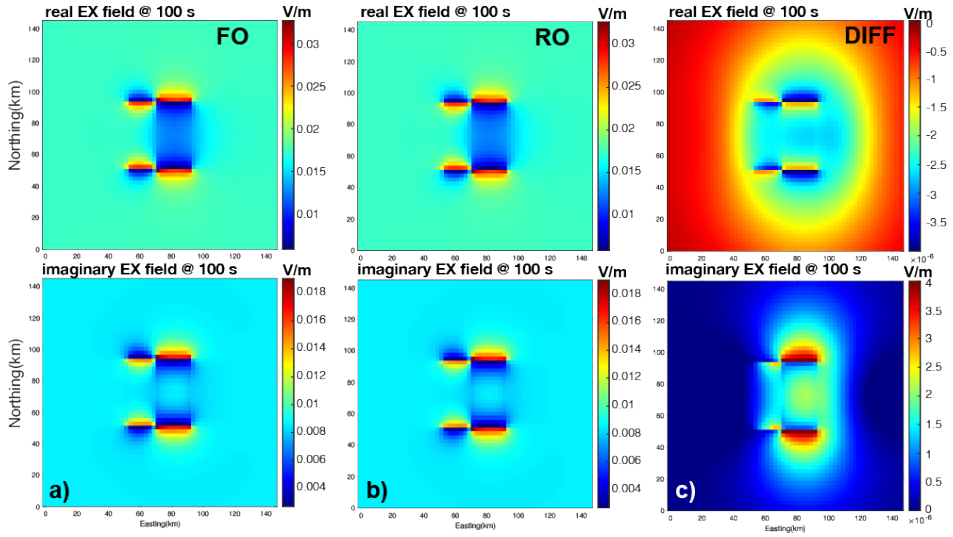

Figure 2: comparison of the XY polarization MT Ex field responses of the COMMEMI-3D2 model. Panels a), b) represent the result from full order and reduced order systems; c) shows difference between a) and b);

REFERENCES

Manassero, M. C., Afonso, J. C., Zyserman, F., Zlotnik, S., & Fomin, I. (2020) A reduced order approach for probabilistic inversions of 3-D magnetotelluric data I: general formulation. Geophysical Journal International, 223(3), 1837–1863.

Quarteroni, A., Manzoni, A., Negri, F. (2016) Reduced Basis Methods for Partial Differential Equation. Springer, Cham, 2016, 92:13-165.

Zhdanov, M. S., Varentsov, I. M., Weaver, J. T., Golubev, N. G., & Krylov, V. A. (1997). Methods for modelling electromagnetic fields Results from COMMEMI—the international project on the comparison of modelling methods for electromagnetic induction. Journal of Applied Geophysics, 37(3–4), 133–271.

Hybrid OCCAM-Conjugate Gradients Inversion Algorithms with Applications to Marine CSEM data

Gary D. Egbert[1], Naser Meqbel[2] and Paulo Werdt[2]
[1]CEOAS, Oregon State University, Corvallis OR, USA
[2]Observatório Nacional, Rio de Janiero, Brazil

SUMMARY

Egbert (2012) developed a hybrid multi-transmitter (mTX) OCCAM-Conjugate Gradient (CG) algorithm and illustrated basic ideas on a simple 2D MT inverse problem. Here we present results of application of these ideas to a more computationally challenging problem, 3D marine controlled-source EM (mCSEM). There are two main aspects of our approach. First, we save results of calculations required for an iterative solution of the data-space Gauss-Newton (GN) normal equations and use these to construct a low dimensional approximation of the full Jacobian. Once computed, this allows rapid computation of trial inverse solutions for a range of regularization parameters, so Occam-type schemes become practical even for very large problems. The hybrid is based on the Golub-Kahan bidiagonalization of the Jacobian matrix. Second, every transmitter (Tx; i.e., different frequency, or location) requires solution of a separate adjoint problem, associated with the gradient of the data misfit for that separate Tx dataset. By saving results of these distinct calculations (instead of summing them, to compute the gradient of the total data misfit) we can form a more complete approximation to the Jacobian. Furthermore, with suitable modifications to the iterative CG algorithm (Egbert, 2012), more rapid (fewer adjoint and forward solves) and stable solution of the G-N equations can be achieved. We demonstrate the effectiveness of our methods using synthetic datasets based on a realistic 3D resistivity model constructed for the Campos Basin on the Brazilian margin. We also demonstrate how the mTX algorithm can be useful for joint inversion of multiple EM data types, specifically for combining MT and mCSEM data. The hybrid scheme allows for efficient exploration of relative weights for the different measured data types, using the approximate Jacobian. The approximated Jacobian can also be used for linearized uncertainty and resolution analysis of the solutions obtained.

Keywords: EM Geophysics, Inversion Methods, mCSEM

INTRODUCTION

In this work we discuss some new approaches to minimization of the quadratic penalty functional

$$\Phi(\mathbf{m},\mathbf{d}) = \big(\mathbf{d}-\boldsymbol{f}(\mathbf{m})\big)^{\mathrm{T}}(\mathbf{d}-\boldsymbol{f}(\mathbf{m})) + \lambda\mathbf{m}^{\boldsymbol{T}}\mathbf{m} \qquad (1)$$

where $\mathbf{m}$ is the model parameter $\mathbf{d}$ the data vector, and $f(\mathbf{m})$ the forward mapping. Note that as our focus here is on minimization algorithms, we ignore data and model "covariances" in the data misfit and model regularization terms in (1). In practice this simple generic form may be obtained by suitable transformation of model and data space vectors. Gradient-based linearized search schemes such as NLCG or LBFGS have proven to be an effective and efficient way to minimize the quadratic penalty functional. However, there are potential advantages to a Gauss-Newton (GN) approach such as OCCAM (Constable et al., 1987), as we discuss. In the simplest approach a GN scheme requires computation of the full Jacobian (sensitivity) matrix $\mathbf{J}$, followed by computation of a cross-product matrix such as $\mathbf{J}^T\mathbf{J}$, and then solution of a large system of linear normal equations. In a data-space variant of the OCCAM scheme (Siripunvaraporn et al., 2005) the normal equations take the form

$$(\mathbf{J}\,\mathbf{J}^T + \lambda\mathbf{I})\mathbf{b} = \hat{\mathbf{d}} = \mathbf{d} - \boldsymbol{f}(\mathbf{m}_n) + \mathbf{J}\mathbf{m}_n \qquad (2)$$

with the updated model parameter at iteration $n+1$ computed as $\mathbf{m}_{n+1} = \mathrm{J}^T\mathbf{b}$. In the OCCAM scheme the parameter λ is varied, initially to minimize data misfit, then to find the smallest model consistent with the desired misfit tolerance. OCCAM thus automatically optimizes the regularization (tradeoff) parameter.

While OCCAM has been widely used in 1D and 2D inverse problems, application in 3D is more challenging, due to the need to compute the full Jacobian, to form the

large cross-product matrices, and to solve a large system of normal equations. These equations can also be solved using conjugate gradients (CG) without first computing $\mathbf{J}$. Each step requires multiplication of arbitrary model vectors (e.g.,m_n) by $\mathbf{J}$, and data vectors (e.g., $\mathbf{b}$) by $\mathbf{J}^T$. These operations involve one forward/adjoint solution, respectively, of the 3D EM PDE. While this CG approach makes a GN approach more practical, it is not immediately obvious how to implement OCCAM – seemingly, the CG iterations must be run repeatedly for different values of the regularization parameter λ.

Here we make two points: First, we can save results of calculations required for an iterative CG solution of the data-space Gauss-Newton (GN) normal equations and use these to construct a low dimensional approximation of the full Jacobian. Once computed, this allows rapid computation of trial inverse solutions for a range of regularization parameters, so Occam-type schemes become practical even for very large problems. Second, every transmitter (Tx; i.e., different frequency, or location) requires solution of a separate adjoint problem, associated with the gradient of the data misfit for that separate Tx dataset. By saving results of these distinct calculations (instead of summing them, to compute the gradient of the total data misfit) we can form a more complete approximation to the Jacobian, and solve the G-N equations with fewer adjoint and forward computations.

METHODS

The Basic Hybrid Algorithm (BDORTH): After K steps Lanczos bi-diagonalization of the Jacobian matrix produces the decomposition

$$\mathbf{J}^T\mathbf{U}_K = \mathbf{V}_K\mathbf{B}_K \qquad (3)$$

Here $\mathbf{U}_K = [\boldsymbol{u}_1, \ldots, \mathbf{u}_K]$ and $\mathbf{V}_K = [\,\mathbf{v}_1, \ldots\ , \mathbf{v}_K]$ are orthogonal matrices whose columns are, respectively, data and model space vectors, and $\mathbf{B}_K$ is bidiagonal. Each step in the algorithm requires multiplication by $\mathbf{J}^T$ and $\mathbf{J}$. Saving these matrices (i.e., K data and model space vectors) we can project the Jacobian and data vectors, into a K dimensional subspace and solve the equivalent of Eq. (2)

$$(\mathbf{U}_K^T\mathbf{J}\,\mathbf{J}^T\mathbf{U}_K + \lambda\mathbf{I})\mathbf{b}_\lambda = (\mathbf{B}_K\mathbf{B}_K^T + \lambda\mathbf{I}) = \mathbf{U}_K^T\,\hat{\mathbf{d}} \qquad (4)$$

The approximate model space solution is then computed as $\mathbf{m}_\lambda = \mathbf{V}_K\mathbf{b}_\lambda$. This can be computed for any λ making an approximate OCCAM scheme possible. We refer to this algorithm here as "BDORTH". This is an example of what has often been referred to as a hybrid algorithm for the iterative solution of linear equations.

Multi-transmitter Extension (BDMTX): In this variant we save computations (both data and model space vectors $\mathbf{U}_K$ and $\mathbf{V}_K$) separately for each transmitter (Tx; different source dipole source location or different frequency) separately. Because each Tx requires independent forward and adjoint calculations (the costliest step in the inversion) the additional computational burden is minimal (although memory requirements are generally increased). Egbert (2012) describes a modified Lanczos scheme that works well. We summarize briefly here:

We have $j = 1, \ldots, J$ transmitters. At each step $k = 1, \ldots K$ in the iterative algorithm we compute and save J data space vectors $\mathbf{u}_{jk}$, and model space vectors $\mathbf{v}_{jk}$ one each for each Tx, and for each iterative step. We collect these as

$$\mathbf{U}_k = [\mathbf{u}_{11} \ldots \mathbf{u}_{1k} \,|\, \ldots \,|\, \mathbf{u}_{Jk} \ldots \mathbf{u}_{Jk}] = [\mathbf{W}_1 \ldots \mathbf{W}_J] \qquad (5)$$

$$\mathbf{V}_k = [\mathbf{J}_1^T\mathbf{u}_{11} \ldots \mathbf{J}_1^T\mathbf{u}_{1k} \,|\, \ldots \,|\, \mathbf{J}_J^T\mathbf{u}_{Jk} \ldots \mathbf{J}_J^T\mathbf{u}_{Jk}] \qquad (6)$$

The first step ($k = 1$) is initialized as $\boldsymbol{u}_{j1} = \boldsymbol{d}_j/||\boldsymbol{d}_j||$ where $\mathbf{d}_j$ is the data vector for Tx j. To compute data space vectors for t step k we solve the projected normal space equations

$$(\mathbf{V}_k^T\mathbf{V}_k + \lambda\mathbf{I})\tilde{\mathbf{b}} = [\mathbf{d}_1^T\mathbf{U}_{1k} \ldots \mathbf{d}_{N_{Tx}}^T\mathbf{U}_{N_{Tx}k}]^T$$

The coefficient matrix of the symmetric system is $Jk \times Jk$, so even with hundreds of Tx the computational cost is negligible. Then compute the "trial solution" $\mathbf{m}_k = \mathbf{V}_k\tilde{\mathbf{b}}$, multiply by Jacobian for eaxh Tx, $\mathbf{c}_{jk} = \mathbf{J}_j\boldsymbol{m}_k$ and finally compute $\mathbf{e}_{jk} = \mathbf{c}_{jk} - \mathbf{W}_j\ \mathbf{W}_j^T\boldsymbol{c}_{jk}$ and $\boldsymbol{u}_{jk+1} = \boldsymbol{e}_{jk}/||\boldsymbol{e}_{jk}||$. This is iterated until a sufficiently accurate solution to the (nprojected) normal equations is obtained. The scheme is quite similar to the original Lanczos decomposition, although a small linear system must be solved at each step to couple equations for all Tx.

RESULTS

As an illustration of these methods we consider a very simple toy marine CSEM synthetic dataset. The model, and transmitter and receiver configuration is shown in Figure 1. The model is very simple, a local resistive body in a layered background with flat bottom bathymetry (depth of 1000 m). There are 6 Tx locations and threwe frequencies, so the total number of transmitters is 18.

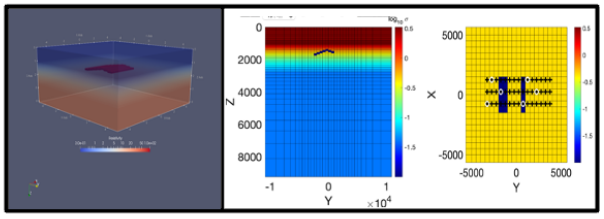

Figure 1: model and data configuration for tests.

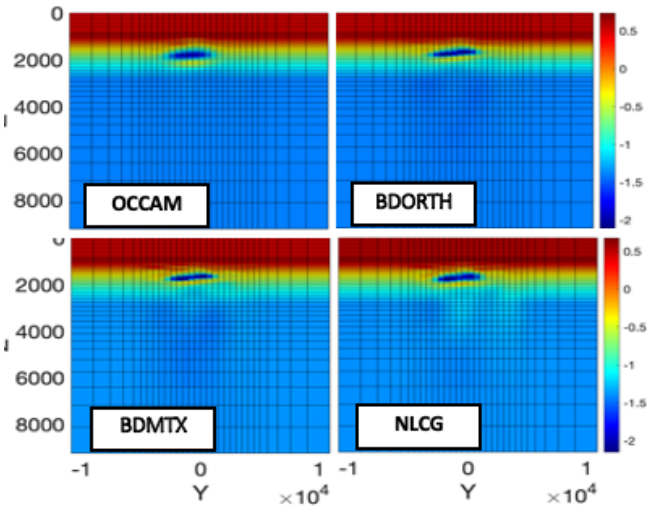

Figure 2: Inversion results for four algorithms: OCCAM, based on full Jacobian computation, BDORTH, the basic hybris scheme based on saving sensitivity computations from the Lanczos bidiagonalization, BDMTX, the multi-transmitter extension, and a the NLCG algorithm, as implemented in the ModEM code of Kelbert et al (2014; extended to CSEM inversion), unpublished). All algortihms converged to similar results for this simple problem. However the OCCAM scheme required 9270 adjoint/forward solves – making this impractical for more realistic problems. Other approaches required only 333 (NLCG), 354 (BDORTH) and 152 (BDMTX).

Results from the new algorithms proposed here, along with from OCCAM (full sensitivity calculation, and a more commonly used gradient search scheme (NLCG), are shown in Figure 2. Number of forward and adjoint solves required are summarized in the figure caption.

Both BDORTH and BDMTX solve the data space normal equations iteratively, generating an approximation to the Jacobian along the way. Convergence is significantly more rapid, and apparently smoother and more stable with the BDMTX approach, as illustrated in Figure 3.

DISCUSSION

We have presented two hybrid schemes, which generate an approximate Jacobian through iterative solution of the data-space normal equations for a Gauss-Newton inversion algorithm. Both are about as efficient (in terms of number of forward and adjoint solves) as a gradient search method such as NLCG, and allow use of an OCCAM approach to choice of regularization parameter. The approximate Jacobian could also be used for linearized resolution analysis, something that is not possible with NLCG. These hybrid schemes may also be useful for joint inversion of, for example, CSEM and MT data. With two different data types the appropriate balance between fitting each type often requires multiple runs with different relative weights. This exploration could be done quite efficiently using the computed approximate Jacobian, especially with the BDMTX scheme.

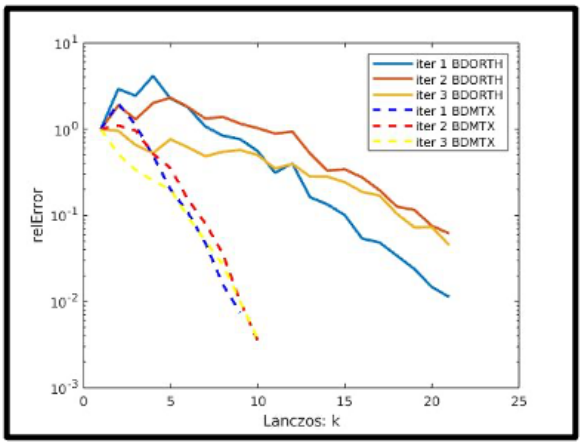

Figure 3: comparison of convergence of the inner loop (iterative solution to normal equations) for 3 outer loop steps. Dashed lines are for the multi-transmitter scheme, which reduces required number of iterations by a factor of roughly 2.5, and shows smoother and more stable convergence behaviour.

REFERENCES

Constable, Steven C., Robert L. Parker, and Catherine G. Constable. "Occam's inversion: A practical algorithm for generating smooth models from electromagnetic sounding data." *Geophysics* 52, no. 3 (1987): 289-300.

Egbert, G.D., 2012. Hybrid conjugate gradient-Occam algorithms for inversion of multifrequency and multitransmitter EM data. *Geophysical Journal International*, *190*(1), pp.255-266.

Siripunvaraporn, Weerachai, Gary Egbert, Yongwimon Lenbury, and Makoto Uyeshima. "Three-dimensional magnetotelluric inversion: data-space method." *Physics of the Earth and planetary interiors* 150, no. 1-3 (2005): 3-14.

7th International Symposium on Three-Dimensional Electromagnetics
Vancouver, BC, Canada, November 13–15, 2023

Impacts of magnetic permeability on electromagnetic data collected in settings with steel-cased wells

Lindsey J. Heagy[1] and Douglas W. Oldenburg[1]
[1]University of British Columbia Geophysical Inversion Facility

Summary

Electromagnetic methods are increasingly being applied in settings with steel infrastructure. These include applications such as monitoring of CO_2 sequestration or even assessing the integrity of a wellbore. In this abstract, we examine the impacts of the magnetic permeability of a steel-cased well on electromagnetic responses in grounded source experiments. We consider a vertical wellbore and simulate time and frequency domain data on 3D cylindrical meshes. Permeability slows the decay of surface electric fields in the time domain and contributes to a phase shift in the frequency domain. We develop our understanding of how permeability alters currents within, and external to, the casing by focussing first on the time domain response and translating insights to the frequency domain. Following others, we rewrite Maxwell's equations to separate the response into terms that describe the magnetization and induction effects. Magnetic permeability impacts the responses in two ways: (1) it enhances the inductive component of the response in the casing, and (2) it creates a magnetization current on the outer wall of the casing. The interaction of these two effects results in a poloidal current system within the casing. It also generates anomalous currents external to the casing that can alter the geometry and magnitude of currents in the surrounding geologic formation. This has the potential to be advantageous for enhancing responses in monitoring applications.

Keywords: Controlled source electromagnetics (CSEM), Downhole methods, Numerical modelling, Electrical properties, Magnetic properties

Introduction

There is growing interest in the use of electromagnetic (EM) methods in applications where fluids are injected or extracted from the subsurface. In most of these settings, steel-cased wells and/or pipelines are present. The presence of steel infrastructure can be a complicating factor for the use of EM. In a cross-well or surface-to-borehole survey where magnetic field sensors are deployed in a borehole, steel casing attenuates signals (Augustin et al., 1989; Wu & Habashy, 1994; M. Wilt et al., 1996; Cuevas, 2014). Additionally, steel infrastructure has an EM response that contributes "noise" that must be accounted for in numerical simulations or inversions. Although steel casings are a complicating factor for numerical modelling and inversions, multiple authors have shown that they can act as "extended-electrodes" that can help excite targets at depth and enhance signals that may not be observable had there been no steel-casing present (Schenkel & Morrison, 1994; Hoversten et al., 2015; Yang et al., 2016; Puzyrev et al., 2017). Another major area of interest is to evaluate the integrity of a well or pipeline M. J. Wilt et al. (2020); Beskardes et al. (2021). A recent special issue of The Leading Edge provides an overview of a range of applications where EM is applied in settings with steel-cased wells (Weiss & Daley, 2022).

Regarding the challenge of handling complicated scenarios involving steel pipes, solutions are established for simulating DC resistivity experiments in settings with steel infrastructure Schenkel & Morrison (1994); Yang et al. (2016); Heagy & Oldenburg (2019a). Notably the hierarchical finite element approach developed in Weiss (2017) enables complicated scenarios such as multiple lateral wells to be simulated. As compared to DC resistivity, time-varying EM experiments can be advantageous because they enable us to collect more data with the same survey geometry.

For numerical simulations of grounded-source EM in settings with steel casing, there have also been developments for finite volume or finite element simulations (Um et al., 2015; Commer et al., 2015; Haber et al., 2016; Heagy & Oldenburg, 2019b). Several authors have taken the approach of replacing a casing with a series of electric dipoles as supported by the analysis in (Cuevas, 2014) or adopted the related method-of-moments approach for simulating conduc-

tive infrastructure (Tang et al., 2015; Patzer et al., 2017; Kohnke et al., 2018; Orujov et al., 2020).

Although much work has been carried out on the use of EM and steel-cased wells, most of the efforts have focussed on conductivity only. This is reasonable since it is the high conductivity of steel, $\sim 10^6$ S/m, that primarily controls the response. But, for many applications of interest, we are faced with scenarios where the EM signals of targets are small; this motivates our interest in the influence of magnetic permeability on an EM response. In this abstract, we synopsize the elements which we feel are important. A more elaborate analysis can be found in Heagy & Oldenburg (2023); Heagy (2018).

Impacts of permeability on EM data

Our synthetic example, shown in Figure 1, is inspired by the CaMI site in Alberta (M. J. Wilt et al., 2020; Beskardes et al., 2021). The well is 500m long and has a conductivity of 5×10^6 S/m. The background conductivity is 0.1 S/m. The basic experiment is a grounded source experiment where one electrode is connected to the top of the casing and the return electrode is 500m from the well. For numerical simulations, we use the 3D cylindrical code described in (Heagy & Oldenburg, 2019b).

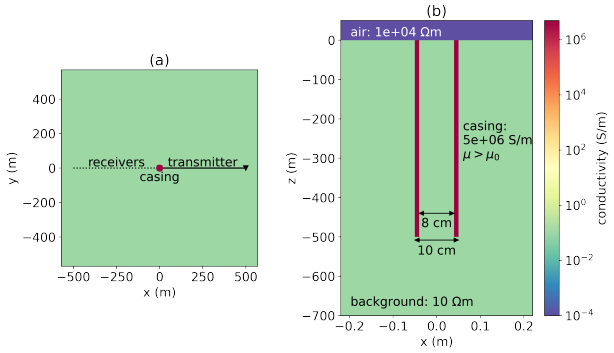

Figure 1: (a) Survey geometry and (b) model of vertical casing in a halfspace.

Frequency domain data

We run simulations that vary the permeability from $\mu_r = 1$ to $\mu_r = 200$ and use a 5Hz transmitter frequency. In Figure 2, we show the radial electric field measured along a line opposite to the transmitter wire (as shown in Figure 1a).

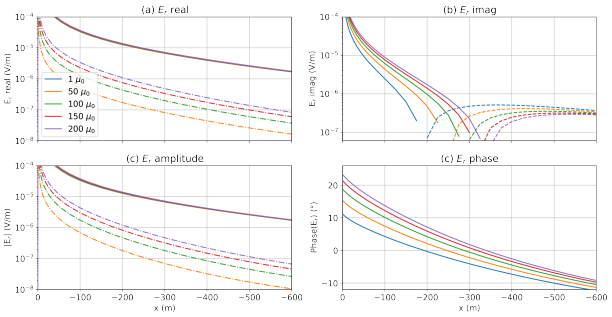

Figure 2: Radial electric field data for a top-casing experiment at 5Hz: (a) real, (b) imaginary, (c) amplitude, and (d) phase. Solid lines indicate positive values and dashed lines indicate negative values. In (a) and (c) the difference between the permeable well scenarios and a non-permeable well ($\mu_r = 1$) is shown with the dash-dot lines.

Magnetic permeability has a substantial impact on the imaginary component. Importantly, it is noticed that there is a change of the sign of the electric field and the location of the cross-over changes with the permeability of the well. Between a well with $\mu_r = 1$ and $\mu_r = 150$, the location of the cross-over has moved by >100m. We can also see the impact in the phase; there is a difference of 10° near the well between the $\mu_r = 1$ and $\mu_r = 150$ wells. This is comparable to the differences noted by Cuevas & Pezzoli (2018) in numerical experiments or borehole-to-surface EM. The difference in the real component is less dramatic, but for a well with $\mu_r = 150$, there is a 7% difference from the non-permeable well at small offsets from the well. Since the real component is larger in magnitude than the imaginary components, the amplitude of the electric field is dominated by the behaviour of the real component, and thus less impacted by permeability.

To illustrate the impacts of permeability as a function of frequency, we choose the location $x = -100$m, $y = 0$m and plot the radial electric field data measured at the surface for frequencies ranging from 0.1 Hz to 100 Hz. For this model, there is minimal impact on the real component for frequencies less than 2 Hz. As the frequency increases, we begin to see differences in the real component. At 10 Hz, which is typically considered "low" frequency, the real part differs by approximately 20% between the model with a relative casing permeability of $\mu_r = 150$ and a non-permeable well. The imaginary component is more substantially impacted by permeability; there is a factor of 4 between the data for $\mu_r = 150$ and $\mu_r = 1$ for low

frequencies. These effects are also very evident in the amplitude and phase plots where phase differences of 5-10 degrees are evident. At shorter offsets, the magnitude of the fields, and the difference between the permeable and non-permeable well scenarios is larger. Similarly, with increasing distance from the well, the magnitudes and differences decrease.

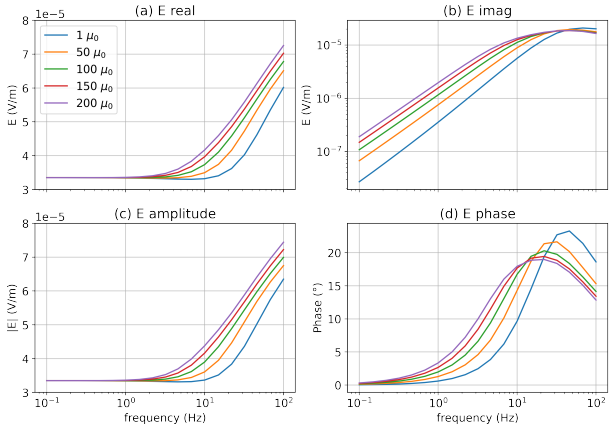

Figure 3: Radial electric field data at x=-100m, y=0m as a function of frequency.

Time domain data

In Figure 4, we show the radial electric field as a function of time at the location $x = -100$m, $y = 0$m. At times less than 1ms, there is minimal difference between the simulated data for each of the models. At 10ms, we can see a substantial difference between the permeable and non-permeable models. As has been noted by (Pavlov et al., 2001) and others, permeability slows the decay, and similarly, the time at which we observe a sign-change in the radial component of the electric field. At sufficiently late times (>200ms), we no longer see the impacts of the casing in the data.

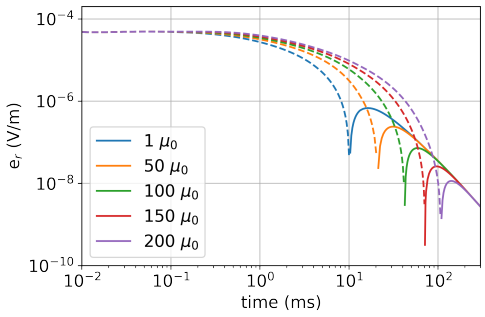

Figure 4: Radial electric field data at x=-100m, y=0m for a time domain EM experiment.

Currents in the formation

To unravel the role of magnetic permeability and its impacts, we will examine the time-domain EM response of a conductive, permeable casing. In Figure 5 we show a cross-section of currents through the earth for 3 models: (a) a halfspace, (b) a halfspace that includes a conductive casing (5×10^6 S/m), and (c) a halfspace with a casing that is conductive and permeable (5×10^6 S/m, $150\mu_0$).

The top row, at t=0ms, is the DC resistivity solution. After t=0, the current in the transmitter is shut off, and image currents, which oppose the change in magnetic field, are induced in the Earth (Nabighian, 1979). These currents are in the same direction as the current in the source wire and this causes a circulation of current as the galvanic and image currents interact. Both currents diffuse down and out through time.

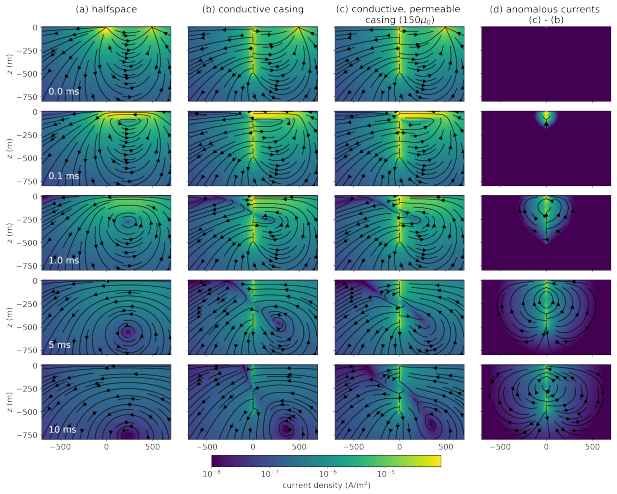

Figure 5: Cross sections showing the current density through time for a time domain EM experiment.

There is no influence of magnetic permeability in the DC limit. However, the impacts of permeability are seen later in time as the currents decay more slowly in the casing and surrounding formation; this is consistent with the delay in the decays shown in Figure 4. In panel (d), we show the difference between the permeable and non-permeable casing scenarios. At early times, the largest difference broadly aligns in depth with where the image current is. At later times, the image current has diffused past the length of the well, and we see differences along the entire depth-extend of the well. We also note that the difference is cylindrically symmetric, having only radial and vertical components.

Currents within the casing

The additional currents arising as a result of permeability are not simply amplifying the currents due to a conductive casing, there is also an impact on the geometry of the currents. To examine why this is, we zoom in to the currents within the casing in Figure 6. The top row shows the conductive well and the bottom row shows the conductive, permeable well ($150\mu_0$). There are two main features to note. First, the magnitude of the currents (indicated by colour) is larger at later times in the permeable well than in the conductive well, particularly after ~5ms. The other feature to note is the geometry of the currents. For the conductive well, we see that the currents are flowing downwards in the casing through time. However, for the conductive, permeable well, we see that at later times, a poloidal current system develops where currents flow downwards along the inner casing wall and upwards near the outer edge of the casing.

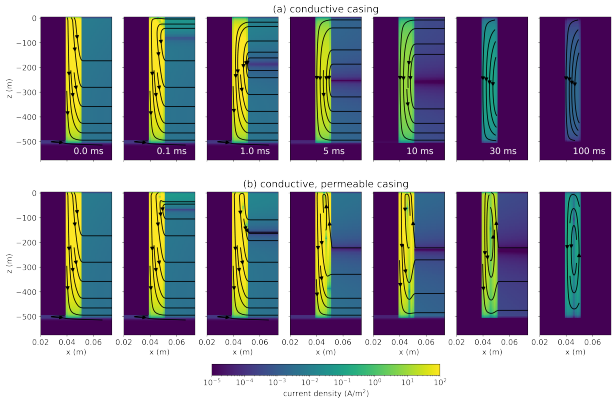

Figure 6: Cross sections of currents within (a) a conductive casing and (b) a conductive, permeable casing. Not to scale.

To understand this poloidal current system, we refer to Maxwell's equations. We illustrate this in Figure 7: (a) a current is applied to the casing; (b) by Ampere's law, vertical currents produce a toroidal magnetic field; (c) by the constitutive relationship between the magnetic flux density and the magnetic field (Ohm's law for magnetics), magnetic flux is concentrated inside of permeable materials; (d) the magnetic flux is changing through time which creates a poloidal electric field; (e) currents are concentrated in conductive materials according to Ohm's law leading to a poloidal current system.

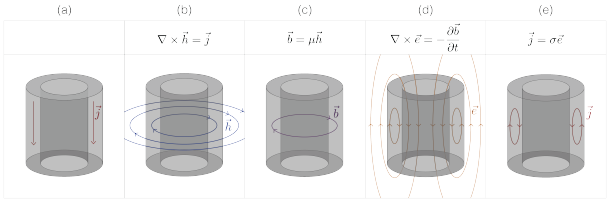

Figure 7: Sketch demonstrating how a poloidal current system can arise inside of a conductive, permeable casing.

Explaining the poloidal current system

The cartoon in Figure 7 is obviously a simplification of the physics, but it provides a useful conceptual model. To provide a more quantitative argument, we follow Pavlov et al. (2001); Noh et al. (2016), and re-write Maxwell's equations as

$$\nabla \times \vec{b} = \nabla \ln \mu_r \times \vec{b} + \mu\sigma\vec{e} \tag{1}$$

The two terms on the right-hand side both explicitly contain magnetic permeability; we refer to these as the magnetization and induction terms, respectively. In the inductive term, the permeability acts to enhance the inductive response in a manner equivalent to increasing the conductivity. The magnetization term is what alters the geometry. We note that $\nabla \ln \mu_r$ is zero everywhere except where there is a discontinuity in the relative permeability; this occurs at the walls of the casing. The divergence of the log-permeability gives us two delta functions when $\mu_r > 1$, a positive value on the inside of the casing and a negative value on the outside. Since there is negligible current in the hollow interior of the well as compared to the casing, $\vec{b}$ on the inner casing wall is negligible. Therefore, the main contribution that the magnetization term makes is on the outer casing wall. Since $\nabla_r \ln \mu_r$ is negative at the outer casing wall and b_θ is too, their cross product is a positive quantity in the z-direction. We can interpret this as a current that is scaled by the permeability. This means the magnetization term contributes an upward current on the outside portion of the casing.

Frequency domain EM response of a conductive, permeable well

When moving from the time domain to the frequency domain, we can translate our understanding of how permeability influences the EM response by recognizing that responses at early times are analogous to high frequencies and those at late times are analogous to

low frequencies. An important distinction is that, in a frequency domain experiment, the transmitter is always on, meaning the real component always contains a galvanic or DC component.

In the time domain, the permeability of the casing made a larger impact at later times, implying we should observe impacts of permeability at low frequencies. At low frequencies, permeability can have a substantial impact on the imaginary components, but whether it impacts the real component depends on the magnitude of the inductive response relative to the galvanic response. For example, in Figure 3, we see that permeability has no noticeable impact on the real component below 1 Hz for this example. In the imaginary component, there is a factor of 3 difference between the well with $\mu_r = 150$ and a non-permeable well, but this translates to a phase difference of only a few degrees because the galvanic component is so dominant. As the frequency is increased, the inductive part of the response also increases. At 10Hz, the inductive component of the response is substantial, and for the example in Figure 3, the real part of the electric field for the well with $\mu_r = 150$ is 20% larger than the non-permeable well. Similarly, there is a >20% difference in the amplitude.

Discussion

We have shown that permeability influences the EM response of a grounded-source experiment with steel-cased wells in two ways:

1. it enhances the induction component of the response
2. it introduces a magnetization current on the outer casing wall that opposes the induction currents.

Faraday's law couples the induction and magnetization components in a time or frequency domain experiment and, as a result, a poloidal current system develops within the casing. For the current system to arise, the casing must be both highly conductive and magnetic.

The resultant implications in the surrounding formation are: (a) additional radial "leak-off" currents change the radial component of the current density within the formation, and (b) the amplification of the azimuthal component of $\partial\vec{b}/\partial t$ within the casing can alter the radial and vertical currents in the formation.

The anomalous currents can affect the excitation of a target within the formation. In a time-domain experiment, an increased permeability slows the decay of currents in the well and provides a longer time window over which a target may be excited. This could be advantageous for helping detect a target in a time-domain EM experiment. In a frequency domain experiment, the source field is always on, and therefore whether the anomalous currents enhance or reduce our ability to excite a target depends upon the frequency and the location of the target. As we showed, even in experiments that would generally be considered "low frequency" (e.g. < 10 Hz), permeability can have a measurable impact on data collected at the surface.

The role of permeability in the EM response also has implications for how simulations involving conductive, permeable casings can be achieved numerically. On a practical note, when discretizing the casing with standard finite volume or finite element codes, the mesh must be fine enough in the radial direction in order to be able to simulate a poloidal current. This could not be accomplished if the mesh was only a single cell wide. By using a cylindrical mesh, we are able to sufficiently refine the mesh without enormous computational cost. However, a cylindrical mesh is limited in the geometries that can be simulated. Horizontal or deviated wellbore geometries cannot be captured with a cylindrically symmetric mesh.

To simulate more complex, 3D scenarios, multiple authors have suggested replacing a conductive casing with a series of current elements or electric dipoles (Cuevas, 2014), or using a related method of moments approach (Kohnke et al., 2018; Tang et al., 2015) for simulations. Several authors have suggested that such approaches could be extended to include the impacts of permeability by including a model of magnetic dipoles along the axis of the casing (e.g. Patzer et al. (2017); Kohnke et al. (2018)). However, this would imply that the anomalous currents are in the azimuthal direction, which is not what we observe in a grounded-source EM experiment. How to capture the effects of permeability in a practical manner in 3D numerical simulations is an area for future research. A further complicating factor is that, in practice, the magnetic permeability of steel casings is generally unknown. Thus, there are also research opportunities in the development of strategies for estimating casing properties from EM data.

Conclusions

We have addressed the problem of understanding how magnetic permeability contributes to the EM response of a conductive, permeable well in grounded source EM experiments. As others have shown, vari-

able magnetic permeability contributes to the EM response through magnetization and induction components. The interplay of these terms is particularly interesting in the context of steel-cased wells because steel is orders of magnitude more conductive than the surrounding geology.

Within the casing, the combination of the magnetization and induction terms results in a poloidal current system. The nature of this response is important for several reasons. First, the permeability of a well can alter the geometry and the magnitude of currents in the surrounding geologic formation. For certain survey geometries, this can be advantageous for exciting a response in a target of interest. Second, our results illustrate the potential importance of including permeability in numerical simulations of EM experiments in settings with steel infrastructure. This poses a practical challenge because standard finite volume or finite element approaches require that the mesh be refined sufficiently to capture the fine-scale effects within the casing, while being large enough to simulate the geologic structures of interest. We circumvented this challenge by working with a simple model of a vertical casing in a halfspace. An opportunity for future research is to explore strategies for addressing the "upscaling" problem and capturing the impacts due to permeability on a coarser scale for 3D simulations. Another complicating factor is that often magnetic permeability is unknown, so another avenue of future research is to develop strategies to develop an approach for estimating permeability from EM data.

The ability to perform numerical simulations and collect high-quality data continues to improve, and this opens up opportunities to increase the utility of electromagnetics in applications where signals may be subtle or the settings complex. Understanding the details of what contributes to an EM response will be important for extracting insights from those data. We hope that our work contributes to that understanding and helps in the utilization of EM methods in settings with steel infrastructure.

REFERENCES

Augustin, A. M., Kennedy, W. D., Morrison, H. F., & Lee, K. H. (1989, January). A theoretical study of surface-to-borehole electromagnetic logging in cased holes. *Geophysics*, *54*(1), 90–99.

Beskardes, G. D., Weiss, C. J., Um, E., Wilt, M., & MacLennan, K. (2021). The effects of well damage and completion designs on geo-electrical responses in mature wellbore environments. *Geophysics*, *86*(6).

Commer, M., Hoversten, G. M., & Um, E. S. (2015, March). Transient-electromagnetic finite-difference time-domain earth modeling over steel infrastructure. *Geophysics*, *80*(2), E147–E162.

Cuevas, N. H. (2014, September). Analytical solutions of EM fields due to a dipolar source inside an infinite casing. *Geophysics*, *79*(5), E231–E241.

Cuevas, N. H., & Pezzoli, M. (2018, April). On the effect of the metal casing in surface-borehole electromagnetic methods. *Geophysics*, *83*(3), E173–E187.

Haber, E., Schwarzbach, C., & Shekhtman, R. (2016, September). Modeling electromagnetic fields in the presence of casing. In *SEG Technical Program Expanded Abstracts 2016* (pp. 959–964). Dallas, Texas: Society of Exploration Geophysicists.

Heagy, L. J. (2018). *Electromagnetic methods for imaging subsurface injections*. Unpublished doctoral dissertation, University of British Columbia.

Heagy, L. J., & Oldenburg, D. W. (2019a). Direct current resistivity with steel-cased wells. *Geophysical Journal International*, *219*(1), 1–26.

Heagy, L. J., & Oldenburg, D. W. (2019b, April). Modeling electromagnetics on cylindrical meshes with applications to steel-cased wells. *Computers & Geosciences*, *125*(November 2018), 115–130. (arXiv: 1804.07991)

Heagy, L. J., & Oldenburg, D. W. (2023, August). Impacts of magnetic permeability on electromagnetic data collected in settings with steel-cased wells. *Geophysical Journal International*, *234*(2), 1092–1110.

Hoversten, G. M., Commer, M., Haber, E., & Schwarzbach, C. (2015). Hydro-frac monitoring using ground time-domain electromagnetics. *Geophysical Prospecting*, *63*(6), 1508–1526.

Kohnke, C., Liu, L., Streich, R., & Swidinsky, A. (2018, March). A method of moments approach to model the electromagnetic response of multiple steel casings in a layered earth. *GEOPHYSICS*, *83*(2), WB81–WB96.

Nabighian, M. N. (1979, October). Quasi-static transient response of a conducting half-space; an approximate representation. *Geophysics*, *44*(10), 1700–1705.

Noh, K., Oh, S., Seol, S. J., Lee, K. H., & Byun, J. (2016). Analysis of anomalous electrical conductivity and magnetic permeability effects using

a frequency domain controlled-source electromagnetic method. *Geophysical Journal International*, *204*(3), 1550–1564.

Orujov, G., Anderson, E., Streich, R., & Swidinsky, A. (2020, November). On the electromagnetic response of complex pipeline infrastructure. *Geophysics*, *85*(6), E241–E251.

Patzer, C., Tietze, K., & Ritter, O.(2017). Steel-cased wells in 3-D controlled source em modelling. *Geophysical Journal International*, *209*(2), 813–826.

Pavlov, D. A., Zhdanov, M. S., Pavlov, D. A., & Zhdanov, M. S.(2001). Analysis and interpretation of anomalous conductivity and magnetic permeability effects in time domain electromagnetic data part I: Numerical modeling. *Journal of Applied Geophysics*, *46*(4), 217–233.

Puzyrev, V., Vilamajo, E., Queralt, P., Ledo, J., & Marcuello, A.(2017). Three-Dimensional Modeling of the Casing Effect in Onshore Controlled-Source Electromagnetic Surveys. *Surveys in Geophysics*, *38*(2), 527–545. (Publisher: Springer Netherlands)

Schenkel, C. J., & Morrison, H. F. (1994). Electrical resistivity measurement through metal casing. *Geophysics*, *59*(7), 1072–1082.

Tang, W., Li, Y., Swidinsky, A., & Liu, J. (2015, November). Three-dimensional controlled-source electromagnetic modelling with a well casing as a grounded source: a hybrid method of moments and finite element scheme. *Geophysical Prospecting*, *63*(6), 1491–1507.

Um, E. S., Commer, M., Newman, G. A., & Hoversten, G. M.(2015, June). Finite element modelling of transient electromagnetic fields near steel-cased wells. *Geophysical Journal International*, *202*(2), 901–913.

Weiss, C. J.(2017). Finite-element analysis for model parameters distributed on a hierarchy of geometric simplices. *Geophysics*, *82*(4), E155–E167. (ISBN: 0016-8033)

Weiss, C. J., & Daley, T.(2022, February). Introduction to this special section: Life of the well. *The Leading Edge*, *41*(2), 82.

Wilt, M., Lee, K. H., Becker, A., Spies, B., & Wang, S. (1996, January). Crosshole EM in steel-cased boreholes. In *SEG Technical Program Expanded Abstracts 1996* (pp. 230–233). Society of Exploration Geophysicists.

Wilt, M. J., Um, E. S., Nichols, E., Weiss, C. J., Nieuwenhuis, G., & Maclennan, K.(2020). Casing integrity mapping using top-casing electrodes and surface-based electromagnetic fields. *Geophysics*, *85*(1), E1–E13.

Wu, X., & Habashy, T. M.(1994, March). Influence of steel casings on electromagnetic signals. *Geophysics*, *59*(3), 378–390. (ISBN: 0016-8033)

Yang, D., Oldenburg, D. W., & Heagy, L. J. (2016, September). 3D DC resistivity modeling of steel casing for reservoir monitoring using equivalent resistor network. *SEG Technical Program Expanded Abstracts 2016*, 932–936. (Publisher: Society of Exploration Geophysicists)

3D inversion of frequency-domain controlled source electromagnetic data for hydraulic fracturing fluid imaging with the effect of steel casings

Ying Hu[1], and Dikun Yang[1]
[1] Department of Earth and Space Sciences, Southern University of Science and Technology

SUMMARY

Proper utilization of steel casings in the oil and gas development can amplify surface controlled source electromagnetic (CSEM) responses arising from small conductivity perturbations in the reservoir. This work established the capability of recovering the 3D distribution of injected fluid during the operation of fracturing with the presence of arbitrarily complex steel casings. Our approach incorporates steel casings into the conductivity model through the use of edge conductivity, a newly proposed physical property parameter defined as the product of the intrinsic conductivity and cross-sectional area of casing pipe. By assigning edge conductivities to mesh edges and taking them into account in the finite volume formulation, we efficiently capture the effects of casings without any mesh refinement. The inverse problem is solved by the Gauss-Newton method with an objective function containing the smoothness constraints on models. Through a synthetic example involving realistic host rock resistivities and horizontal wells, we show that our algorithm can successfully map the directional flow of injected fluid flow using the top-casing source and electric field data acquired near the well head.

Keywords: 3D Inversion, CSEM, Steel casing, Hydraulic fracturing

INTRODUCTION

Electromagnetic methods are widely applied in assessing reservoir conditions, stimulating reservoir volume, and monitoring fracturing fluid migration during hydraulic fracturing operations (Commer et al., 2020; Hoversten and Schwarzbach, 2021; Li and Yang, 2021).

Hydraulic fracturing imaging models typically involve steel casings with minimal radii and thicknesses significantly smaller than the overall size of rock formations. The presence of steel casings can generate distortion in CSEM data, necessitating sophisticated data processing techniques. However, numerous studies have acknowledged the positive contribution of steel casings to electromagnetic methods: they can enhance observed signals on the surface, especially for deep reservoirs with highly conductive hydraulic fracturing fluids (Weiss et al., 2016; Heagy and Oldenburg, 2022; Hu et al., 2022).

A number of inversion approaches for hydraulic fracturing fluid have been proposed. Some of them have focused on optimizing survey configurations to avoid simulating steel casings or to enhance signal amplitudes (Grayver et al., 2014; Um et al., 2020; Hoversten and Schwarzbach, 2021). Others have simplified hydraulic fracturing fluids into two-dimensional octagonal or non-rectangular shapes (Zhang et al., 2020; Li and Yang, 2021). There are also studies relying on the location data, enforcing robust spatial constraints, or incorporating additional information during the inversion process. (Commer et al., 2020; Noh et al., 2020).

In this study, we develop the 3D simulation algorithm that does not only take cell conductivities defined in mesh cells but also allows assigning edge conductivities to the mesh edges to present steel casings. During the inversion process, we recover the electrical conductivity of the region of interest while fixing the edge conductivities of the casings as a prior. By integrating the edge conductivity modeling into the 3D inversion, we enhance the accuracy of subsurface fluid imaging, and assist the monitoring of the fluid injection.

METHODS

Forward Modeling

Our inversion is based on a 3D-modified finite-volume electromagnetic modeling algorithm (Hu et al., 2022). The governing partial differential equation for the total electric field in CSEM applications is obtained by eliminating the magnetic field in the Maxwell's equations:

$$\nabla \times \nabla \times \boldsymbol{E} + i\omega\mu\sigma\boldsymbol{E} = -i\omega\mu\boldsymbol{J_s}, \qquad (1)$$

where $\boldsymbol{E}$ represents the electric field, ω is the angular frequency, μ is the magnetic permeability, σ and ε represent the electrical conductivity and permittivity, and $\boldsymbol{J_s}$ is the external current source.

In Figure 1(a), the yellow-highlighted region represents a control volume that contains four conductive rectangular prisms oriented along the y-direction. The red-highlighted solid line represents a section of steel casing coinciding

with an edge of the control volume. Applying Stokes' theorem to equation (1), we derive

$$\oint_{\Gamma} \boldsymbol{H} \cdot d\Gamma = \iint_{S} \nabla \times \boldsymbol{H} \cdot d\,S = \iint_{S} (\sigma \boldsymbol{E} + \boldsymbol{J_s}) \cdot d\,S \quad (2)$$

Considering the relatively small cross-sectional area of the steel casing, we can neglect its exact geometric details. Instead, we can use the concept of edge conductivity, which is the product of the cross-sectional area and electrical conductivity, and then readily compute the average electrical conductivity by using edge conductivity (Hu et al., 2022). Similar simulation strategies have also been developed for the finite element method (Weiss, 2017).

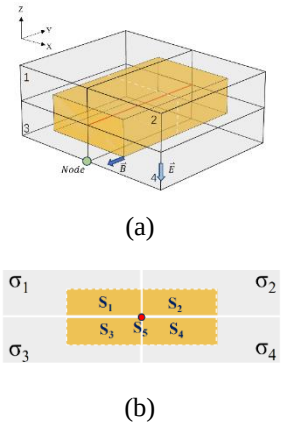

(a)

(b)

Figure 1: Modified finite volume method in a Cartesian, rectangular mesh. (a) A control volume defined around an edge in the y-direction. (b) Calculation of the averaged conductivity.

Our algorithm uses the rectilinear mesh. To simulate arbitrary well paths in 3D space, our code approximate well paths using the surrounding mesh edges. The conductance of a casing segments not directly on mesh edges is redistributed to the nearest eight edges using orthogonal decomposition and tri-linear interpolation, with contributions from neighboring casing segments summed up for the total edge conductivity calculation.

We carry out two casing-in-whole-space simulations, one original and the other as the rotated version of the original (Fig. 2) to validate the algorithm for arbitrary well paths. The background conductivity and the relative location information in the two simulations are identical. The findings depicted in Fig. 3 validate the accuracy of the algorithm. The rotation of the original configuration results in the casing not aligned perfectly with the grid. In both configurations, the amplitude and phase consistently follow a specific pattern. At the observation offsets beyond 125 meters from the steel casing, the relative differences are mostly within 8% for the amplitude and phase.

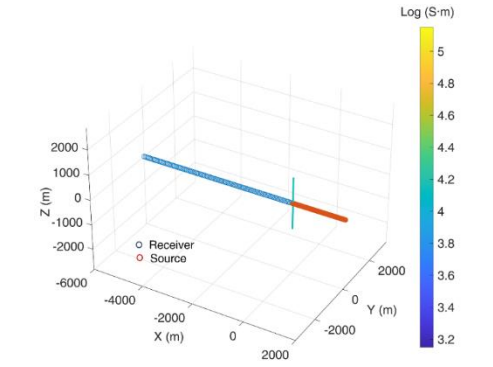

(a)

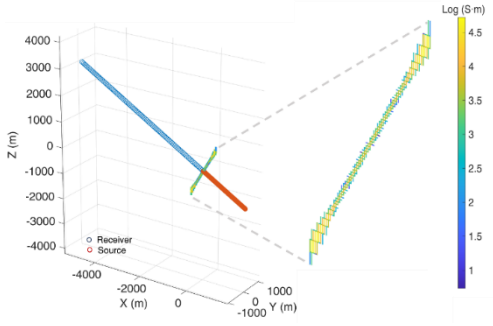

(b)

Figure 2: Tilted well test. (a) The original and (b) rotated configuration. The steel casing is represented by non-zero edge conductivities on the color-coded mesh edges. The source is a grounded wire connecting the mid-point of a finite-length casing and a remote point.

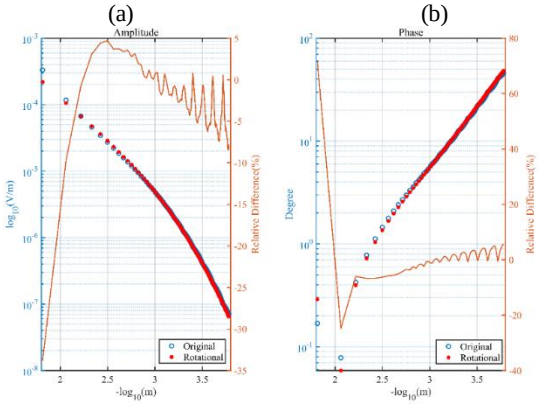

Figure 3: Electric field data at receivers in Figure 2 at 1 Hz. (a) Amplitude; (b) Phase angle.

Inverse modeling algorithm with steel casings

Our inversion relies on a universal frequency-domain electromagnetic inversion framework with the objective function as follows

$$\phi(\mathrm{m}) = \frac{1}{2}\|W_d[F(m) - d_{obs}]\|_2^2 + \frac{\beta}{2}\left\|W_m(m - m_{ref})\right\|_2^2 \quad (3)$$

where W_d is a data-weighting matrix; d_{obs} and $F(m)$ are observed and predicted data, respectively; W_m is the model weighting matrix; m_{ref} is the reference model containing a variety of prior geological information; and $\frac{\beta}{2}$ is a regularization parameter. In our algorithm, the model in equation (3) is a stack of the cell, face, and edge conductivity model vectors. The smoothness constraint are applied to the face and edge conductivity parameters if they are to be recovered in the inversion

$$W_m = \begin{bmatrix} W_c & & \\ & W_f & \\ & & W_e \end{bmatrix}, m_{ref} = \begin{bmatrix} m_c \\ m_f \\ m_e \end{bmatrix}. \quad (4)$$

We employ a Gauss-Newton approach to solve the optimization problem that minimizes equation (3). The model updates are calculated by iteratively solving

$$[Re\{J^H W_d{}^H W_d J\}+\beta W_m{}^T W_m]\delta m = -[\mathrm{Re}\{J^H W_d{}^H W_d [F(m) - d_{obs}]\} + \beta W_m{}^T W_m(m - m_{ref})]. \quad (5)$$

Here, δm is a model update vector, and $J \in \mathrm{X}^{N_d \times N_m}$ is the weighted sensitivity matrix that represents the partial derivatives of the data to the model parameters. The matrix on the left-hand side corresponds to the regularized approximate Hessian, while the right side represents the negative gradient indicating the descent direction.

In some cases, it is possible to directly solve and store the sensitivity matrix, a method referred to as explicit solving. However, storing the sensitivity matrix can consume significant memory resources when dealing with a large volume of data or a high number of model parameters. The limitation becomes especially relevant when considering frequency-domain 3D inversion with steel casing, where the model parameters include the cell, face, and edge elements. As a result, this paper opts for an implicit approach to compute the sensitivity matrix for matrix-vector product operation required by equation (5):

$$J \cdot \delta m = \mathrm{Q}\boldsymbol{A^{-1}}\mathrm{diag}(\boldsymbol{E}) \cdot \boldsymbol{A_{m2e}} \cdot \mathrm{diag(m)} \cdot \delta m, \quad (6)$$

$$J^H \cdot \delta m = \mathrm{diag(m)} \cdot \boldsymbol{A_{m2e}}^{\mathrm{T}} \cdot \mathrm{diag}(\boldsymbol{E}) \cdot \left(\boldsymbol{A^{-1}}\right)^{\boldsymbol{H}} \cdot \mathbf{Q}^{\mathrm{T}} \cdot \delta m, \quad (7)$$

where **A** represents the forward operator and Q represents the data projection matrix. A sparse matrix $\boldsymbol{A_{m2e}}$ can map conductivity values from cell centers to edges. We establish two categories of model parameters for the inversion process: active and inactive. All model parameters are utilized in the forward modeling, but updates are exclusively applied to those designated as active during the inversion.

NUMERICAL EXPERIMENTS

We validate our computational framework of inversion using a synthetic fracturing monitoring example. Specifically, we design simulations involving three steel-cased wells positioned at a depth of 1900 m within a layered background model. The separation between the vertical wells is 50 m, while for the horizontal well is 350 m. The central wellhead is directly connected to an electrical current source of 1 A at 0.01 Hz, with a remote electrode situated 2 km away. To capture the complete electrical field pattern, we employ a uniform measurement grid around the central wellhead, covering a 300×300 m area with measurements every 25 m (Fig. 4(a)).

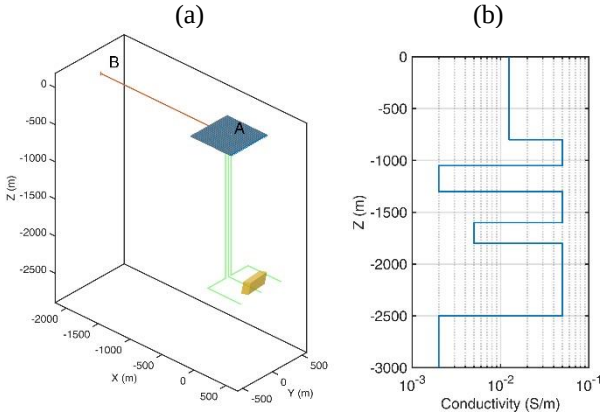

Figure 4: Setup of the synthetic inversion example. (a) The three steel-cased wells, source electrodes, receivers, and injected fluid; (b) Layered background conductivity model.

The injected fluid was represented by a conductive block measuring 150 × 300 × 200 m, with a conductivity of 1 S/m. This block is asymmetrically distributed with respect to the middle well, representing a flow towards the +y direction. The synthetic data generated through forward modeling serve as the observed data for the subsequent inversion. In the inversion, a constant edge conductivity value of 150,000 S·m for all well sections is assumed.

To accurately define the active region for recovery of fluid's cell conductivity, the information of perforation position is used as a prior. Such information constrains active cells within a reasonable region: 0 to 500 m in the x-direction, -500 to 500 m in the y-direction, and -1800 to -2200 m in the z-direction.

Our inversion results successfully recovered the preferential fluid flow towards the +y direction (Fig. 5). This phenomenon was attributed to the enhanced sensitivity of our survey to horizontal fluid movements, a consequence of the parallel configuration of the wells. The blurred boundaries in our inversion results were anticipated outcomes of the smoothness constraint. The synthetic example indicates the effectiveness of our approach in capturing the underlying fluid dynamics. The amplitude and phase of the surface data have also been well-fitted (Fig. 6).

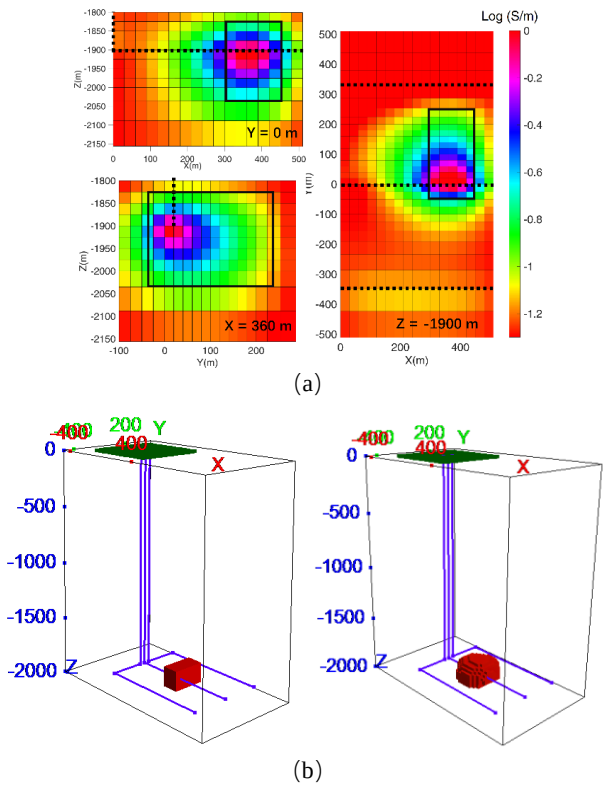

Figure 5: Inversion results of the hydraulic fracturing fluid. (a) The model is sliced at Y =0 m, X = 360 m, and Z = -1900 m. The solid black lines represent the true fluid model and the dotted lines indicate the well. (b) 3D views of the true model (left) and recovered model (right) with the steel casings.

CONCLUSION

Our study established the capability of 3D CSEM inversion in the presence of steel casings. We address the complexity and cost associated with rigorously modeling of steel casing in CSEM inversions by incorporating edge conductivity into the model. Our approach eliminates the need for intricate mesh refinement, and updates only specific model elements exclusively during the inversion, simplifying the overall computational procedure. These strategies ensure that our algorithm is computationally efficient and cost-effective.

Our proposed algorithm stands out for its simplicity, speed, and practical implementation. It does not demand extensive computational resources or intricate mesh adjustments, making it a viable choice for real-world applications. The effectiveness of our approach is demonstrated through a practical example of fracturing monitoring, in which the directional flow of injected fluid is recovered as a 3D conductivity model by using a top-casing source and surface receivers.

ACKNOWLEDGMENTS

This work was funded by the National Natural Science Foundation of China (no. 41974087). The computational work was supported by Center for Computational Science and Engineering at Southern University of Science and Technology.

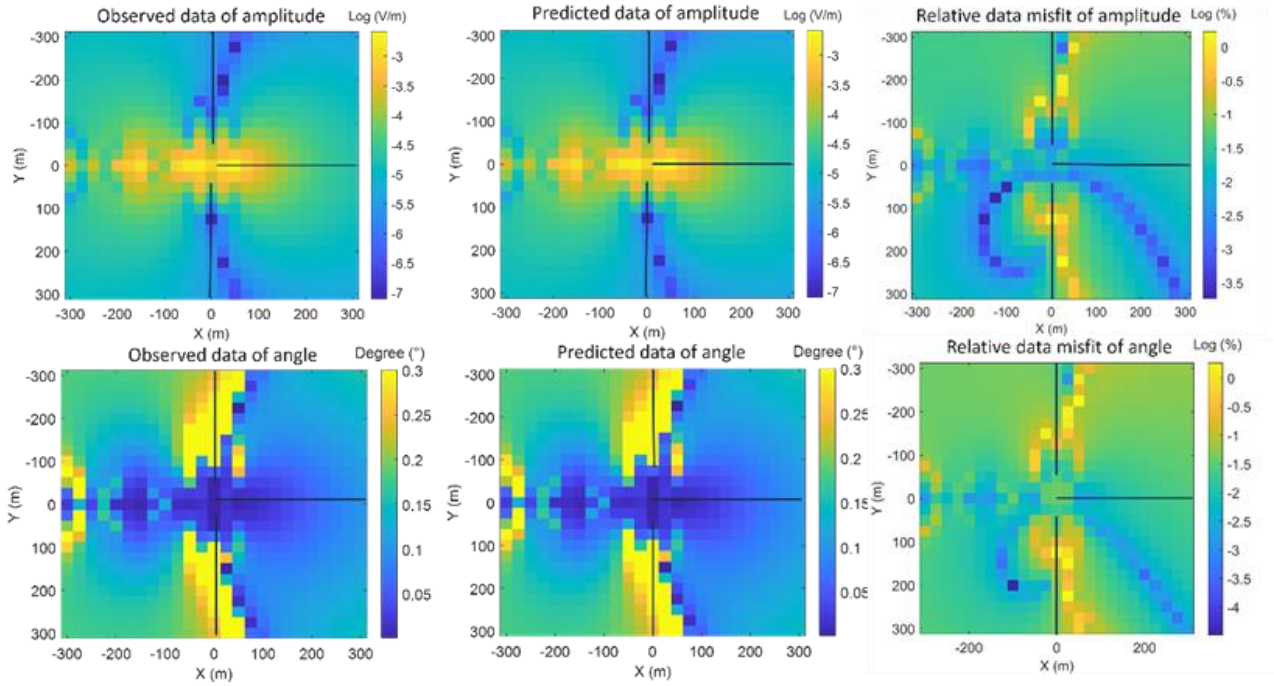

Figure 6: Data fitting of the inversion. The first row is for the amplitude, and the second row for the phase angle. The solid black lines represent the projection of the casings. A top-casing source is connected to the middle wellhead.

REFERENCES

Commer, M., S. Finsterle, and G. Hoversten, 2020, Three-dimensional fracture continuum characterization aided by surface time-domain electromagnetics and hydrogeophysical joint inversion—proof-of-concept: Computational Geosciences, 24, 1–15.

Grayver, A. V., R. Streich, and O. Ritter, 2014, 3D inversion and resolution analysis of land-based CSEM data from the Ketzin CO2 storage formation: Geophysics, 79, 820–830.

Heagy, L. J., and D. W. Oldenburg, 2022, Electrical and electromagnetic responses over steel-cased wells: The Leading Edge, 41, 83–92.

Hoversten, G. M., and C. Schwarzbach, 2021, Monitoring hydraulic fracture volume using borehole to surface electromagnetic and conductive proppant: GEOPHYSICS, 86, E93–E109.

Hu, Y., D. Yang, Y. Li, Z. Wang, and Y. Lu, 2022, 3-D Numerical Study on Controlled Source Electromagnetic Monitoring of Hydraulic Fracturing Fluid With the Effect of Steel-Cased Wells: IEEE Transactions on Geoscience and Remote Sensing, 60, 1–10.

Li, Y., and D. Yang, 2021, Electrical imaging of hydraulic fracturing fluid using steel-cased wells and a deep-learning method: GEOPHYSICS, 86, E315–E332.

Noh, K., K. Ha Lee, S. Oh, S. Jee Seol, and J. Byun, 2020, Location-based parameterization of controlled-source electromagnetic data inversion for the monitoring of hydraulic fracturing with magnetically enhanced proppants: GEOPHYSICS, 85, E27–E39.

Um, E. S., J. Kim, and M. Wilt, 2020, 3D borehole-to-surface and surface electromagnetic modeling and inversion in the presence of steel infrastructure: GEOPHYSICS, 85, E139–E152.

Weiss, C. J., 2017, Finite-element analysis for model parameters distributed on a hierarchy of geometric simplices: GEOPHYSICS, 82, E155-E167.

Weiss, C. J., D. F. Aldridge, H. A. Knox, K. A. Schramm, and L. C. Bartel, 2016, The direct-current response of electrically conducting fractures excited by a grounded current source: GEOPHYSICS, 81, E201–E210.

Wilt, M. J., E. S. Um, E. Nichols, C. J. Weiss, G. Nieuwenhuis, and K. MacLennan, 2020, Casing integrity mapping using top-casing electrodes and surface-based electromagnetic fields: GEOPHYSICS, 85, E1–E13.

Zhang, R., Q. Sun, X. Zhang, L. Cui, Z. Wu, K. Chen, D. Wang, and Q. H. Liu, 2020, Imaging Hydraulic Fractures Under Energized Steel Casing by Convolutional Neural Networks: IEEE Transactions on Geoscience and Remote Sensing, 58, 8831–8839.

3D inversion of onshore controlled source electromagnetic data in the Kusatsu-Shirane Volcano

Keiichi Ishizu[1], Yasuo Ogawa[1], Kuo Hsuan Tseng[1], Takahiro Kunitomo[2], Norihiro Kitaoka[2], Grant Caldwell[3], Takuto Minami[4], Sohei Serita[1], Hiroshi Ichihara[5], Ted Bertrand[3], and Wiebke Heise[3]
[1] Volcanic Fluid Research Center, Tokyo Institute of Technology, Tokyo, Japan
[2] Ontake Science Lab, Nagano, Japan
[3] GNS Science, Lower Hutt, New Zealand
[4] Department of Planetology, Kobe University, Kobe, Japan
[5] Earthquake and Volcano Research Center, Nagoya University, Nagoya, Japan

SUMMARY

A controlled source electromagnetic (CSEM) method uses artificial sources to explore subsurface resistivity structures. We obtained CSEM data in the Kusatsu-Shirane Volcano, Japan where phreatic eruptions have occurred in the past. Eight receivers deployed 4–6 km away from a transmitter recorded CSEM signals from 0.5 km north-south and 1.0 km east-west dipole transmitter. Due to stacking of the long observation time of one week, most of the processed CSEM data showed low standard errors of <2%. We applied three-dimensional inversion to the CSEM data. The inversion is based on the data-space Occam algorithm and its forward modelling part uses the finite difference method. The inversion yielded a resistivity model that sufficiently explained the observed data. The resistivity structure specified a low resistivity anomaly (C1) and a conductor (C2) and a resistor (R1) below C1. We interpret that C1 is a clay cap layer, C2 is a liquid-phase hydrothermal reservoir, and R1 is a two-phase vapor-liquid hydrothermal reservoir. These structures are associated with occurrences of phreatic eruptions and monitoring these structures in the future is effective for understanding phreatic eruptions.

Keywords: Volcanic hazards and risks, Controlled source electromagnetics (CSEM), Magnetotellurics, Inversion

INTRODUCTION

A controlled source electromagnetic (CSEM) method employs artificial sources to investigate the subsurface resistivity structures. CSEM method is robust for noise effects because the injected current can be adjusted against the noise. Furthermore, by customizing the transmitting waveforms and positions of the transmitter and receiver, the CSEM survey can increase the detectability of a target structure.

The Kusatsu-Shirane Volcano is known for occurrences of phreatic eruptions. The phreatic eruptions are associated with the clay cap layer and hydrothermal reservoir below the clay cap layer. Understanding the distributions of these structures is necessary for revealing the mechanism of phreatic eruption occurrences. We aim to investigate the distribution of these structures related to the occurrences of phreatic eruptions.

Noise level is relatively high in this study area. Thus, we consider a CSEM method for investigating the Kusatsu-Shirane Volcano. The CSEM survey used a transmitter with 0.5 km north-south and 1.0 km east-west dipoles and eight receivers.

INVERSION RESULT AND DISCUSSION

Our CSEM survey uses an Electromagnetic-Accurately Controlled, Routinely Operated Signal System (EM-ACROSS). The EM-ACROSS is useful for obtaining low-error CSEM response in a noisy environment. The basic feature of EM-ACROSS is that it can repetitively transmit the precisely controlled signals. The precisely controlled signals are useful for stacking of long-term observation data. The stacking of long long-term data may yield CSEM responses with low errors.

EM-ACROSS transmitted the current from 0.5 km north-south and 1.0 km east-west dipole and eight receivers deployed 4–6 km away from a transmitter (Figure 1). The receivers recorded the transmitter signals for a week. Due to stacking of the long observation time of one week, most of the processed CSEM data showed low standard errors of <2%.

We use 3D CSEM inversion code developed by Ishizu et al., (2022). This inversion code is based on the data-space Occam algorithm. The data-space algorithm is useful for reducing computational costs when the data number is much less than the number of model parameters. The forward modeling algorithm of the inversion code applies the finite difference method with a primary-secondary

field approach. The primary-secondary can prevent the numerical singularity at the source positions. The primary field is analytically computed using the 1D primary model. The linear system for the finite difference method is solved using a sparse direct solver of PARDISO.

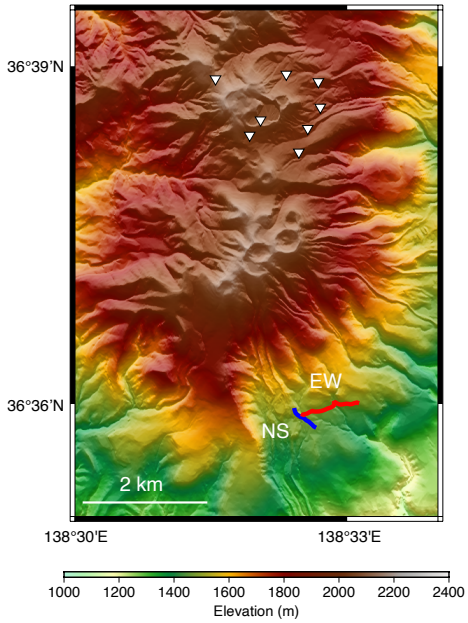

Figure 1: Map of the survey area. The locations of the transmitter and receivers are overlaid on the map.

We inverted the observed CSEM data consisting of five-component electromagnetic data (Ex, Ey, Hx, Hy, and Hz) with a frequency range of 0.1–50 Hz. The initial model for the inversion was 10 Ωm half-space. We used 80 × 70 × 81 cells in x, y, and z directions for model discretization. The RMS misfit for the initial model was 19. The inversion obtained a resistivity model after 27 iterations with an RMS misfit of 1.5. The model responses sufficiently fit the observed data.

The resulting resistivity model specified important structures for the Kusatsu-Shirane Volcano: a clay cap layer (C1) and a hydrothermal reservoir (C2 and R1) below the clay layer (Figure 2). The resistivity values vary in the hydrothermal reservoir. We interpret the high resistivity zone (R1) is a two-phase vapor-liquid hydrothermal reservoir and the low resistivity zone (C2) is a liquid-phase hydrothermal reservoir. These structures are associated with occurrences of phreatic eruptions.

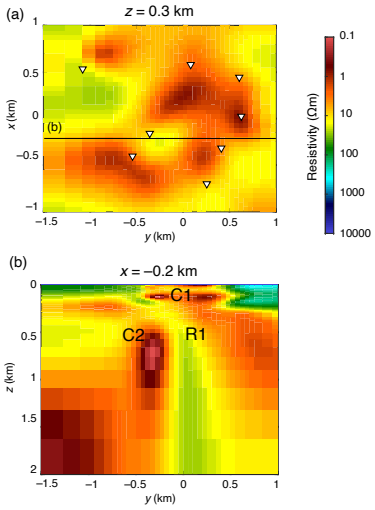

Figure 2: Inversion result. (a) Horizontal 2D section and (b) Vertical 2D section of the resistivity model. White triangles show receivers.

Conclusions

We conducted a CSEM survey using two sources and eight receivers in the Kusatsu-Shirane Volcano. EM-ACROSS was used for the CSEM survey. Due to the long observation time of one week, the CSEM survey obtained the CSEM data with low errors. The five-component data with the frequency range of 0.1–50 Hz were analyzed using the 3D inversion code. The resulting resistivity model specified important structures for the Kusatsu-Shirane Volcano: a bell-shaped clay layer and a hydrothermal reservoir below the clay layer. The resistivity values vary in the hydrothermal reservoir. We interpret the high resistivity zone is a two-phase vapor-liquid hydrothermal reservoir and the low resistivity zone is a liquid-phase hydrothermal reservoir. These structures are associated with occurrences of phreatic eruptions and monitoring these structures in the future is effective for understanding phreatic eruptions.

Acknowledgments

We thank the Japan Society for the Promotion of Science, KAKENHI for supporting this presentation (grant numbers 20H01992, 22K14104, and 23K17803).

References

Ishizu, K., Siripunvaraporn, W., Goto, T. N., Koike, K., Kasaya, T., & Iwamoto, H. (2022). A cost-effective three-dimensional marine controlled-source electromagnetic survey: Exploring seafloor massive sulfides. Geophysics, 87(4), E219-E241.

Interferographic TEM Beamforming Resolution

Bryan James[1], Kyubo Noh[2], Andrei Swidinsky[2], Johannes Stoll[3], and Daryl Ball[4]
[1]Electromagnetic Geophysical Imaging Solutions, LLC
[2]University of Toronto, Department of Earth Sciences
[3]Mobile Geophysical Technologies GmbH
[4]Glencore Canada Corporation

SUMMARY

A new method called Interferographic Transient Electromagnetics (ITEM), for semi-airborne multi-source, multi-receiver TEM data, is described using beamforming techniques to synthetically form impulsive distributions of TEM fields that partially unmix TEM signal returns from the subsurface and improve resolution of subsurface geoelectric structure. ITEM differs from application of the wave propagation synthetic aperture concept to diffusive EM geophysics, which achieves no vertical compaction. ITEM achieves full beamforming by using both spatial and temporal sets of subsurface electric field distributions to form a space-time digital filter that yields significant impulsive TEM field compaction in both horizontal and vertical dimensions. The ITEM concept is described for a 2D geometry. ITEM processing is applied to a reference model set of electric field distributions as well as both reference model and acquired magnetic field profiles. The resulting filtered distributions are translated into a subsurface resistivity image using a simple image formation process. An example for a synthetic geoelectric structure is provided that demonstrates ITEM processing and subsurface imaging. A further simulated test of ITEM resolution improvement is based on determining the minimum visible distance between two conductors in comparison to that seen in the original TEM fields. An initial test of ITEM processing on field TEM data is performed on data acquired at Raglan Mine, Quebec.

Keywords: transient electromagnetics, beamforming, semi-airborne, imaging

INTRODUCTION

Many applications of electromagnetic (EM) geophysics could benefit from improvements in localized spatial resolution of geoelectric properties. The achievable resolution is significantly constrained by the diffusing distribution of current density induced in the subsurface which loses curvature increasingly with time (or decreasing frequency) and depth of diffusion. Measured magnetic fields above the earth's surface are coupled to all of the subsurface current density at all locations, with the result that there is considerable overlap in signals from different zones, limiting resolution.

A promising avenue for EM resolution improvements is to sharpen the electric field distribution in the earth created by EM sources, whether by synthetic or physically real means. In a variety of adjacent technical disciplines [such as Radio Frequency signals intelligence (Tuncer and Friedlander, 2009), synthetic aperture radar (Moreira et al, 2013; Jakowatz et al, 2012), radio astronomy (Levanda et al, 2009), and medical imaging (Jensen, et al, 2006; Feng et al, 2001)] a very powerful technique is the weighted combination of multiple sources and/or sensors to create a synthetic aperture (SA). A SA increases the lateral focusing of a signal that is controlled by the overall length of the source or receiver set. A key characteristic of wave propagation SA techniques is that range resolution is very good due to the inherent separation of propagating signals in time. This ingredient is greatly reduced for the EM diffusion geophysics case, and significantly weakens the utility of the SA concept for EM applications. Even so, efforts toward the use of SA concepts have been made in frequency-domain marine controlled source EM (Fan et al, 2010; Knaak et al, 2015; Tu and Zhdanov, 2020). A SA EM method has been described for terrestrial application to mineral exploration problems by Kolaj and Smith (2015).

While the SA concept is powerful for wave propagation problems, it is only a means to the end called beamforming. Beamforming is the concept of synthetically creating the ability to sense a signal coming from, or send a signal going to, a highly localized point in space. SA beamforming for wave propagation is solely a spatial filter, with coefficients adapted for different target locations. The SA concept is incomplete, however, for EM diffusion beamforming precisely because of the substantial loss of time separation of returns from different ranges (depths). For EM diffusion a SA achieves no vertical EM field compaction. Beamforming itself is the more useful concept for sharpening diffusive TEM field structure.

We pursue maximal synthetic concentration of the electromagnetic field for any point in the subsurface as this will provide enhanced spatial resolution of subsurface features. The beamforming approach uses a field

interference approach accomplishing both constructive and destructive interference to concentrate field structure where desired and reduce the field everywhere else. Therefore, the new beamforming algorithm is called Interferographic TEM (ITEM) to reflect this physics basis, as well as to avoid confusion with SA processing. Accomplishing full beamforming for TEM requires a multi-dimensional filter operating both over a number of sources as well as over time. Here the use of the time dimension serves as a proxy for the z-direction, since diffusion steadily penetrates to greater depths as time increases. The use of multiple TEM sources in an integrated manner is not new (James and Borns, 1993; Wright et al., 2002; Oldenburg et al., 2013). Designing filters to combine the subsurface electric fields from multiple sources over time into a compact synthetic subsurface electromagnetic field structure is a new step for TEM applications.

A prime candidate for a terrestrial ITEM geophysics system is the semi-airborne survey design (Elliott, 1998; Smith et al., 2001), consisting of multiple sources on the ground and airborne magnetic field receivers. Much recent activity is occurring in drone-based semi-airborne EM geophysics as it rapidly gains in utility (Ito et al., 2014; Becken et al., 2020; Stoll et al., 2020).

ITEM Beamforming and Resistivity Imaging

We formulate a 2-D problem, assuming data distributed in (x,t), to form a subsurface image in a (x,z) plane, to simplify the concept description. This development uses an array of grounded wire sources distributed in the 'x' direction, that are oriented in the 'y' direction (orthogonal to the profile). Loop sources work as well.

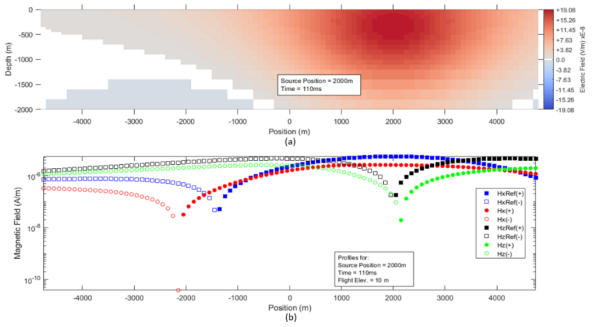

Figure 1: (a) X-Z cross-section of E_y in the earth at time = 110 ms for a grounded wire source oriented in the 'y' direction at position x = 2000 m for a halfspace model of 10 ohm-m. (b) Example H_x and H_z profiles, simulated as collected by a drone flying 10 m above the earth surface, corresponding to E_y in (a). Square symbols denote reference data. Circles denote acquired data. Positive values are filled symbols; negative values are open symbols. Blue denotes reference H_x and black denotes reference H_z. Acquired field data are red for H_x and green for H_z.

The TEM beamforming algorithm uses the electric field (E) distributions (e.g., see Figure 1), for a reference model, for a number of source positions (NX_s) as well as for all of the times (NT) collected ($NX_s \cdot NT = N_{st}$ unique E distributions) to construct, via weighted summation, a virtual E_f distribution ('*f*' for filter) centered on a desired subsurface location. E_f is as localized as possible given the set of individual subsurface E distributions available as inputs. The space-time weights form a digital filter. The physical effect is equivalent to generating an interference pattern from the numerous individual E distributions (weights create both constructive and destructive interference) to build an E_f distribution centered at a desired position that is much more compact than occurs for any original E distribution at that position at one time from one source. The computation of weights is performed for a gridded subsurface (with $NX \cdot NZ = N_{xz}$ locations) where a unique set of (x_s,t) weights occurs for each subsurface position.

The ITEM weight coefficient derivation closely follows that in Fuchs (2007) for medical magnetoencephalogram (MEG) imaging. In TEM geophysics the electric field is everywhere in the subsurface and so ITEM forms smeared impulsive E_f distributions. ITEM weights constitute a beamformer that creates compact E_f distributions centered at all desired subsurface positions in a x-z plane. The weights are then also applied to acquired and reference model magnetic field data to form filtered magnetic field profiles, H_f.

We find a set of coefficients $W(x_s,t;x,z)$, where x_s is source position and t is time, that produces electric field distributions that are maximally compact and centered at subsurface positions denoted by '*x,z*'. The solution for the beamformer weights uses the Lagrange multipliers method. The beamformer coefficients are, in matrix form,

$$\mathbf{W} = \frac{\mathbf{C}^{-1} \cdot \mathbf{E}^{\mathrm{T}}}{\mathbf{E} \cdot \mathbf{C}^{-1} \cdot \mathbf{E}^{\mathrm{T}}} . \qquad (1)$$

W is a N_{st} by N_{xz} matrix, **E** is the set of input E distributions, and **C** is the correlation matrix of all input E distributions. The filtering equations to obtain E_f distributions and H_f profiles are, in matrix form,

$$\mathbf{E}_{\mathrm{f}} = \mathbf{E} \cdot \mathbf{W} \quad , \text{and} \qquad (2)$$

$$\mathbf{H}_{\mathrm{f}} = \mathbf{H} \cdot \mathbf{W} . \qquad (3)$$

Figure 2 is an example of *W* variations for a simple 10 ohm-m halfspace reference model for producing an E_f distribution centered on one cell position. The weighting coefficients display oscillatory behavior which have the equivalent physical effect of constructive and destructive interference. The interference result is shown in Figure 3. Most of the resulting interference pattern across the subsurface grid are small amplitude sidelobes (destructive

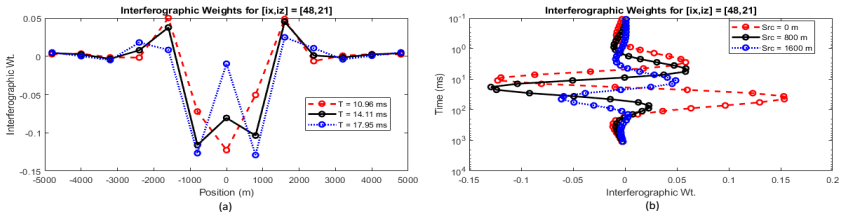

Figure 2: Selected weighting coefficients for the E_f distribution centered on one subsurface position calculated for the halfspace reference model. (a) Weights vs. source positions for 3 adjacent times. (b) Weights vs. time for 3 adjacent sources; early times reflect shallow E distributions and later times reflect deeper E distributions.

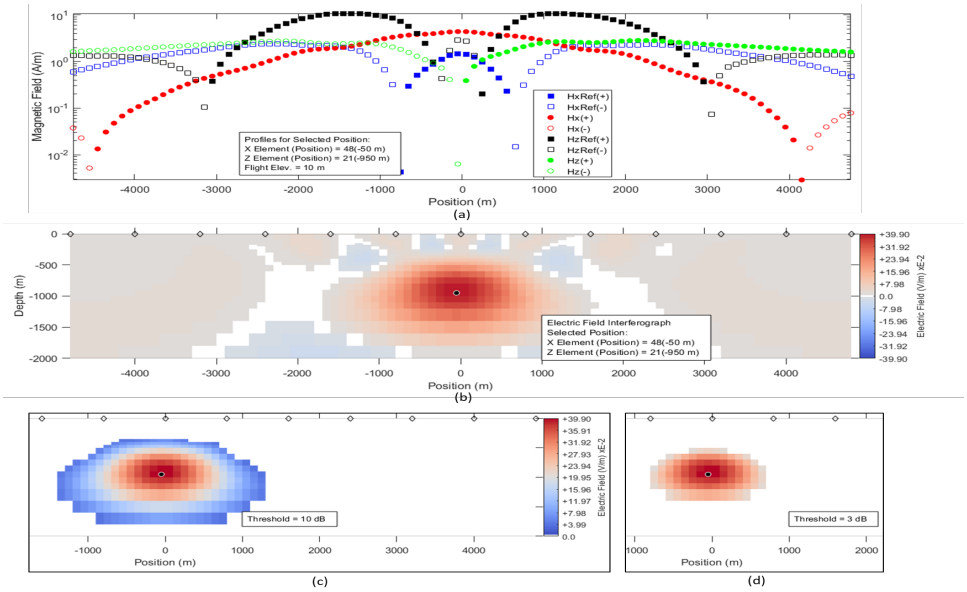

Figure 3: Filtering results for one element in the subsurface. (a) Calculated H_f profiles, simulated as being collected by a drone flying 10 m above the earth surface. Symbols are as described for Figure 1. (b) Calculated E_f distribution. The diamond symbols at the top of the cross-section denote the source positions used for calculation inputs. (c) E_{ft} distribution after 10 dB threshold. (d) E_{ft} distribution after 3 dB threshold. The colorbar displayed in (c) is also used for (d). The E_f and E_{ft} distributions all display a black dot at the designated cell position.

interference), leaving one main lobe that is as small as the inputs allow (constructive interference).

The raw E_f distributions (e.g., Figure 3(b)) should be reduced to some part of their main lobe for purposes of synthesizing a resistivity image. Figure 3 shows E_{ft} ('t' for threshold) for both 10 dB and 3 dB (½ of peak amplitude) thresholds. 3 dB follows signal processing norms and is the ITEM default.

The difference between acquired and reference H_f data, for a specific (x,z) subsurface position, is used in an image formation process (IFP) where it is related back to the E_{ft} distribution centered at (x,z). An increase in acquired H_f relative to reference H_f indicates greater current density J, and vice versa; greater J translates into higher conductivity, and vice versa, for the elements in that compact distribution – a linear relationship is assumed. The linear assumption is good for small resistivity contrasts but increases in error for larger changes. This IFP exclusively uses the H_x data at present; the H_{xf} profiles are maximum and almost symmetric above the E_{ft} distribution in Figure 3(a). In contrast, the H_{zf} profiles are more complicated. The algorithm is as follows.

Each filtered output, for each and every (x_i,z_i) position, is a distribution in the (x_k,z_k) domain. 1) Compute the $H_{xf}(x_k)$ profile residual for each (x_i,z_i). 2) Sum over all of the $E_{ft}(x_i,z_i)$ distributions for each (x_k,z_k). 3) Repeat the summation but with the $H_{xf}(x_k)$ profile residual multiplied with the associated $E_{ft}(x_k,z_k)$ values (i.e., point-by-point in x_k) for each (x_i,z_i). 4) Ratio the residual H mediated summation by the simple E summation, which is an estimate of the change in current density, Δj, in each cell. This ratio maps into a resistivity estimate, ρ_{est}, for each (x_k,z_k) cell as

$$\rho_{est}(x_k, z_k) = \rho_{ref}(x_k, z_k)/(1 + \Delta j(x_k, z_k)). \quad (4)$$

Issues arise with (4) for $\Delta j <= -1$; as Δj approaches -1 the $1 + \Delta j$ term is changed to $10^{\Delta j}$, which is nonlinear.

Results

A simulated test for semi-airborne survey design is utilized with 13 grounded wire sources, each 1000 m long, oriented in the y-direction (perpendicular to x-direction profile) that are separated by 800 m, for a total profile length of 9600 m. A subsurface grid of dimensions 9600 m in x and 2000 m in z is used for the subsurface E distributions. H measurements for each source are simulated for a drone 10 m above the earth's surface. The simulated model is the buried basin shown in Figure 4. The acquired data displayed in Figure 3 are for this simulated buried basin. The resistivity image resulting from ITEM processing is shown in Figure 5. This image result uses a gradational layered reference model of increasing resistivity with depth. This first result can be used to generate a new reference model, and the ITEM process repeated, in an iterative cycle until convergence is achieved between the acquired and reference H_{xf} data. First ITEM processing of TEM field data, from Raglan Mine in northern Quebec, is shown in Figure 6.

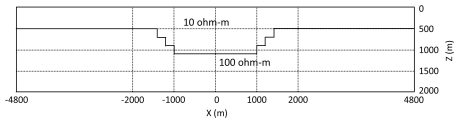

Figure 4: Buried basin model used to simulate acquired magnetic field profile data for ITEM processing.

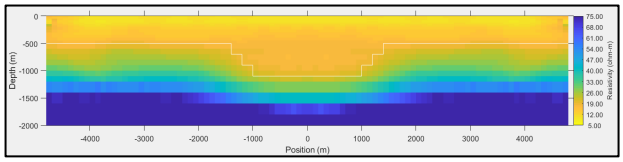

Figure 5: Resistivity image for ITEM processing of simulated buried basin data. The basin model is superimposed.

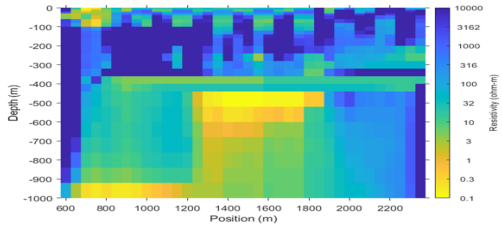

Figure 6: Resistivity image from ITEM processing of TEM field data at Raglan Mine, Quebec.

Finally, a resolution exercise in which the minimum visible distance between two conductors is found is conducted to highlight the reduction in minimum distance achieved with ITEM processing vs. the original TEM magnetic profile data. The ITEM results show a reduction of about 40% in the minimum visible separation in this comparison.

Discussion

ITEM beamforming is a method to synthetically sharpen the shape of the TEM field. In effect, it partially *unmixes* the signal returns from different parts of the medium. This enables improved resolution relative to the resolution achievable with the original TEM field structure in which the signal returns are highly *mixed*. The signal mixing/unmixing concept being used here is completely analogous to the wave propagation case for synthetic aperture radar (SAR). In SAR a single RF beam actually has broad coverage of a ground scene, with all of the signal returns from different scene elements mixed together. The use of many such broad RF beams from different positions covering the same ground scene enables the SA processing method to unmix all of the signal returns from the many scene elements and produce an image with very high spatial resolution that is mostly set by the RF signal frequency (and equivalent wavelength) as well as the length of the SA. For TEM the signal returns come from earth elements distributed both laterally and vertically. The degree of signal return unmixing from ITEM processing is set by the location of the TEM sources as well as the spatial variation of the diffusing TEM field, which is much broader than the SAR case. This limit to signal return unmixing sets the degree of geoelectric structural resolution attainable.

Conclusion

A new method of TEM data synthesis called Interferographic TEM is introduced. ITEM implements a full beamforming solution as a space-time digital filter to increase localization of EM field structure in filtering results for both subsurface E distributions and H profiles. The new method uses distributions in both space and time to achieve field compaction in both lateral and vertical dimensions. These interferographic products are used to produce a resistivity image section. An example for a simulated structure shows a good resistivity image facsimile of the structure is obtained by ITEM processing. A first field example with ITEM processing is also shown for TEM data at Raglan Mine, Quebec. The process may be generalized into an iterative cycle to improve results until model convergence is reached. Also, a two-conductor resolution test shows ITEM reduces the minimum separation at which the two are visibly distinguishable in comparison to the original TEM profiles by about 40%.

REFERENCES

Becken, M., Nittinger, C., Smirnova, M., Steuer, A., Martin, T., Petersen, H., Meyer, U., Mörbe, W., Yogeshwar, P., Tezkan, B., Matzander, U., Friedrichs, B., Rochlitz, R., Günther, T., Schiffler, M., and Stolz, R., and the DESMEX Working Group, 2020, DESMEX: A novel system development for semi-airborne electromagnetic exploration: GEOPHYSICS, **85**, no. 6, E253-E267.

Elliott, P., 1998, The Principles and practice of FLAIRTEM: Exploration Geophysics, **29** (1/2), 58-60.

Fan, Y., Snieder, R., Slob, E., Hunziker, J., Singer, J., Sheiman, J., and Rosenquist, M., 2010, Synthetic aperture controlled source electromagnetics: Geophys. Res. Lett., **37**, no. 13, L13305.

Feng, D., Xu, Y., Ku, G., and Wang, L., 2001, Microwave-induced thermoacoustic tomography: Reconstruction by synthetic aperture: Medical Physics, **28**, no. 12, 2427-2431.

Fuchs, A., Beamforming and Its Applications to Brain Connectivity, 2007, In *Handbook of Brain Connectivity. Understanding Complex Systems.* Springer, Berlin, Heidelberg, pp. 357-378.

Ito, H., Kaieda, H., Mogi, T., and Jomori, A., 2014, Grounded electrical-source airborne transient electromagnetics (GREATEM) survey of Aso Volcano, Japan: Exploration Geophysics, **45**, no.1.

Jakowatz, C., Wahl, D., Eichel, P., Ghiglia, D., and Thompson, P., Spotlight-Mode Synthetic Aperture Radar: A Signal Processing Approach, 2012, Springer Science+Business Media.

James, B., and Borns, D., 1993, Transient electromagnetic two-dimensional subsurface resistivity imaging near the Waste Isolation Pilot Plant, Carlsbad, New Mexico: SAND report, Sandia National Laboratories, Albuquerque, New Mexico.

Jensen, J., Gammelmark, K., and Pedersen, M., 2006, Synthetic aperture ultrasound imaging: Ultrasonics, **44**, pp. e5-e15.
Knaak, A., Snieder, R., Suilleabhain, L., Fan, Y., and Ramirez-Mejia, D., 2015, Optimized 3D synthetic aperture for controlled-source electromagnetics: GEOPHYSICS, **80**, no. 6, E309-E316.

Kolaj, M., and Smith, R., 2015, A multiple transmitter and receiver electromagnetic system for improved target detection: GEOPHYSICS, **80**, no. 4, E247-E255.

Levanda, R., and Leshem, A., 2009, Synthetic aperture radio telescopes: IEEE Signal Processing Magazine, **27**, no. 1, 14-29.

Moreira, A., Prats-Iraola, P., Younis, M., Krieger, G., Hajnsek, I., and Papathanassiou, K., 2013, A tutorial on synthetic aperture radar: IEEE Geoscience and Remote Sensing Magazine, **1**, no. 1, 6-43.

Oldenburg, D., Haber, E., and Shekhtman, R., 2013, Three dimensional inversion of multisource time domain electromagnetic data: GEOPHYSICS, **78**, no. 1, E47-E57.

Smith, R., Annan, A., and McGowan, P., 2001, A comparison of data from airborne, semi-airborne, and ground electromagnetic systems: GEOPHYSICS, **66**, no. 5, 1379–1385.

Stoll, J., Noellenburg, R., Kordes, T., 2020, Semi-Airborne electromagnetics using a multicopter: Fast Times, **25**, no. 3, 106-113.

Tu, X., and Zhdanov, M., 2020, Robust synthetic aperture imaging of marine controlled-source electromagnetic data: IEEE Transactions on Geoscience and Remote Sensing, **58**, no. 8, 5527-5539.

Tuncer, E., and Friedlander, B., (Eds.), 2009, Classical and modern direction-of-arrival estimation: Academic Press.

Wright, D., Ziolkowski, A., and Hobbs, B., 2002, Hydrocarbon detection and monitoring with a multichannel transient electromagnetic (MTEM) survey: The Leading Edge, vol. 21, 852-864

Understanding problems in old MT data using modern methods

Alan G. Jones[1], Randall Mackie[2] and Wolfgang Soyer[2]
[1] ManoTick GeoSolutions (MTGS), Manotick, Ontario, Canada
[2] CGG Multiphysics Imaging, Milan, Italy

SUMMARY

Although the natural-source magnetotelluric method is relatively simple compared to controlled-source EM methods, the MT impedance estimates sometimes pose difficulties for modelling/inversion. Here we focus on two well-known legacy datasets that have never been completely understood. The first of these is the BC87 dataset, which exhibits Phase Roll Out of Quadrant (PROQ) for low frequency PhaYX data at all sites on the Nelson batholith, but none of the sites off the batholith. The second is Okak Bay, with very unusual dropping RhoA values at some sites close to an imaged and drilled conductor at some 500 m. Using a modern 3D MT inversion code that incorporates galvanic distortion, we can fit the PROQ effects in the BC87 data, but the model may not be geologically meaningful. The Okak Bay data remain enigmatic. An updated version of the code that inverts log(Z) and phaZ instead of Real(Z) and Imag(Z) does come close to having the steep RhoA curves, but not completely.

Keywords: 3D MT inversion, BC87, Okak Bay

INTRODUCTION

The natural-source magnetotelluric method (MT) is one that is seeing increasing usage across the globe, particularly commercially for imaging mineral deposits and geothermal systems. Although modelling and inversion tools are well advanced, there remains some data that still present significant challenges.

We examine two legacy datasets here, BC87 and Okak Bay using modern 3-D inversion. Both of these datasets have aspects that were perplexing at the time.

We conclude that fundamentally more data are needed at both locations in order to really understand the subsurfaces beneath them.

BC87

The BC87 dataset was acquired by Phoenix Geophysics in 1987 as the first test of contracting MT data for Lithoprobe through a Lithoprobe grant to Doug Oldenburgh. Data were acquired at a total of 27 locations from the Purcell Anticlinorium over the Kootenay Arc and the Nelson batholith onto the Omineca Belt (Fig. 1). The data were acquired in site-pairs, with approximately 2 km spacing between them, because in those days timing for remote-referencing was accomplished through a cable connection between the two sites. A description of the data can be found in Jones (1993).

One distinctive feature of the BC87 data is that the low frequency phases for the E-W electric field, i.e., PhaYX, at sites ON the batholith all go out of their quadrant, whereas at sites OFF the batholith this Phase Roll-Out of Quadrant (PROQ) doesn't happen.

An example is site 02 in the middle of the batholith, and the data are plotted in Fig. 2. Note the PhaYX data (blue symbols) leaves the 3rd quadrant by 2 s period and rotates into the 4th quadrant.

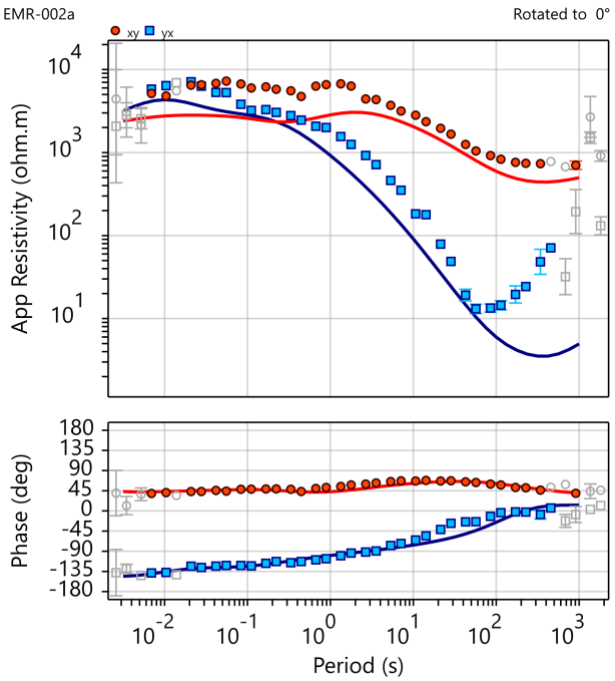

Figure 2: MT data at site 02. Solid lines are the model fit. Red = XY; Blue = YX.

A contour plot of the out-of-quadrant phases shows the PROQ effect limited to the extent of the batholith.

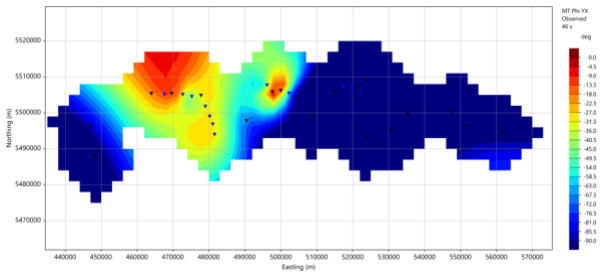

Figure 3: Out-of-quadrant PhaYX phases at 46 s period.

Despite these data being one of the datasets examined in the first MT Data Inversion Workshops (MT-DIW2), held in Cambridge, UK, in 1992, and quite a few authors looking at them, a satisfactory explanation has never been proffered. 3D galvanic distortion of a regional 2D Earth was unsatisfactory (Jones et al., 1993), as were other suggestions.

Additional data are available for this area and were acquired in 1988 by Advanced Energy Technology (AET) using their newly-developed EMAP system. The bipoles were 1000 feet in length, and the remarkable PROQ effect was seen in all of the data on the batholith. The change occurred over one dipole length, from off-batholith to on-batholith.

We undertook extensive 3D inversion of these data using the RLM-3D code of Randy Mackie (Mackie et al, 2020), which allows for galvanic distortion (Soyer et al, 2018).

The current best model is shown in Fig. 4. Weird 3D geometries of near-surface conductors in the area of the Nelson batholith combined with very large crustal conductors to the south are imaged. The geological interpretation is that there is a conducting sequence at the base of the batholith, and the conductor to the south is known from regional data in SE BC and NW Montana on the Purcell Anticlinorium (Gupta & Jones, 1995).

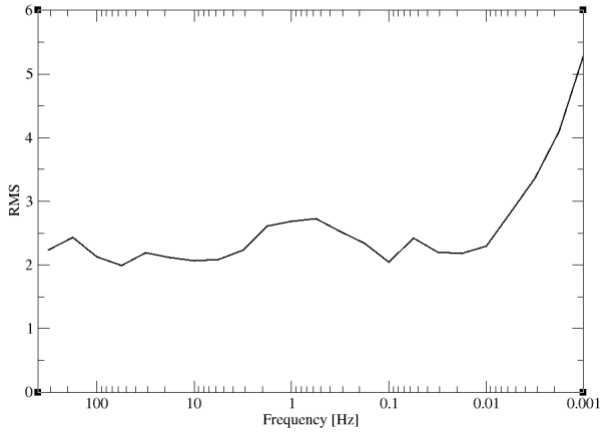

Figure 5: BC87 Average misfit by frequency.

The misfits to this model show a bias, with high misfits at low frequencies (Fig. 5).

OKAK BAY

The second puzzling dataset comes from Okak Bay in northern Labrador. This 46-site dataset (locations shown in Fig. 6) was acquired for a commercial client (Gallery Resources) by Phoenix Geophysics in 1997. The survey area was chosen based on a magnetic high, with the hope that another Voisey's Bay was there.

Initial RRI inversions by Phoenix suggested a shallow anomaly, and a deeper very extensive one. Drilling (OK1-M1, OK-M2/OK-M3 locations in Fig. 6) found the shallow anomaly, but not the deeper one.

One aspect of the dataset is the very steeply-declining RhoA curves at low frequencies <10 Hz, exemplified by site *gal005* (Fig. 7). The decline is greater than 45° (solid line on the RhoA plots), and is inconsistent with the phase responses (dashed lines on the RhoA plots).

2D analyses by Jones and Garcia (2003) showed this RhoA-Pha inconsistency, which possibly led to the erroneous deep highly conducting body. Jones and Garcia (2003) inverted data along the various transects down to only 10 Hz in 2D, and a pseudo-3D model was constructed from the 2D models.

Trials were made of all sites, the core of sites, and of site *gal005* on its own, allowing extreme rapid variations in conductivity by turning the smoothing off, and allowing extreme galvanic distortion.

The current best 3D model (Fig. 8) shows a conductive anomaly exactly where the pseudo-3D model, created from 2D inversions, placed it.

Although the final model from 3D inversion was able to fit reasonably well (Fig. 9), it was not able to match the steep RhoA drop at site gal005 (Fig. 10).

Also the average RMS at each frequency shows a very strong bias, with high and low frequencies being poorly fit, and mid-band frequencies being very well fit (Fig. 11). This plot is an exemplar that a single number does not well describe how close a model is to the data, and higher level statistics need to be considered (Jones, 2018).

To address this problem of misfitting RhoA at *gal005* at low frequencies, the code was modified to invert for log(|Z|)-phaZ instead of Real(Z)-Imag(Z), and emphasis was placed on fitting the impedance amplitudes. This was somewhat more successful, although not entirely. The fit when inverting only site gal005 in shown in Fig. 12.

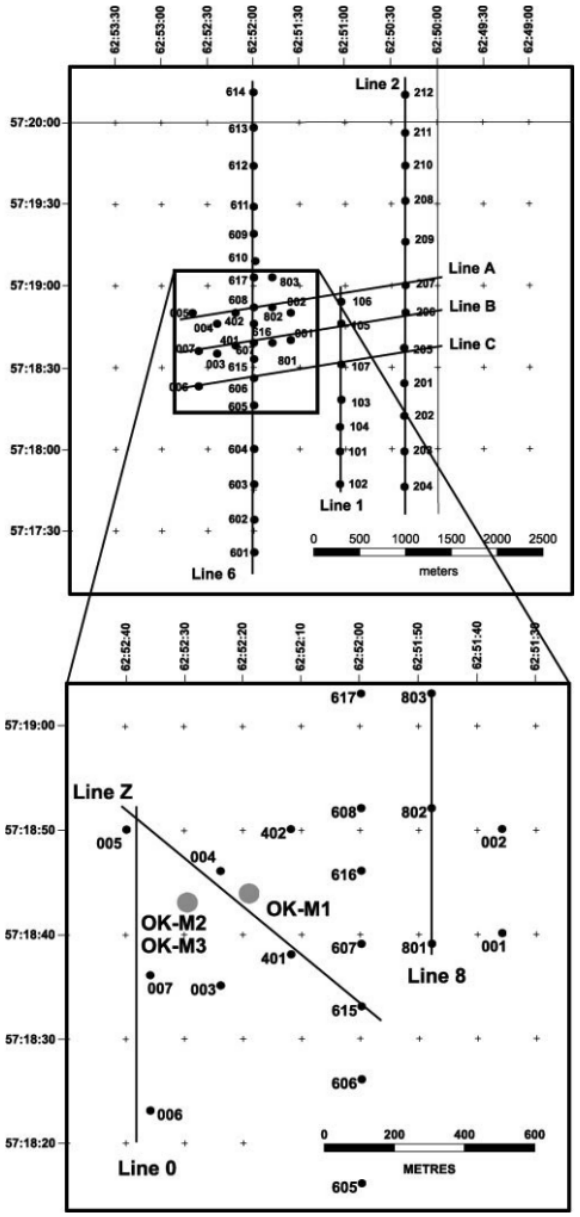

Figure 6: Map of AMT site locations in the Okak Bay deposit area. The AMT sites were assigned to the nine profiles shown (0, 1, 2, 6, 8, A, B, C, Z). Also shown are the locations of the drillholes OK-M1 and OK-M2/OK-M3.

CONCLUSIONS

Although we have come a long way since the Dark Ages of the 1970s when one of us (AGJ) first started making MT measurements, and MT has become a very viable geological tool, there are still challenges. These two datasets show us some of the modelling and statistical challenges.

Unfortunately, with both of them we are data poor – we need far more data in order to fully understand them.

Also, there is the question as to the veracity of the low frequency RhoA data for site *gal005* of the Okak Bay dataset.

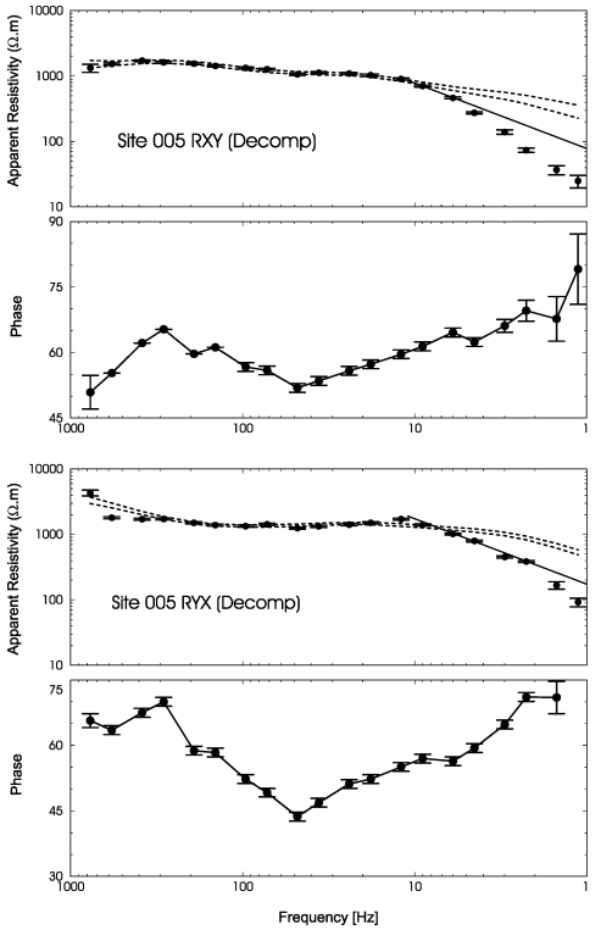

Figure 7: Derived low-frequency tensor decomposed apparent-resistivity data for site 005 together with their prediction (dashed lines show ± one standard error) from the phase data using Parker and Booker's (1996) Rho$^+$ algorithm. The solid lines in the apparent resistivity plots show the decay for an infinitely conducting substratum. Also shown are the decomposed phase data.

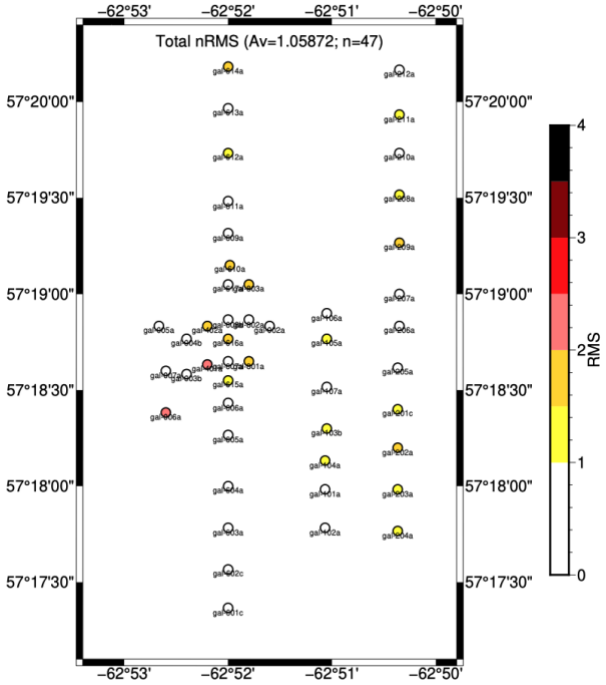

Figure 9: Total RMS for all sites.

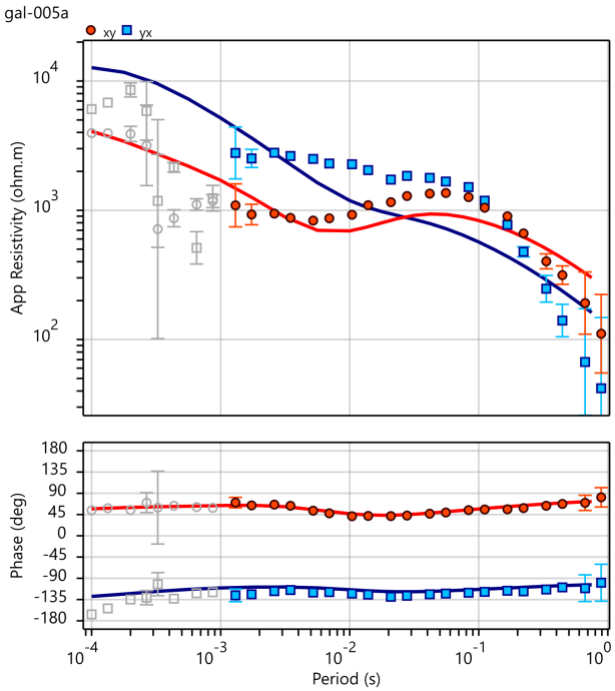

Figure 10: Best fitting model to site gal005.

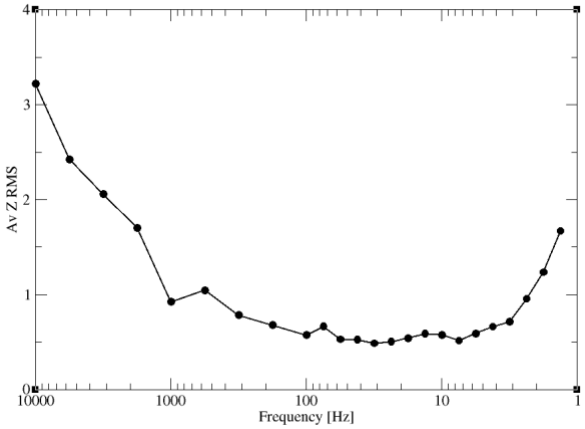

Figure 11: Average Z RMS at each frequency.

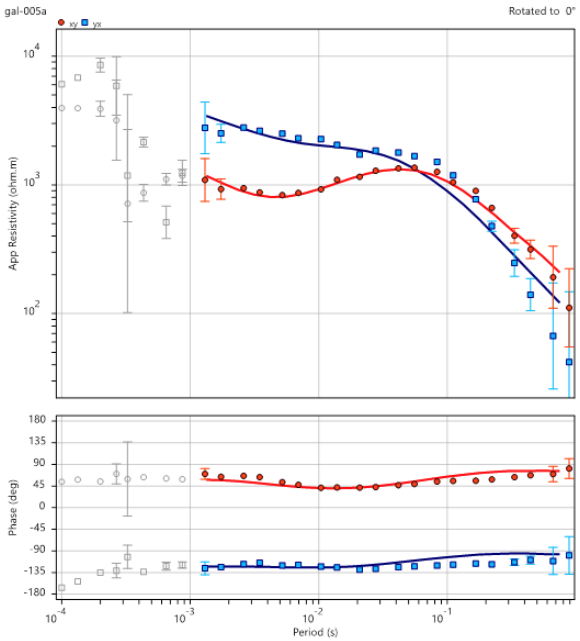

Figure 12: Fit of the 3D model to gal005 using the code inverting for log(|Z|)-PhaZ.

ACKNOWLEDGMENTS

BC87 and EMAP88 were acquired by Phoenix Geophysics and Advanced Energy Technology respectively, and they are both thanked for their attention to detail.

Lithoprobe funded BC87 and EMAP88.

The Okak Bay dataset was also acquired by Phoenix Geophysics for Gallery Resources.

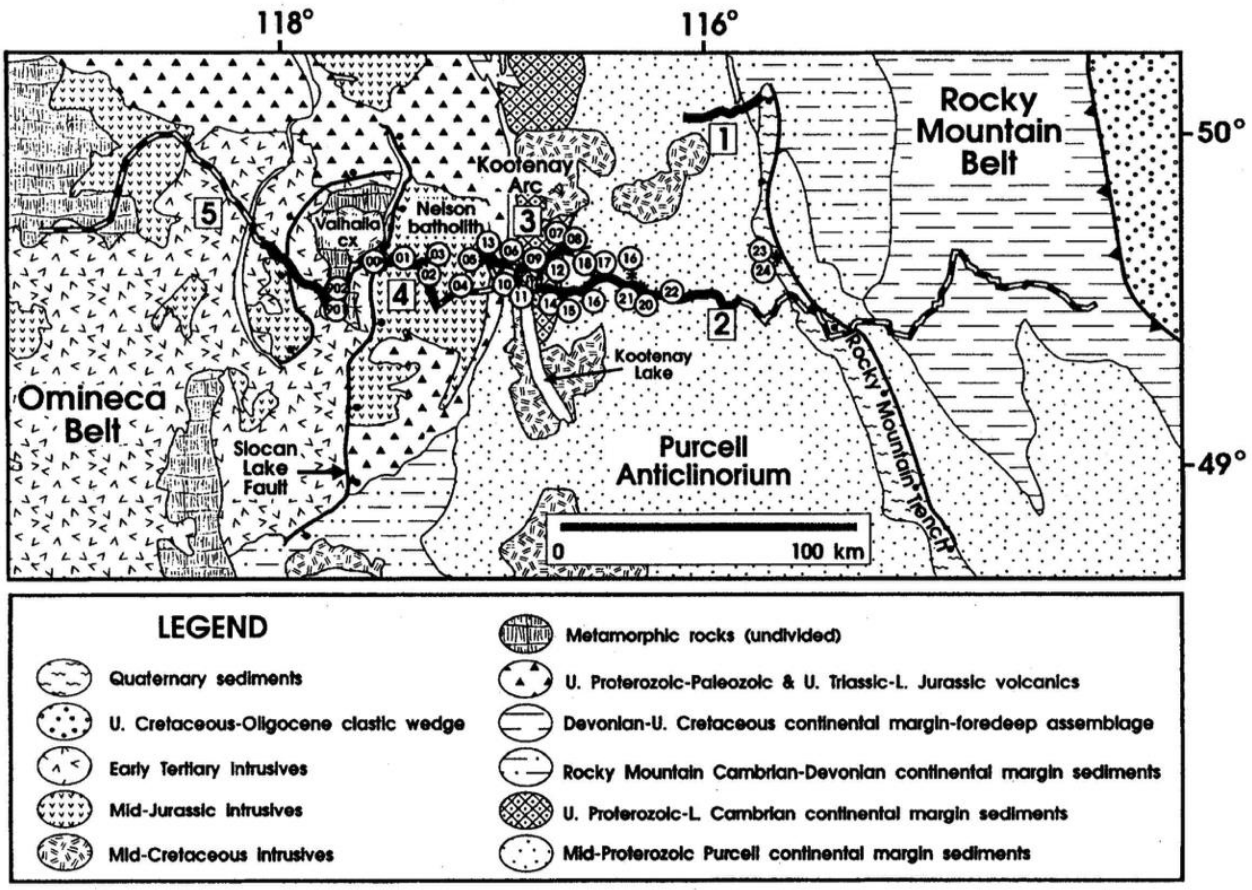

Figure 1: Simplified geology map of the region (based on COOK et al., 1988) showing the locations of the MT sites (numbers in circles), the seismic reflection lines (solid lines with associated numbers in squares) and seismic refraction receiver points (dashed line). Overlapping circles indicate local/remote 10-channel pairs.

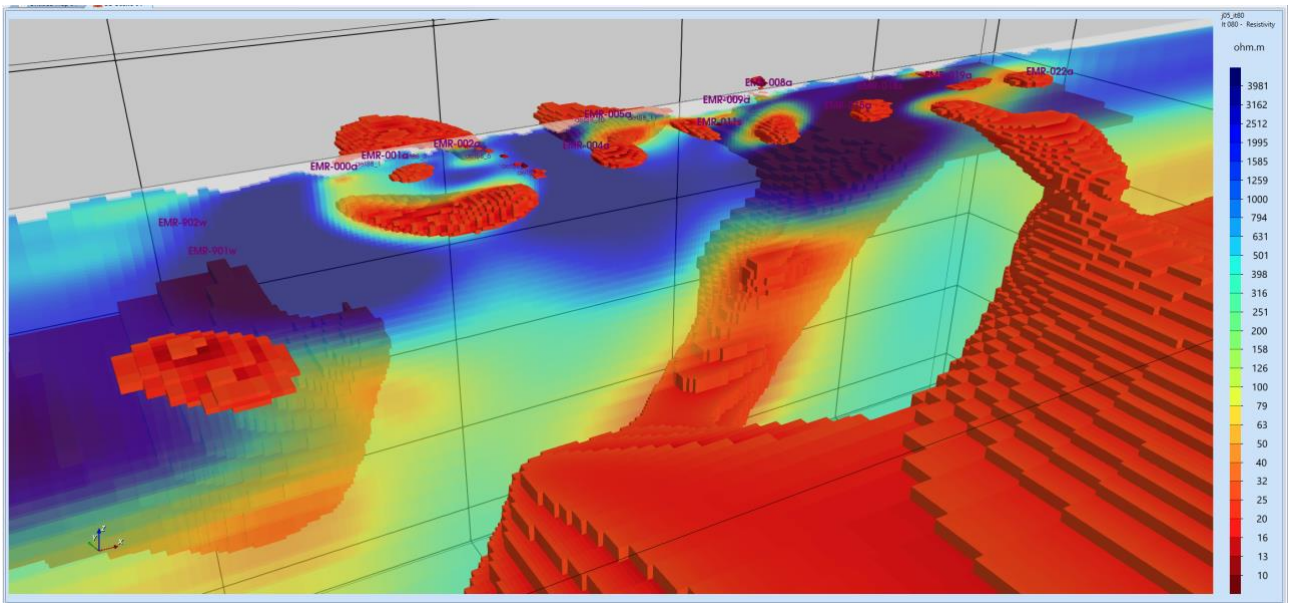

Figure 4: Current best 3D model to the BC87/EMAP88 data. The solid surface is 30 Ωm.

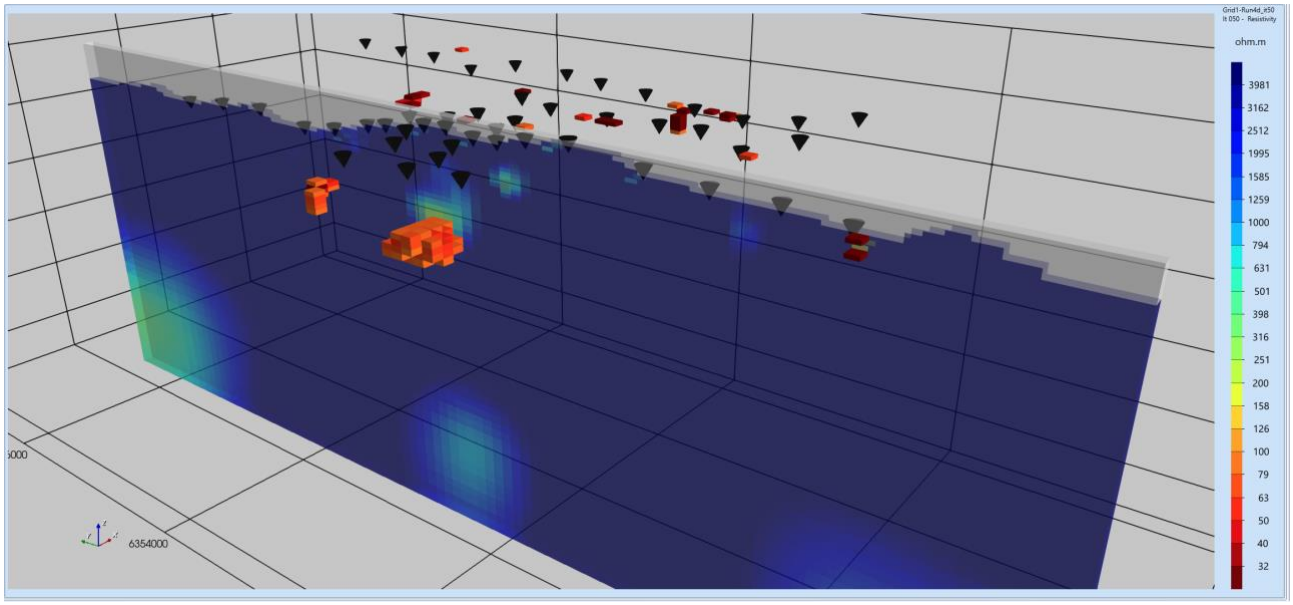

Figure 8: Current best 3D model of the Okak Bay dataset. The surface is at 100 Ωm, and the slice is along Line 6. View from the SW towards the NE.

REFERENCES

Gupta, J. C., & Jones, A. G. (1995). Electrical conductivity structure of the Purcell Anticlinorium in southeast British Columbia and northwest Montana. *Canadian Journal of Earth Sciences*, *32*, 1564-1583.

Jones, A. G. (1993). The BC87 dataset - tectonic setting, previous EM results, and recorded MT data. *Journal of Geomagnetism and Geoelectricity*, *45*(9), 1089-1105.

Jones, A. G. (2018). *Beyond chi-squared: Additional measures of the closeness of a model to data*. Paper presented at the Society of Exploration Geophysicists Annual Meeting, Anaheim, CA.

Jones, A. G., & Garcia, X. (2003). Okak Bay AMT data-set case study: Lessons in dimensionality and scale. *Geophysics*, *68*(1), 70-91. <Go to ISI>://WOS:000180930700005

Jones, A. G., Groom, R. W., & Kurtz, R. D. (1993). Decomposition and modelling of the BC87 dataset. *Journal of Geomagnetism and Geoelectricity*, *45*(9), 1127-1150. Article.

Mackie, R. L., M. A. Meju, F. Miorelli, R. V. Miller, C. Scholl, and A. S. Saleh, 2020, Seismic image-guided 3D inversion of marine CSEM and MT data: Interpretation, 8, no. 4, SS1–SS13, doi: 10.1190/INT-2019-0266.1.

Soyer, W., Mackie, R.L., and Miorelli, F., 2018, Optimizing the Estimation of Distortion Parameters in Magnetotelluric 3D Inversion: 80th EAGE Conference and Exhibition, Copenhagen, Denmark.

7th International Symposium on Three-Dimensional Electromagnetics
Vancouver, BC, Canada, November 13–15, 2023

Including geological orientation information into geophysical inversions with unstructured tetrahedral meshes

Mitra Kangazian[1], and Colin G. Farquharson[1]
[1]Memorial University of Newfoundland, St. John's, NL, Canada, Department of Earth Sciences

Summary

A gradient-based roughness operator that has the capability of including geological orientation information such as strike and dip angles into minimum-structure inversions using unstructured tetrahedral meshes is proposed. In contrast to the majority of the gradient-based methods that consider a cell in a package with its neighbours to form these types of roughness operators, our proposed method calculates the roughness operators between the two adjacent cells. Hence, the proposed method is able to construct models with sharper boundaries for the scenarios in which the regularization function is measured by an ℓ_1 norm compared to the methods that consider a cell in a package with its neighbours.

Keywords: Geological orientation information, Roughness operators, Unstructured tetrahedral meshes

Introduction

Roughness operators were introduced into geophysical inversion— minimum-structure or Occam's style of inversion— to reduce the non-uniqueness of the inverse problem (Constable et al., 1987) and to enable one to incorporate a priori information into the inversion framework to obtain more plausible models (e.g., Li & Oldenburg, 2000). Incorporating a priori information such as structural orientation information (strike, and dip angles) into the inversion, particularly for survey methods with limited depth resolution such as gravity, magnetics, electric, and electromagnetic methods such as magnetotellurics (MT), is important.

Designing roughness operators that allow one to incorporate geological orientation information into inversions using unstructured tetrahedral meshes is not as straightforward as for inversions using structured meshes due to the complex geometry of the unstructured meshes (Lelièvre & Farquharson, 2013). Perhaps the most simple and robust method of forming the roughness operators for unstructured tetrahedral meshes is the one that calculates the physical property differences across the internal mesh faces (Günther et al., 2006). However, this method or the methods proposed by Usui (2015) and Özyildirim et al. (2017) are not able to incorporate geological orientation information such as strike, dip, and tilt angles into the inversion framework.

A few methods have been proposed that enable one to incorporate geological orientation information into the inversions using unstructured tetrahedral meshes. The majority of these methods consider a cell in a package with its neighbors to form the roughness operators. For example, Lelièvre & Farquharson (2013) consider a cell in a package with its neighbours that share a common edge/face, Key (2016) consider a cell in a package with its neighbours that share a common node, and Jordi et al. (2018) go beyond the nearest neighbours of each inversion cell using the correlation function to form the roughness operators. Although these methods are able to incorporate geological information into the inversion framework successfully, they are not able to construct models with sharp boundaries for the scenarios in which the regularization function is measured by an ℓ_1 norm due to the package issue.

To address this package issue, we adapt and extend the method proposed by Günther et al. (2006), called xyz-Günther, to form the roughness operators that allow the inclusion of geological information into the inversion framework and to construct piecewise-constant, blocky models for the scenarios that the regularization function is measured using an ℓ_1 norm. Ekblom's measure (Ekblom, 1973) is adopted to measure the regularization function due to its being numerically well-behaved. The iteratively reweighted least squares (IRLS) method (e.g., Farquharson & Oldenburg, 1998) is utilized to minimize the inverse problem. In the following, the minimum-structure inverse problem is briefly described, then the xyz-Günther method and its capability on synthetic gravity data of a dipping prism are investigated.

Minimum-structure inversion

The objective function that we design to do a minimum-structure inversion consists of a data-misfit term, ϕ_d, and a regularization term, ϕ_m, (e.g., Constable et al., 1987; Smith & Booker, 1988),

$$\Phi(\mathbf{m}) = \phi_d(\mathbf{m}) + \beta\phi_m(\mathbf{m}), \tag{1}$$

where the model vector $\mathbf{m}$ contains the physical property values of the inversion cells. The trade-off parameter, β, controls the relative contribution of the data-misfit and the regularization terms in the objective function. The data-misfit term measures the difference between the observed noisy data, d_i^{obs}, and predicted data, d_i^{pred}, which is scaled by the standard deviation of the noise, σ_i:

$$\phi_d(\mathbf{m}) = \sum_{i=1}^{N_d} \Big(\frac{d_i^{obs} - d_i^{pred}(\mathbf{m})}{\sigma_i} \Big)^2, \tag{2}$$

where N_d is the number of data points. The regularization term consists of a roughness term, ϕ_r, and a smallness term, ϕ_s, (Li & Oldenburg, 1998),

$$\phi_m(\mathbf{m}) = \alpha_r\, \phi_r(\mathbf{m}) + \alpha_s\, \phi_s(\mathbf{m}), \tag{3}$$

where the roughness term measures the amount and type of model structure and the smallness term measures the difference between the constructed model and the reference model, m_{ref},

$$\begin{aligned} \phi_m(\mathbf{m}) =& \alpha_r \int_v \Big(W(\mathbf{r})\, \frac{\partial m}{\partial r} \Big)^p \, dv + \\ & \alpha_s \int_v \Big(W(\mathbf{r})\, (m - m_{ref}) \Big)^p dv, \end{aligned} \tag{4}$$

where p represents an ℓ_p-norm measure and $W(\mathbf{r})$ is the distance/depth/sensitivity weighting function. Potential data such as gravity and magnetic data have limited depth resolution (Li & Oldenburg, 1998), hence, weighting functions are applied to the roughness and smallness terms to counteract the natural decay of the kernels with depth and consequently prevent the construction of the features in the model near the surface (Lelièvre & Oldenburg, 2009).

The roughness term $\dfrac{\partial m}{\partial r}$ in Eq. 4 follows the approach of Günther et al. (2006) and measures the physical property differences between two adjacent cells (and is not a full gradient of the model). This roughness term in this form is not able to incorporate geological orientation information into the inversion framework. To address this problem, we adopt and extend this method, called xyz-Günther, such that one be able to incorporate geological information into the inversion framework.

xyz-Günther method

Our proposed method calculates the directional derivatives, $\dfrac{\partial m}{\partial r}\hat{r}$, instead of the derivatives, $\dfrac{\partial m}{\partial r}$, of the physical properties between the two adjacent cells,

$$\begin{aligned} \alpha_r \left(\frac{\partial m}{\partial r}\hat{r} \right) = \left(\frac{\partial m}{\partial r}\frac{1}{r} \right) \Big\{ & \alpha_x\,(x_2 - x_1)\,\hat{i} + \\ & \alpha_y\,(y_2 - y_1)\,\hat{j} + \alpha_z\,(z_2 - z_1)\,\hat{k} \Big\}, \end{aligned} \tag{5}$$

where r is the distance between the centres of the two adjacent cells, and $\hat{r}$ is the unit vector directed between the centres of the two adjacent cells. The x_1, y_1, z_1 and x_2, y_2, z_2 are the coordinates of the centres of the two adjacent cells.

To obtain the roughness operators in the geology coordinate system, we follow Li & Oldenburg (2000) and apply the rotation matrix $\mathbf{R}$ which contains orientation information of geological structure on the roughness operators calculated in the Cartesian coordinate system (i.e., Eq.5):

$$\left(\frac{\partial m}{\partial x'}, \frac{\partial m}{\partial y'}, \frac{\partial m}{\partial z'} \right)^T = \mathbf{R} \left(\frac{\partial m}{\partial x}, \frac{\partial m}{\partial y}, \frac{\partial m}{\partial z} \right)^T. \tag{6}$$

To construct models with sharp boundaries, the regularization function can be measured by non-ℓ_2-norm measures (e.g., Farquharson & Oldenburg, 1998; Farquharson, 2008). Ekbloms's measure (Ekblom, 1973), which is a perturbed version of an ℓ_p norm, is adopted to measure the regularization function due to its being numerically well-behaved:

$$\rho(x_i) = (x_i^2 + \varepsilon^2)^{p/2}, \tag{7}$$

where x_i are elements of the vector that is supposed to be minimized, and ε is a small number. As the ε gets small, this measure approaches an ℓ_p norm. The iteratively reweighted least squares (IRLS) method (e.g., Farquharson & Oldenburg, 1998) is utilized to minimize our objective function.

Examples

To evaluate the capability and the performance of the proposed xyz-Günther method, the vertical component of the surface gravity data of a dipping prism (Fig. 1) is inverted. The strike, dip, and tilt angles of the dipping prism are (0°, 45°, 0°). The linear trend approach (Lelièvre & Farquharson, 2013) was implemented and applied to the same model to investigate

the package issue. To invert the data, Gaussian noise with zero mean and standard deviation of 1% of the maximum absolute value of the data was added to the synthetic data generated using Okabe's method (Okabe, 1979).

Fig. 2 illustrates the constructed density models of the dipping prism for the scenarios that the regularization function is measured by an ℓ_2 norm. The left, middle, and right panels are, respectively, associated with the density models constructed by the original method of Günther et al. (2006), the xyz-Günther method, and the linear trend approach (Lelièvre & Farquharson, 2013) by assigning smoothness weights $(\alpha'_x,\ \alpha'_y,\ \alpha'_z)$=(1.0, 1.0, 10^4) everywhere in the inversion domain. The constructed density models using the xyz-Günther method (panels b & e) and the linear trend approach (panels c & f) have a better representation of the dipping prism than the model constructed using the Günther et al. (2006) method (panels a & d) due to incorporating geological information into the inversion framework.

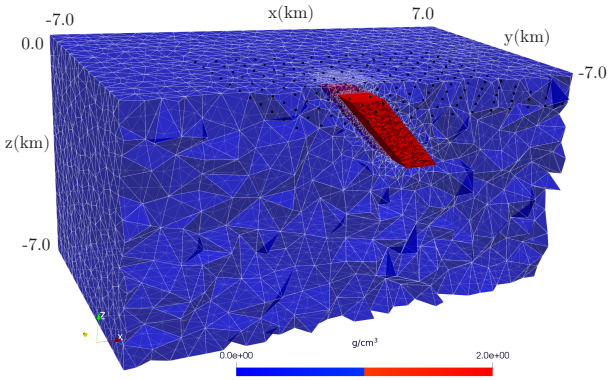

Figure 1: A 3D view of the dipping prism model.

In contrast to the fuzzy and smeared-out density models constructed by an ℓ_2 norm (Fig. 2), the density models constructed by an ℓ_1 norm (Fig. 3) are piecewise-constant, and blocky with sharper boundaries. The left, middle, and right panels are associated, respectively, with the density models constructed by the Günther et al. (2006) method, the xyz-Günther method, and the linear trend approach (Lelièvre & Farquharson, 2013) by assigning $(\alpha'_x,\ \alpha'_y,\ \alpha'_z)$= (1.0, 1.0, 10^3) everywhere in the inversion domain. Although the constructed density models using the xyz-Günther method (panels b & e) and the linear trend approach (panels c & f) have a better representation of the dipping prism extension compared to the model constructed using the Günther et al. (2006) method (panels a & d), the constructed density models using the Günther et al. (2006) method still demonstrate that the subsurface structure is not vertical and has a dip. The density models constructed using the Günther et al. (2006) method (panels a & d) suggest that the diagonal matrices that Farquharson (2008) introduces into the inversion framework using structured meshes to impose a dip on the models constructed by an ℓ_1 norm are not needed for the inversions using unstructured tetrahedral meshes.

The constructed density models using the Günther et al. (2006) method and the xyz-Günther method have a sharper boundary than the model constructed using the linear trend approach due to the package issue. The package issue that the linear trend approach suffers from gets more severe for the methods that consider a larger number of neighbour cells of the inversion cell to form the gradient operators (e.g., Key, 2016; Jordi et al., 2018).

The top panels in Figs. 2 & 3 demonstrate the density models constructed by applying the depth weighting function outside the roughness operators, i.e., the proper location, and the bottom panels of Figs. 2 & 3 demonstrate the density models constructed for the scenarios that the depth weighting function is applied inside the roughness operators. These examples demonstrate that, although applying the depth weighting function inside or outside the roughness operators measured by an ℓ_2 norm does not affect the density models, applying this function inside or outside the roughness operators measured by an ℓ_1 norm does affect the constructed density models. The density models constructed by applying the depth weighting function inside the roughness operators have a trend and are not as sharp as the density models constructed by applying the depth weighting function outside the roughness operators.

Conclusion

The synthetic gravity examples demonstrate that the proposed method xyz-Günther is able to incorporate geological orientation information effectively into the inversion procedure. This method is also able to construct more piecewise-constant models with sharper boundaries compared to the models constructed using methods that consider each cell in a package with its neighbours if the regularization term is measured by an ℓ_1 norm instead of an ℓ_2 norm. The examples also show that applying the depth weighting function inside or outside of the roughness operators measured by an ℓ_1 norm does affect the constructed models. Future work will involve implementing the xyz-Günther method to electromagnetic inversion.

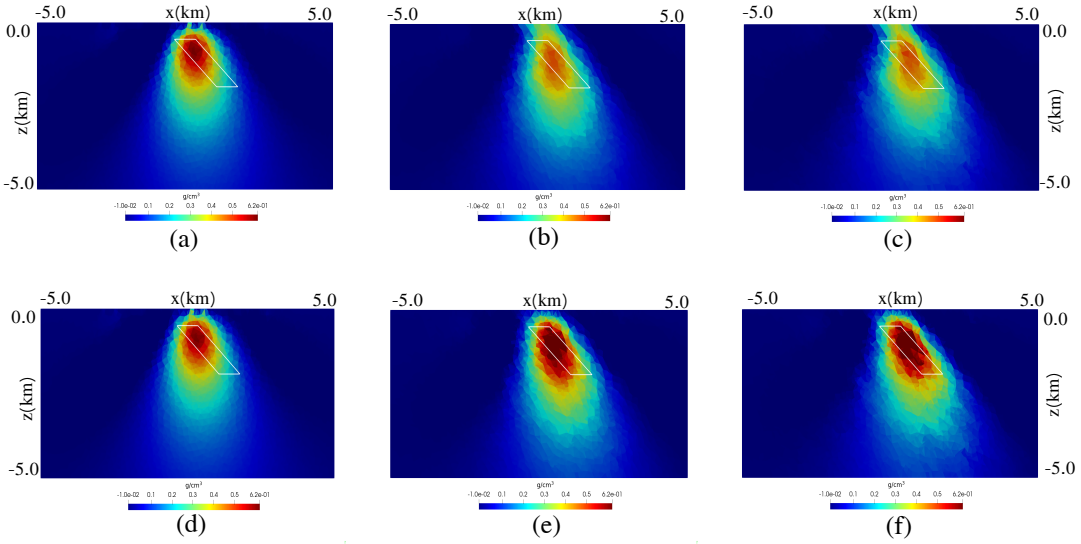

Figure 2: Vertical sections along the x-axis of the density models constructed using an ℓ_2 norm. The left, middle, and right panels correspond to the 3D density models constructed using the Günther et al. (2006) method, the xyz-Günther method, and the linear trend approach (Lelièvre & Farquharson, 2013), respectively. The top and bottom panels correspond to the scenarios that the depth weighting function is applied outside and inside of the gradient operators, respectively. The white solid line indicates the location of the true model.

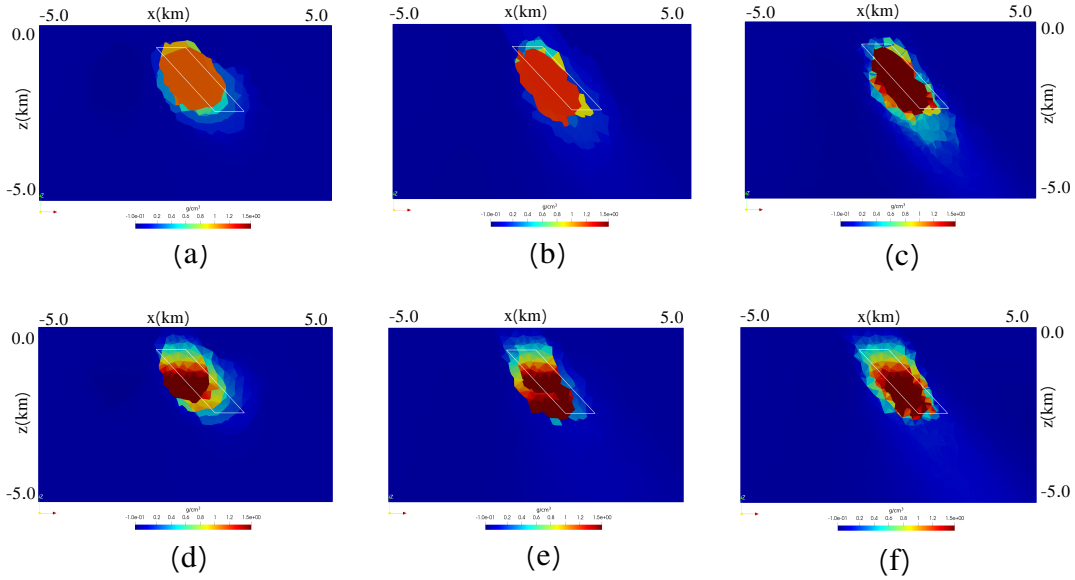

Figure 3: Vertical sections along the x axis of the density models constructed using an ℓ_1 norm. The left, middle, and right panels correspond to the 3D density models constructed using the Günther et al. (2006) method, the xyz-Günther method, and the linear trend approach (Lelièvre & Farquharson, 2013), respectively. The top and bottom panels correspond to the scenarios that the depth weighting function is applied outside and inside of the gradient operators, respectively. The white solid line indicates the location of the true model.

REFERENCES

Constable, S. C., Parker, R. L., & Constable, C. G. (1987). Occam's inversion: a practical algorithm for generating smooth models from electromagnetic sounding data. *Geophysics*, *52*(3), 289–300.

Ekblom, H. (1973). Calculation of linear best l p-approximations. *BIT Numerical Mathematics*, *13*, 292–300.

Farquharson, C. G. (2008). multidimensional minimum-structure inversions. *73*(1).

Farquharson, C. G., & Oldenburg, D. W. (1998). Non-linear inversion using general measures of data misfit and model structure. *Geophysical Journal International*, *134*(1), 213–227.

Günther, T., Rücker, C., & Spitzer, K. (2006). Three-dimensional modelling and inversion of dc resistivity data incorporating topography - II. Inversion. *Geophysical Journal International*, *166*(2), 506–517.

Jordi, C., Doetsch, J., Günther, T., Schmelzbach, C., & Robertsson, J. O. (2018). Geostatistical regularization operators for geophysical inverse problems on irregular meshes. *Geophysical Journal International*, *213*(2), 1374–1386.

Key, K. (2016). MARE2DEM: A 2-D inversion code for controlled-source electromagnetic and magnetotelluric data. *Geophysical Journal International*, *207*(1), 571–588.

Lelièvre, P. G., & Farquharson, C. G. (2013). Gradient and smoothness regularization operators for geophysical inversion on unstructured meshes. *Geophysical Journal International*, *195*(1), 330–341.

Lelièvre, P. G., & Oldenburg, D. W. (2009). A comprehensive study of including structural orientation information in geophysical inversions. *Geophysical Journal International*, *178*(2), 623–637.

Li, Y., & Oldenburg, D. W. (1998). 3-d inversion of gravity data. *Geophysics*, *63*(1), 109–119.

Li, Y., & Oldenburg, D. W. (2000). Incorporating geological dip information into geophysical inversions. *Geophysics*, *65*(1), 148–157.

Okabe, M. (1979). Analytical Expressions for Gravity Anomalies Due To Homogeneous Polyhedral Bodies and Translations Into Magnetic Anomalies. *Geophysics*, *44*(4), 730–741.

Özyildirim, Ö., Candansayar, M. E., Demirci, I., & Tezkan, B. (2017). Two-dimensional inversion of magnetotelluric/radiomagnetotelluric data by using unstructured mesh. *Geophysics*, *82*(4), E197–E210.

Smith, J. T., & Booker, J. R. (1988). Magnetotelluric inversion for minimum structure. *Geophysics*, *53*(12), 1565–1576.

Usui, Y. (2015). 3-D inversion of magnetotelluric data using unstructured tetrahedral elements: Applicability to data affected by topography. *Geophysical Journal International*, *202*(2), 828–849.

Targeting epithermal Au-Ag using helicopter VTEM time domain electromagnetic, magnetic and radiometric data at Lawyers Project, North-Central BC, Canada.

Karl Kwan[1], Jean M. Legault[1], Jim Greig[2], Ewan Webster[2], and Mark Hanki[3]
[1]Geotech Ltd., Aurora ON CAN
[2]Benchmark Metals., Vancouver BC CAN
[3]Apex Geoscience Ltd., Vancouver BC CAN

SUMMARY

In September 2018, Geotech Ltd. completed a VTEM helicopter time-domain electromagnetic, magnetic and radiometric survey on behalf of Benchmark Metals Inc. over the Lawyers property, in northcentral BC. The magnetic results reveal a strong spatial relationship between sharp magnetic lineaments and the known mineralization. Radiometric results show that mineralization is characterized by hydrothermal alteration resulting in potassium enrichment, manifested as K/Th highs. The VTEM electromagnetic results identified local EM anomalies representing both discrete and structural conductors. However, none of the EM anomalies making up conductive zones coincide with the known epithermal mineralization, instead all the known Au-Ag deposits and occurrences are located in zones of high apparent resistivity. Subsequent analysis of the VTEM data analysed using AIIP mapping revealed that all the known Au-Ag mineralized zones coincide with moderate to high Cole-Cole time constant (TAU) anomalies, consistent with relatively coarse-grained polarizable material, such as disseminated sulphides or hydrothermally altered clays. The previous targeting approach focused on individual analyses of magnetic, structural, radiometric, EM resistivity and AIIP results, then arriving at a targeting model, based on geologically and geophysically based considerations. A new approach for targeting uses a semi-automated, machine-learning (ML) assisted approach that includes: Structural Complexities (SC), Self-Organizing Map (SOM) classifications, and Supervised Deep Neural Network (SDNN) targeting of the geophysical data. The new targeting approach has further reduced the number of priority targets from previous five (5) to three (3), which includes most of the known epithermal Au-Ag occurrences, as well as two areas for follow-up.

Keywords: Epithermal, time domain, electromagnetics, resistivity, magnetics, radiometrics, mineral-targeting

INTRODUCTION

Benchmark Metals' Lawyers Gold-Silver Project, situated 45 km northwest of Kemess South Mine in BC's Golden Horseshoe region (Figure 1) of north-central British Columbia, is host to a large, low sulphidation epithermal system known as the Lawyers Trend that contains a total indicated mineral resource of 40.3 Mt at 1.19 g/t Au and 38.7 g/t Ag. At the heart of the Lawyers Trend are the structurally-controlled Cliff Creek, Dukes Ridge, Phoenix and AGB zones that are located within a large 5 km by 8 km radiometric anomaly that is coincident with potassic alteration associated with the low-sulphidation epithermal system. The property straddles an important stratigraphic horizon between the Upper Triassic Stuhini Group and Lower Jurassic Hazelton Group that defines an important geological unconformity that hosts many of the deposits in the Golden Horseshoe (Stone et al., 2021).

Originally explored in the late 1960's, mineralization at Lawyers was identified by the 1980's and lead to the development of the Lawyers gold-silver mine that operated from 1989-1992 and produced 171,200 oz gold and 3.6M oz silver in that 4-year period. In the years following, exploration had focused on targeting high grade veins within the large epithermal system. Benchmark Metals has been actively exploring the Lawyers property since 2018, with a low- grade bulk tonnage targeting model approach, using extensive geological mapping, drilling, soil and rock geochemistry, ground, drone and airborne geophysics, which led to a NI 43-101 compliant mineral resource estimate in 2021 (Stone et al., 2021).

The Stone et al. (2021) report documented the targeting approach on helicopter TDEM, aeromagnetic and spectrometric data (Khaled et al., 2018) performed by Kwan et al. (2019), which was subsequently presented in Legault et al. (2022). This paper presents a new targeting approach that uses a semi-automated, machine-learning (ML) assisted approach that includes: Structural Complexities (SC), Self-Organizing Map (SOM) classifications, and Supervised Deep Neural Network (SDNN) approach to mineral targeting.

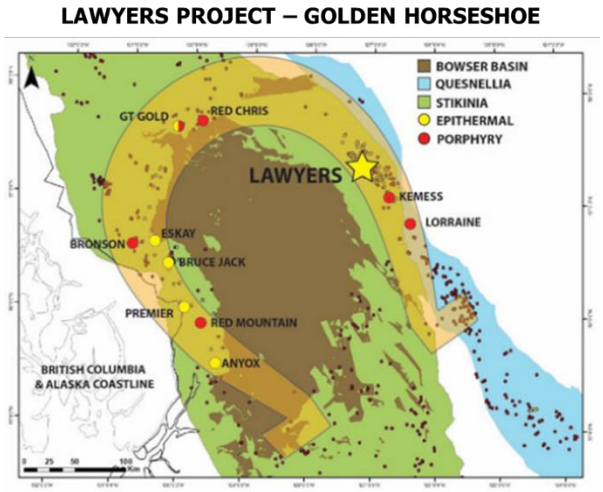

Figure 1: Lawyers Project property location, and schematic of Golden Horseshow mineral district in northwestern British Columbia (modified after www.benchmark metals.com).

Geology and Mineralization

Lawyers property is predominantly underlain by a shallow northwest-dipping sequence of volcanic and sedimentary rocks of the Lower Jurassic Toodoggone Formation (Hazleton Gp). The Lower cycle Toodoggone rocks are comprised of thick sequences (>300 m) of dacitic and andesitic tuffs and flows. The most dominant structural features are NW-NNW (310-340°) striking faults that are subvertical to steeply SW or NE dipping (Figures 2 & 3). These host the mineralized epithermal systems NW structures and associated mineralization are locally offset by E-W and SW-NE trending strike-slip faults (Stone et al., 2021).

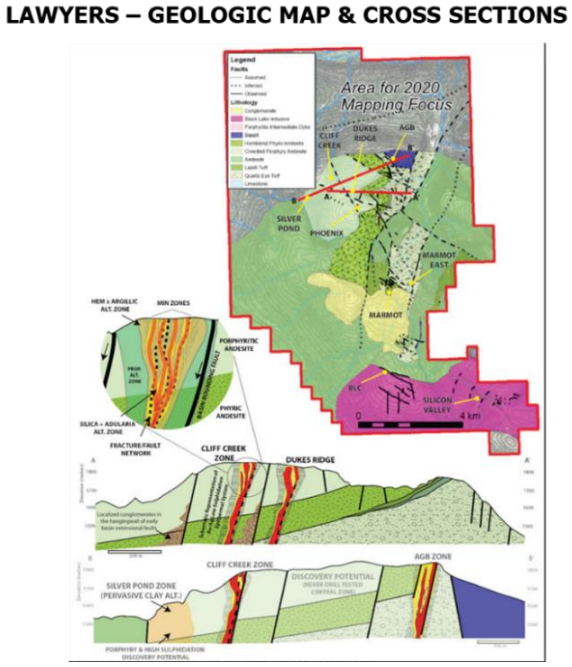

Figure 2: Lawyers Project geologic map (top) and schematic geologic cross sections (modified after www.benchmark metals.com).

Lawyers rocks are typically weakly altered, but gold-silver mineralization is associated with intense silicification and potassic alteration. Advanced argillic and qtz-sericite also present in some zones. Mineralization includes both low sulphidation (LS) in central & east (AGB, Cliff Ck, Duke Ridge) parts of the property and high sulphidation (HS) in the western (Silver Pond) part of the block, as shown in Figure 3 (Stone et al., 2021).

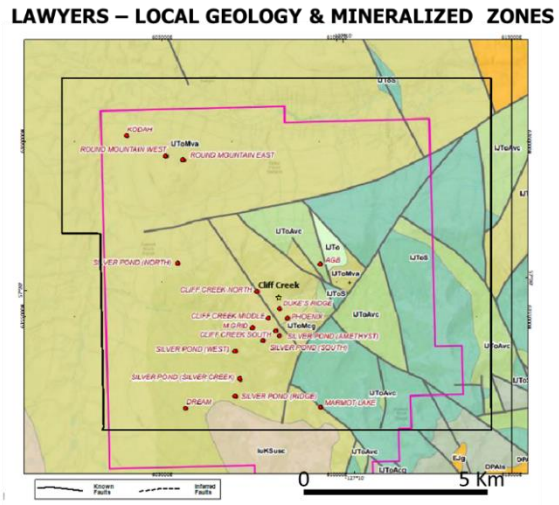

Figure 3: Lawyers Project local geology, mineral occurrences, and deposits, and known faults (modified after www.benchmarkmetals.com).

METHOD AND RESULTS

Helicopter TDEM, Magnetic and Radiometrics

In September 2018, Benchmark contracted Geotech Ltd. to complete a VTEM (Witherly et al., 2003) helicopter time-domain electromagnetic, magnetic and radiometric survey over the central and northern parts of the Lawyers property (Khaled et al., 2018). A total of 1,272 line-km was flown over a 115 km^2 area along 100 m spaced EW lines and 1 km spaced NS tie-lines. The VTEM Terrain system consisted of a 17.6m diameter, 4-turn transmitter loop (250k NIA @ 30Hz), a coincident-coplanar Z-component receiver (40ch 0.036-9.3ms), a caesium magnetometer, and RSX-5 spectrometer. The survey objectives were to map resistivity, magnetic susceptibility, and gamma radiation related to low to high sulphidation epithermal gold and silver targets in Lawyers camp.

The total field magnetic results (Figure 4) reveal a strong spatial relationship between sharp magnetic lineaments, magnetic lows, and the known mineralization. In order to quantify the structural elements, the magnetic data were

subjected to a structural complexity (SC) analysis, using the Geosoft CET (Centre for Exploration Targeting) grid analysis extension (www.seequent.com). The magnetic ridges shown in Figure 4 have been derived using the method described in Holden et al. (2012). The structural complexity highs are in the SW region concentrated with known Au-Ag occurrences.

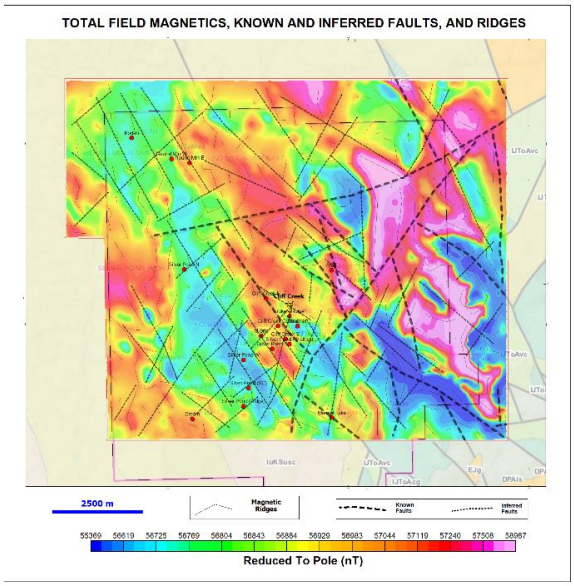

Figure 4: Total field magnetic intensity, over mineral occurrences & known/inferred faults (dashed lines), and magnetic ridges obtained from CET analysis.

Radiometric results show that the Lawyers Property mineralization is characterized by hydrothermal alteration resulting in potassium enrichment, commonly manifested as K/eTh highs (Figure 5).

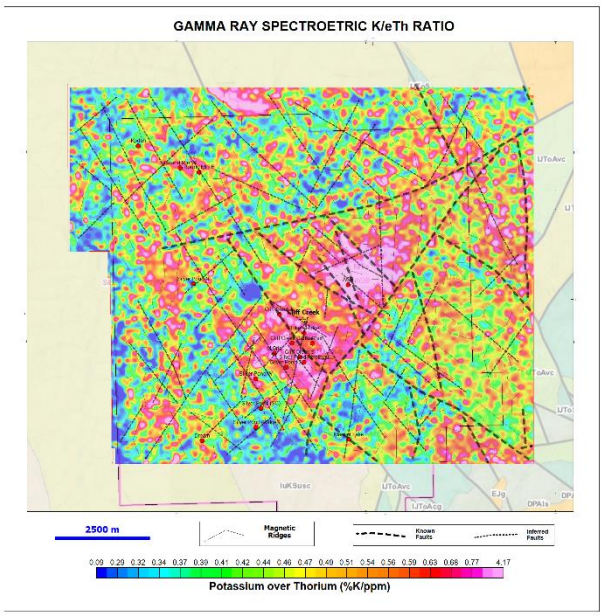

Figure 5: Gamma Ray Spectrometric K/eTh Ratio, over mineral occurrences & known/inferred faults (dashed lines), and magnetic ridges.

The VTEM dBz/dt EM decay constant map in Figure 6 includes the location of local EM anomalies centres represented by both large area and structural conductors. However, as shown, none of the EM anomalies making up conductive zones coincide with the known epithermal mineralization. Instead, all the known Au-Ag deposits and occurrences are located in zones of low TAU corresponding to high apparent resistivity (Figure 77a).

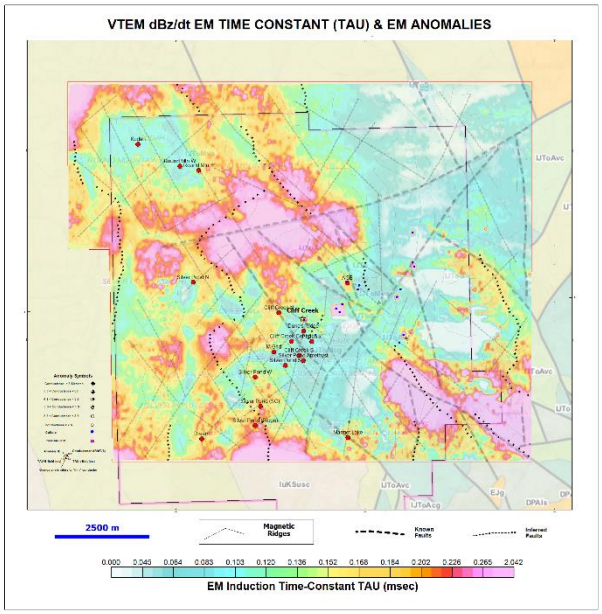

Figure 6: VTEM dBz/dt EM time constant TAU and EM anomaly picks, over mineral occurrences & known/inferred faults (dashed lines), and magnetic ridges.

VTEM AIIP and 1D Inversion Results

Layered Earth (LE) 1D inversions of the VTEM data were carried out using GALEI code. The VTEM data were analysed for AIP effects (Kratzer and Macnae, 2012) using the AIIP (airborne inductively induced polarization) mapping tool (Kwan et al., 2015, 2016, 2018). The 1D resistivity -100 m depth slice and the AIIP Cole-Cole apparent resistivity data are displayed in Figure 7a & 7b, respectively. The two resistivity maps are different because the 1D inversions do not account of AIIP effects in the VTEM data.

The AIIP mapping revealed that all the known Au-Ag mineralized zones coincide with moderate to high Cole-Cole time constant (TAU) anomalies in resistive zones that are consistent with relatively coarse-grained polarizable material, such as disseminated sulphides or hydrothermally altered clays. The product of the AIIP apparent resistivity and the Cole-Cole TAU (termed ResTau), presented in Figure 8, has proven to be a useful

parameter for identifying low sulphidation epithermal Au-Ag mineralization elsewhere on the property.

Mineral Targeting Epithermal Au-Ag Deposits

Previous targeting of VTEM results at Lawyers (Kwan et al., 2019; Legault et al., 2022) focused on individual analyses of magnetic, structural, radiometric, EM resistivity and AIIP results, then arriving at a targeting model, based on geologically and geophysically based considerations, resulting in five (5) priority targets. A new mineral targeting approach, based on recent examples of semi-automated, machine-learning (ML) assisted targeting (Kwan and Legault, 2023; Legault et al., 2023ab) has been tested for epithermal gold-silver using the Lawyers VTEM, magnetic and radiometric survey results.

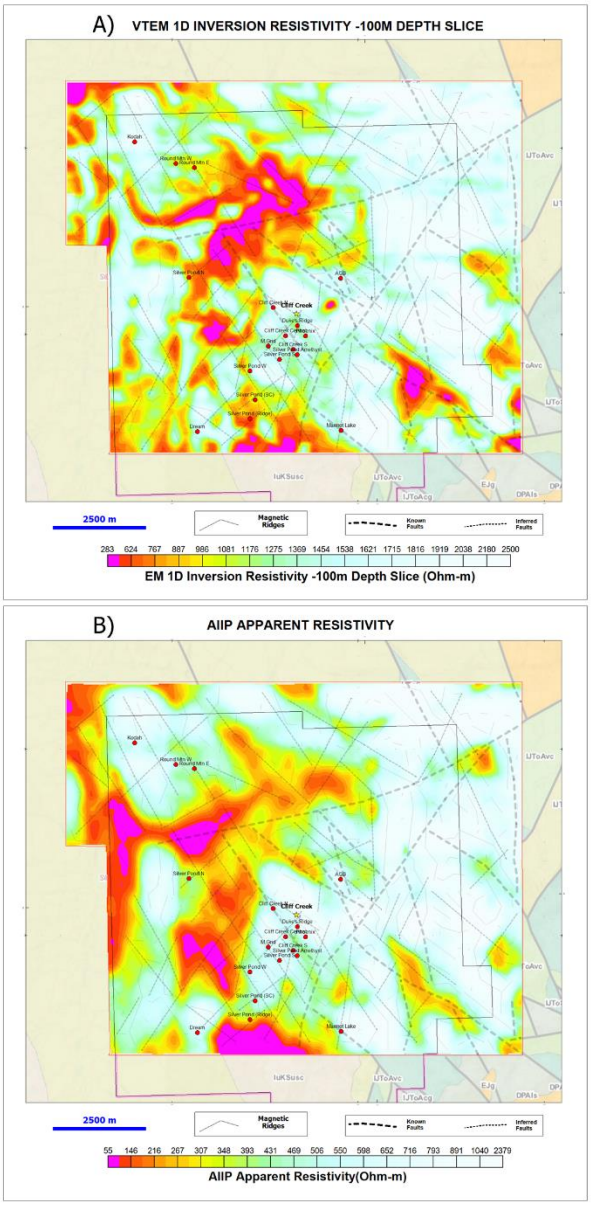

Figure 7: (A) VTEM 1D Inversion resistivity depth slice (-100m), and (B) AIIP Cole-Cole apparent resistivity, over mineral occurrences & known/inferred faults (dashed lines), and magnetic ridges.

The approach includes: 1) Structural Complexities (SC), 2) Self-Organizing Map (SOM) classifications, and 3) Supervised Deep Neural Network (SDNN) targeting of the geophysical data.

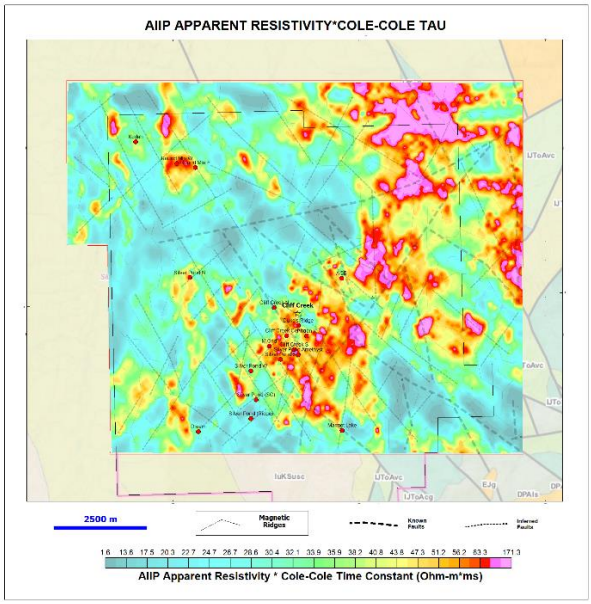

Figure 8: VTEM AIIP ResTau (Resistivity*Time Constant) Product, over mineral occurrences & known/inferred faults (dashed lines), and magnetic ridges.

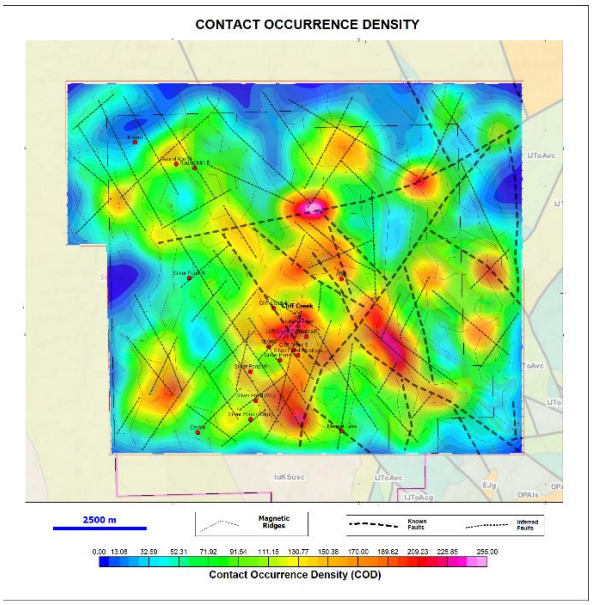

Figure 9: Structural complexity (SC) analysis of magnetic data, showing the Contact Occurrence Density (COD), over mineral occurrences &

known/inferred faults (dashed lines), and magnetic ridges.

As mentioned earlier, the RTP magnetic data have been analysed for structural complexity using the Geosoft CET grid analysis tool (Holden et al., 2012). The CET SC analysis tool outputs two parameters: i) the Contact Orientation Density (COD), and the Orientation Entropy (OE). Figure 9 presents the SC-derived COD image. As shown, the structural complexity highs are mainly found in the southcentral region that coincides with known Au-Ag occurrences.

Self-Organizing Maps (SOM) are a potent tool in analysing and classifying multiple datasets. The SC data, the K/eTh, and the AIIP apparent resistivity and Cole-Cole Tau products are classified using the Geosoft SOM GX tool (https://geosoftgxdev.atlassian.net). The SC data, the K/eTh, and the AIIP apparent resistivity and Cole-Cole Tau products are classified using SOM. Most of the anomalous SOM classes (9 to 17) coincide with the known Au-Ag mineralization in the SW and central regions of the Lawyers property (Figure 10).

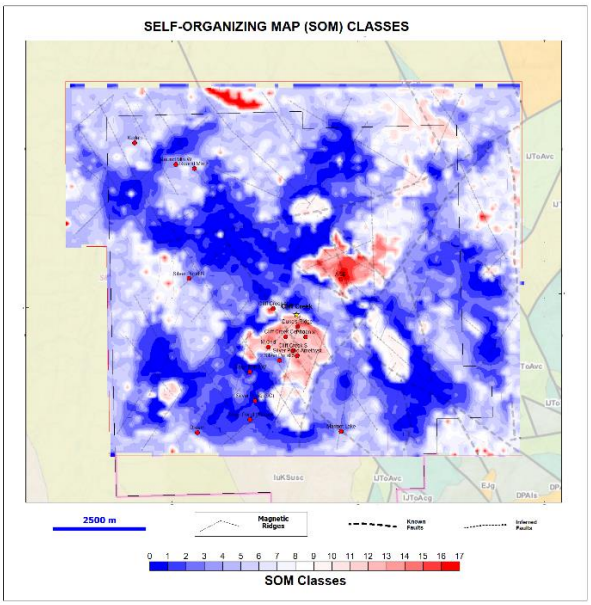

Figure 10: The anomalous SOM classes cover most of the known Au-Ag occurrences.

The final targeting preparation was done using the Google TensorFlow version TF 2.30 (https://www.tensorflow.org/) and its Supervised Deep Neural Network (SDNN) module. The training of the SDNN was performed using the SC, SOM, K/eTh, and AIIP apparent resistivity-tau product from an area with known Au-Ag deposit (Cliff Creek), Figure 11A. The top 6% probability is selected for Au-Ag targeting, Figure 11B.

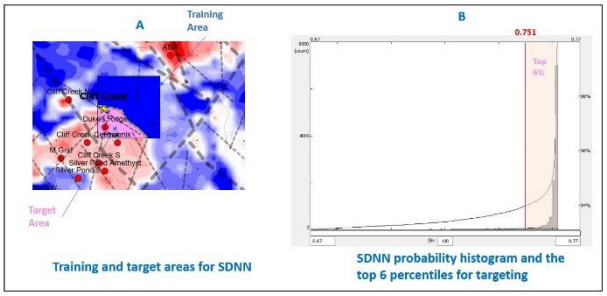

Figure 11: (A) Training area for SDNN, (B) top 6% target probability cut-off for targeting.

The top 6% targeting probabilities over the DEM data, and the selected targets, LET_1 to LET_3 are presented in Figure 12. The selected targets are in topographic highs and therefore unlikely to be overburden related.

CONCLUSION

Structural complexity analyses of the magnetic data at Lawyers Project have identified a strong spatial relationship between the known and inferred faults and calculated ridges and the known mineralization. Analyses of the EM results has shown that none of the observed conductive anomalies coincide with known epithermal Au-Ag showings. Instead, all the known mineral occurrences are located in zones of high resistivity. Gamma ray spectrometric results have shown that the known mineral occurrences are located in high to moderate K/eTh ratio anomalies. AIIP results at Lawyers Project suggest that the product of AIIP apparent resistivity and Cole-Cole time constant (Res*Tau) could be a useful targeting tool.

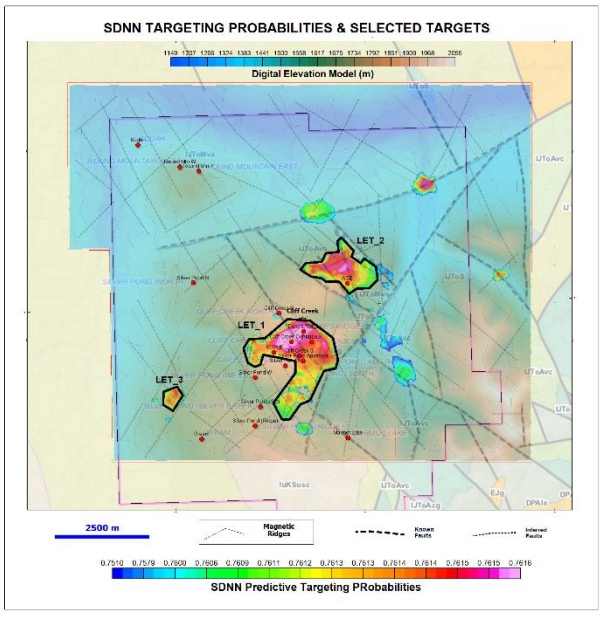

Figure 12: The SDNN top 6% probabilities over the DEM data and the selected potential epithermal Au-Ag targets.

Previous targeting of VTEM results at Lawyers (Kwan et al., 2019; Legault et al., 2022) focused on individual analyses of magnetic, structural, radiometric, EM resistivity and AIIP results, then arriving at a targeting model, based on geologically and geophysically based considerations, resulting in five (5) priority targets. A new approach for targeting, presented here, uses a semi-automated, machine-learning (ML) assisted approach that includes: Structural Complexities (SC), Self-Organizing Map (SOM) classifications, and Supervised Deep Neural Network (SDNN) targeting of the geophysical data.

Using SOM and SDNN results, the previous five (5) have been reduced to just three (3) priority targets, which include most of the known epithermal occurrences and include other areas for follow-up. It is also worth noting that the targeting of epithermal Au-Ag mineralization is done by a semi-automated processes which require little human intervention or bias. Importantly, the structural complexities, computed using known and inferred faults, also played a critical role in targeting.

ACKNOWLEDGMENTS

The authors wish to thank Benchmark Metals, Apex Geoscience and Geotech for allowing us to present these results.

REFERENCES

Holden, E.-J., Wong, J. C., Kovesi, P., Wedge, D., Dentith, M., Bagas, L., 2012. Identifying structural complexity in aeromagnetic data: An image analysis approach to greenfields gold exploration. Ore Geology Reviews 46: 47–59.

Khaled, K., Shei, T.C., Prikhodko, A., and Orlowski, K., 2018. Report on helicopter-borne versatile time domain electromagnetic (VTEM), aeromagnetic and gamma-ray spectrometry geophysical survey, over Lawyers Project, Kemess Creek, BC, for Benchmark Metals Ltd.: Internal report (GL180180), 62 p.

Kratzer, T. and Macnae, J.C., 2012. Induced polarization in airborne EM, Geophysics, 77, E317-327.

Kwan, K., and Legault, J.M., 2023. Gold targeting of fixed wing aeromagnetic Data using structural complexity, self-organizing map and supervised deep neural network analyses: A case study from the Red Lake camp, Superior Province, Ontario, Canada: IMAGE 2023 conference extended abstracts, 4 p.

Kwan, K., Han, Z., Khaled, K. and Prikhodko, A., 2019. Interpretation report on a helicopter-borne versatile time domain electromagnetic (VTEM), aeromagnetic and gamma-ray spectrometry geophysical survey, over Lawyers Project, Kemess Creek, BC, for Benchmark Metals Inc. Internal report (GL180180) for Benchmark Metals Inc., 52 p.

Kwan, K., Legault, J.M., Johnson, I., Prikhodko, A. and Plastow, G., 2018. Interpretation of Cole-Cole parameters derived from helicopter TDEM data – Case studies, Extended Abstract, SEG Anaheim 2018 International Exposition and 88th Annual Meeting, 5 p.

Kwan, K., Prikhodko, A., Legault, J.M., Plastow, G., Xie, J. and Fisk, K., 2015. Airborne Inductive Induced Polarization Chargeability Mapping of VTEM data, ASEG-PESA 24th International Geophysical Conference and Exhibition, Perth, Australia., 4 p.

Kwan, K., A. Prikhodko, J.M. Legault, G. Plastow, J. Kapetas, and M. Druecker, 2016.Airborne EM, aeromagnetic and gamma-ray spectrometric data over the Cerro Quema high sulphidation gold deposits, Panama, *Exploration Geophysics*, 47, 179-190.

Legault, J.M., Kwan, K., Greig, J., Webster, E., Hanki, M., and Wilson, R., 2022. Helicopter Time Domain EM-AIIP, Magnetic and Radiometric Case Study over the Lawyers Epithermal Gold-Silver Project, North-Central BC, Canada. SAGA, Extended Abstracts, 4 p.

Legault, J.M., Kwan, K., Greig, J., Webster, E., Hanki, M., and Wilson, R., 2023. Targeting epithermal Au-Ag using helicopter TDEM, magnetic and radiometrics data at Lawyers Project, North-Central BC, Canada., 8th International Airborne Electromagnetics Workshop, Extended Abstracts, 5 p.

Legault, J.M., Kwan, K., and Ebert, S., 2023. ZTEM airborne natural field EM-magnetic and mineral targeting results over the Berg porphyry copper project, near Houston, British Columbia: 8th International Airborne Electromagnetics Workshop, Extended Abstracts, 6 p.

Stone, W., Wu., Y., Barry, J., Puritch, E, Ray, B., Wright, F., and Mioska, M., 2021. Technical Report and Updated Mineral Resource Estimate of the Lawyers Gold-Silver Property, Omineca Mining Division, British Columbia, Canada, NI 41-101 Technical Report for Benchmark Metals Inc. by P&E Mining Consultants Inc., 478 p.

Witherly, K., Irvine, R. and Morrison, E., 2004. The Geotech VTEM time-domain helicopter EM system, 74th Meeting SEG, Expanded Abstracts, 1217-1220.

3D ZTEM Airborne Natural Field EM & Magnetic Inversion and Mineral Targeting Results over the Berg Porphyry Copper Project, near Houston, British Columbia.

Jean M. Legault[1], Karl Kwan[2] and Shane Ebert[2]
[1]Geotech Ltd., Aurora ON CAN
[2]Surge Copper Corp., Vancouver BC CAN

SUMMARY

A ZTEM natural field helicopter EM and magnetic survey was flown over the Berg copper-molybdenum-silver project in the Huckleberry district, near Houston in central British Columbia, Canada. Mineralization at Berg surrounds a quartz monzonite intrusion. Analyses of the airborne geophysical responses, using 2D-3D inversions, show combined well-defined ring-like resistivity low surrounding a resistive core and similar annular magnetic high and low signatures over the known and suspected porphyry deposits, similar to those previously found in ZTEM surveys over other porphyry deposits in the Western Cordillera. A mineral targeting approach is implemented that uses a semi-automated, machine-learning (ML) assisted method that includes: 1) Structural Complexities (SC), 2) Self-Organizing Map (SOM) classifications, and 3) Supervised Deep Neural Network (SDNN) targeting of the geophysical data. The new targeting approach has identified both the Berg and Bergette porphyry copper occurrences, as well as two other areas for follow-up that also host known mineral showings.

Keywords: Porphyry, ZTEM, electromagnetics, resistivity, magnetics, mineral-targeting

INTRODUCTION

In May 2021, Surge Copper Corp. announced plans for a new district wide exploration program over its Ootsa and Berg Projects in the Huckleberry district, near Houston, north central British Columbia, including a ZTEM (Z-axis Tipper Electromagnetic; Lo and Zang, 2008) geophysical survey (Surge, 2021). The Ootsa-Berg project (Figure 1) is host to 4 advanced porphyry projects, including the undeveloped Berg copper-molybdenum-silver porphyry deposit. In June-July 2021 a ZTEM helicopter natural field electromagnetic and magnetic survey was flown over Ootsa-Berg and the results that focus on the Berg porphyry copper deposit and nearby occurrences are described in this study.

The Berg and Ootsa properties are adjoined on the west side, with Berg project lying immediately northwest of Imperial Metals' Huckleberry porphyry Cu-Mo-Ag mine and mill complex, and the Ootsa property to the southeast (Figure 1-2). The two properties cover a total combined area of >120,000 hectares and encompass the Seel-Huckleberry-Berg porphyry trend. The Berg claims were initially prospected in the late 1920's by Cominco but the Berg porphyry system was discovered by Kennecott following trenching and drilling in 1964. Subsequent exploration drilling by operators Placer Dome, Terrane Metals, Thompson Creek Metals, Centerra Gold and now Surge Copper total over 56,000 metres in 224 holes. A resource estimate in 2021 established a measured and indicated mineral resource of 610 Mt grading 0.27% Cu, 0.03% Mo and 3 g/t Ag. The Berg deposit currently remains undeveloped (Norton et al., 2021).

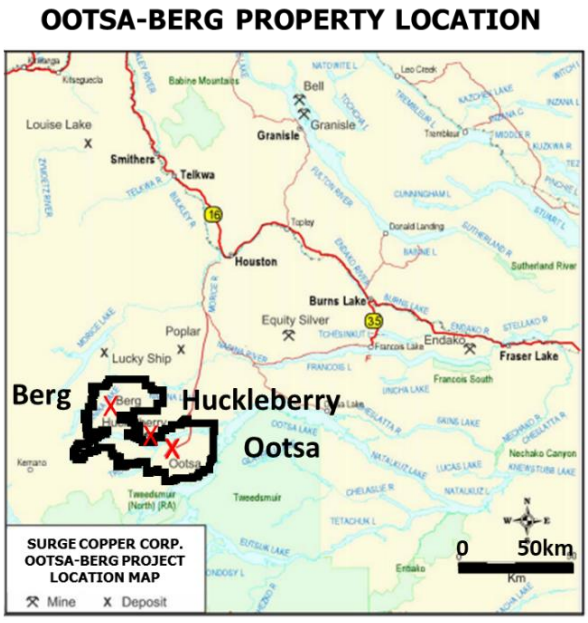

Figure 1: Ootsa-Berg Property location, showing nearby Huckleberry Mine and regional deposits in north central British Columbia (modified after Purich et al., 2016).

ZTEM (z-axis tipper electromagnetic; Lo and Zang, 2008; Legault et al., 2012) helicopter natural field EM has been widely used in porphyry copper exploration for >15 years in mapping resistivity contrasts that characterize porphyry copper deposit alteration systems (Hoschke, 2011). ZTEM case-study examples over porphyry deposits include Lo and Zang (2008) in Safford, Arizona; Holtham

and Oldenburg, (2010) at Bingham Canyon, Utah, Izarra et al. (2011) at Copaquire, Chile, and Burge (2014) at Cobre Panama. ZTEM examples in Western Cordillera include Sattel et al. (2010) at Mt Milligan, BC, and Lee et al. (2017) at Morrison, BC, and Paré et al. (2012) at Pebble, Alaska.

The Berg ZTEM-Magnetic case study has been presented in Legault et al. (2022). This paper adds to that study by presenting a new targeting approach, described in Kwan et al. (2023) and Legault et al. (2023) that uses a semi-automated, machine-learning (ML) assisted approach that includes: Structural Complexities (SC), Self-Organizing Map (SOM) classifications, and Supervised Deep Neural Network (SDNN) approach to mineral targeting.

Geology and Mineralization

Berg (Figure 2) is a classic calc-alkaline Cu-Mo porphyry deposit, which are typically marked by complex alteration zones that are usually centred around an intrusive complex. The Berg mineralization forms an annulus along the contact between the 50 Ma quartz monzonite stock and the hornfelsed Hazelton Group volcanic rocks and quartz diorite which it intrudes (Norton et al., 2021).

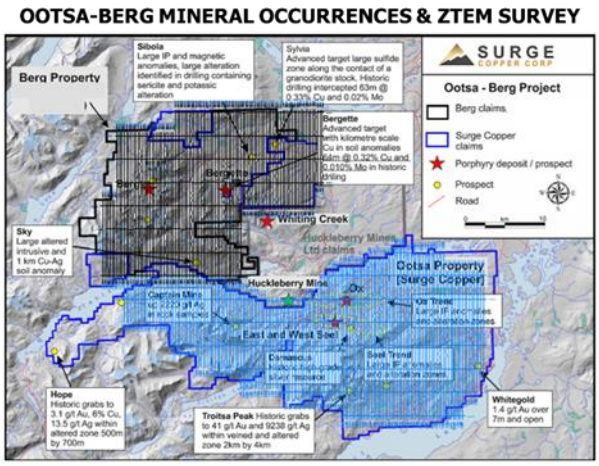

Figure 2: Plan view of the Ootsa-Berg porphyry project, showing the four main porphyry occurrences (Berg, Bergette, Ox, Seel) and nearby Whiting Creek prospect and Huckleberry Mine (green star), with ZTEM flight lines (Berg-black & Ootsa-blue) overlain on contoured topography (modified after www.surgecopper.com).

Hypogene mineralization at Berg is characterized by several generations of veining. Disseminated mineralization containing copper and molybdenum is only important in the outer anulus of the quartz monzonite stock and in the adjacent volcanic rocks and quartz diorite. Associated alteration envelopes are either potassic or sericitic. A well-developed supergene enrichment blanket is superimposed on the hypogene mineralization, and consists mainly of chalcocite, covellite and digenite, with trace amounts of copper oxides in the overlying leached cap. The surrounding phyllic and propylic alteration zones are typically poor in Cu+/-Mo sulphides (Norton et al, 2021). Mineralization at Berg is open to depth and outward from the Berg monzonite Stock. The deposit has been shown to have excellent vertical continuity with significant mineralization intersected greater than 550m below surface (www.surgecopper.com).

Another known mineral occurrence of importance on the Berg property is the Bergette prospect that lies 10 km east of the Berg deposit (Figure 2-Figure 3). Bergette consists of a large gossan and mineralization is marked by strong Cu-Mo response in soils, across a 2x5 km northeast trending zone. Limited drilling and mapping indicate that Bergette is underlain by Hazleton Group volcanic and sedimentary rocks, intruded by granodioritic Sibola stock. Sulphides occur in breccias and fractures. An AeroTEM III (Allard, 2007) helicopter TDEM survey over the Berg-Bergette area in 2010 shows that Bergette has a similar size resistivity response (Norton et al., 2021).

At the Tara/Sibola occurrence, roughly 5.5 km NE of Bergette (Figure 2 & Figure 3), low-grade porphyry-style mineralization is hosted in a felsic stock and occurs within the central part of a broad qtz-sericite-pyrite alteration zone (S. Ebert, SCC, pers. comm., 03-2022).

METHOD AND RESULTS

Helicopter ZTEM and Magnetic Survey Results

Helicopter-borne geophysical surveys were carried out over the Ootsa-Berg Project from June 8th to 30th, 2021, on behalf of Surge Copper Corp. Principal geophysical sensors included a Z-Axis Tipper electromagnetic (ZTEM) system (Lo and Zang, 2008), and a caesium magnetometer. Two Geotech ZTEM base station sensors measured the orthogonal, horizontal X and Y components of the natural EM field. Data from the three coils are used to obtain the Tzx and Tzy Tipper (Labson et al., 1985) in-phase and quadrature components at six frequencies in the 30 to 720 Hz band. A total of 4,224 line-kilometres were flown, including approximately 1,779 ln-km at Berg, along 300m spaced, north-south oriented flight lines and 3 km spaced east-west tie lines.

Figure 3 presents the reduced to pole (RTP) total magnetic intensity results, and the corresponding Berg porphyry and other mineral occurrences from Figure 2. The magnetic results highlight a prominent, large (~1.5x1.5 km), magnetic low feature centred on the Berg porphyry, which is in turn surrounded by a reverse C-shaped magnetic high. Worthwhile noting that similar ring-like magnetic patterns observed over the porphyry copper cluster at Cobre Panama are interpreted to represent demagnetized areas due to porphyry-related phyllic alteration (Burge, 2014; Legault et al., 2016). Conversely,

Bergette lies within a magnetic high but is indistinct. Tara/Sibola occurs in low magnetic rocks but lies adjacent to a small, intrusion like magnetic high feature. Other distinctive circular or ring-like magnetic high and low signatures are noted across the Berg Project.

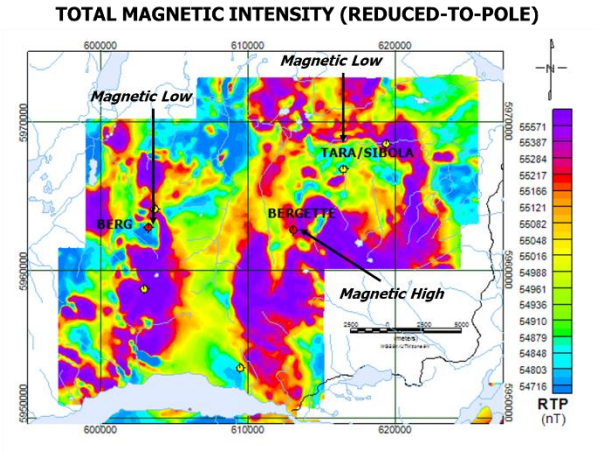

Figure 3: Total magnetic intensity (reduced to pole), showing Berg porphyry and other occurrences from Figure 2, and highlighting some features of interest.

Figure 4 presents the ZTEM tipper data, displayed as the Total Divergence (DT; Lo and Zang, 2008) at the 90 Hz frequency. The In-Phase DT image maps resistivity variations in plan, in addition to artefacts caused by topography (Sattel and Witherly, 2012). The DT image highlights the pronounced circular or ring-like pattern anomaly over the Berg porphyry, which also agrees with the annular geology and alteration patterns that occur within the deposit. Similar ring-like patterns are observed in ZTEM data over other porphyries in Western Cordillera, such as Pebble, Morrison, and Mt Milligan, and elsewhere. Other circular/ring-like DT signatures are also defined across the Berg survey area, including at Bergette, whereas Tara/Sibola lies along strike with a linear conductive feature in the DT.

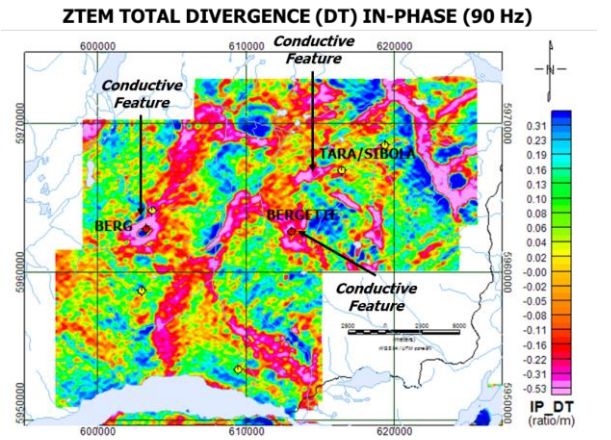

Figure 4: ZTEM In-phase Total Divergence (DT) at 90Hz, showing Berg porphyry and other occurrences from Figure 2, and highlighting some features of interest.

ZTEM and Magnetic Inversion Results

The ZTEM data have been converted to equivalent resistivity-depth distributions by 3D ZTEM inversion using the UBC MT3dinv code (Holtham and Oldenburg, 2008), respectively. The 3D inversion accounts for topography and used a 750 ohm-m half-space apriori start model. Figure 5 presents the 3D inversion result at -300m depth. The images in Figure 4 and Figure 5 resemble each other reasonably well, including well defined conductive centre that coincides with the main Berg porphyry. However, in addition to removing artifacts due to topography that affect the DT, the 3D inversion depth slice defines additional conductive anomalies not seen in the DT results, including Bergette.

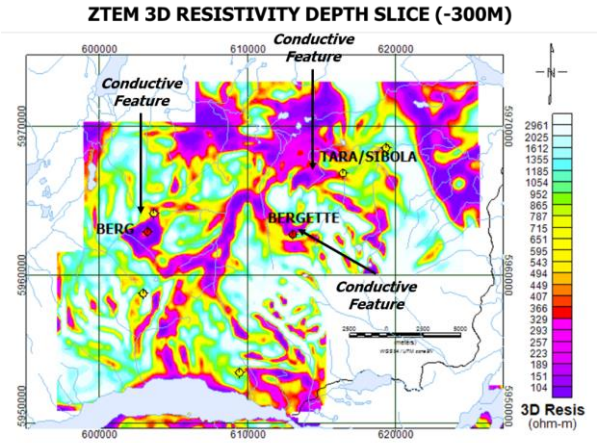

Figure 5: ZTEM 3D resistivity (red polygon) at -300m depth, highlighting some features of interest.

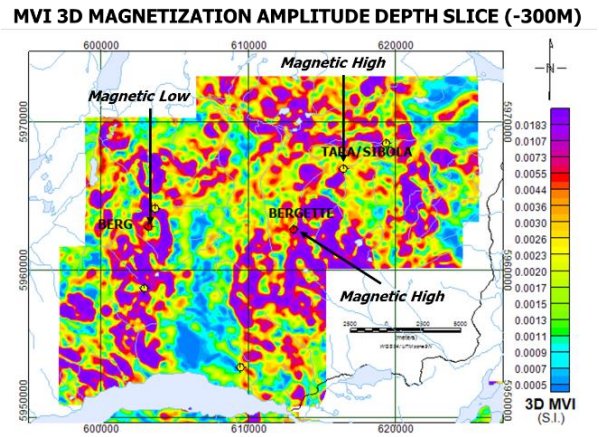

Figure 6: 3D MVI magnetization amplitude depth slice at -300m depth, highlighting some features of interest.

Figure 6 presents the corresponding 3D magnetization amplitude depth slice at -300m, obtained from the Geosoft VOXI MVI 3D inversion code (Ellis et al., 2012), which accounts for magnetic remanence. Berg is clearly marked by a ring-like magnetization high that surrounds a low magnetic core, most likely reflecting alternating magnetite enrichment and depletion due to hydrothermal alteration. In contrast, as seen in the RTP results, Bergette and Tara/Sibola both coincide with high magnetization amplitude signatures.

Figure 7 presents the multi-parameter 3D inversion results as cross-sections along north-south line L1200 across the centre of the Berg porphyry copper deposit. As shown in Figure 7b, the ZTEM inversion signature over Berg porphyry features a slightly more resistive inner core that is surrounded by a more conductive outer shell, agreeing with the annular lithologic, mineralization and alteration halo known to exist at Berg. The 3D inversion results further suggest that Berg's conductive phyllic halo extends to great depth as well as outward into the country rocks. Figure 7a presents the corresponding 3D MVI magnetization amplitude section for L1200. The section shows that Berg occurs in a relative magnetic susceptibility low, likely reflecting magnetite depletion due to porphyry related hydrothermal alteration.

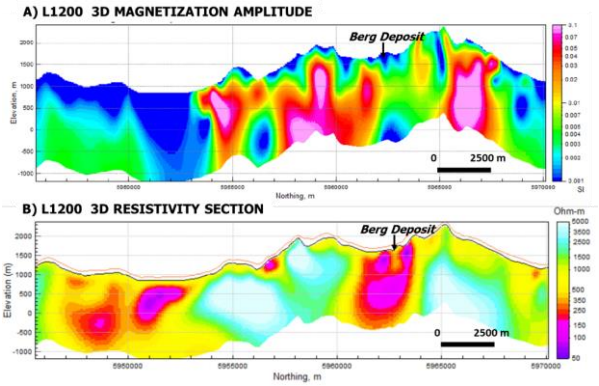

Figure 7: Multi-parameter 2D-3D inversion cross-sections along north-south L1200 across Berg porphyry deposit: a) 3D MVI magnetization amplitude inversion; and b) 3D ZTEM resistivity inversion.

Mineral Targeting Porphyry Copper Deposits

Using recent examples of semi-automated, machine-learning assisted targeting using airborne geophysics applied to orogenic and epithermal gold-silver (Kwan and Legault, 2023; Legault et al., 2023), a similar mineral targeting approach has been tested for hidden porphyry copper deposits using the Berg ZTEM and magnetic survey results. The approach uses a semi-automated, machine-learning (ML) assisted method that includes: 1) Structural Complexities (SC), 2) Self-Organizing Map (SOM) classifications, and 3) Supervised Deep Neural Network (SDNN) targeting of the geophysical data.

The RTP magnetic data have been analyzed for structural complexity (SC), using the Geosoft CET (Center for Exploration Targeting) grid analysis tool (Holden et al., 2012). The CET SC analysis tool outputs two parameters: i) the Contact Orientation Density (COD), and the Orientation Entropy (OE). Figure 8 presents the SC-derived COD image. As shown, the structural complexity highs are concentrated in areas with known porphyry occurrences.

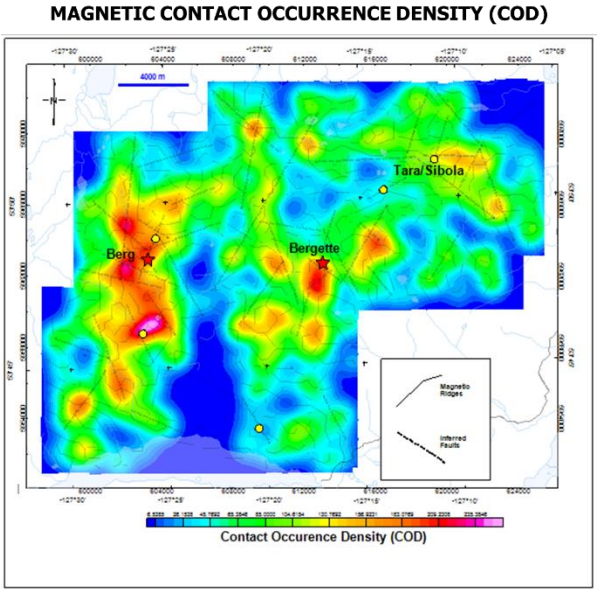

Figure 8: Structural complexity (SC) analysis of magnetic data, showing the Contact Occurrence Density (COD), over mineral occurrences and inferred faults (dashed lines), and magnetic ridges.

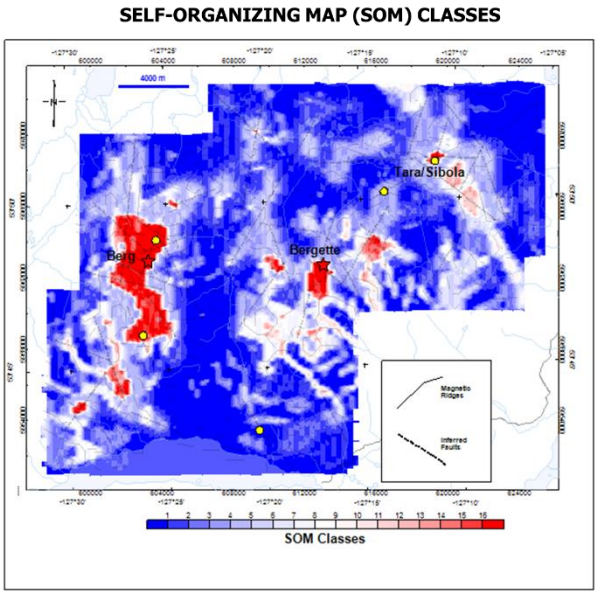

Figure 9: Self Organizing Map (SOM) results, showing anomalous SOM classes covering all the known porphyry copper occurrences.

Self-Organizing Map (SOM) are useful tools in analysing and classifying multiple datasets. The magnetic SC data (COD + OE), the 3D ZTEM inversion data (-300m resistivity depth-slice), and the 3D MVI inversion data (-300m magnetization amplitude depth-slice) were used as inputs and classified using the Geosoft SOM GX tool (https://geosoftgxdev.atlassian.net). As shown in Figure 9, the anomalous SOM classes (12 to 17) coincide with the known porphyry copper occurrences, namely Berg and Bergette, as well as lesser showings.

The final mineral targeting step used the Supervised Deep Neural Network (SDNN) module in Google TensorFlow version TF 2.30 (https://www.tensorflow.org/). The training of the SDNN was performed on the Berg deposit area (Figure 10a) using the magnetic COD and OE layers, the SOM classification results, the ZTEM 3D -300 m resistivity depth slice, and the MVI 3D -300 m magnetization amplitude depth slice information. The top 3.3% probability was selected for porphyry targeting (Figure 10b).

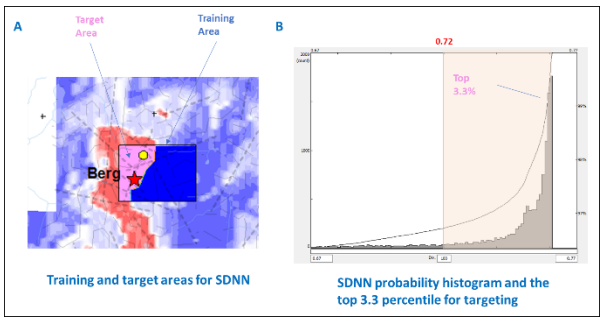

Figure 10: (A) Berg deposit training area for SDNN, (B) top 3.3% target probability cut-off for targeting.

The SDNN targeting was then applied to the entire Berg survey area, using similar multi-parameter data inputs as used in the initial SDNN training. Figure 11 presents the top 3.3% targeting probabilities over the DEM data, and the selected targets, T1-T4, which include Berg (T1) and Bergette (T2) as well as two other targets that also host known mineral showings and therefore represent potential areas for follow-up.

CONCLUSION

The ZTEM and magnetic results from the Berg Project present an excellent opportunity to study the geophysical signatures over an undeveloped yet significant porphyry copper deposit and the surrounding region. The Berg survey has led to the successful characterization of the known porphyry deposit based on resistivity and magnetic susceptibility. The ZTEM survey results, augmented by 3D inversions, appear to map all the known porphyry deposits and occurrences at Berg, including the Bergette target. 3D ZTEM inversion analyses appear to confirm the bedrock source of conductivity that extend from surface to >500m depths. The magnetic and ZTEM results at Berg closely resemble those previously found in ZTEM surveys in the Western Cordillera, such as Morrison, Pebble, and Mt Milligan, including alteration-related, ring-like conductive highs that surround higher resistivities in the core and similar ring-like magnetic highs surrounding magnetic lows in the porphyry centres. The magnetic response is expected to be caused by magnetite enrichment in the outer halo and depletion in the centre. The increased conductivity within the mineralized porphyries at Berg show reasonable correlation with moderate to weak intensity phyllic alteration associated with hypogene mineralization.

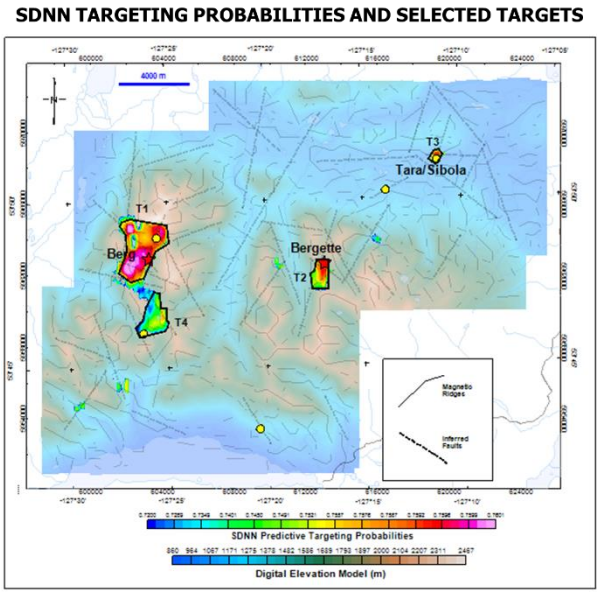

Figure 11: The SDNN top 3% probabilities over the DEM data and the selected potential porphyry targets (T1-T4), including Berg (T1) and Bergette (T2).

Finally, an approach for porphyry targeting has been tested, which uses a semi-automated, machine-learning (ML) assisted method that includes: 1) Structural Complexities (SC), 2) Self-Organizing Map (SOM) classifications, and 3) Supervised Deep Neural Network (SDNN) targeting of the geophysical data. SC analysis of magnetic results has shown a close relationship between areas of structure intersection density and orientation diversity and the known porphyry occurrences. The SOM analysis showed the most anomalous classes coincide with the known porphyry copper occurrences, and other showings. Finally, the SDNN analysis, using Berg deposit as a training area, identified four main target areas that include both Berg and Bergette, as well as two other known mineral showings and that represent potential areas for follow-up.

ACKNOWLEDGMENTS

The authors wish to thank Surge Copper Corp. and Geotech for allowing us to present these results.

REFERENCES

Allard, M., 2007, On the Origin of the HTEM Species: In "Proceedings of Exploration 07: Fifth Decennial International Conference on Mineral Exploration" edited by B. Milkereit, 2007, p. 355-374.

Burge, C., 2014, A new porphyry copper deposit at Cobre Panama project: presented at PDAC Prospectors and Developers Convention, Discoveries and Developments session, Toronto, Canada.

Ellis, R.G., de Wet, B., and Macleod, I.N., 2012, Inversion of magnetic data for remanent and induced sources: 21ST ASEG Annual Conference and Exhibition, Extended Abstracts, 4 p.

Holden, E.-J., Wong, J. C., Kovesi, P., Wedge, D., Dentith, M., Bagas, L., 2012. Identifying structural complexity in aeromagnetic data: An image analysis approach to greenfields gold exploration. Ore Geology Reviews 46: 47–59.

Holtham, E., and Oldenburg, D.W., 2008, Three-dimensional forward modelling and inversion of Z-TEM data: 78TH SEG Annual International Meeting, Expanded Abstracts, 564-568.

Holtham, E., and Oldenburg, D.W., 2010, Three-dimensional inversion of ZTEM data: Geophysical Journal International, 182, 168-182.

Hoschke, T., 2011, Geophysical signatures of copper-gold porphyry and epithermal gold deposits, and implications for exploration: CODES-ARC Center of Excellence in Ore Deposits, University of Tasmania, 47 p.

Izarra, C., Legault, J.M. and Latrous, A., 2011, ZTEM airborne tipper AFMAG results over the Copaquire porphyry, northern Chile: 81ST SEG Annual International Meeting, Expanded Abstracts, 1257-1261.

Kwan, K., and Legault, J.M., 2023, Gold targeting of fixed wing aeromagnetic Data using structural complexity, self-organizing map and supervised deep neural network analyses: A case study from the Red Lake camp, Superior Province, Ontario, Canada: Unpublished abstract submitted to IMAGE 2023 conference.

Labson, V. F., Becker, A., Morrison, H.F., and Conti, U. [1985] Geophysical exploration with audio frequency natural magnetic fields. Geophysics, 50, 656–664.

Lee, B.M., Unsworth, M., Hubert, J., Richards, J.P., and Legault, J.M., 2017, Geophysical Prospecting, 6, 397-421.

Legault, J.M., 2012, Ten years of passive airborne AFMAG EM development for mineral exploration: 82ND SEG Annual International Meeting, Expanded Abstracts, 5 p.

Legault, J.M., Wijns, C., Izarra, C., and Plastow, G., 2016, The Balboa ZTEM Cu-Mo-Au porphyry discovery at Cobre Panama: 25TH ASEG-PESA-AIG Geophysical Conference and Exhibition, Extended Abstracts, 6 p.

Legault, J.M., Jahandari, H., and Ebert, S., 2022, ZTEM airborne natural field EM and magnetic case study over the Berg porphyry copper project, Huckleberry District, British Columbia: IMAGE, expanded abstracts, 5 p.

Legault, J.M., Kwan, K., Greig, J., Webster, E., and Hanki, M., 2023, Targeting epithermal Au-Ag using helicopter TDEM, magnetic, and radiometric data at Lawyers Project, North-Central BC, Canada: Unpublished expanded abstract submitted to AEM 2023 conference.

Lo, B., and Zang, M., 2008, Numerical modelling of Z-TEM (airborne AFMAG) responses to guide exploration strategies: 78th SEG Annual International Meeting, Expanded Abstracts, 1098-1101.

Norton, C., Huang, J., and Lui, D., 2021. Updated Technical Report and Mineral Resource Estimate on the Berg Project, British Columbia: Technical (NI 43-101) report to Surge Copper Corp., prepared Tetra Tech Canada Inc., 146 p.

Paré, P., Gribenko, A.V., Cox, L.H., Cuma, M., Wilson, G.A., Zhdanov, M.S, Legault, J.M., Smit, J. and Polomé, L., 2012, 3D inversion of SPECTREM and ZTEM airborne electromagnetic data from the Pebble Cu-Au-Mo porphyry deposit, Alaska: Exploration Geophysics, 43, 104-115.

Purich, E., Ray, B., Barry, J., Hayden, A., Yang, D., Schmidtt, H.R., 2016, Updated Resource Estimate and Preliminary Economic Assessment on the Ootsa Property, British Columbia, Canada: NI 43-101 Technical Report (No. 306) for Gold Reach Resources Ltd., by P & E Mining Consultants Inc. 433 p.

Sattel, D., Thomas, S. and Becken, M., 2010, An analysis of ZTEM data over the Mt Milligan porphyry copper deposit, British Columbia: 80th SEG Annual International Meeting, Expanded Abstracts, 1729–1733.

Sattel, D. and Witherly, K., 2012, Extracting information from ZTEM data with 2D inversions: 21ST ASEG Annual Conference and Exhibition, Extended Abstracts, 4 p.

Surge Copper Corp., 2021, Surge Copper Announces 2021 Exploration Plans: Press Release May 12, 2021, www.surgecopper.com.

7th International Symposium on Three-Dimensional Electromagnetics
Vancouver, BC, Canada, November 13–15, 2023

An adaptive finite element solver for three-dimensional electromagnetic inductions

Jianbo Long
Centre for Geophysical Forecasting, Norwegian University of Science and Technology
Department of Earth Sciences, Memorial University of Newfoundland

Summary

Forward modelling of three-dimensional (3-D) electromagnetic (EM) data over realistic Earth models remains important but also challenging due to complexities in mesh design and high computational costs. Typical examples of realistic Earth models in terms of electrical conductivity distribution include high conductivity contrast (e.g., highly conductive ore bodies in mineral deposit explorations, seawater effects in marine magnetotelluric and controlled-source EM surveys), realistic topography and bathymetry (e.g., seafloor) and extreme geometries (e.g., small steel-cased wells). In these scenarios, generating and manipulating 3-D meshes with sufficient quality required by corresponding numerical algorithms in modelling EM responses are difficult and time-consuming even with the state-of-the-art meshing tools.

To solve such challenge, an adaptive finite element solver designed for EM data over 3-D models is being developed. The Maxwell's equations for electric and magnetic fields are transformed into the second-order Helmholtz equation for the electric field which is then numerically solved using edge-based finite element method. The Earth model is discretized using unstructured tetrahedral meshes to provide maximum conformity in approximating realistic geometries with a minimum amount of cells in the mesh.

The adaptive EM solver takes advantage of the open-source finite-element package `MFEM` in terms of adaptively refining the tetrahedral mesh. The adaptive mesh refinement in the package supports local iterative refinements (i.e., goal-oriented refinement), and both conformal and non-conformal subdivisions of selected tetrahedra of the mesh. As to finite element method, the package supports various orders of basis functions using hierarchical finite element approach, leading to the potential capability of p-adaptivity of the EM solver.

To demonstrate the capability of the developed solver so far, a 3-D frequency-domain controlled-source EM survey that comprises a long electric wire source (of length 100 m) at the surface and a rectangular conductor (conductivity of 1 S/m, dimension of 1 km by 1 km by 100 m) buried in a uniform, resistive subsurface (conductivity of 0.01 S/m) is used. This survey mimics a typical EM survey for metallic mineral deposits. The modelling accuracy and performance of the newly developed solver are illustrated by comparing the modelled responses to those obtained using a previously developed, stand-alone high-order finite-element solver.

Keywords: three-dimensional modelling, finite element, numerical method, adaptive

7th International Symposium on Three-Dimensional Electromagnetics
Vancouver, BC, Canada, November 13–15, 2023

Using convolutional neural networks to classify UXO with multicomponent electromagnetic induction data

Jorge Lopez-Alvis[1], Lindsey J. Heagy[1], Douglas W. Oldenburg[1], Stephen Billings[2] and Lin-Ping Song[2]
[1]University of British Columbia
[2]Black Tusk Geophysics

Summary

Electromagnetic induction (EMI) methods are commonly used to classify unexploded ordnance (UXO) in both terrestrial and marine settings. Modern time-domain systems used for classification are multicomponent which means they acquire many transmitter-receiver pairs at multiple time-channels. We developed a convolutional neural network (CNN) that classifies UXO directly from EMI data. Analogous to an image segmentation problem, our CNN preserves the spatial dimensions of the input and produces a high-resolution classification map. The CNN is trained using synthetic data generated with a dipole forward model considering all possible UXO and clutter objects. A physics-based parameterization of the clutter classes is used to maximize clutter discrimination. Our approach was tested on data acquired with the UltraTEMA-4 system in the Sequim Bay marine test site. Including spatially correlated noise in our training dataset significantly improved our classification results for field data. For this test dataset, our CNN-based approach detects all UXOs and discriminates ∼70% of the clutter.

Keywords: electromagnetic induction, UXO classification, convolutional neural network

Introduction

The use of EMI systems to detect and classify UXO on land is well established. Recently, systems such as the UltraTEMA-4 (Funk et al., 2022) have also been designed for underwater munitions. Advanced systems aim to reduce costs related to excavation and interrogation by discriminating non-UXO objects in a single pass. These systems usually rely on many sources and receivers and create spatially dense data which has high information content since the targets are illuminated from different angles.

The usual workflow for clearing a site consists of generating a map from EMI data from which anomalies of interest are picked, then classification is done for each of these anomalies and a target list is obtained. Picking anomalies from a gridded image created from sensor data is done by setting some threshold value of amplitude chosen to maximize the detection of ordnance expected at the site without including anomalies from sensor noise or smaller items. Once the anomalies are picked, classification is done using a physics-based inversion approach where polarizability curves are estimated from the EMI data. These curves are then compared with those in a library to look for a match based on some misfit and a class is assigned (see e.g. Pasion et al., 2007).

In this work, we develop a workflow that takes EMI data directly and produces a classification map using two CNNs from which a final single class may be assigned to each anomaly detected. Both CNNs have the same architecture but the first one is only used to detect anomalies from metallic objects while the second creates the classification map.

Methods

We use two CNNs to detect and classify UXOs from EMI data. The input for the CNNs was defined as a two-dimensional data map considering a fixed number of transmitter cycles in the along-track direction and the spatial extent of the receivers in the cross-track direction. Analogous to an image segmentation problem, our CNN outputs a classification map that preserves the spatial dimensions of the input (Figure 2). The label masks used for training are defined using the magnitude of dB/dt (computed from x,y,z components measured at receivers), adding them up for all the transmitters and thresholding this sum at a specific value (Figure 3). Data is processed per-line using a fixed sliding window with steps equal to one and a simple voting scheme is used to get a single class value per receiver location.

We train the CNNs using synthetic data generated with a dipole forward model considering all possible UXO and clutter objects. This forward model uses polarizability curves from a library; each object in the library has three polarizability curves associated with three orthogonal axes aligned with its geometry. This dipole model has been shown to be accurate for compact objects such as UXOs. The clutter objects were designed based on the following physics-based parameterization for the polarizability curves (Pasion & Oldenburg, 2001):

$$L(t) = kt^{-\beta} \exp(-t/\gamma) \quad (1)$$

Where $L(t)$ denotes the polarizability as a function of time t and k, β and γ are parameters related to the decay of the EM signal in the object. Using this model, we estimate the values of k, β and γ for the UXOs in the library. Since we have a polarizability curve $L(t)$ for each of the three axes, there are a total of 9 parameters to be estimated. Then, we set a distance threshold value, above which, the remaining parameter space is filled with values that we attribute to clutter (Figure 1).

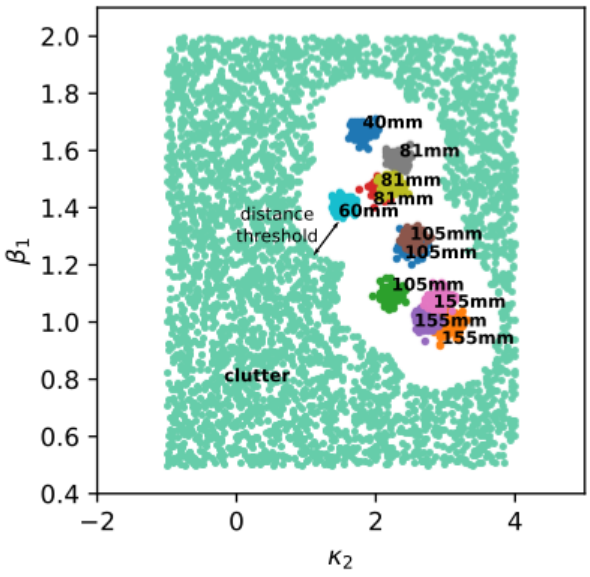

Figure 1: Parameter space depicting clutter design strategy; shown is a simplified 2D parameter space while our approach uses a 9-dimensional parameter space.

The architecture of both CNNs is the same but the first one is trained as a binary classifier that outputs a map which labels data as either background or TOI (target of interest) whereas the second one is a multi-class classifier that outputs a map with UXO type class. This two-step approach is mainly done due to the need to separate anomalies and background data in order to estimate spatially correlated noise from the field data and add it to the training data. This step was found crucial to improve classification results of field data with our CNN.

The output of the second CNN is a classification map which may also be expressed as a set of probability maps, each showing the data points likelihood of belonging to a certain class. To obtain a single class for each anomaly identified, we simply take the average probability values for all data points within a certain cell surrounding the anomaly (such cells are picked manually from the previous binary map) and select the class with the highest average probability (Figure 4).

Test data

We tested our approach using field data acquired with the UltraTEMA-4 system in the Sequim Bay marine test site (Funk et al., 2022). The first CNN of our workflow was trained with 20,000 examples of synthetic data and binary label masks, while the second CNN was trained with 400,000 examples of data and multi-class label masks. Classification results for the field data show that our approach detects all UXOs and discriminates ~70% of the clutter (Figure 5).

A preprocessing step was used to remove the EM response of conductive seawater and sediments but some spatially correlated noise still remains in the data. Our workflow is able to cope with this by using the first CNN to separate background signal from anomalies in the field data. Then, we randomly sample pieces of this background signal and add them to the training dataset of the second CNN.

Discussion

A key feature of our CNN is its segmentation-like architecture. Compared to a first version of the CNN (Heagy et al., 2020), this new architecture is able to provide higher-resolution classification maps which do not require interpolation and therefore is less likely to miss small objects. However, our CNN has not been trained for multi-target scenarios (two objects close together i.e. in the same spatial window) hence it may lead to errors for such cases. In future work, we plan to explore this multi-target scenario by including these cases in the training dataset of our CNN.

The clutter design is also an important part of our approach. As with any machine learning approach, the CNN needs to be trained with examples not only of all UXOs but also with all possible clutter objects. The physics-based parameterization used here (Equation 1) attempts to exhaustively cover all possible clutter objects by setting a distance in the parameter space. The value for this distance has to be tuned in order to maximize clutter discrimination without decreasing UXO detection. This distance may be chosen using a line of synthetic data that includes both UXOs and objects with the expected dimensions of clutter and/or with a field calibration line that is usually available for UXO clearance projects.

Other choices such as grouping the UXO objects, adding random noise to the training dataset and averaging probabilities for overlapping (sliding) windows have also slightly improved the performance of our second CNN.

Conclusion

Modern EMI systems used for UXO classification collect spatially dense data with sufficient information to classify different types of UXO and discriminate clutter. The traditional approach for classification is based on inversion and polarizability curve matching. We developed a CNN-based approach for UXO classification directly from EMI data. Our approach uses two CNNs, the first one for anomaly detection and the second one for classification. Their architectures follow an image segmentation structure where the output preserves spatial dimensions of the input and therefore produce high resolution classification maps. The CNNs were trained with synthetic data using a dipole model and considering UXOs and all possible clutter objects, which were designed in a physics-based parameter space. Spatially and temporally correlated noise that is consistent with that of the field is also added to the training dataset to improve classification results. Our workflow was applied to marine EMI dataset from a test site where it successfully detected all of the UXOs while discriminating ~70% of the clutter.

Acknowledgments

This work is supported by SERDP project MR22-3487.

REFERENCES

Funk, R., Gamey, T. J., & Billings, S. (2022, March). ULTRATEMA-4 marine dynamic classification system field trials. In *SAGEEP 2022*.

Heagy, L. J., Oldenburg, D. W., Pérez, F., & Beran, L. (2020, September). Machine learning for the classification of unexploded ordnance (UXO) from electromagnetic data. In *SEG Technical Program Expanded Abstracts 2020* (pp. 3482–3486). Society of Exploration Geophysicists.

Pasion, L. R., Billings, S. D., Oldenburg, D. W., & Walker, S. E. (2007). Application of a library based method to time domain electromagnetic data for the identification of unexploded ordnance. *Journal of Applied Geophysics*.

Pasion, L. R., & Oldenburg, D. W. (2001, June). A Discrimination Algorithm for UXO Using Time Domain Electromagnetics. *Journal of Environmental and Engineering Geophysics*, *6*(2), 91–102. (Publisher: Environmental & Engineering Geophysical Society)

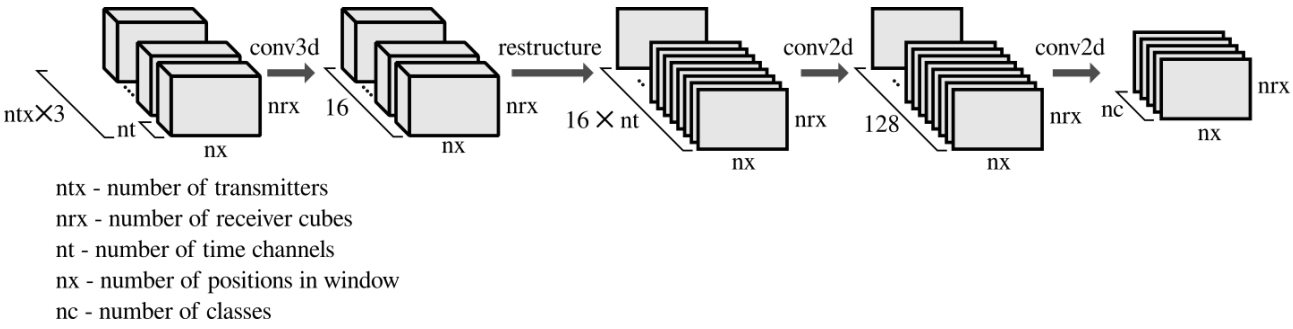

Figure 2: Proposed CNN architecture to detect and classify UXO directly from EMI data.

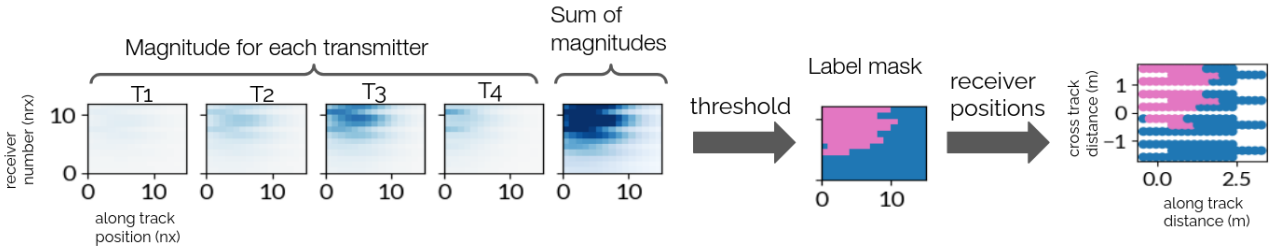

Figure 3: Defining label masks from EMI data.

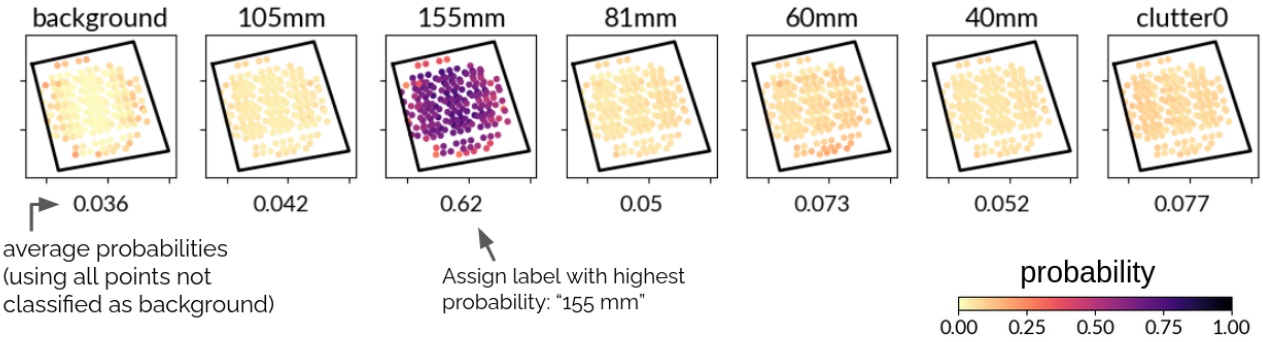

Figure 4: Computing average probabilities to assign a final label from the CNN output.

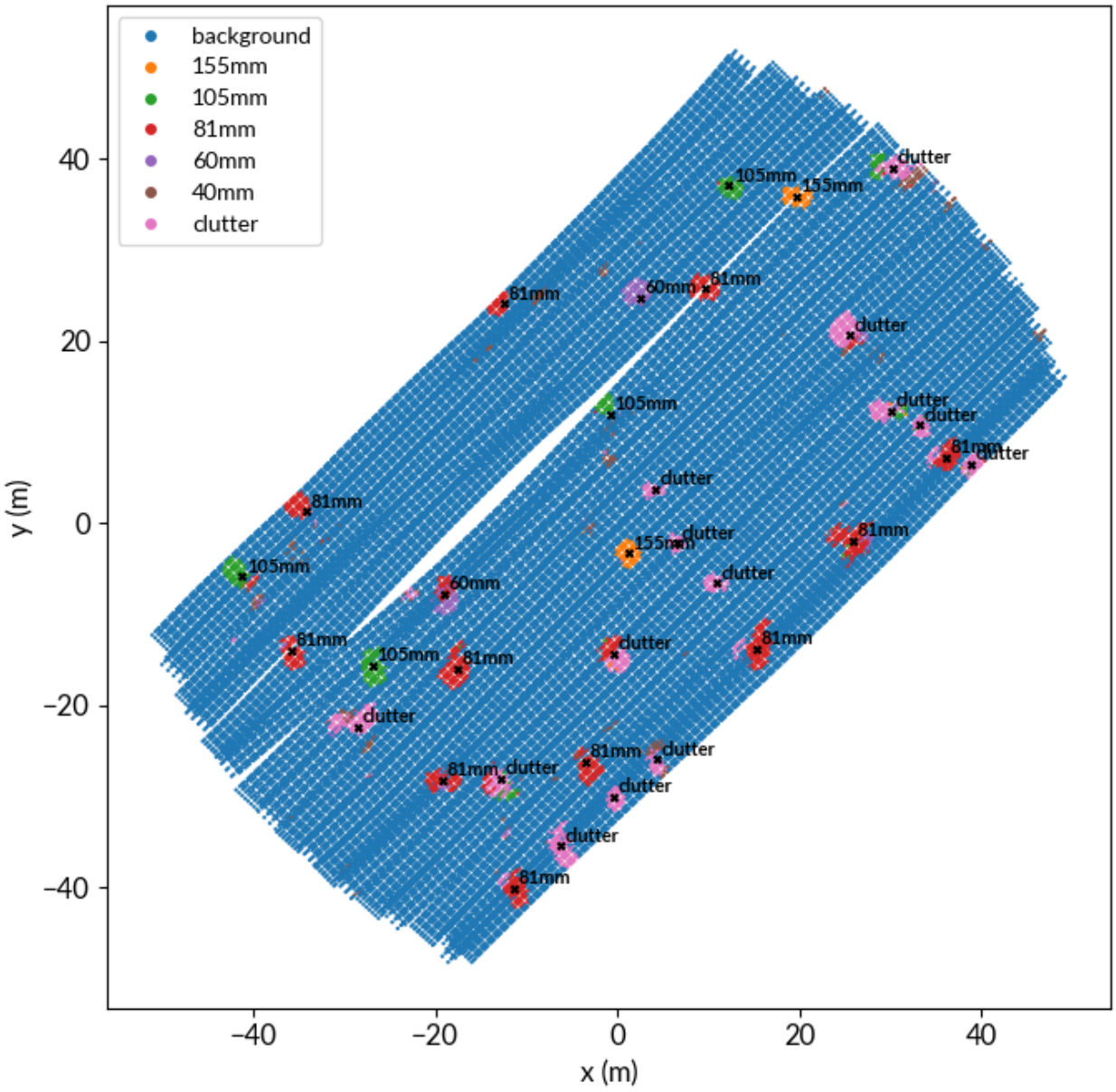

Figure 5: Classification for Sequim Bay field data (2021), colors indicate the classification map produced by the CNN and shown labels are given by our voting system.

7th International Symposium on Three-Dimensional Electromagnetics
Vancouver, BC, Canada, November 13–15, 2023

Surface geometry inversion of TEM data for thin, dipping conductors

Xushan Lu[1], Colin Farquharson[1] and Peter Lelièvre[2]
[1]Department of Earth Sciences, Memorial University of Newfoundland, St. John's, NL, Canada
[2]Department of Mathematics and Computer Science, Mount Allison University, Sackville, NL, Canada

Summary

We investigate a new method called surface geometry inversion (SGI) for the inversion of transient electromagnetic (TEM) data. Our SGI parameterizes the model in terms of the coordinates of the nodes used to specify the tessellated surface that defines the interface between different geological units. The SGI then inverts for the locations of these nodes. The constructed model directly provides the geometry of the target, which can be more useful than a fuzzy image of conductivity for an exploration project. Our SGI only has the data misfit term in the objective function. A genetic algorithm (GA) is used to solve the over-determined problem in the optimization. We use a finite-element solver with unstructured tetrahedral meshes to solve the TEM forward modeling problem used to evaluate the data misfit of each candidate model in the GA population. We investigate a new parameterization method specifically designed for thin, plate-like structures. We test our SGI and the new parameterization method using a real dataset collected in the Athabasca Basin, Canada.

Keywords: Surface geometry inversion, transient electromagnetic, genetic algorithm, finite-element method

Introduction

Transient electromagnetic (TEM) methods have been widely used in mineral exploration to target graphitic faults (Lu et al., 2021) and volcanogenic massive sulphide deposits (Malo-Lalande et al., 2020) which typically have a thin, steeply dipping structure. In recent years, significant progress has been made in the 3D minimum-structure inversion of EM data and such inversions have seen routine use in exploration projects (Yang et al., 2019). However, it is well known that the minimum-structure inversion algorithms tend to construct models with smooth features when using the l_2 measure of model roughness as a regularization term to reduce the non-uniqueness. The smooth models can be problematic for thin, steeply dipping geological structures commonly seen in mineral exploration projects because the anomalous conductive zone in the constructed model can be many times larger than the true thickness of the thin conductor (Yang et al., 2019). It is therefore difficult to extract the information on the true location of the thin conductor, making it challenging for drill targeting.

We are investigating a different method we call surface geometry inversion (SGI) in an attempt to construct models with distinct boundaries with surrounding rocks. The SGI method can work directly with 3D explicit surfaces constructed based on realistic, arbitrarily shaped geological targets, and the constructed model is consistent with the 3D computer models that geologists use during exploration, which typically use tessellated surfaces to represent the interfaces between different geological units. Our SGI method only focuses on localized anomalous targets whose boundary interfaces are represented by tessellated triangular facets.

Different from previous potential data SGI (Galley et al., 2021), the background physical property model has to be incorporated for TEM problems. The background model can either be obtained from a trial-and-error modeling or from voxel inversion. To deal with thin, steeply dipping conductors, we develop a new parameterization method. Instead of parameterizing the entire outer surface of the target, we only use a triangular surface mesh to represent the center of the plate-like target. We then reconstruct the thin structure from the parameterization surface. To calculate the TEM forward response of each model, TetGen (Si, 2015) is used to automatically generate the unstructured tetrahedral mesh for the entire model once it's built. We then solve the forward modeling problem using a finite-element (FE) solver based on Li et al. (2018).

We use a real-data example from a uranium exploration project to show that our SGI can successfully construct a thin and bending conductor model that matches well with drilling data.

Methods

Model parameterization

We use a bending surface comprised of triangular facets to parameterize thin conductors. As shown in Figure 1, to reconstruct the thin conductor, the surface is first duplicated and then the original and newly duplicated surfaces are moved in opposite directions. The direction is calculated by the average of the normal vectors of all triangles in the original parameterization surface sharing the node. To create a conductor of varying thicknesses at different parts, different distances could be applied when moving different node pairs. Eventually, the two surfaces are sewn together to obtain the thin conductor. During the SGI, we only allow the nodes to be moved perpendicular to the strike of the conductor.

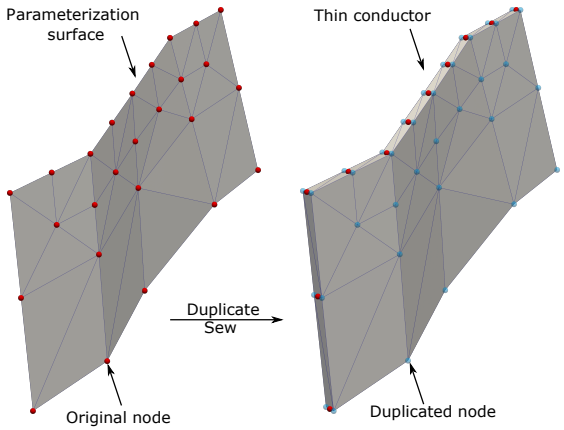

Figure 1: The thin conductor is obtained from sewing the original surface and its duplicate after moving them along the normal direction of the surface.

The physical properties within an anomalous body can also be included as inversion parameters. We subdivide the conductor by simply connecting the four nodes of two edges that correspond to the same edge in the original parameterization surface into two triangles. Afterwards, the number of subdivided volumes becomes equal to the number of triangles in the parameterization surface. We assign a constant physical property value to all tetrahedral cells inside the same volume after the mesh discretization.

Surface geometry inversion

Our inversion minimizes an objective function which only contains a data misfit term. The normalized χ^2 measure of misfit is used here, which can be written as

$$\Phi = \frac{1}{N}\sum_{i=1}^{N}\frac{\left(d_i^{pre}-d_i\right)^2}{\sigma_{SD_i}^2}, \tag{1}$$

where d_i and d_i^{pre} are the ith observed and predicted data, respectively; σ_{SD_i} is the uncertainty assigned to that datum; and N is the number of data. The minimization of Equation 1 is an overdetermined problem as there are typically more data than model parameters for EM problems. Moreover, Equation 1 is significantly non-linear. Consequently, a global optimization algorithm, GA, is used to minimize Equation 1.

To obtain the first generation of the GA population, we randomly perturb the facets' vertices of an input surface model, referred to as the initialization model, within a predefined volume. For real data examples, the initialization model is a best guess of the real Earth and therefore is included in the initial population. The topology of the initial model is preserved while the facets' vertices are changed during the inversion. The volume used to initialize the first generation is called the initialization volume and the volume used to bound new candidate models is called the search volume. The search volume can be different from the initialization volume but here we use the same volume for both.

Example

The Preston Lake Project is a uranium exploration project located just south of the Athabasca Basin in Saskatchewan Province, Canada (Figure 2). In December, 2017, a moving-loop TEM (MLTEM) survey was conducted. Data were collected on six profiles, with a total length of 18 km (Figure 3). A 100 by 100 m transmitter loop was used and the receiver offset was 200 m. In total, 20 channels of three-component dB/dt and B-field data were collected but we only inverted the B-field data. Later, six holes (purple diamonds in Figure 3) were drilled and five holes encountered graphite-bearing fault conductors with a thickness ranging from a few meters to nearly 20 m. The early-time data are noisy, which is possibly caused by a heterogeneous near surface conductivity distribution, so the first eight channels of the measured data are discarded.

The data from L2400E and L3200E were inverted. The data from the stations at either end of the profile were excluded from the inversion as they do not contain information of the conductor. We assigned σ_{SD} as the maximum value of the instrument standard deviation and 5% of the datum plus a noise floor of 0.001

pT. A background conductivity model was obtained from trial-and-error modeling with a model comprising a conductor buried in a layered Earth model.

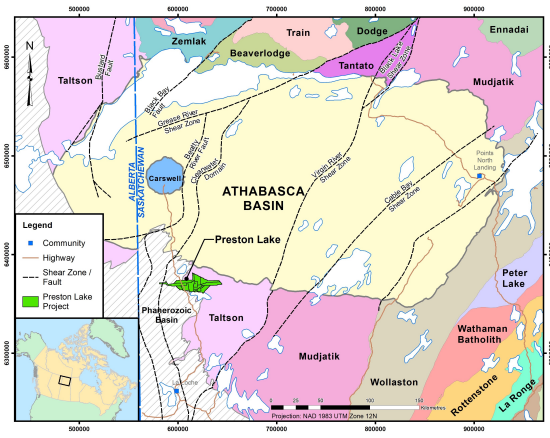

Figure 2: Precambrain geological domain map of northern Saskatchewan, Canada. The Preston Lake Project is located just outside the Athabasca Basin (pale yellow) to the southwest as indicated by the green shaded area (after Lu et al., 2021).

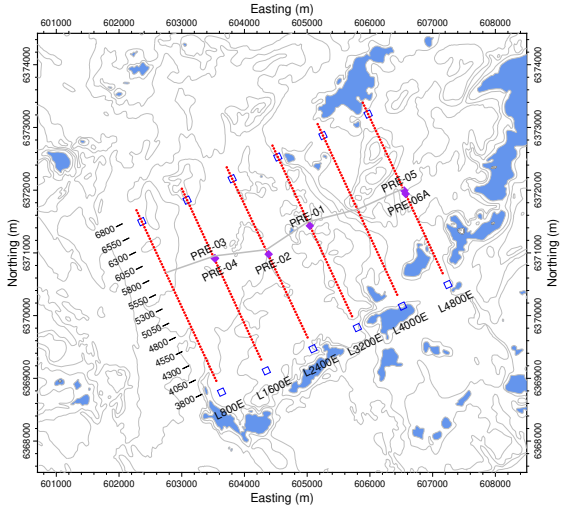

Figure 3: The North Grid of the 2017 MLTEM survey. The blue rectangles represent the first and the last transmitters of each profile while the red dots mark all the receivers in each profile. The purple diamond symbols represent drill holes. The gray line represents the conductor trend.

There were 26 nodes connected into 34 triangles in the parameterization surface (Figure 4). All nodes in the model were only allowed to move perpendicularly to the strike direction estimated from the trial and error modeling. We also inverted the conductivities of different parts of the conductor. In total, the number of inversion parameters was 60 (26 nodes moving perpendicularly to the strike direction plus 34 regions having unique conductivity values).

We ran the inversion on seven computing nodes each with 40 CPUs running at 2.5 GHz. There are 280 MPI processes each with one OpenMP thread. The size of the GA population was 279 and the responses for all the models in the population were being calculated in parallel. The inversion took on average 34.2 minutes for each iteration and the total time for the inversion to finish 200 iterations was about 114 hours.

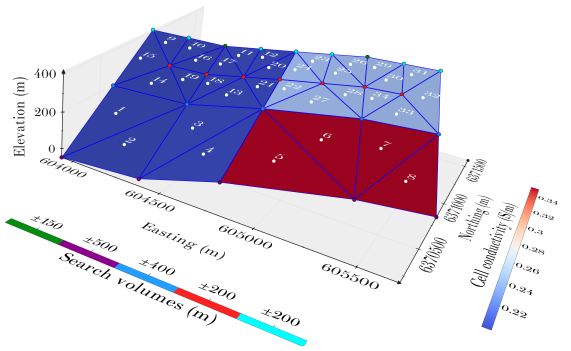

Figure 4: The initialization surface used for the SGI of the Preston Lake data. Each of the triangles is assigned with a fixed conductivity.

The data misfit drops from about 43.8 to 15.9 in 200 iterations (Figure 5). The curve becomes flat after 175 iterations and we consider the inversion has converged. Figure 6 shows the data fitting of Profile L3200E. The data fitting is good in general, except for early-time channels in the inline and vertical components. The relatively worse match between the predicted and observed data for the in-line and vertical components for the first few channels is indicative of an insufficiently accurate background model. This issue can be potentially resolved by using a background model obtained from a voxel inversion instead of trial-and-error modeling. Additionally, we only used a small number of nodes in the parameterization surface, which may be insufficient to represent the subtle features in the real geometry of the conductor.

Figure 7 shows the parameterization surface from the SGI constructed model. The conductor intersects with the graphitic fault at almost the exact true location (the red section of the two color bars used to represent the two drill holes PRE-01 and PRE-02). The good agreement between the constructed model and the drilling data indicates the SGI is successful. The conductor bends to the south and north,

respectively, at profiles L2400E and L3200E in the constructed model, which is consistent with the general trend revealed in the MLTEM survey as well as drilling data for the entire grid. The geometry of the conductor stabilizes after about 70 iterations.

Discussion

Compared with minimum-structure inversion, our SGI algorithm requires more computational resources but it can provide constructed models that are more consistent with the kinds of thin, steeply dipping conductors encountered during mineral exploration (and the 3D computer models used by geologists to represent such targets). Additionally, the uncertainty information of the inversion parameters can be obtained via a Markov Chain Monte Carlo sampling method as shown by Galley et al. (2020). Such uncertainty information can be critically important when it comes to drill targeting and risk mitigation. A priori geological information is important for our SGI as it's used to build the initialization model which has a significant impact on the final constructed model. As observed in the example, an inaccurate background conductivity model may cause difficulties for the SGI to fit the entire data set, and constructing the background model from a voxel inversion could potentially solve this issue. Consequently, we consider our SGI as a tool that can be used to refine the geological model at later stages of exploration projects.

Conclusion

We have implemented the surface geometry inversion algorithm for 3D TEM data inversion. Our parameterization method allows for flexible and efficient parameterization of thin, plate-like conductors. The constructed model of the SGI placed the conductor at the correct location according to the drilling data. The geometric information about the conductor is more useful than a fuzzy conductivity image one would get from a minimum-structure inversion, with which drill targeting is difficult.

Acknowledgments

This project is financially supported by National Sciences and Engineering Research Council of Canada and Orano Canada Inc. Digital Research Alliance of Canada (alliancecan.ca/en) and ACENET (acenet.ca) provided the computing resources and invaluable technical advices.

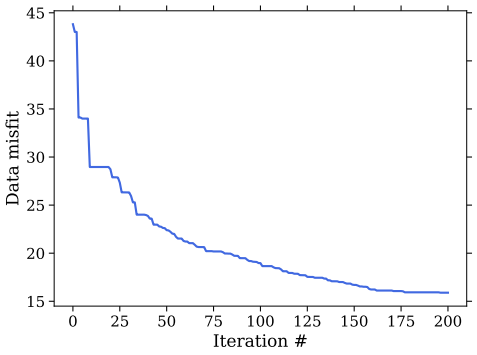

Figure 5: The convergence curve for the SGI of the Preston Lake data.

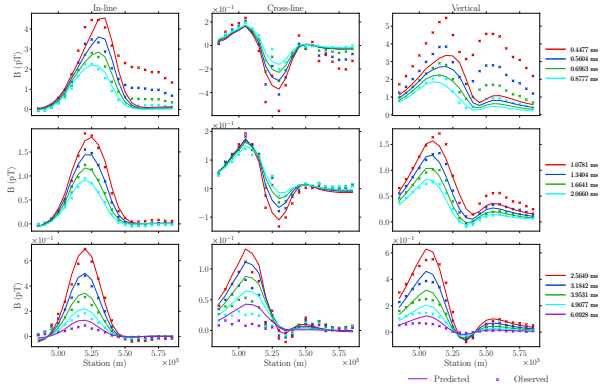

Figure 6: The data fitting of Profile L3200E. The observed data are shown with a cross symbol (x) while the predicted data are shown with solid lines.

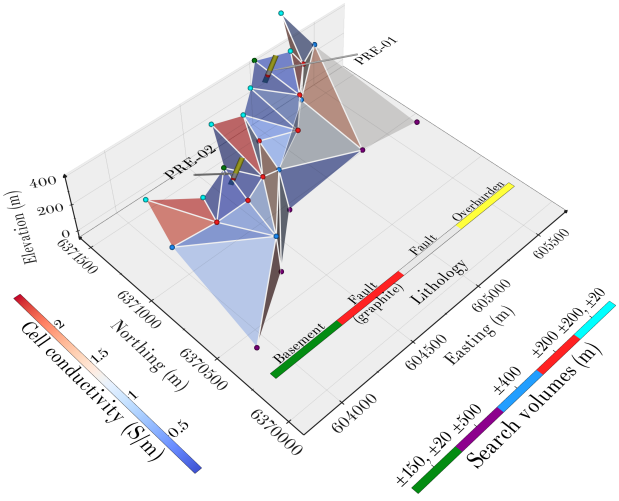

Figure 7: The parameterization surface corresponding to the constructed model of the Preston Lake data SGI.

REFERENCES

Galley, C., P. Lelièvre, A. Haroon, S. Graber, J. Jamieson, F. Szitkar, I. Yeo, C. Farquharson, S. Petersen, and R. Evans, 2021, Magnetic and Gravity Surface Geometry Inverse Modeling of the TAG Active Mound: Journal of Geophysical Research: Solid Earth, **126**.

Galley, C. G., P. G. Lelièvre, and C. G. Farquharson, 2020, Geophysical inversion for 3D contact surface geometry: GEOPHYSICS, **85**, K27–K45.

Li, J., X. Lu, C. G. Farquharson, and X. Hu, 2018, A finite-element time-domain forward solver for electromagnetic methods with complex-shaped loop sources: GEOPHYSICS, **83**, E117–E132.

Lu, X., C. G. Farquharson, J.-M. Miehé, and G. Harrison, 2021, 3D electromagnetic modeling of graphitic faults in the Athabasca Basin using a finite-volume time-domain approach with unstructured grids: GEOPHYSICS, **86**, B349–B367.

Malo-Lalande, C., M. Boisvert, E. Adam, and C. Grondin, Feburary 2020, Exploring for Magmatic Ni-Cu-PGE Ore Bodies with Magnetics, Electromagnetics and Reflection Seismic in a Challenging Geological Setting in Nunavik, QC: CSEG Recorder, **45**, 1–18.

Si, H., 2015, TetGen, a Delaunay-Based Quality Tetrahedral Mesh Generator: ACM Transactions on Mathematical Software, **41**, 1–36.

Yang, D., D. Fournier, S. Kang, and D. W. Oldenburg, 2019, Deep mineral exploration using multi-scale electromagnetic geophysics: The Lalor massive sulphide deposit case study: Canadian Journal of Earth Sciences, **56**, 544–555.

Copper permalloys for fluxgate magnetometer sensors

B. Barry Narod[1], David M. Miles[2]
[1]University of British Columbia
[2]University of Iowa

SUMMARY

Fluxgate magnetometers are commonly used to provide high-fidelity vector magnetic field measurements. The magnetic noise of the measurement is typically dominated by that intrinsic to a ferromagnetic core used to modulate (gate) the local field as part of the fluxgate sensing mechanism. A polycrystalline molybdenum-nickel-iron alloy (6.0–81.3 Mo Permalloy) has been used in fluxgates since the 1970s for its low magnetic noise. Guided by previous investigations of high permeability copper-nickel-iron alloys, we investigate alternative materials for fluxgate sensing by examining the magnetic properties and fluxgate performance of that permalloy regime in the range 28–45 % Cu by weight. Optimizing the alloy constituents within this regime enables us to create fluxgate cores with both lower noise and lower power consumption than equivalent cores based on the traditional molybdenum alloy. Racetrack geometry cores using six layers of ~30 mm long foil washers consistently yield magnetic noise around 4–5 pT/√Hz at 1 Hz and 6–7 pT/√Hz at 0.1 Hz meeting the 2012 1-second INTERMAGNET standard of less than 10 pT/√Hz noise at 0.1 Hz.

Keywords: fluxgate, magnetometer, copper-permalloy,

INTRODUCTION

In December 2007 one of us (Narod) rediscovered a paper by von Auwers and Neumann (1935), titled in English "On Iron- Nickel-Copper Alloys of High Initial Permeability," and this eventually set into motion our examination of copper permalloys as potentially useful materials for fluxgate magnetometer sensors. Specifically, we are interested in copper permalloy's potential to simultaneously provide low magnetic noise and low power consumption in a fluxgate sensing application. With the assistance of colleagues at Zentralanstalt für Meteorologie und Geodynamik [ZAMG, now Geosphere Austria] we had located a loose paper copy in a box of collected papers, situated in the library of the Austrian Academy of Sciences in Vienna, a collection which conveniently for us had been catalogued by their librarians. This paper was last cited in 1961 (Puzei, 1961), and had disappeared from living memory. A single citation of it in Bozorth (1951) had caused us to spend several years searching for it. The collection of copper permalloy data included in von Auwers and Neumann (1935), extraordinary in both quantity and quality, are reproduced in translation:

https://egusphere.copernicus.org/preprints/2023/egusphere-2023-2191/

THE CASE FOR COPPER PERMALLOYS

Miles et al., (2022) presented along with 6%Mo permalloy our first trial of a copper permalloy. This alloy consisted of 28% copper, 62% nickel and balance iron, which we designate 28Cu62Ni. The case for 28Cu62Ni went as follows:
We knew that 6%Mo permalloy has several properties that are thought advantageous for fluxgate sensor materials. These are 1) minimum magnetocrystalline anisotropy, 2) minimum bulk magnetoelastic anisotropy, 3) minimum saturation magnetization of all such materials satisfying 1) and 2), and 4) a requirement for slow cooling during heat treatment, to minimize residual stress (Pfeifer, 1966; English and Chin, 1967; Pfeifer and Boll, 1969). These papers all placed the zero-crossings satisfying 1) and 2) over a range of compositions including 4-6% molybdenum. But from their Figures 6%Mo uniquely also satisfied both 3) and 4), and these papers' Figures ultimately drove the choice to use 6%Mo in a new generation of fluxgate magnetometers.

Our first trial with a copper fluxgate sensor made from 28Cu62Ni (Miles et al., 2022) produced performance results comparable to a nominally identical sensor made from 6%Mo permalloy, and for some parameters such as power consumption the 28Cu62Ni alloy sensor outperformed. The success of our initial copper alloy trial encouraged us to expand our investigations of

copper permalloys, seeking more resolution in composition and extending our fluxgate sensor builds to alloys with much higher copper contents. It is well known that lower $\boldsymbol{B}_{sat}$ leads to improved noise performance.

The choices for our alloy compositions were guided by von Auwers and Neumann (1935). For the copper contents we selected the range 28-45%Cu. For our minimum copper-content alloys we chose 28%Cu with about 60%Ni. This coincided with the maximum initial permeability measured by von Auwers and Neumann (1935). This collection included 52 specimens, with the composition range plotted in Fig. 1.

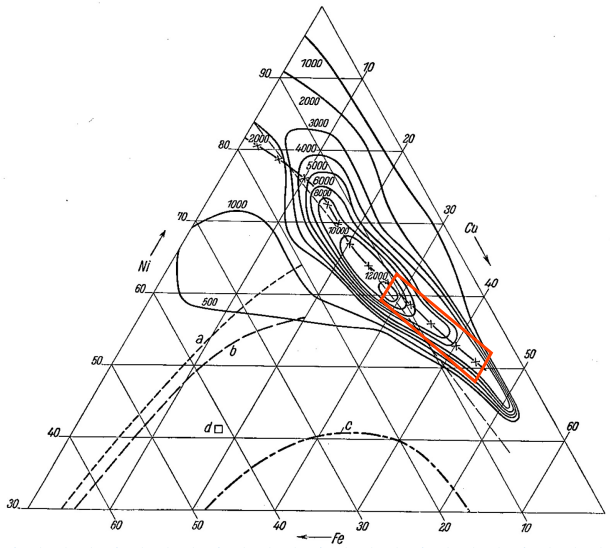

Figure 1. The range of copper-permalloy compositions in our study, outlined in red and superimposed on von Auwers and Neumann (1935) Fig. 8.

DISCUSSION

We measured DC resistivity, saturation induction, initial permeability, DC coercivity on fifty of our alloy specimens. Four of our specimens were further tested for Curie temperatures and were built into racetrack fluxgate sensors for further performance testing. Noise and power consumption results are presented in Fig. 2.

All our magnetic properties data with discussions, and a discussion of a century of history of copper permalloys, are now published as a research paper:

https://egusphere.copernicus.org/preprints/2023/egusphere-2023-2191/

The reader is directed to this publication.

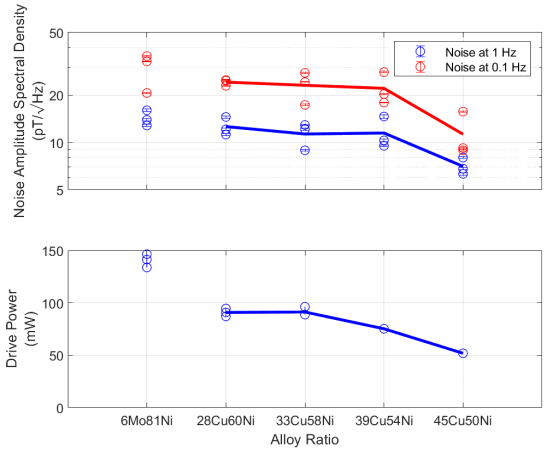

Figure 2. Fluxgate noise PSD and power consumption for five alloys.

We expected that as we increased copper content both power consumption and noise PSD would be reduced, the former from the lower field strength needed for saturation and the latter due to the well-known relation between saturation and noise PSD. These relations were both confirmed. What we did not know in advance was how hypothetical poorer magnetic anisotropy levels might impact the measured magnetic properties and noise levels. Narod (2014) predicted that such impacts should vary only slowly with anisotropy and our data confirm that. By far the biggest impact magnetic properties have on sensor noise performance is that of saturation induction.

CONCLUSION

Our investigation of the 28-45% copper permalloy regime's magnetic properties has led us to alloys which have yielded fluxgate sensors with noise PSD and power consumption improvements over those of the legacy 6Mo81.3Ni permalloy composition. Racetrack sensors of our lowest noise and power alloy, 45Cu50Ni, have noise PSD levels well below 10pT/√Hz at both 1.0Hz and 0.10Hz, easily satisfying the 1-second INTERMAGNET requirement (Turbitt, 2014).

Our first alloy selected for further sensor testing, 43Cu52Ni, shares its 100C T_c with our lowest noise alloy, 45Cu50Ni, but has much higher initial permeability. Many uses for low noise magnetic sensors require long durations of data collection, and sensor stability, over both time and temperature is an issue. Our future investigations must address these properties.

Our present results have relied heavily on the existence of the data presented by von Auwers and Neumann (1935), but no such comprehensive examination of

molybdenum permalloys was ever undertaken. There may yet be room for improvement of molybdenum permalloys in fluxgate sensors, with molybdenum content higher than that of the legacy 6% materials. In our future work we plan to investigate these alloys.

The performance of these new alloys is expected to enable further miniaturization of the fluxgate sensor while preserving geophysically useful magnetic sensing performance.

ACKNOWLEDGMENTS

That authors wish to thank Christian Hansen, Andrew Schmitt, Matt Miller, and Toby Tompkins for their work manufacturing and machining the permalloy samples, Tino Smith for his work assembling the fluxgate cores, and John Bennest for his work characterising $\boldsymbol{B/H}$ loops. This research has been supported by the National Aeronautics and Space Administration (grants no. 80NSSC19K0491 and 80GSFC18C0008).

REFERENCES

von Auwers, O. and Neumann, H. (1935) Über Eisen–Nickel–Kupfer-Legierungen hoher Anfangspermeabilität. In *Spec. Print. Sci. Publ. Siemens-Fact*., Julius Springer, XIV, 92–108.

Puzei, I. M. (1961) The Influence of Cu, Si, Cr and Mo on the Magnetic Anisotropy and Saturation Induction of Ni-Fe Monocrystals. In *The Physics of Metals and Metallogaphy*, 12, 136-138 (Fiz Metal. Metalloved, 12, 3, 453-455).

Bozorth, R. M.: Ferromagnetism, in facsimile, edited by: Perkins, W., IEEE Press, Piscataway, NJ, 1951 (1993 edition).

Miles, D. M., Dvorsky, R., Greene, K., Hansen, C. T., Narod, B. B., and Webb, M. D. (2022). Contributors to fluxgate magnetic noise in permalloy foils including a potential new copper alloy regime, In *Geosci. Instrum. Method. Data Syst*., 11, 111–126, https://doi.org/10.5194/gi-11-111-2022.

Pfeifer, F. (1966) Zum Verständnis der magnetischen Eigenschaften technischer Permalloylegierungen. In *Z. Metallkd*., 57, 295–300.

Pfeifer, F. and Boll, R. (1969) New soft magnetic alloys for applications in modern electrotechnics and electronics. In *IEEE T. Mag*., 5, 3, 365-370, https://doi.org/10.1109/TMAG.1969.1066595.

English, A. T. and Chin, G. Y. (1967) Metallurgy and magnetic properties control in permalloy. In *J. Appl. Phys*., 38, 1183–1187, https://doi.org/10.1063/1.1709532.

Narod, B. B. (2014) The origin of noise and magnetic hysteresis in crystalline permalloy ring-core fluxgate sensors. In *Geosci. Instrum. Method*. Data Syst., 3, 201–210, https://doi.org/10.5194/gi-3-201-2014.

Turbitt, C. (2014) INTERMAGNET Definitive One-Second Data Standard, INTERMAGNET Technical Note TN6, https://intermagnet.org/docs/technical/im_tn_06_v1_0.pdf.

Enhancing Subsurface Imaging in Mineral Exploration through Optimized large-scale Semi-Airborne Surveys: Synthetic Modelling and field Data

Saeed Nazari, Raphael Rochlitz, and Thomas Günther
Leibniz Institute for Applied Geophysics, Hannover, Germany
Correspondence: saeed.nazari@leibniz-liag.de

SUMMARY

This study investigates the optimization of Semi-Airborne Electromagnetic (SAEM) surveys for enhanced subsurface imaging in mineral exploration. Synthetic modelling and advanced inversion techniques are employed to analyse the impact of various survey parameters. The study emphasizes the advantages of multi-component inversion, optimal receiver spacing, transmitter length, and orientation for accurate target recovery. It highlights the utility of multi-transmitter systems in overcoming challenges posed by distortion and masking of anomalies. The study further explores real data utilization and the challenges of large-scale surveys. It presents an innovative approach of interpolating inversion results from smaller patches to create an initial model for large-scale inversion, enabling efficient processing of extensive survey data. The research contributes practical insights to refine SAEM surveys, offering an equilibrium between resolution and cost for enhanced mineral exploration.

Keywords: SAEM surveys, electromagnetic inversion, mineral exploration, large-scale inversion, Survey design.

INTRODUCTION

Semi-airborne electromagnetic (SAEM) surveys have gained prominence in mineral exploration due to their capability to rapidly cover extensive areas (Kearey et al. 2002, Dentith and Mudge. 2014). However, the efficient imaging of deep conductive targets remains a challenge in geophysical exploration (Chen and Sun. 2020, Ke et al. 2023). In this context, this abstract delves into the process of optimizing SAEM surveys by dissecting the impact of various survey parameters on subsurface imaging quality. The findings are aimed at refining the practical implementation of SAEM surveys to enhance mineral exploration (Nazari et al. 2023).

The division of extensive survey areas into distinct patches (single flight area that include a Transmitter is called a single patch) is introduced as a strategy, exemplified by survey zones in the Harz region that is known for its mineral deposits. The benefits of multi-patch inversion are discussed. To address the computational demands of large-scale surveys, the concept of interpolating inversion results into a larger mesh is proposed for more efficient large-scale inversions.

METHODS

Our investigation employs synthetic modelling and real data inversion techniques in tandem with advanced inversion methods. We solve the total-field formulation of the Maxwell equations based on finite element forward operator custEM (Rochlitz et al. 2023), and pyGIMLi (Rücker et al. 2017) with a conjugate gradient inverse solver (Günther et al. 2006).

This method uses ground-based transmitters and airborne magnetic field receivers. By simulating diverse survey scenarios, we systematically analyse the influence of different parameters on the accuracy of electromagnetic inversion results. Then importance of single and multi-patch inversion, in handling large-scale surveys with real data and synthetic examples discussed.

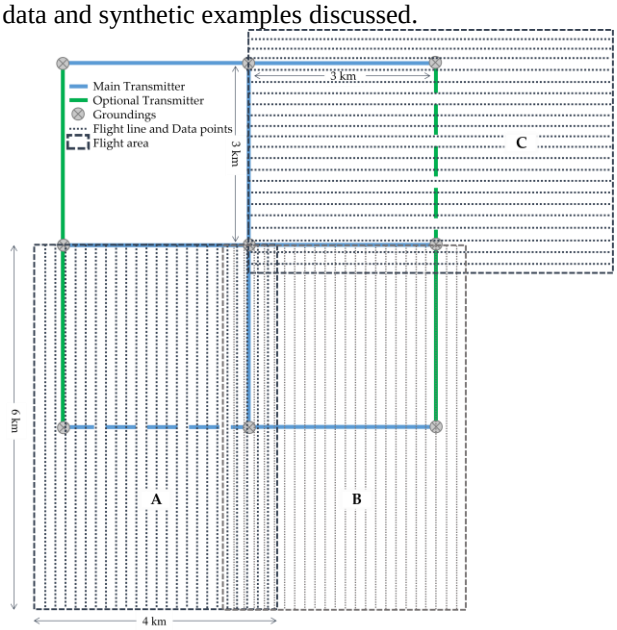

Figure 1: Recommended (Nazari et al. 2023) optimized survey layout (to be adapted to field conditions). The length of all transmitters and spacing between parallel transmitters was 3 km, using common groundings that reduced logistic effort. Three of the overlapping flight patches are given as examples (each covering an area of 24 km^2): (A) over the lower-left Tx (dashed blue), (B) over the lower-right Tx (solid blue), and (C) over the optional Tx (dashed green).

The simplest case in using real data is that we have only one transmitter (single patch) and several receiver points

like patch A in Figure 1. In this case, for example, one flight for a single transmitter can cover an area of 6 x 4 km. In single-patch mode, fine discretization can be used, which helps to separate anomalies. In this case, the number of data is small, and the covered area is small, which means that the inversion uses less resources.

Results of synthetic modeling

The study of Nazari et al. (2023) explores the effectiveness of various techniques in enhancing the accuracy and resolution of semi-airborne electromagnetic (SAEM) surveys for mineral exploration.

1. Multi-Component Inversion: three-component inversion improves accuracy and boundary recovery in the results over single component by enhanced resolution.
2. Receiver Spacing: The study in this case suggests a line spacing of 200 m with 100 m in-line spacing as a balanced trade-off between cost and resolution. This parameter more depends on target dimensions.
3. Transmitter length: Optimal recovery of targets within 3 km from the transmitter requires a transmitter length at least twice the target dimension.
4. Multiple Transmitters: The use of multiple transmitters is crucial for more complex structures. Single transmitters can distort results and mask subsequent bodies. Employing two transmitters on both sides of the target enhances resolution and depth accuracy (Figure 2). Parallel transmitters are more effective in areas with prior knowledge of strike, Figure 2 shows result of using 2 transmitters at both side and parallel to the target, in non-2D settings perpendicular are recommended.

The study's key findings emphasize optimizing SAEM surveys for efficient subsurface imaging in mineral exploration. Multi-component inversion, appropriate transmitter orientation, and geological considerations enhance survey resolution. The proposed survey layout (Figure 1) balances resolution and cost.

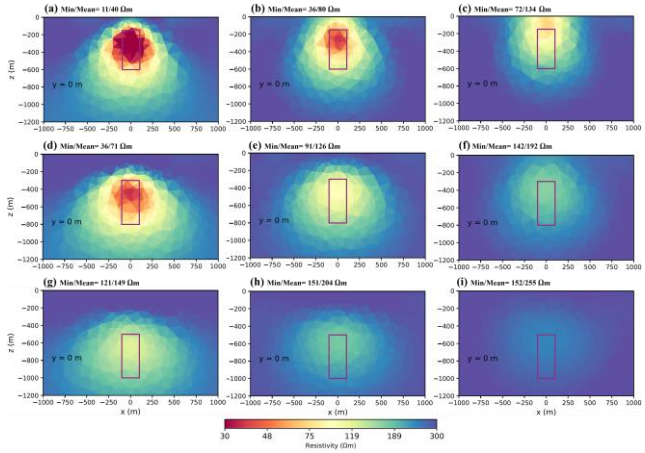

Figure 2: Inversion results for a body located at different depths: (a–c) 150 m; (d–f) 300 m; and (g–i) 500 m from the surface, and for different transmitter separation distances: (a,d,g) 2 km; (b,e,h) 3 km; and (c,f,i) 4 km.

Real Data Example

Figure 3 shows total of about 25 flight areas in Harz (central Germany), of which we focus on three patches in the Bad Grund area. For example, the result of the inversion (completed in 6 hours) of one of the transmitters shown in the Figure 4a/b.

After the data is obtained, it can be checked as a single patch first, but we saw that if more than one transmitter is used, the underground conductivity distribution can be obtained more accurately. For this purpose, the data from several transmitters (multi patches) must be entered into inversion. Figure 4 shows the result for all three white flight areas. In this case, an area of 30 km² has been covered. However, this is more time-consuming, in this case more than 75 hours. As the number of patches increases, even more time is required, as well as more processing resources that easily go beyond computers clusters. In Figure 4, we present the results of single and multi-transmitter Inversions. In subfigures a and b that are outcome of single transmitter inversion (Tx2), we observe a conductive body labelled as "M" on the left side of the image at depth 550 meters below sea level (mbsl). The resolution for this body is notably high, providing a clear and detailed representation. On the right side of subfigures a and b, we encounter a conductive area labelled as "N." This area starts from the 0 mbsl and extends to a significant depth about 1000 mbsl. However, the resolution for "N" is notably poor, particularly as it descends deeper into the subsurface. As discussed earlier, enhancing resolution is of paramount importance in geophysical surveys. One of the most effective strategies to achieve this is to employ multiple transmitters. Subfigures c and d, located on the right side, illustrate the substantial improvement in resolution achieved through the use of multiple transmitters. The poorly resolved conductive area "N" on the right side in the single-transmitter mode becomes highly resolved with multiple transmitters. This enhanced resolution extends to a depth of 1000 mbsl. Additionally, the resolution of conductive body "M" also experiences a noticeable enhancement, although to a lesser degree. In the multi-transmitter mode in the "O" area, a previously unseen conductive area comes to light. This new discovery was concealed in the single-transmitter mode, showcasing the significance of using multiple transmitters in subsurface exploration.

Single patches showed in Figure 3, cover about 300 square kilometres. An idea that can be used to avoid this problem is the case that

1. the inversion is performed as a single patch,
2. the results of these single patches are interpolated to a mesh that includes all the areas with larger cell sizes and combined by using a coverage-weighted mean of all patches,

3. The latter is used as the input of the Large-scale inversion.

We show this process here with a synthetic example. We consider a simple model that consists of a thin dipping plate along with the background. We survey this area using two different patches (Figure 5a and b). Then we enter each of these single patches separately into inversion. Then we interpolate the inversion result into a larger mesh that includes all areas as Figure 5d shows. Now we consider this larger mesh as the initial model for large-scale inversion.

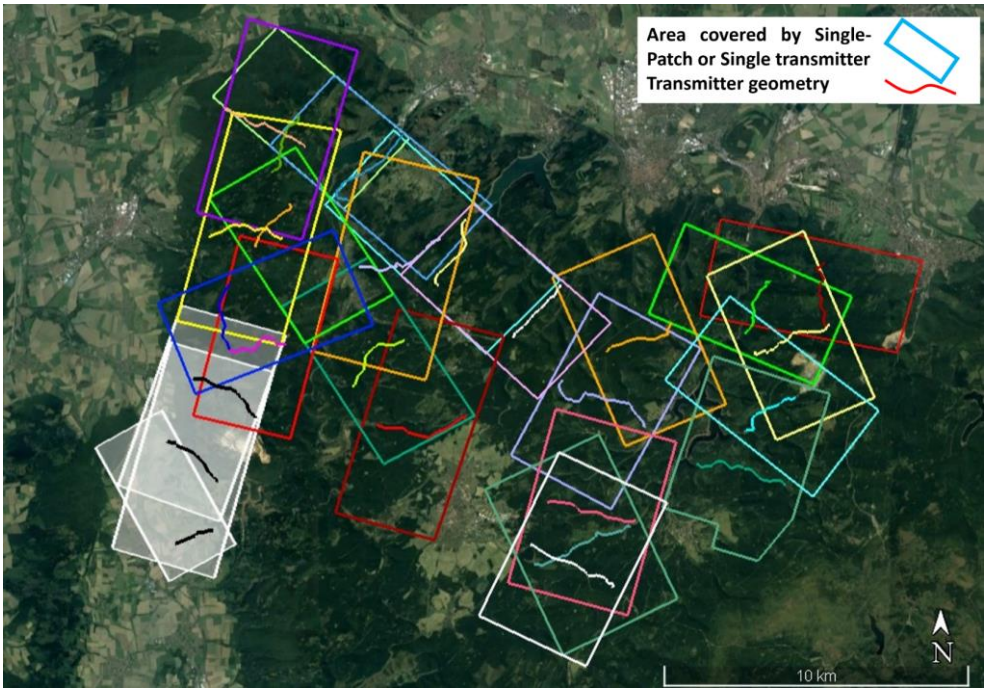

Figure 3: Survey areas (patches) in Harz region Germany. White areas with Black transmitters are patches used in Fig.4

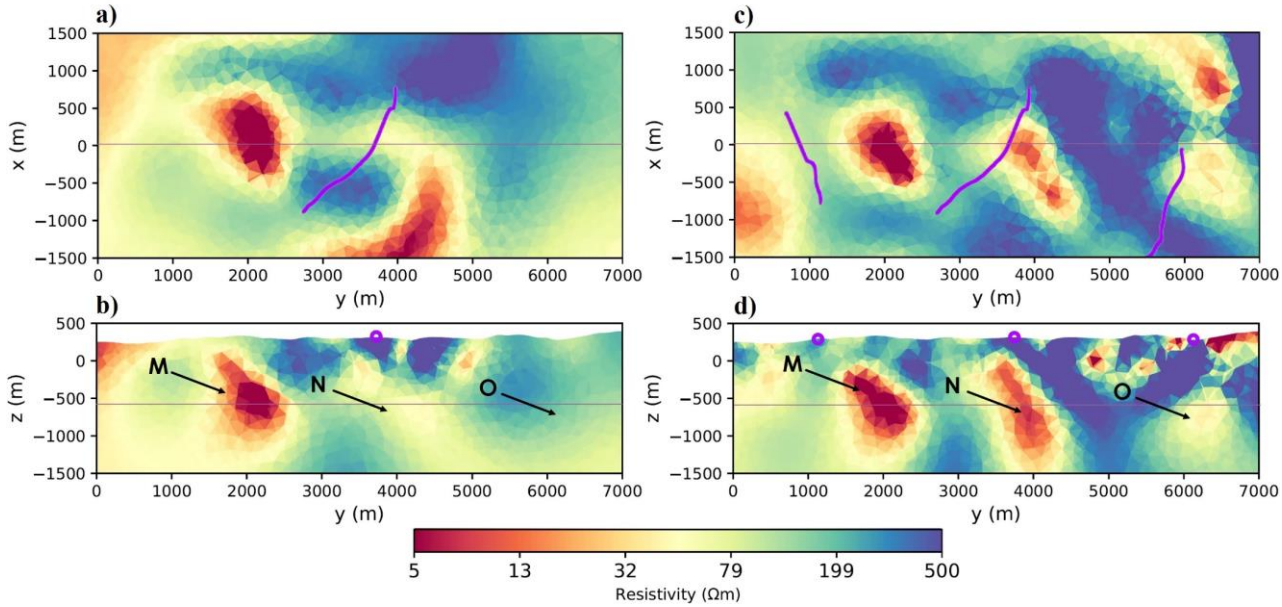

Figure 4: Left: Inversion result for single Tx2 (middle one in Fig. 3). (a) Z-plane view 550 mbsl, (b) X-plane view. **Right:** Multi-patch inversion result using three transmitters. (c) Z-plane view 550 mbsl, (d) X-plane view. The thin lines show the location of the corresponding slice. Purple lines and circles are the transmitters.

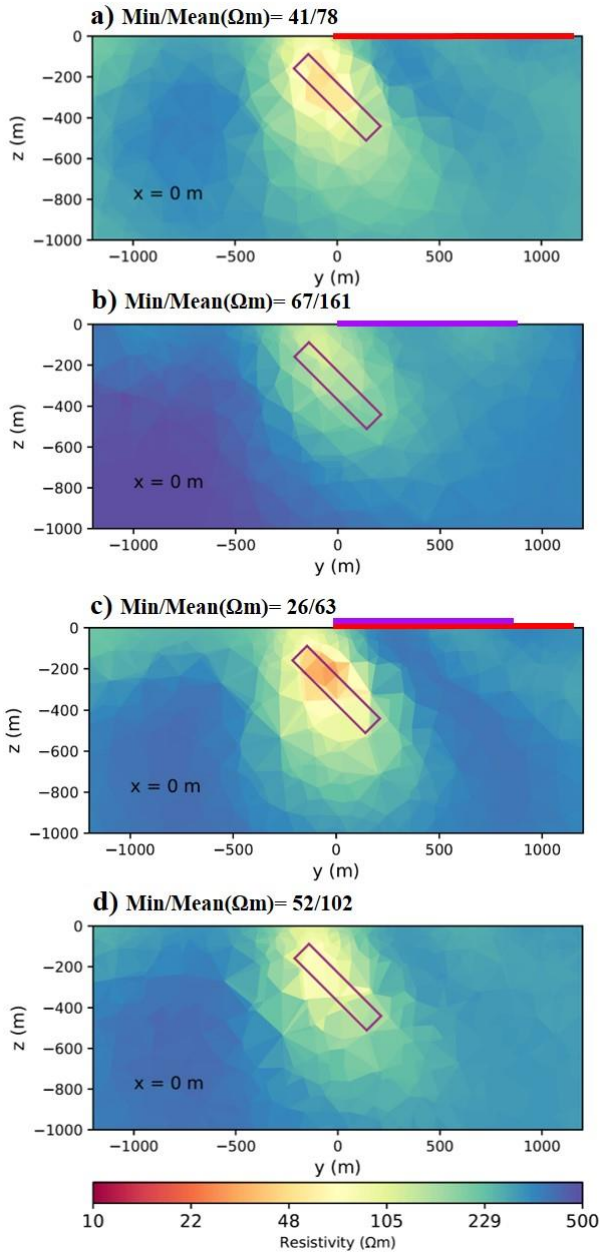

Figure 5: a) Single-patch inversion result of Tx1 or red line. b) Single-patch inversion result of Tx2 or purple line. c) Multi-Patch inversion result for Tx1 and Tx2 d) Both Inversion results of Tx1 and 2 are interpolated into this larger mesh.

DISCUSSION

Large-scale inversions offer several advantages over single-patch inversions in geophysical exploration and modelling. Based on what we showed in figures 2, 4 and, 5 these advantages are:

1.Improved resolution: Large-scale inversions can incorporate data from a broader area, resulting in enhanced resolution and accuracy of subsurface structures. By considering data from multiple patches or flight lines, the overall picture becomes more comprehensive, allowing for better identification and characterization of geological features.

2. Reduction of artifacts: Single-patch inversions might suffer from artifacts or anomalies caused by the limited coverage of the survey area or the transmitter itself. Large-scale inversions can mitigate these issues by providing a more data points.

3. Geological Complexity: Geological settings are often complex, and features can extend beyond the boundaries of a single patch. Large-scale inversions can account for the continuity and connectivity of geological structures that span across multiple patches. This is particularly important in scenarios where important features might be missed in isolated inversions.

4. Enhanced Interpretation: Combining data from different patches allows for a more holistic interpretation of the subsurface. Geological structures can be better correlated and understood when viewed in the context of a larger area, leading to more accurate and insightful geological models.

5. Improved Anomaly Detection: Large-scale inversions can help identify subtle anomalies that might not be evident in smaller-scale inversions. By analysing anomalies over a larger area, patterns and correlations can emerge that provide valuable insights into the distribution of subsurface materials.

6. Better Depth resolution: Inversions performed over a larger area can provide improved depth Resolution, allowing for the imaging of deeper geological features. This is particularly important in cases where valuable mineral deposits or other geological structures are located at significant depths.

In summary, large-scale inversions offer a more comprehensive and accurate representation of the subsurface compared to single-patch inversions. They are particularly valuable in complex geological environments where features extend beyond the boundaries of a single survey patch. The ability to integrate data from a different area leads to improved resolution.

CONCLUSION

The investigation outlined in the abstract demonstrates a comprehensive approach to optimizing SAEM surveys for improved subsurface imaging in mineral exploration contexts. By leveraging synthetic modelling and advanced inversion methodologies, the study underscores the significance of several critical factors in survey design. Multi-component inversion emerges as a strategy to enhance resolution and accuracy, particularly in scenarios with complex geological settings. The study also delves into the complexities of real data utilization and the challenges of conducting large-scale surveys. The proposed approach of interpolating inversion results from smaller patches to facilitate large-scale inversion is the first step solution to address computational limitations while still maintaining modelling accuracy.

ACKNOWLEDGMENTS

The authors express gratitude for the support and resources provided by LIAG and all people participated in the field work and processing, which enabled the execution of this study.

REFERENCES

1. Chen, C.; Sun, H. Characteristic analysis and optimal survey area definition for semi-airborne transient electromagnetics. *J. Appl. Geophys. 180*, 104134, 2020.. https://doi.org/10.1016/j.jappgeo.2020.104134.
2. Dentith, M.; Mudge, S.T. *Geophysics for the Mineral Exploration Geoscientist*; Cambridge University Press: Cambridge, 2014.
3. Günther, T.; Rücker, C.; Spitzer, K. Three-dimensional modelling and inversion of DC resistivity data incorporating topography—II. Inversion. *Geophys. J. Int*, *166*, 506–517, 2006. https://doi.org/10.1111/j.1365-246X.2006.03011.x.
4. Ke, Z.; Liu, Y.; Su, Y.; Wang, L.; Zhang, B.; Ren, X.; Ma, X. Three-Dimensional Inversion of Multi-Component Semi-Airborne Electromagnetic Data in an Undulating Terrain for Mineral Exploration. *Minerals*, *13*, 230, 2023. https://doi.org/10.3390/min13020230.
5. Kearey, P.; Brooks, M.; Hill, I. *An Introduction to Geophysical Exploration*; John Wiley & Sons: Hoboken, NJ, USA, 2002.
6. Nazari, S.; Rochlitz, R.; Günther, T. Optimizing Semi-Airborne Electromagnetic Survey Design for Mineral Exploration. *Minerals*, *13*, 796, 2023. https://doi.org/10.3390/min13060796
7. Rochlitz, R.; Becken, M.; Günther, T. Three-dimensional inversion of semi-airborne electromagnetic data with a second-order finite-element forward solver. *Geophys. J. Int*, *234*, 528–545, 2023. https://doi.org/10.1093/gji/ggad056.
8. Rücker, C.; Günther, T.; Wagner, F.M. pyGIMLi: An open-source library for modelling and inversion in geophysics. *Comput. Geosci*, *109*, 106–123, 2017. https://doi.org/10.1016/j.cageo.2017.07.011.

7th International Symposium on Three-Dimensional Electromagnetics
Vancouver, BC, Canada, November 13–15, 2023

UAV-based semi-airborne CSEM for mineral exploration - 3D joint inversion of scalar and vector magnetometer data

Raphael Rochlitz[1], Philipp Kotowski[2], Thomas Günther[1] and Michael Becken[2]
[1]Leibniz Institute for Applied Geophysics, LIAG, Hanover, Germany
[2]University of Münster, WWU, Münster, Germany

Summary

We performed drone-based semi-airborne electromagnetic (EM) measurements in an active mining area in the Eastern part of the Iberian pyrite belt, Spain. The area is poorly accessible and features rough terrain with height undulations up to 400 m. Using drones as carrier for magnetic field receivers offered areal accessibility as a cost-effective alternative to helicopter-towed EM systems with simplified logistics. We analyzed data in two overlapping frequency ranges, 1-128 Hz and 30-1024 Hz, recorded with a scalar and a vector magnetic field receiver, respectively. We added capabilities to invert both data sets jointly with the open-source 3D inversion tools custEM/pyGIMLi and discuss the results using this procedure compared to single-dataset inversion.

Keywords: Controlled-source, Electromagnetic Theory, Semi-airborne, 3D inversion, UAV

Introduction

Within the last decades, electromagnetic geophysical methods were continuously developed and have shown to be indispensable for the exploration of mineral deposits, hydrocarbon reservoirs, groundwater or geothermal resources, and others. Amongst them, semi-airborne electromagnetic (EM) surveys have recently received renewed interest. They combine the advantages of fast data collection using airborne receivers (Rx) and strong signals emitted by ground-based transmitters (Tx). For instance, Mogi et al. (2009) show that penetration depths of several hundreds down to 1000 meters can be reached with such setups while covering multiple square-kilometers of area.

Becken et al. (2020) presents the DESMEX system analyzing the recorded EM data in the frequency domain. Meanwhile, the rapid development of UAVs (Figure 1) as carriers for geophysical equipment allowed a transition from helicopter-towed Rx to UAV-towed Rx with significantly reduced costs and simpler logistics. In the most recent years, working groups around the globe developed different controlled-source EM systems (Q. Wu et al., 2019; Vilhelmsen & Døssing, 2022; Bastani & Joahansson, 2022; J. Wu et al., 2023). Becken et al. (2022) present a new measurement system for mineral exploration using a scalar optically pumped magnetometer (*MagArrow*). We performed a second survey with an equivalent setup in cooperation with Sandfire MATSA in the active mining area of the Eastern Iberian pyrite belt, Spain and used in addition a second vector magnetic field receiver introduced by Kotowski et al. (2022), the *SHFT* sensor. We refer to the scalar and vector sensors as SM and VM.

The two different receivers complement each other well being sensitive below 256 Hz (SM) and above 32 Hz (VM). For the inversion of the data, we extended the 3D open-source inversion tools based on custEM and pyGIMLi to allow on the one hand, the handling of CSEM data recorded with a SM and on the other hand, the joint inversion of multiple EM data sets. In this work, we present and discuss the inversion results of the aforementioned semi-airborne data set.

Figure 1: UAV with SHFT sensor attached in survey area north of Huelva, Spain.

Methodology

We process the data following the procedures described by Becken et al. (2020, 2022). The inversion procedure builds mainly upon the methodology presented by Grayver et al. (2013), whereat we use a finite-element discretization on unstructured tetrahedral meshes and a total electric field formulation to calculate the EM responses and corresponding sensitivities with custEM (Rochlitz et al., 2023). In this paper, we describe in detail the methodology for inverting arbitrary three-component CSEM data with a Gauss-Newton minimization approach, implemented in pyGIMLi (Rücker et al., 2017). We minimize the objective function

$$\Phi = \|\mathbf{W}_d(\mathbf{d}-\mathbf{f}(\mathbf{m}))\|_2^2 + \lambda\|\mathbf{W}_m\mathbf{m}\|_2^2 \rightarrow \min\ . \quad (1)$$

with the error-weighting matrix $\mathbf{W}_d$, data vector $\mathbf{d}$, forward response $\mathbf{f}(\mathbf{m})$, regularization parameter λ, and smoothness operator $\mathbf{W}_m$. To solve the minimization problem iteratively, we begin from a starting model $\mathbf{m}^0$, and update the next model $\mathbf{m}^{k+1} = \mathbf{m}^k + \tau^k\Delta\mathbf{m}^k$ with the model update $\Delta\mathbf{m}^k$ that is obtained from solving the inverse sub-problem

$$\begin{aligned}(\mathbf{J}^T\mathbf{W}_d^T\mathbf{W}_d\mathbf{J} + \lambda\mathbf{W}_m^T\mathbf{W}_m)\Delta\mathbf{m}^k = \\ \mathbf{J}^T\mathbf{W}_m^T\mathbf{W}_m(\mathbf{d}-\mathbf{f}(\mathbf{m}^k)) - \lambda\mathbf{W}_m\mathbf{W}_m^T\mathbf{m}^k \quad (2)\end{aligned}$$

with the sensitivity matrix $\mathbf{J}$. The step length τ^k is determined by an inexact line-search procedure that searches by linear interpolation (Günther et al., 2006).

We can use the procedure primarily developed for helicopter-based semi-airborne CSEM data directly for inverting also the UAV-based induction-coil receiver data. The 3D inversion of SM data relies on the technique described by Becken et al. (2022) for 2.5D inversion. The measured EM signal vector B superposes on the main field but leaves its direction nearly unchanged (Figure 2a). They calculate in each iteration the field component and corresponding sensitivity for a receiver-component oriented in the direction of the Earth's magnetic field (taken from the IGRF model), which requires the calculation of all three magentic field components (Figure 2b). Since the survey geometry and inversion domain discretized in the tetrahedral mesh are rotational invariant, we first rotate the complete modeling domain including Rx and Tx locations by respecting the local IGRF declination and inclination angles to align the new z' axis with the geomagnetic main field vector (Figure 2c). Now, it is only necessary to calculate the z' magnetic field component and sensitivity in each iteration, which corresponds to the field recorded by the SM. Thereby, we require only one instead of three expensive sensitivity calculations for each receiver compared to the original procedure.

For all single and joint inversions, we decided to use an identical mesh to calculate the responses for the induction coil data in the earth-fixed coordinate system and for the SM data in the rotated system as described above. This procedure avoids additional interpolation steps and related errors and enables the comparison of data coverages. Methods for jointly inverting multiple EM data sets were presented by several authors (Mackie et al., 2007; Commer & Newman, 2009; Abubakar et al., 2011). Due to the similarity of the two data sets and comparable data quality, we simply stacked together the data vectors $\mathbf{d}$ in the objective function in this work. Correspondingly, the sensitivity matrices $\mathbf{J}$ of both data sets were stacked. All data points are weighted with their corresponding errors.

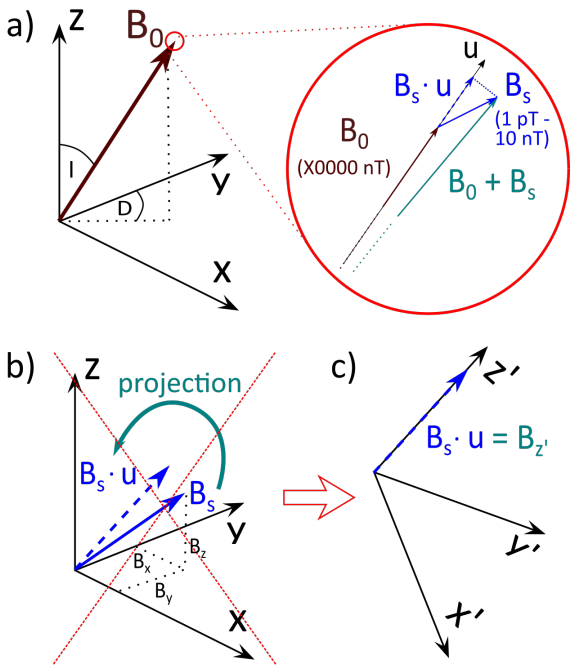

Figure 2: a) Geomagnetic field $\mathbf{B}_0$ described by declination $\mathbf{D}$ and inclination $\mathbf{I}$. The magnitude of the vector sum $|\mathbf{B}_0 + \mathbf{B}_s|$, with $\mathbf{B}_s$ denoting the secondary magnetic field originating from the active Tx, is approximated by its projection onto the main field, $|\mathbf{B}_0| + |\mathbf{B}_s \cdot u|$,
b) Calculating response in Cartesian coordinates and project afterwards,
c) Calculate response for $B_{z'}$ component aligned to geomagnetic field direction in a correspondingly rotated mesh; figure modified afterBecken et al. (2022).

Results

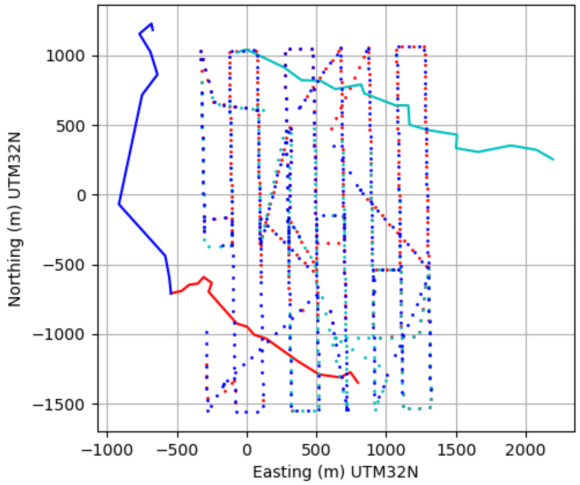

Figure 3: Tx (lines) and Rx positions (dots) of the six overlapping flight area, the Rx colors match the corresponding Tx.

In total, we covered a common measurement area of approximately 1.6 km × 2.6 km. Within all six flight areas, we recorded scalar as well as vector data for three different Tx (Figure 3), using a 100 % duty cycle signal with base frequencies of 1 Hz and 32 Hz. Figure 4 provides an example of processed data. Here, we illustrate the real and imaginary parts of the vertical transfer function of the VM data at 256 Hz. The good consistency of the data holds in general. Nevertheless, the horizontal components of the VM data contain segments of poor data quality which are related to locations of sign reversals. Here, we added relative errors of 5 % to an absolute noise floor of 2 pT/A for both Rx types and excludes data points with more than 100% relative error afterwards. With this procedure we eliminated data within the noise level from the inversion. With $\Re$ and $\Im$ parts, in total 20 k data points were used for the joint inversion.

We performed multiple inversion runs for both, the individual data sets and jointly, to optimize the mesh and regularization parameters. In the final version, we use a tetrahedral mesh with comparatively small triangles (max. 400 m^2) at the surface to adequately represent the rough topography and a volume constraint of 500,000 m^3 to allow smaller conductors to evolve. This setup results in 236 k cells (model parameters). The regularization parameter λ was 1, decreasing by a factor of 0.8 in each iteration. The 3D view of the final inversion results in Figure 5 shows overall alternating conductive and resistive structure which follow the regional geological strike direction.

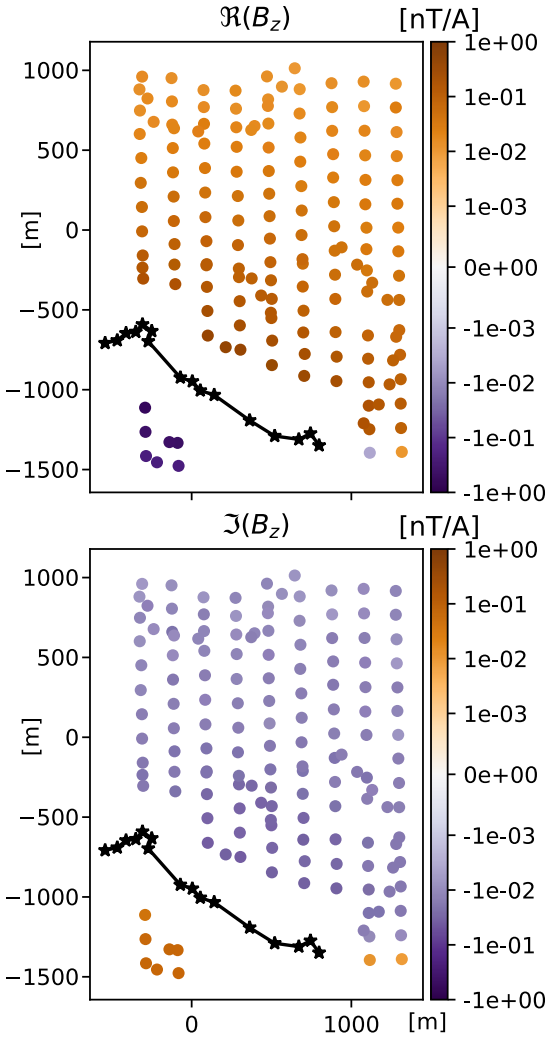

Figure 4: Data example: Vertical component of VM @256 Hz for Tx1.

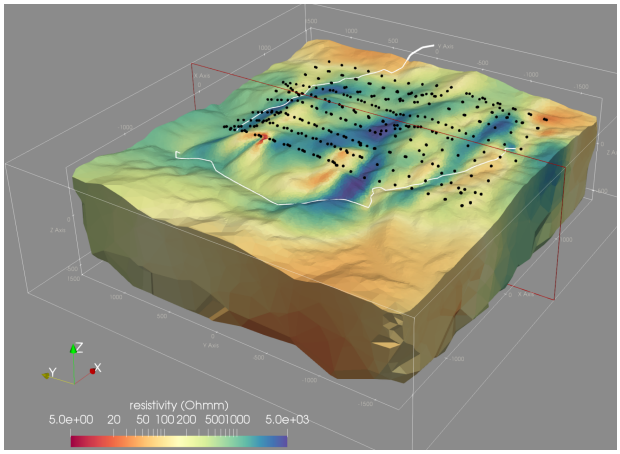

Figure 5: 3D view of joint inversion result, white lines at surface: Tx, black dots: Rx, frame refers to the location of the slice in Figure 6.

The joint inversion converged from a χ^2 value of 21 down to 1.2. The individual runs of SM and VM data resulted in final χ^2 of 1.08 and 1.22, respectively. Figure 6 presents the recovered resistivity model along a slice perpendicular to the strike direction through the center of the 3D model. In this visualization, we used a coverage threshold (scaled by cell sizes and model parameters) of 1e-5 to avoid displaying features which are most likely effects of the regularization rather than covered by data.

The results indicate four individual and comparatively small conductive structures at different depths from the surface down to maximum 1 km. By analyzing more slice towards East and West, it becomes evident that the recovered conductors match well with the regional geological strike direction. The model recovered from the VM data only exhibits great similarities with the joint inversion. Inverting only the SM data at lower frequencies leads to a generally similar result, but with smoother contrasts. In addition, we observe that the two individual conductors at around y=1000 m in Figure 6 are merged to a single anomaly, indicating a higher equivalence.

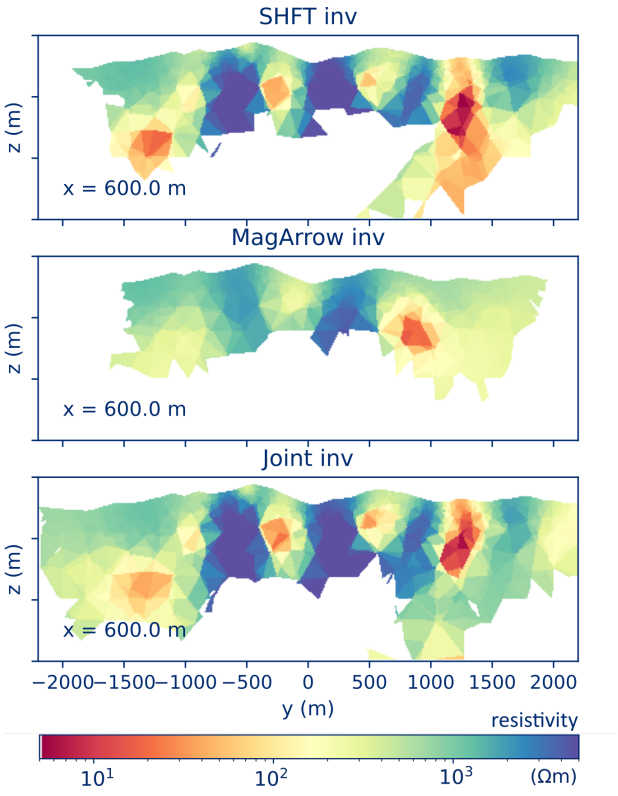

Figure 6: Cross section through inversion results, top: three-component VM data only, center: SM data only, bottom: joint inversion of both data sets; only cells with a scaled coverage of >1e-5 are displayed.

Discussion

The SM data yield a lower coverage compared to VM data, even though lower frequencies are accessed. We attribute the smaller coverage of the individual SM data inversion and the dominance of the VM data in the joint inversion to the different amount of data used (1 vs. 3 independent observations at each Rx position and Tx). It would be possible to increase the influence of the SM data artificially by using a higher weighting factor, but we don't see any physical justification for such a modification. Instead, we are confident that robust data error estimates for our SM and VM data (and any other Rx sensors in general) calculated during the processing are the best option to weight our data sets and points properly. The development of such error estimates is work in progress. Even though not presented here, the fit of the final SM response for the individual and joint inversion is almost identical. This observation, the lower coverage of the SM and generally smoother inversion results indicates a higher model equivalence compared to the VM. It is to discussion if doubling the measurement time with two receiver systems is worth the efforts considering the limited contribution of the SM to the final recovered resistivity distribution. However, we present only a single case here and other targets could lead to different observations.

Conclusion

We performed UAV-based semi-airborne electromagnetic measurements in a mostly inaccessible active mining area. The VM data recorded was more suited to resolve the conductivity structure in detail down to more than 500 m depth using three-component data with frequencies between 32 and 756 Hz. The SM data with a good signal quality between 1 and 64 Hz showed in general similar capabilities to recover the subsurface resistivity structure, but with less resolution. The joint inversion results were dominated by the VM data. Against expectations due to the lower frequencies involved, we did not observe deep structures only recovered with the SM data in this study area. However, only by adding these data it was possible to recover the bottom of a deep conductor using joint inversion. Using both receiver types and performing a joint inversion can effectively increase the model robustness and support the interpretation of conductive targets in mineral exploration and beyond. The development of novel vector magnetic field sensors sensitive at low frequencies in combination with an adequate motion noise compensation could significantly contribute to enhance the presented measurement concept.

Acknowledgments

We thank the colleagues from DMT and Sandfire MATSA for the allowing us to survey in an active mining area and the great support during field work. We acknowledge all colleagues from LIAG and the University of Münster participating in the field work for their contributions during the challenging data acquisition. The work was funded as part of the DESMEX II project by the Germany Ministry for Education and Research (BMBF) in the framework of the research and development program Fona-r4 under grant 033R130DN.

REFERENCES

Abubakar, A., Li, M., Pan, G., Liu, J., & Habashy, T. (2011). Joint mt and csem data inversion using a multiplicative cost function approach. *Geophysics*, *76*(3), F203–F214.

Bastani, M., & Joahansson, H. (2022). A new data acquisition system for uav-borne vlf-lf measurements. two case studies in sweden. In *Nsg2022 3rd conference on airborne, drone and robotic geophysics* (Vol. 2022, pp. 1–5).

Becken, M., Kotowski, P. O., Schmalzl, J., Symons, G., & Brauch, K. (2022). Semi-airborne electromagnetic exploration using a scalar magnetometer suspended below a multicopter. *First Break*, *40*(8), 37–46.

Becken, M., Nittinger, C. G., Smirnova, M., Steuer, A., Martin, T., Petersen, H., et al. (2020). Desmex: A novel system development for semi-airborne electromagnetic exploration. *Geophysics*, *85*(6), E253–E267.

Commer, M., & Newman, G. A. (2009). Three-dimensional controlled-source electromagnetic and magnetotelluric joint inversion. *Geophysical Journal International*, *178*(3), 1305–1316.

Grayver, A. V., Streich, R., & Ritter, O. (2013). Three-dimensional parallel distributed inversion of csem data using a direct forward solver. *Geophysical Journal International*, *193*(3), 1432–1446.

Günther, T., Rücker, C., & Spitzer, K. (2006). Three-dimensional modelling and inversion of DC resistivity data incorporating topography – II. Inversion. *Geophysical Journal International*, *166*(2), 506-517.

Kotowski, P. O., Becken, M., Thiede, A., Schmidt, V., Schmalzl, J., Ueding, S., et al. (2022). Evaluation of a semi-airborne electromagnetic survey based on a multicopter aircraft system. *Geosciences*, *12*(1), 26.

Mackie, R., Watts, M. D., & Rodi, W. (2007). Joint 3d inversion of marine csem and mt data. In *Seg international exposition and annual meeting* (pp. SEG–2007).

Mogi, T., Kusunoki, K., Kaieda, H., Ito, H., Jomori, A., Jomori, N., et al. (2009). Grounded electrical-source airborne transient electromagnetic (GREATEM) survey of Mount Bandai, north-eastern Japan. *Exploration Geophysics*, *40*(1), 1–7.

Rochlitz, R., Becken, M., & Günther, T. (2023). Three-dimensional inversion of semi-airborne electromagnetic data with a second-order finite-element forward solver. *Geophysical Journal International*, *234*(1), 528–545.

Rücker, C., Günther, T., & Wagner, F. (2017). pyGIMLi: An open-source library for modelling and inversion in geophysics. *Computers & Geosciences*, *109*, 106–123.

Vilhelmsen, T. B., & Døssing, A. (2022). Drone-towed controlled-source electromagnetic (csem) system for near-surface geophysical prospecting: on instrument noise, temperature drift, transmission frequency, and survey set-up. *Geoscientific Instrumentation, Methods and Data Systems*, *11*(2), 435–450.

Wu, J., Zhi, Q., Li, X., Chen, X., Li, B., Huang, Y., et al. (2023). Loop source semi-airborne TEM system and its application in landslide detection. *Chinese Journal of Geophysics*, *66*(4), 1758–1770.

Wu, Q., Li, D., Jiang, C., Ji, Y., Wen, Y., & Luan, H. (2019). Ground-source airborne time-domain electromagnetic (gatem) modelling and interpretation method for a rough medium based on fractional diffusion. *Geophysical Journal International*, *217*(3), 1915–1928.

7th International Symposium on Three-Dimensional Electromagnetics
Vancouver, BC, Canada, November 13–15, 2023

FEMALY: A Finite Element MAtlab LibrarY for Electromagnetics

Klaus Spitzer[1], Jan Blechta[2,3], Jana Börner[1], Ralph-Uwe Börner[1], Michael Eiermann[4], Oliver Ernst[2], Mathias Scheunert[1]
[1]Institute of Geophysics and Geoinformatics, TU Bergakademie Freiberg, Germany
[2]Faculty of Mathematics, TU Chemnitz, Germany
[3]Mathematical Institute, Charles University, Prague, Czechia
[4]Institute for Numerical Mathematics and Optimisation, TU Bergakademie Freiberg, Germany

Summary

We present a finite element software library written in Matlab for the numerical simulation and inversion of electromagnetic fields in two and three dimensions. It is designed in a modular way to easily plug together fundamental building blocks for various electromagnetic applications from DC to the inductive range in the frequency and even time domain. External modules comprise the mesh generator and the equation solver library. Through its homogeneous software concept the adoption to any field application is relatively simple and makes the code suitable to open source distribution. We introduce the key features of this library including Lagrange and Nédélec finite elements formulated on unstructured tetrahedral grids, a Gauss-Newton inversion approach using linear Raviart-Thomas elements for H1 regularization, and the ability to incorporate any geometric feature such as topography, bathymetry and internal voids like caves, tunnels and mine buildings. The library is currently being tested with large real data sets to confirm its usefulness as a tool for practical data interpretation. Therefore, case studies for the magnetotelluric, direct current resistivity, controlled source electromagnetic and induced polarization methods in the field and laboratory are briefly outlined as examples with challenging geometric features.

Keywords: Finite elements, unstructured tetrahedral grids, Gauss-Newton inversion, regularization, Matlab

Introduction

The electromagnetics (EM) working group of the Freiberg Institute of Geophysics and Geoinformatics looks back on a long history of research in the field of simulation and inversion of geo-electromagnetic problems. Together with the Faculties of Mathematics of the Universities of Chemnitz and Freiberg, a wide variety of individual software solutions have been developed over the years. A collaborative software project over the last four years has enabled us to pool, unify, and re-implement the essential parts of the acquired knowledge into a single finite element (FE) software library written in Matlab, which is currently being tested and on its way to becoming an open source software for the EM community. After outlining the governing physics in terms of the underlying partial differential equations (PDE's) we present the key features of this library that allow for the implementation of the forward and inverse problem of any type of geophysical electromagnetic application in 2D and 3D ranging from the quasi-static to the inductive case in the frequency domain with arbitrary configuration of sources and receivers. Afterwards, we showcase successful applications in magnetotellurics (MT), direct current (DC) resistivity, controlled source electromagnetics (CSEM) and induced polarization (IP) as versatile examples with complex geometries.

The Forward Problems

The library provides solutions to the quasi-static EM case, typically the DC resistivity method, as well as passive and active induction methods in the diffusive domain.

For the quasi-static case, the equation of continuity for the scalar electric potential V in a domain Ω

$$\nabla \cdot (\sigma \nabla V) = -I\delta(\boldsymbol{x} - \boldsymbol{x}_0), \tag{1}$$

is solved for a point source of strength I and given electric conductivity σ. σ becomes complex-valued if IP effects are considered (Kemna, 2000).

In the diffusive induction case, a curl-curl-type of PDE in the frequency domain is considered using a time-harmonic e^{iwt} behavior (i imaginary unit, ω an-

gular frequency, t time) reading

$$\nabla \times (\mu^{-1} \nabla \times \boldsymbol{E}) - k\boldsymbol{E} = i\omega \boldsymbol{J}^S \tag{2}$$

where $k = i\omega(\sigma - i\omega\varepsilon)$ is the wavenumber, $\boldsymbol{E}$ the electric field, μ the magnetic permeability, ε the electric permittivity, and J^S some source term with the physical dimension of a current density. Appropriate boundary conditions have to be determined in each case. The FE method builds upon the transformation of the strong formulation of the boundary value problems (1) and (2) into the weak formulation of the problem with the identity only given in the sense of an inner product. To implement the approach we refer to the discrete formulation of the variational form which is achieved using the Galerkin approach that reduces the Ansatz function space $\mathcal{V}$ to a test function space $\mathcal{V}_h \in \mathcal{V}$ as the FE subspace of cellwise polynomial functions of order p over the spatial partition $\mathcal{T}_h$. This results in the reformulation of (1) and (2) as large linear systems of linear equations to be rapidly solved.

All solutions can be determined via optional total or secondary field approaches, the latter of which modify the right hand sides of eqs. (1) and (2) for the secondary sources with respect to a known background model. All material parameters can alternatively be selected as anisotropic. For further details, see Monk (2003), Schwarzbach et al. (2011), and Franke-Börner (2012).

The Inverse Problem

We have incorporated a standard regularized Gauss-Newton inversion approach minimizing a data objective functional Φ_d and a model objective functional Φ_m weighted by an unknown regularization parameter α reading

$$\begin{aligned} \Phi(\mathbf{m}) &= \Phi_d + \alpha \Phi_m = \\ \tfrac{1}{2}\|\mathbf{f}(\mathbf{m}) - \mathbf{d}\|_2^2 &+ \alpha ||\mathbf{W}(\mathbf{m} - \mathbf{m}_{\text{ref}})||^2 \rightarrow \min_{\mathbf{m}} \end{aligned} \tag{3}$$

subject to $\mathbf{A}(\mathbf{m})\mathbf{u} = \mathbf{b}$. Here, $\mathbf{u}$ is the discrete solution vector (primary solution) of the PDE, $\mathbf{d}$ is the measured data, $\mathbf{f}(\mathbf{m}) = \mathbf{Q}\mathbf{A}(\mathbf{m})^{-1}\mathbf{b}$ the forward operator generating the modeled data, $\mathbf{m}$ the model parameter vector, $\mathbf{W}$ the parameter weighting matrix, $\mathbf{Q}$ the measurement operator extracting and transforming the solution at the observation locations ($\mathbf{Qu} \approx \mathbf{d}$), and $\mathbf{m}_{\text{ref}}$ is a reference model defining a preferred region of the model space. The linearized normal equations for an iterative process, i.e., for $\mathbf{m}_{k+1} = \mathbf{m}_k + \Delta\mathbf{m}$ then read

$$\begin{aligned} \left(\mathbf{J}^T(\mathbf{m}_k)\mathbf{J}(\mathbf{m}_k) + 2\alpha\mathbf{W}^T\mathbf{W}\right)\Delta\mathbf{m} = \\ \mathbf{J}^T(\mathbf{m}_k)[\mathbf{f}(\mathbf{m}_k) - \mathbf{d}] + 2\alpha\mathbf{W}^T\mathbf{W}(\mathbf{m}_{\text{ref}} - \mathbf{m}_k). \end{aligned} \tag{4}$$

with the Jacobian $\mathbf{J}(\mathbf{m}_k) = \frac{\partial \mathbf{f}(\mathbf{m})}{\partial \mathbf{m}_k}$. The weighting matrix $\mathbf{W}$ represents a regularization operator applicable to piecewise constant model parameters on unstructured grids and weak formulations. We have chosen to implement a smoothness regularization according to Schwarzbach & Haber (2013) in which the penalty function measures the norm of a weak gradient of the conductivity field using Raviart-Thomas elements of lowest order RT_0. This ensures the normal components between elements to be continuous. A discrete representation of the model objective functional then reads:

$$\Phi_m = (\mathbf{m} - \mathbf{m}_{\text{ref}})^T \mathbf{D}\mathbf{M}_{RT_0}^{-1}\mathbf{D}^T(\mathbf{m} - \mathbf{m}_{\text{ref}}) \rightarrow \min_{\mathbf{m}}. \tag{5}$$

with $\mathbf{W}^T\mathbf{W} = \mathbf{D}\mathbf{M}_{RT_0}^{-1}\mathbf{D}^T$, $\mathbf{M}_{RT_0}$ denoting the RT_0 mass matrix and $\mathbf{D}$ the discrete divergence operator. For more details, see Nocedal & Wright (2006); Weißflog (2016); Scheunert et al. (2016); Wang et al. (2018); Blechta & Ernst (2023).

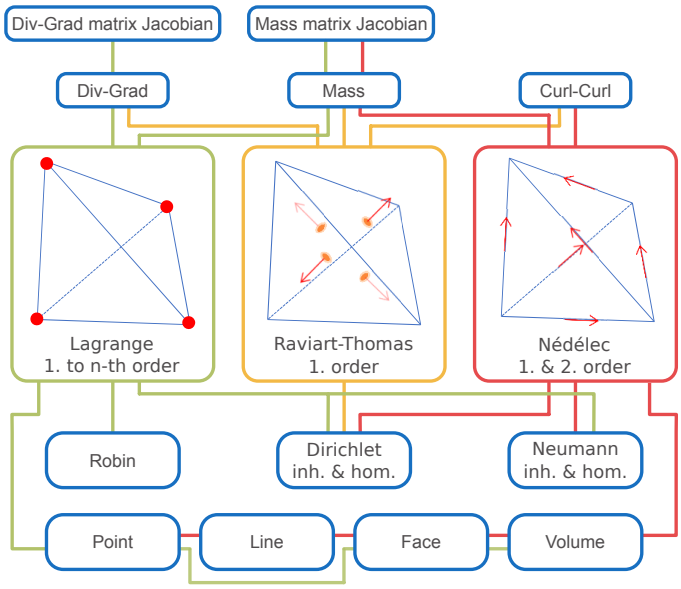

Figure 1: Building blocks for the forward modeling procedure: differential operator and their derivatives (top), types of FE (center), boundary conditions and source types (bottom).

The Code

The simulation and inversion code is entirely written in Matlab. It consists of FE forward modeling and

inversion building blocks and uses two external software packages: Gmsh (Geuzaine & Remacle, 2009) for the generation of unstructured tetrahedral meshes $\Omega = \bigcup_{\Omega_h \in \mathcal{T}_h} \Omega_h$ and MUMPS for the rapid solution of the resulting systems of linear equations (Amestoy et al., 2001). The following list gives an overview of the structure of the library.

- FE building blocks (see also Fig. 1)
  - Finite element definitions, i.e. basis functions of $\mathcal{V}_h$ with respect to $\mathcal{T}_h$:

    $V = \sum_i u_i \phi_i \quad \in H_h^1(\Omega) \quad \rightarrow$ Lagrange
    $\mathbf{E} = \sum_i u_i \boldsymbol{\psi}_i \quad \in H_h(\mathrm{curl}, \Omega) \quad \rightarrow$ Nédélec
    $\mathbf{p} = \sum_i u_i \boldsymbol{\chi}_i \quad \in H_h(\mathrm{div}, \Omega) \quad \rightarrow$ Raviart-Thomas
  - Bilinear forms, i.e. left-hand side, with respect to piecewise constant parameters $p = \sum_h p_h \Theta_h$ on Ω_h:

    $u_i \int_{\Omega_h} p_h \nabla \phi_i \cdot \nabla \phi_j \, \mathrm{d}V \quad \rightarrow$ Div-Grad
    $u_i \int_{\Omega_h} p_h \, \nabla \boldsymbol{\psi}_i \times \nabla \boldsymbol{\psi}_j \, \mathrm{d}V \quad \rightarrow$ Curl-Curl
    $u_i \int_{\Omega_h} p_h \, (.)_i \cdot (.)_j \, \mathrm{d}V \quad \rightarrow$ Mass
  - Linear forms, i.e. right-hand side, for continuous source functions:

    $\int_{\Omega_h} \delta(\boldsymbol{x}) \phi_i \, \mathrm{d}V \quad \rightarrow$ Point
    $\int_{\Gamma_h} f(\boldsymbol{x}) \boldsymbol{\psi}_i \cdot \boldsymbol{\tau} \, \mathrm{d}s \quad \rightarrow$ Line
    $\int_{\partial\Omega_h} \boldsymbol{f}(\boldsymbol{x}) \boldsymbol{\psi}_i \cdot \boldsymbol{n} \, \mathrm{d}A \quad \rightarrow$ Face
  - Jacobian, based on primary (.) and adjoint (.)′ solutions with respect to source s and receiver r and P^0 basis functions Θ_h:

    $\int_{\Omega_h} \Theta_h \nabla V_{i,s} \cdot \nabla V'_{j,r} \, \mathrm{d}V \quad \rightarrow$ Div-Grad Jacobian
    $\int_{\Omega_h} \Theta_h \boldsymbol{E}_{i,s} \cdot \boldsymbol{E}'_{j,r} \, \mathrm{d}V \quad \rightarrow$ Mass Jacobian

    (Lagrange, Nédélec)
- Boundary conditions
  - Dirichlet
  - Neumann (Lagrange, Nédélec)
  - Robin (Lagrange)
- Inversion building blocks
  - Scalable iterative solver (Blechta & Ernst, 2023) for H1-regularized normal equations
  - Gauss-Newton approach
  - Explicit Jacobian assembly
  - Line search (Armijo) (Nocedal & Wright, 2006)
- Gmsh mesh generation (Geuzaine & Remacle, 2009), DEM interpolation (Shepard, 1968) as shown in Fig. 2, VTK or XDMF export to Paraview (Ayachit, 2015)
- MUMPS parallel direct solver (Amestoy et al., 2001)
- Rational best approximation (Börner et al., 2008) for time integration

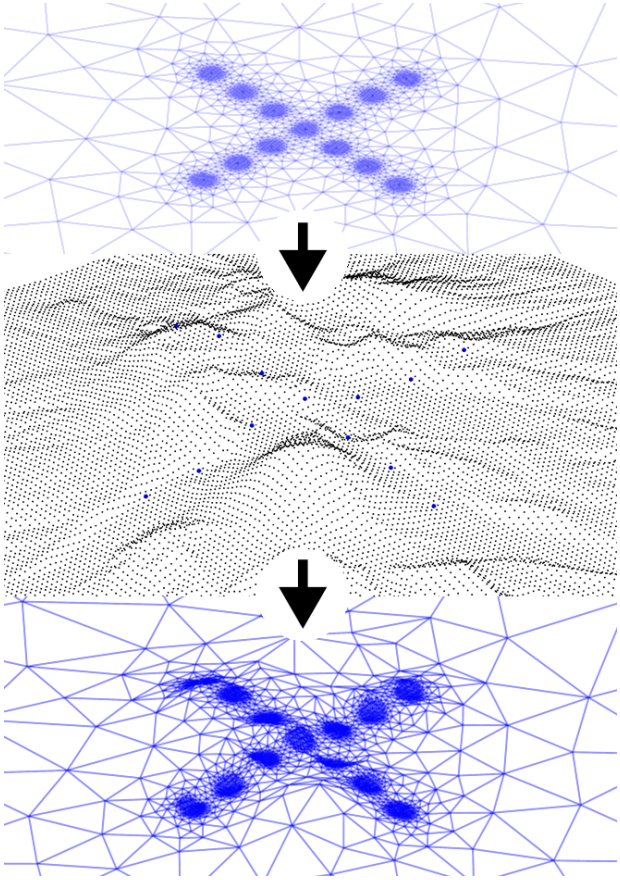

Figure 2: 2D surface with mesh refinement around sources/receivers (top), DEM with receiver locations shown as blue dots (center), 3D surface by adjusting mesh nodes using inverse distance weighting or C1 splines (bottom)

Applications

The following applications demonstrate the flexibility of the code and showcasing its successful performance for large, state-of-the-art field data sets collected in highly demanding geometric environments.

DC Resistivity in a Subsurface Mining Environment

The first example shows an in-mine DC resistivity survey in the 'Reiche Zeche', an educational ore mine

in the mining district of Freiberg, Germany (Fig. 3). The inner surface of the tunnel was scanned with a laser resulting in several hundred thousand geometry points being reduced to about 10000 points by triangulation. 80 electrodes were placed along the tunnel wall to conduct a Wenner-type survey cycling through the electrode positions with ten different spacings resulting in a total of 635 observations.

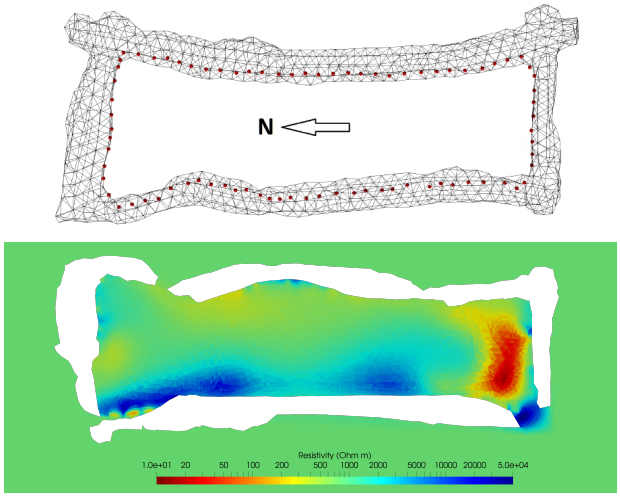

Figure 3: 3D Inversion of DC resistivity data collected in a subsurface mining gallery in Freiberg's 'Reiche Zeche'. Tunnel geometry with electrode locations (red dots, top) and inversion result (bottom). The shown tunnel system is approximately 35 m wide and 10 m high.

Magnetotellurics in Rugged Terrain

This section shows the inversion of a large MT data set from Mount Tarawera on New Zealand's North Island acquired by the Institute of Geological and Nuclear Sciences GNS (Bertrand et al., 2022). 68 MT sites were deployed over an area of 25 x 30 km^2 around the Tarawera Dome Complex between 2006 and 2017.

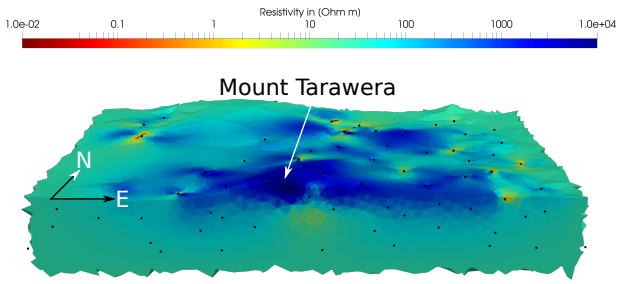

Figure 4: Preliminary inversion of a MT data set in the vicinity of Mount Tarawera, New Zealand.

For the 3D inversion, we have used 16 periods between 0.013 s and 341.297 s. Particular emphasis was put on an appropriate representation of the rugged topography. In a first attempt, we adapted the level of detailedness of the digital terrain model using an inverse distance weighting scheme. At the moment, we are working on a more elaborate sensitivity-guided refinement scheme because it became evident that some data were strongly affected by the terrain, particularly at sites less than 2 km away from steep slopes. Fig. 4 shows one of the inverted models.

Controlled-source Electromagnetics for Mine Monitoring

Based on surface-to-mine field campaigns at a large salt deposit we worked out the sensitivity footprint for the low-frequency (∼5 Hz to ∼300 Hz) CSEM sounding that uses large-scale line sources at the surface and oriented three-component magnetic sensors within the mine (Fig. 5). The mine is threatened by

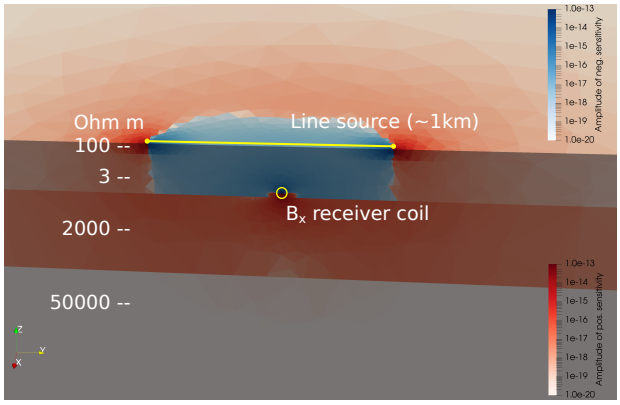

Figure 5: Sensitivity distribution (real part) for an exciting line source (∼40 Hz) on top of a layered halfspace for a surface-to-mine experiment in a Potash mine.

water intrusion dissolving the salt rapidly and creating large subsurface voids that lead to hazardous sinkholes at the Earth surface. To support the establishment of a monitoring system for the water infiltration into the mining galleries we carried out both, virtual experiments and sensitivity analyses for the surface-to-mine configuration as well as for a suggested mine-to-surface sounding with reversed source/receiver configurations. Moreover, first three-dimensional inversions were carried out with a preliminary data set (not shown here).

Induced Polarization in a Volcanic Environment

This application presents the inversion of IP data from a field survey at the rim of La Fossa crater on Vulcano Island, Italy. The multi-electrode data set, mainly dipole-dipole configuration, comprises 14 profiles of 14 electrodes each with 1 m spacing and 9 frequencies ranging from 91 mHz to 20 kHz. The domain model incorporates topography data from drone measurements. The obtained complex resistivity distributions in Fig. 6 highlight the fumarole-feeding hydrothermal system in the crater rim, revealed by consistently low resistivity and high phase shift.

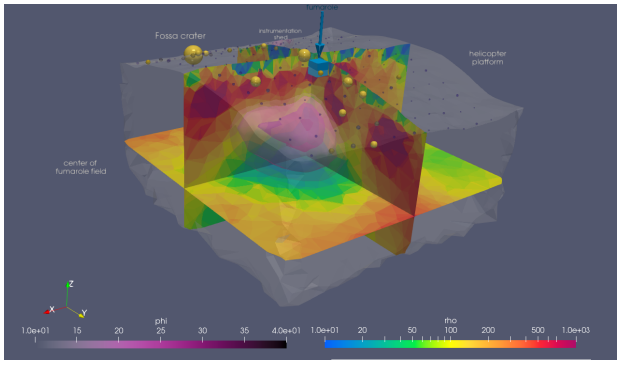

Figure 6: Resistivity and phase distribution beneath an active fumarole on the summit of La Fossa crater, Vulcano Island.

A Virtual Laboratory Experiment

The last application we present is a virtual accompaniment of a DC resistivity/IP laboratory experiment concerning the dynamic flow of electrically effective tracer fluids through a sample cylinder. Fig. 7 shows the geometry of the sample cylinder with current electrodes at the circular end faces and ring-shaped potential electrodes in narrow notches on the cylinder jacket. The conductivity distribution includes a spherical anomaly in the center part of the probe (top left). The top right-hand subplot shows the electric potential and the bottom left-hand subplot the current density. The sensitivity distribution shows the typical zones of positive and negative values (bottom right). Interestingly, the highest sensitivity values are reached at the contact line of the notches with the cylinder and not at the surface of the ring electrodes which is an important feature of the monitoring concept.

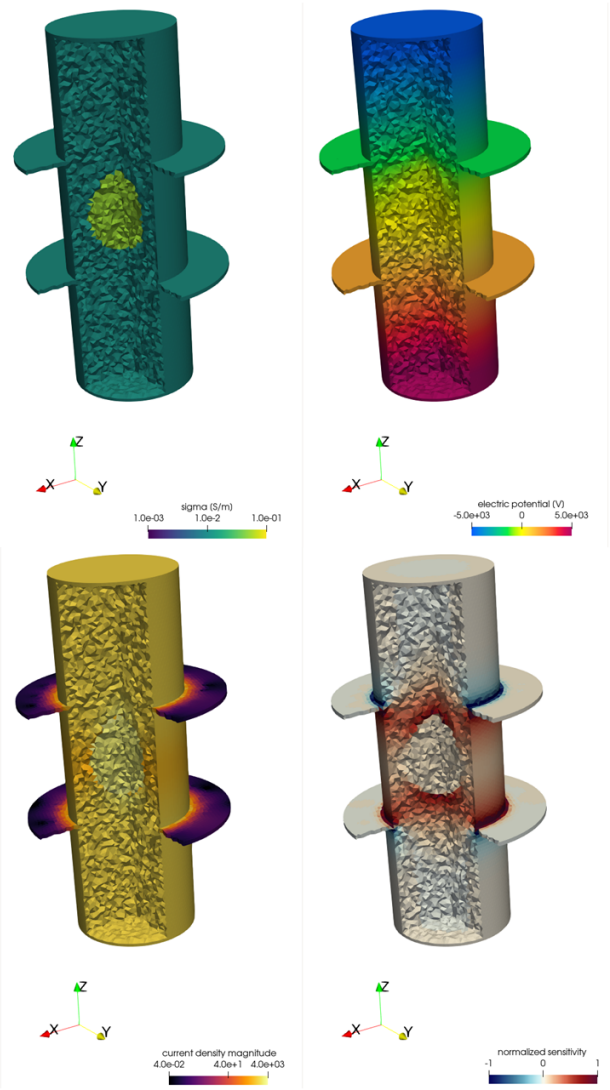

Figure 7: Laboratory cylindrical probe with current electrodes at the top and the bottom and two potential electrodes at the outer ring surfaces of disc-shaped bosses (top left: conductivity, top right: electric potential, bottom left: current density, bottom right: sensitivity).

Discussion and Conclusions

We have presented our finite element library for the simulation and inversion of electric/electromagnetic methods in geophysics and showcased some applications that we have worked on so far. The library is modular and homogeneously written in Matlab. It is planned to make the library available to the international community after our tests are completed.

The choice of the Matlab programming language has advantages and disadvantages. The advantages are a high-level programming language with the benefits

of an integrated development environment and convenient, straightforward, and math-oriented coding. Matlab has proven to be a long-term stable computing environment. However, the acquisition of a commercial license, which hinders the free exchange on a scientific level, can be seen as a disadvantage. Still, we believe that Matlab is widely available even in public and academic institutions and guarantees an enduring scientific software development.

All computationally intensive segments are processed through parallelizable external libraries. Visualization is done using Paraview. The interfaces are clearly defined, so that the external modules can be exchanged easily. Docker images may be provided in future for an uncomplicated setup and installation. Ready-made sample applications will be included which, as an easy starting point, can be adapted to individual new applications. We do hope that the present software development will be helpful to the community.

Acknowledgments

We thank the German Research Foundation (DFG) for continuous support over the years, the German Federal Ministry of Education and Research (BMBF) for funding within the GeoTechnologien Program, the EU for providing funding for the junior research group GeoSax within the European Social Funds (ESF) program, and all the collaborators and students who contributed.

REFERENCES

Amestoy, P. R., Duff, I. S., L'Excellent, J.-Y., & Koster, J. (2001). A fully asynchronous multifrontal solver using distributed dynamic scheduling. *SIAM Journal on Matrix Analysis and Applications*, *23*(1), 15-41.

Ayachit, U. (2015). *The paraview guide: A parallel visualization application*. Clifton Park, NY, USA: Kitware, Inc.

Bertrand, E., Kannberg, P., Caldwell, T., Heise, W., Constable, S., Scott, B., et al. (2022). Inferring the magmatic roots of volcano-geothermal systems in the rotorua caldera and okataina volcanic centre from magnetotelluric models. *Journal of Volcanology and Geothermal Research*, *431*, 107645.

Blechta, J., & Ernst, O. G. (2023). Efficient solution of parameter identification problems with h^1 regularization. *SIAM Journal on Scientific Computing*. (accepted for publication)

Börner, R.-U., Ernst, O. G., & Spitzer, K. (2008, 06). Fast 3-D simulation of transient electromagnetic fields by model reduction in the frequency domain using Krylov subspace projection. *Geophysical Journal International*, *173*(3), 766-780.

Franke-Börner, A. (2012). *Three-dimensional finite element simulation of magnetotelluric fields on unstructured grids on the efficient formulation of the boundary value problem*. Phd thesis, TU Bergakademie Freiberg, Freiberg, Germany.

Geuzaine, C., & Remacle, J.-F. (2009). Gmsh: A 3-D finite element mesh generator with built-in pre- and post-processing facilities. *International Journal for Numerical Methods in Engineering*, *79*(11), 1309-1331.

Kemna, A. (2000). *Tomographic inversion of complex resistivity*. Dissertation. Der andere Verlag. (Ruhr-Universität Bochum)

Monk, P. (2003). *Finite element methods for Maxwell's equations*. New York: Oxford University Press.

Nocedal, J., & Wright, S. (2006). *Numerical optimization*. New York: Springer Nature.

Scheunert, M., Ullmann, A., Afanasjew, M., Börner, R.-U., Siemon, B., & Spitzer, K. (2016). A cut-&-paste strategy for the 3-D inversion of helicopter-borne electromagnetic data — I. 3-D inversion using the explicit Jacobian and a tensor-based formulation. *Journal of Applied Geophysics*, *129*, 209-221.

Schwarzbach, C., Börner, R.-U., & Spitzer, K. (2011). Three-dimensional adaptive higher order finite element simulation for geo-electromagnetics-a marine CSEM example. *Geophysical Journal International*, *187*(1), 63-74.

Schwarzbach, C., & Haber, E. (2013). Finite element based inversion for time-harmonic electromagnetic problems. *Geophysical Journal International*, *193*(2), 615-634.

Shepard, D. (1968). A two-dimensional interpolation function for irregularly-spaced data. In *Proceedings of the 1968 23rd acm national conference* (p. 517–524). New York, NY, USA: Association for Computing Machinery.

Wang, F., Morten, J. P., & Spitzer, K. (2018). Anisotropic three-dimensional inversion of CSEM data using finite-element techniques on unstructured grids. *Geophysical Journal International*, *213*(2), 1056-1072.

Weißflog, J. (2016). *Three-dimensional individual and joint inversion of direct current resistivity and electromagnetic data*. Phd thesis, TU Bergakademie Freiberg, Freiberg, Germany.

Comparison of 3D finite-element and finite-difference inversion of magnetotelluric data in Okuaizu geothermal area, northern Japan

Toshihiro Uchida[1] and Yusuke Yamaya[1]
[1]Renewable Energy Research Center, National Institute of Advanced Industrial Science and Technology

SUMMARY

In order to investigate the performance of three-dimensional (3D) inversion of magnetotelluric (MT) data for geothermal exploration, where accurate numerical modeling is indispensable for coping with rough topography, we have utilized two inversion codes, FEMTIC and WSINV3DMT, for 3D inversion of MT data obtained in Okuaizu geothermal area, northern Japan. FEMTIC, a finite-element (FEM) inversion code, can incorporate either tetrahedral elements (Tetra) or deformed non-conforming hexahedral elements (DHexa) in the mesh, while WSINV3DMT, a finite-difference (FDM) inversion code, uses rectangular cells. We prepared the same subset of MT data (all components of the impedance and tipper at 16 frequencies from 58 stations) and set the same noise-floor for running Tetra, DHexa and WSINV3DMT inversions. As a result, all three inversions gave similar 3D models, indicating resistivity anomalies related to the cap rock and the geothermal reservoir in the area. However, the model by WSINV3DMT generated some irregular features; (1) several thin horizontal anomalies of high- and low-resistivities alternately appeared in shallow parts, which was not realistic, and (2) the conductive anomaly at depth of 3-5 km showed extremely low resistivity value. This suggests that the FEM inversion is more stable than FDM when we include the topography in the inversion.

Keywords: magnetotellurics, three-dimensional inversion, finite element, finite difference, topography, Okuaizu geothermal area

INTRODUCTION

Application of the magnetotelluric (MT) method for geothermal exploration has rapidly expanded worldwide since a decade ago. Particularly, three-dimensional (3D) inversion has become a routine task in the interpretation. It is because a few sophisticated 3D inversion codes, such as WSINV3DMT (Siripunvaraporn and Egbert, 2009) and ModEM (Kelbert et al., 2014), are public and help many geothermal engineers. These codes use the finite-difference method (FDM) for the forward modeling. However, it is well known that the numerical accuracy often decreases when we incorporate the topography in the FDM modeling due to the large resistivity contrast between the air and the underground.

3D MT inversion codes that use the finite-element method (FEM) for the forward modeling have been published since several years ago (e.g., Grayver, 2015; Usui, 2015; Kordy et al., 2016; Jahandari and Farquharson, 2017). The FEM can flexibly incorporate the topography variation in the mesh without reducing the numerical accuracy much.

The code, FEMTIC (Usui, 2015), became public domain in 2021. In this study, we ran the 3D inversion of the MT data obtained in Okuaizu geothermal area, northern Japan, using both FEMTIC and WSINV3DMT, and investigated the performance of the codes when we include the topography.

MT DATA

The Okuaizu geothermal area is located in a small caldera that was formed approximately 300,000 years ago (Mizugaki, 2000). All of geological formations surveyed by past geothermal drillings are volcanic origin in Neogene and Quaternary time, except intermittent sedimentary layers and shallow alluvium. A 30 MWe geothermal power plant has been in operation since 1995.

MT surveys were conducted over the Okuaizu geothermal area at two stages (Uchida et al., 2015). The first survey was conducted in 2000 and 2001 as a 2D survey along two long profiles (roughly NE-SW and NW-SE) crossing the central zone of the geothermal area. The second one was a 3D survey in 2010 concentrating in the central zone, with 30 MT stations covering roughly an area of 3.5 km x 3.5 km with an average station interval of 500 m. The MT data were obtained using Phoenix MTU-5A systems, and the remote reference station was deployed at about 200 km north from the survey area. In this study, we set an area of approximately 8 km north-south and 10 km east-west for the 3D interpretation, utilizing the data from 58 MT stations (Figure 1).

INVERSION PROCEDURE

We used two inversion codes, FEMTIC (Usui, 2015; Usui et al., 2017) and WSINV3DMT (Siripunvaraporn

and Egbert, 2009). FEMTIC, a finite-element modeling (FEM) code, can incorporate either tetrahedral elements or deformed non-conforming hexahedral elements in the 3D mesh, while WSINV3DMT, a finite-difference modeling (FDM) code, uses rectangular cells.

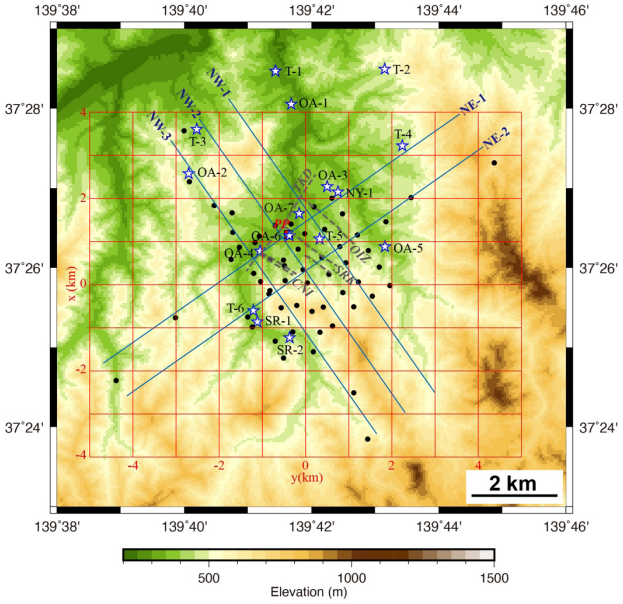

Fig. 1: Location of MT stations (black dots) on a topography contour map in the Okuaizu area. Stars are boreholes by past geothermal surveys and the red square with '*PP*' indicates the location of Yanaizu-Nishiyama geothermal power plant (main building). Grey dashed lines are estimated faults which the geothermal reservoir is associated with. Blue lines are profiles for showing cross-sections and red grids for showing plan views of the 3D model.

Figure 2 shows the mesh setting for the tetrahedral elements (Tetra) and deformed non-conforming hexahedral elements (DHexa) for the FEMTIC code, and rectangular cells for WSINV3DMT (WS3D). The size of the smallest element was less than 25 m for Tetra, while about 30 m horizontally and 25 m vertically for Dhexa near MT stations, and it gradually increased as we moved away from the stations (Fig. 2a, 2b). The size of rectangular cells near the earth surface was 150 m horizontally and 10 m vertically for the WS3D mesh (Fig. 2c). For Tetra, several elements were grouped into a block that was given the same resistivity in the inversion. The smallest block size was less than 40 m near MT stations, and it gradually increased as we moved away from the stations. For DHexa and WS3D, resistivity values of all elements (cells), except the air and sea water, were dealt as unknown parameters individually in the inversion.

The initial model was a homogeneous underground of 30 ohm-meters, which was close to the average value of observed apparent resistivities. Resistivity of the seawater was set as 0.33 ohm-meter. The air resistivity was 10^8 ohm-meters for FEMTIC and 10^7 ohm-meters for WS3D.

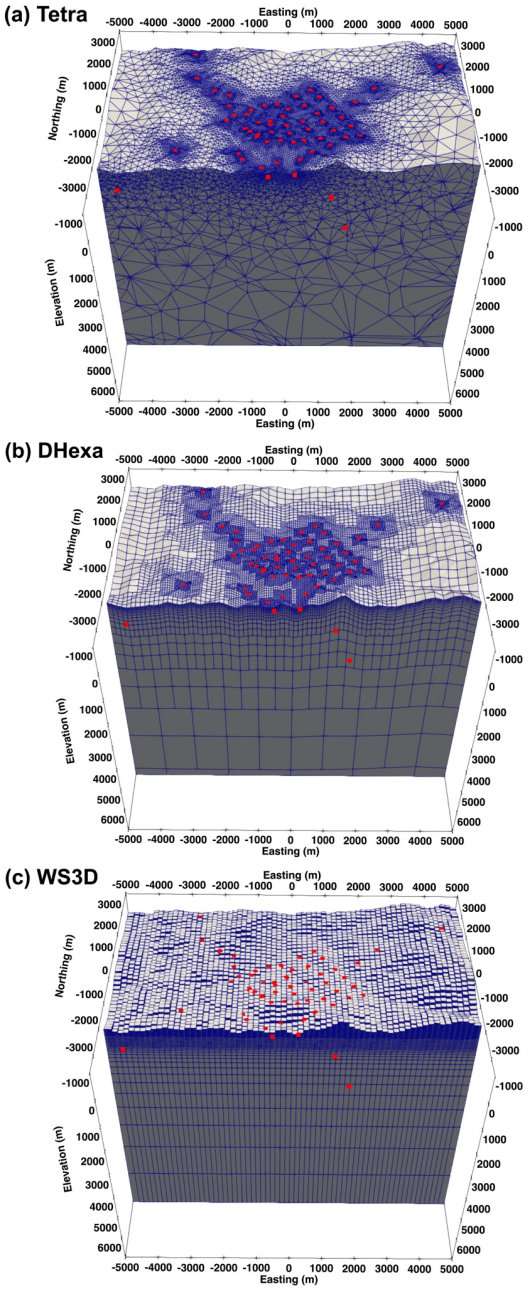

Fig. 2: Mesh setting for (a) tetrahedral (Tetra) elements and (b) deformed non-conforming hexahedral (DHexa) elements for the FEMTIC inversion, and (c) rectangular cells for WSINV3DMT (WS3D) inversion in the core zone of the mesh. Red dots indicate MT stations.

We used the same subset of MT data for all inversions; all components of the impedance and tipper at 16 frequencies (0.00275 – 97 Hz) at 58 stations. We set the same noise-floor for FEMTIC and WS3D; 3% for the off-diagonal components and 9% for the diagonal components of the impedance, and 0.008 for tipper. They were approximately 80% of median values of observation errors of all data used for the inversion. The data quality of this area was not so good at the low frequency band,

because the terminal station of a DC train system was located only some 20 km south, and noises by leak currents from the railway were dominant in the majority of the time-series segments (Uchida et al., 2015).

Galvanic distortion was included as unknowns in the FEMTIC inversion. Final RMS misfit achieved was 1.298, 1.420 and 1.691 for Tetra, DHexa and WS3D, respectively. Note that a target RMS misfit was set as 1.7 for the WS3D inversion in order to prevent the model become too rough.

INVERSION RESULTS

Figure 3 compares elevation-slice sections of the 3D models by Tetra, DHexa and WS3D inversions. Resistivity distribution of Tetra and DHexa is similar from the surface to an elevation of -3 km, but the location of low-resistivity anomaly is different at the -5 km elevation. Resistivity distribution of the WS3D model is generally similar to those of FEMTIC but slightly different for all five sections. Resistivity of the low-resistivity anomaly at -3 km and -5 km elevation is very low in the WS3D model.

Figures 4 and 5 compare resistivity distribution along NE-SW and NW-SE cross-sections. In the central zone, resistivity is generally low from the surface to approximately -1 km elevation. It corresponds with a clay-alteration zone and works as a cap rock of the geothermal reservoir. Below it is a relatively higher resistivity zone that corresponds to the high-temperature reservoir zone. A low-resistivity columnar anomaly of 1 - 2 km diameter and depth extension from -1 to -6 km (or more) elevation exists beneath the location of the power plant. The shape of this columnar anomaly differs between the three models. We can observe that several thin horizontal anomalies of high- and low-resistivities alternately appeared in shallow parts in the WS3D model, which is not realistic (Figures 4c and 5c).

Figure 6 is a bird-eye view of the Tetra model, showing low-resistivity elements of less than 5 ohm-meters. This figure clearly shows the combination of low-resistivity cap rock that includes low-temperature clay minerals (such as smectite) and higher-resistivity reservoir zone that includes high-temperature clay minerals (such as chlorite). In addition, a deep conductor, which may be related to the heat source or high-temperature fluid for the geothermal system, is obtained.

CONCLUSION

We applied two inversion codes, FEMTIC and WSINV3DMT, for the 3D inversion of MT data obtained in Okuaizu geothermal area, incorporating the topography. Both codes successfully generated similar 3D models that indicated good agreement with the geothermal structure. However, there are differences between the three models (Tetra, DHexa and WS3D) and further study is necessary to understand the reliability of the models.

ACKNOWLEDGEMENTS

The authors thank Dr. Yoshiya Usui, the University of Tokyo, for his advice in running his 3D code FEMTIC.

REFENRECES

Grayver, A.V. (2015) Parallel three-dimensional magnetotelluric inversion using adaptive finite-element method. Part I: theory and synthetic study. *Geophys. J. Int.*, **202**, 584-603, doi:10.1093/gji/ggv165.

Jahandari, H., Farquharson, C.G. (2017) 3-D minimum-structure inversion of magnetotelluric data using the finite-element method and tetrahedral grids. *Geophys. J. Int.*, **211**, 1189-1205. doi:10.1093/gji/ggx358.

Kelbert, A., Meqbel, N., Egbert, G.D., Tandon, K. (2014) ModEM: A modular system for inversion of electromagnetic geophysical data. *Computers & Geosciences*, **66**, 40–53. doi:10.1016/j.cageo.2014.01.010.

Kordy, M., Wannamaker, P., Maris, V., Cherkaev, E., Hill, G. (2016) 3-D magnetotelluric inversion including topography using deformed hexahedral edge finite elements and direct solvers parallelized on SMP computers – Part I: forward problem and parameter Jacobians. *Geophys. J. Int.*, **204**, 74–93. doi:10.1093/gji/ggv410.

Mizugaki, K. (2000) Geologic structure and volcanic history of the Yanaizu-Nishiyama (Okuaizu) geothermal field, Northeast Japan, *Geothermics*, **29**, 233-256.

Siripunvaraporn, W., Egbert, G. (2009) WSINV3DMT: Vertical magnetic field transfer function inversion and parallel implementation. *Physics of the Earth and Planetary Interiors*, **173**, 317-329. doi:10.1016/j.pepi.2009.01.013.

Uchida, T., Takakura, S., Ueda, T., Sato, T., Abe, Y. (2015) Three-Dimensional Resistivity Structure of the Yanaizu-Nishiyama Geothermal Reservoir, Northern Japan. *Proceedings of World Geothermal Congress 2015*, Melbourne, Australia, 7p.

Usui, Y. (2015) 3-D inversion of magnetotelluric data using unstructured tetrahedral elements: applicability to data affected by topography. *Geophys. J. Int.*, **202**, 828-849. doi:10.1093/gji/ggv186.

Usui, Y., Ogawa, Y., Aizawa, K., Kanda, W., Hashimoto, T., Koyama, T., Yamaya, Y., Kagiyama, T. (2017) Three-dimensional resistivity structure of Asama Volcano revealed by data-space magnetotelluric inversion using unstructured tetrahedral elements. *Geophys. J. Int.*, **208**, 1359-1372. doi:10.1093/gji/ggw459.

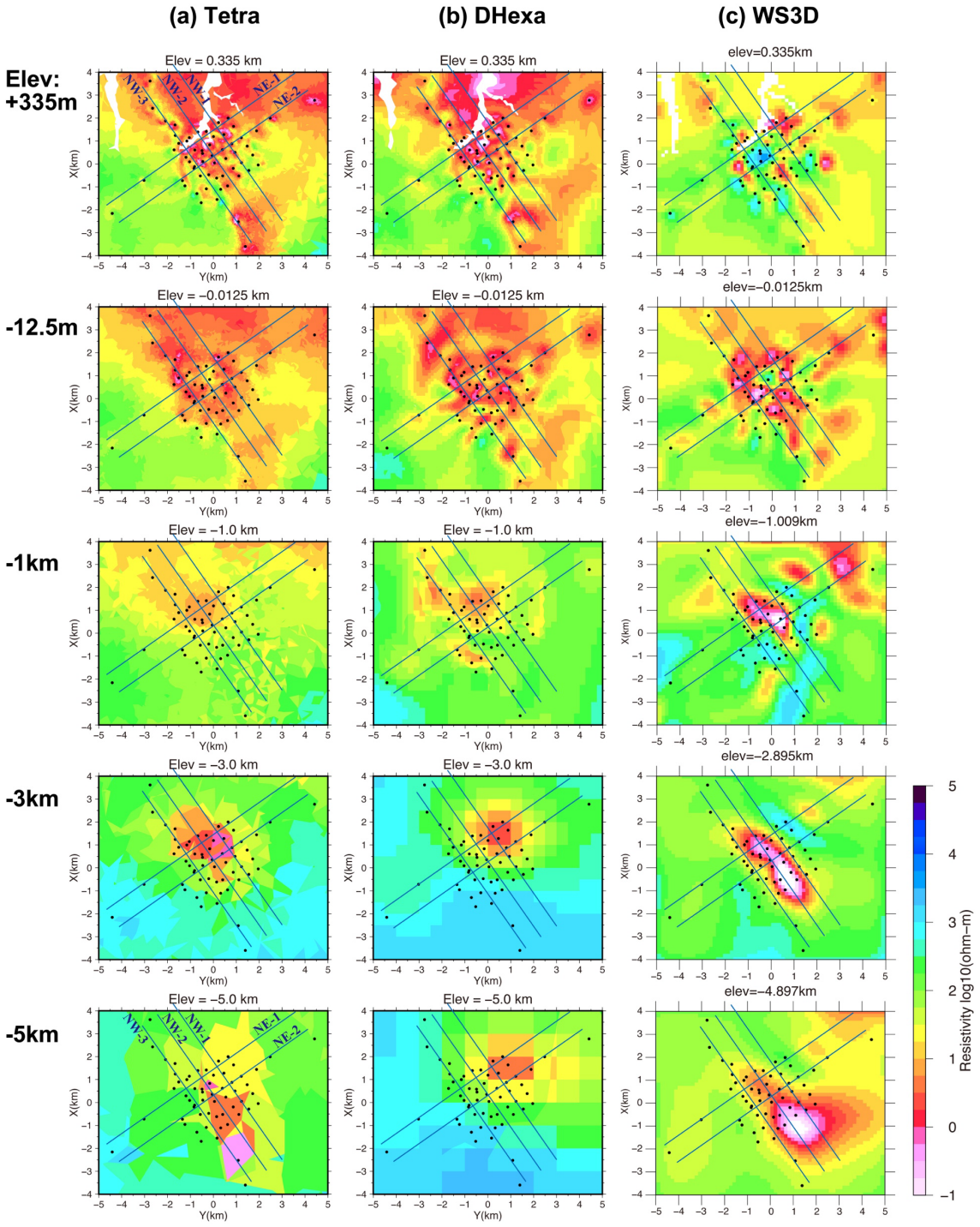

Fig. 3: Plan views of the 3D resistivity models at five elevations of 0.335 km, -0.0125 km, -1 km, -3 km and -5 km for Tetra, DHexa and WS3D inversions, respectively. Black dots are MT stations. Solid lines indicate the profiles shown in Figures 4 and 5.

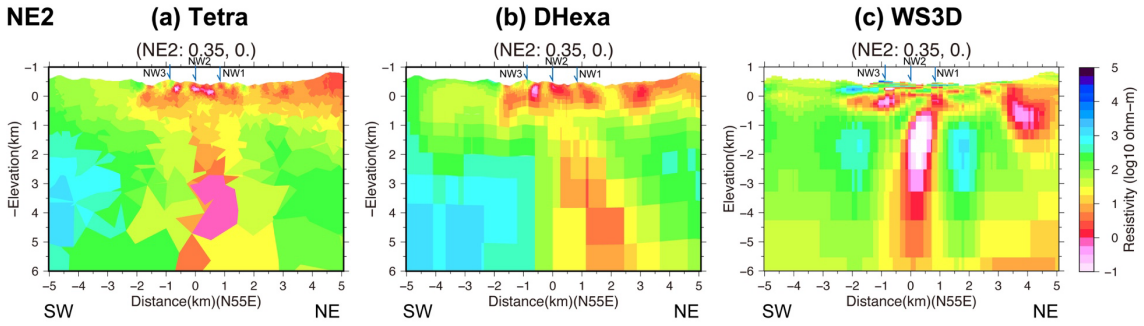

Fig. 4: Resistivity distribution along northeast-southwest cross-section, NE2, for (a) Tetra, (b) DHexa and (c) WS3D inversions. The 0 km distance corresponds to the position of x=0.35 km and y=0 km.

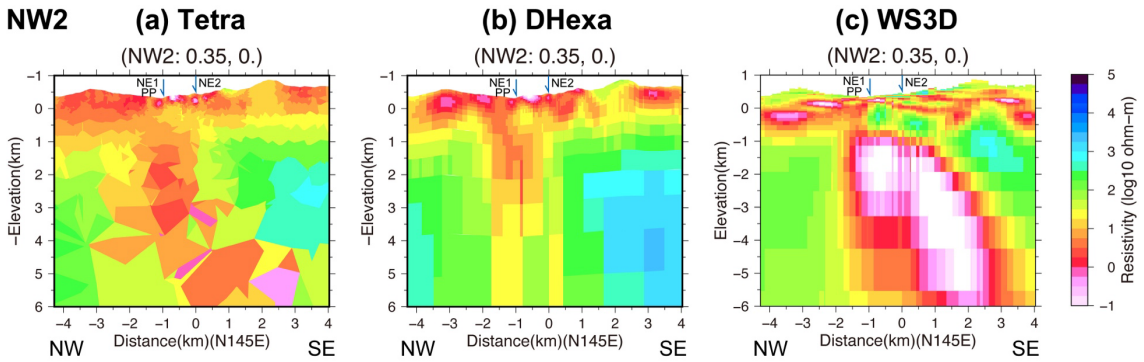

Fig. 5: Resistivity distribution along northwest-southeast cross-section, NW2, (a) Tetra, (b) DHexa and (c) WS3D inversions. The 0 km distance corresponds to the position of x=0.35 km and y=0 km.

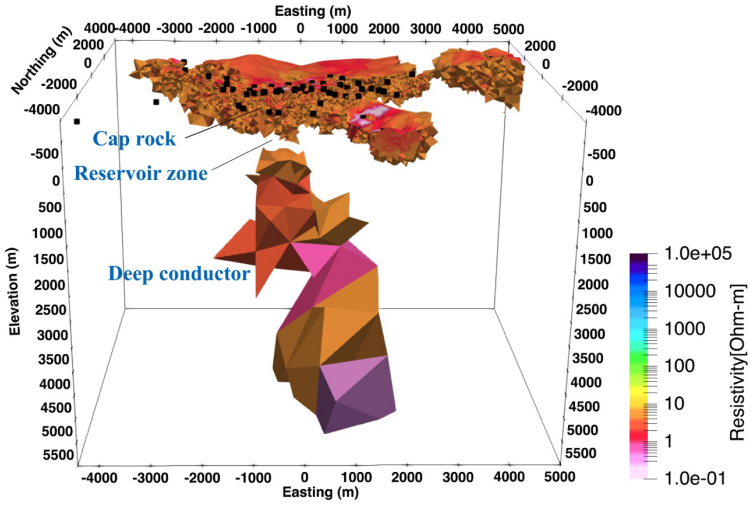

Fig. 6: A bird-eye view (looking from south) of the 3D model by the Tetra inversion, showing elements whose resistivity is lower than 5 ohm-meters.

3D Casing-Source Electromagnetic Modeling for CO_2 Plumes and Enhanced Geothermal Systems Monitoring

Evan Schankee Um and David L. Alumbaugh
Earth and Environmental Sciences, Lawrence Berkeley National Laboratory, Berkeley, CA, USA

SUMMARY

We present a modeling workflow that combines 3D cylindrical-mesh-based and rectangular-mesh-based electromagnetic (EM) modeling codes for efficiently simulating EM responses where steel well casings are employed as part of a grounded electrical source. Our modeling examples include 3D casing source scenarios with a single vertical well, multiple vertical wells, and a deviated steel-cased well. The workflow that is described involves approximating the energized casing with a series of electric dipoles, and has been employed to determine the sensitivity of different EM data acquisition scenarios for monitoring in complex 3D environments such as CO_2 storage and engineered geothermal system (EGS) sites.

Keywords: EM Casing Source, 3D numerical modeling, monitoring, CO_2, and geothermal

INTRODUCTION

Incorporating highly-conductive steel-cased wells into electromagnetic (EM) earth models is motivated by the possibility of utilizing long metal-cased wells as enhanced EM sources. This casing source can amplify source dipole moments and enable greater signal penetration at depth for monitoring subsurface processes (Schenkel and Morrison, 1990; Daily et al., 2004; Marsla et al., 2014; Commer et al., 2015). This enhancement allows us to detect and image deep-localized targets that traditional surface EM survey configurations may not be sensitive enough to identify. Recently, these casing source EM methods have been applied to a range of geophysical problems, including CO_2 monitoring (e.g., MacLennan et al., 2016; Puzyrev et al., 2017), fracture imaging (Weiss et al., 2016; Li and Yang, 2019; Um et al., 2019), enhanced geothermal system monitoring (e.g., Castillo-Reyes et al., 2021; Alumbaugh et al., 2023).

Simulating a hollow casing string in a 3D reservoir-scale or regional-scale EM earth model poses numerical challenges. For example, discretizing a casing in the 3D rectangular coordinate system requires a large number of fine cells due to the thinness of a casing. The exponential increase in required cells with well length makes 3D modeling using true casing geometry less practical in the 3D rectangular coordinate system, even on a parallel computer (e.g., Commer et al., 2015). While 3D cylindrical-mesh-based EM modeling codes (e.g., Heagy and Oldenburg, 2022) excel at accurately discretizing a hollow vertical cased well with a relatively small number of cells, challenges arise in dealing with complex 3D background models or deviated wells that no longer align with the cylindrical coordinate system. Alternatively, Weiss et al (2017) and Li and Yang (2019) use a hierarchical earth model and an equivalent resistor network, respectively to economically represent cased wells. Um et al. (2020) approximate cased wells using a volumeless boundary condition.

This paper presents a 3D EM modelling workflow designed for simulating a 3D casing source EM model having complex background resistivity structures at reduced computational costs compared to explicit casing discretization in the rectangular coordinate system. Rather than developing a new modelling algorithm for casing source EM simulations, we take a synergistic approach by utilizing two existing 3D EM modelling codes: the 3D SimPEG code (Heagy and Oldenburg, 2022) and the 3D finite-element EM code (Um et al., 2020). By integrating the strengths of each code, we leverage their advantages to address challenges in casing EM modelling. Following the demonstration of the workflow concept, we explore its applicability and limitations in dealing with deviated wells and multiple well scenarios.

WORKFLOW FOR SIMULATING EM CASING SOURCE

We first describe a modelling workflow that approximates the EM effects of an energized steel-cased well in a vertical orientation. Subsequently, we explore the applicability and limitations of this workflow in the context of deviated well and multiple well scenarios.

The workflow comprises five steps. First, we create a layered earth model with resistivity structure aligned with that along the path of a vertical well (step 1). This step requires a 3D resistivity model of the area or at least resistivity logging data. Next, we employ the 3D SimPEG code (Heagy and Oldenburg, 2022) to simulate energizing the vertical well. This simulation, fitting naturally within the cylindrical coordinate system, typically completes in less than an hour on a PC. Following the simulation, we extract the vertical electric current density along the outer surface of the well (step 3). The resulting set of equivalent dipoles is then mapped along the well trajectory in the 3D earth model (step 4), which is discretized using

unstructured tetrahedral meshes. Unlike cylindrical meshes, tetrahedral meshes are well suited for discretizing complex geology structures. Last, the resulting 3D model is simulated using the 3D finite-element modelling code (Um et al., 2020).

In the numerical modeling examples presented in this paper, we assume a consistent single casing thickness throughout the well and a uniform current density across the casing's cross-sectional area at each depth. This allows us to simply calculate the total casing current by multiplying the well's cross-sectional area by the current density on its outer surface. However, note that this assumption may not hold when casings are nested, resulting in variations in current distribution across the cross-section. In such cases, modeling the nested well structures is required, and the casing current is computed by integrating the current density over the entire cross-sectional area. While this modeling scenario is more involved, it can still be effectively modeled using the 3D SimPEG code. In short, the workflow is applicable to models that involve both 3D complex background and nested cased well.

3D CASING SOURCE EM MODELING EXAMPLES

1. Single Vertical Steel-Cased Well

First, the workflow is demonstrated with a straightforward example involving a single vertical well energized by a top-casing source configuration. In this example, a steel-cased well is 1 km deep, and the source electrode is connected to the top of the well casing (electrical conductivity: 10^6 S/m; outer radius: 0.1 m; thickness: 0.02 m). The return surface electrode is grounded 2 km away from the well head.

The source frequency is set to 1 Hz. The earth resistivity model is set to a 100 Ohm-m homogeneous half-space. A vertical observation well is situated 500 m away from the source well and vertical electric fields are measured there.

This vertical well problem can be efficiently simulated using the 3D SimPEG code without any additional steps. We first simulate this top-casing source configuration and next extract a set of casing current densities along the source well and vertical electric fields along the observation well. For evaluation, the extracted casing currents are compared against a Method of Moments (MoM) solution (Tang et al., 2015), and this comparison provides good agreement between the two solutions (**Figure** 1a). Subsequently, the extracted casing densities replace the energized steel-cased well in a 3D finite element EM model. The resulting finite element solution at the observation well is compared to the 3D SimPEG solution, again demonstrating good agreement (**Figure** 1b).

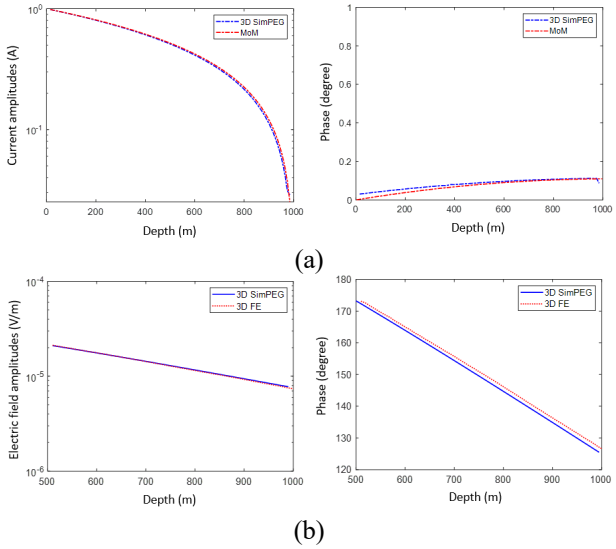

Figure 1. (a) Comparisons between the current density amplitudes calculated using the 3D SimPEG and MoM method. (b) Comparisons between borehole vertical electric field amplitudes calculated using true casing geometry (SimPEG) and equivalent sources (3D FE solutions).

2. Simulating a Multiple Vertical Casing Source EM at a proposed CO_2 Storage Site

Next, we explore the potential of the casing-source EM method for CO_2 sequestration monitoring at the Wyoming CarbonSAFE project (**Figure** 2) adjacent to the Dry Fork Station coal fired power plant in Gillette, Wyoming (Sullivan et al., 2020).

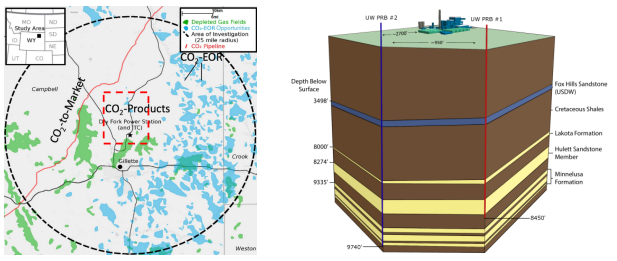

Figure 2. (a) Map showing the location of Dry Fork Station (b) Dry Fork Station Integrated Test Centre (Source: https://www.uwyo.edu/cegr/research-projects/wyoming-carbonsafe.html)

Figure 3a shows the layered resistivity model at the CO_2 storage site estimated from the well logging data and geological information. The layering becomes more detailed in the vicinity of the five proposed injection zones, indicated as indicated in the Table in **Figure** 3a as **. We apply Archie's Law to estimate resistivities for the five injection zones during and after CO_2 injection assuming a CO_2 saturation of 60%. The resulting

resistivity values for the five injections zones are shown in the table below.

	Porosity	Reservoir Resistivity (Sw=1)	Fluid Resistivity	Reservoir Resistivity (Sw=0.4, Sco2=0.6)
Reservoir 1	0.35	3	0.61	30.93
Reservoir 2	0.3	2	0.42	29.46
Reservoir 3	0.2	3	0.35	54.13
Reservoir 4	0.15	4	0.30	83.33
Reservoir 5	0.1	6	0.24	153.09

For numerical purposes, we implement an upscaling procedure for the zones within and between the intended thin injection zones, creating thicker reservoir injection units. Specifically, we consider a 90m thick zone spanning from 2455 to 2545 m depth to represent the upper injection zone in one injection well (PRB1). Additionally, we include a 60m thick zone ranging from 2851 m to 2910 m to cover the planned lower injection intervals in the other injection well (PRB2). This upscaling is necessary to avoid the inclusion of excessively thin and elongated cells within the numerical model which makes the finite element solution numerically costly and less efficient.

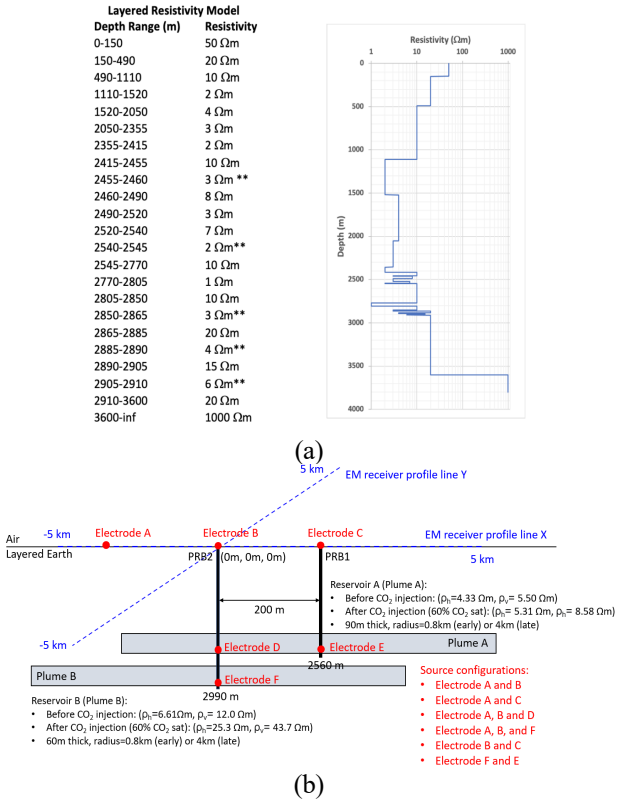

Figure 3. (a) The 1D resistivity model at the Wyoming CarbonSAFE site. (b) The 3D resistivity models used for the Wyoming CarbonSAFE site. The background layered resistivity model outside of the injection zones is described by the thicker layers in Figure 3a. The thinner layers within injection zones have been upscaled to Plume A and B as shown here.

To account for the current flow within the alternating conductive and resistive layers for the models that include the thin layers of injected CO_2, we calculated resistivities within these zones using an anisotropic approach. We determined the vertical resistivity (ρ_v) as the geometric mean of the layer resistivities and the horizontal resistivity (ρ_h) as the harmonic mean. This calculation results in injection zones depicted in **Figure** 3 that exhibit lower resistivity in the horizontal direction compared to the vertical direction, mimicking current flow patterns similar to alternating conductors and resistors. Employing these upscaled resistivity values, we created two distinct plume models, as illustrated in **Figure** 3b: an 'early' plume representing a relatively short time after injection initiation and a 'late' plume simulating conditions akin to 20 years of injection.

Various casing source configurations were tested, as listed in **Figure** 3b. In this study, we highlight a casing source configuration where one electrode is connected to the bottom of PRB2, and the other is connected to the bottom of PRB1. To simulate this setup, we calculate the current densities along PRB2 with one electrode connected to its bottom (electrode F) and the other grounded to the surface (electrode A). Similarly, we repeat the calculation for current densities along PRB1 using electrodes A and E. Note that the opposite current direction is used in the latter case. By superposing these two sets of current densities, we approximate the casing current distribution along the two wells energized by the two bottom electrodes. Note that this is an approximation as any EM interaction between the two cased wells is ignored. At the frequency used here (0.25 Hz) the skin depth within the steel casing assuming a relative magnetic permeability of 100 and an electrical conductivity of 10^6 S/m is approximately 0.10m which is much thicker than the casing itself. Thus, we infer that any EM mutual inductive effects are negligible compared to normal galvanic current leakage, and thus the combined-casing source response can be treated as a summation of the two individual responses. Figure 4 shows that the proposed casing source EM layout can produce measurable perturbations as a result of CO_2 injection over time.

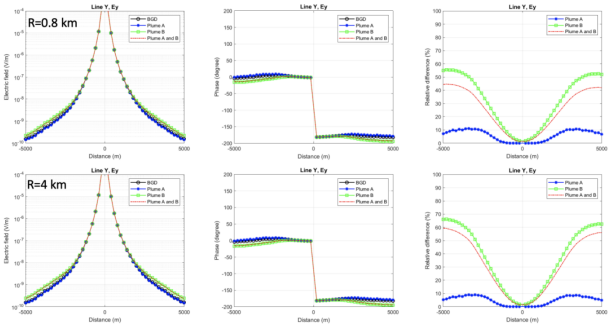

Figure 4. E_y components at 0.25Hz along line Y (**Figure** 3b) for the source connecting points E and F.

3. Deviated Casing Source EM at Utah FORGE site

In the last example we consider energizing a deviated steel-cased well, which is used as an injection well at the Utah FORGE EGS test site (Moore et al., 2019). Our focus is to assess whether casing source EM responses are sensitive to the stimulated zone at the FORGE site. **Figure** 5 shows the locations of the injection well (16-78(32)) as well as the 3D electrical resistivity model which is based on 3D MT inversion (Wannamaker et al., 2020). The size and electrical resistivity of the stimulated zone are based on Discrete Fracture Network modeling analysis (Finnila and Podgorney, 2020). We examine two fracture models. Fracture model 1 has resistivities of 2970 Ωm in the *x*-axis and 190 Ωm in the *y*- and *z*-axes. Fracture model 2 features resistivities of 302 Ωm, 270 Ωm, and 256 Ωm in the *x*-, *y*-, and *z*-axes, respectively. The downhole electrode is positioned at a depth of 1 km in the injection well, while the surface electrode is grounded 1.4 km away from the wellhead. The casing source EM responses are measured in observation wells 58-32 and 78B-32 using a three component high temperature EM sensor called the vertical EM profiling system (VEMP) (Wilt et al., 1997)

To apply the workflow to the deviated well, we construct a layered resistivity model aligning with the resistivity structure along the trajectory of the deviated injection well (16A-78(32)) in the 3D FORGE MT model (**Figure** 5b). Next, a vertical steel-cased well whose depth is the same as the measured length of the deviated well is inserted into the layered model. Finally, using the 3D SimPEG code, we simulate energizing the vertical well. The casing current densities are extracted along the vertical well from the SimPEG model and distributed along the actual trajectory of the deviated well in the 3D earth model. Note that the effects of casing's magnetic permeability are not considered here.

An important question is whether the casing current distribution from the verticalized steel-cased well can reasonably represent that of the true deviated well. In general, the current distribution from a verticalized well may not always closely resemble its deviated counterpart, because of the differing impact of a surface-grounded return electrode. In the context of the FORGE site, however, the proposed workflow is expected to be effective due to several key factors: 1) a highly-conductive steel-cased well is embedded in highly-resistive granite bedrock within the zone where measurements will be made, 2) the shallow area where the well is vertical is covered with conductive sediments, 3) the downhole electrode is positioned at a substantial depth (i.e., 1 km) beneath the surface, and 4) a return electrode on the surface is grounded sufficiently distant (i.e., 1.4 km) from the well. Hence, at the FORGE site, the primary factor influencing casing current distribution and the rate at which the current 'leaks' into the formation is reasonably assumed to be the resistivity contrast between the casing and the background resistivity, rather than the position of the return electrode or other factors. Thus, it is logically inferred that the current distribution along the vertical well reasonably represents the distribution for the deviated well. **Figure** 6 shows casing source EM responses with and without fractures, indicating measurable signal amplitudes and sensitivity to both fracture models.

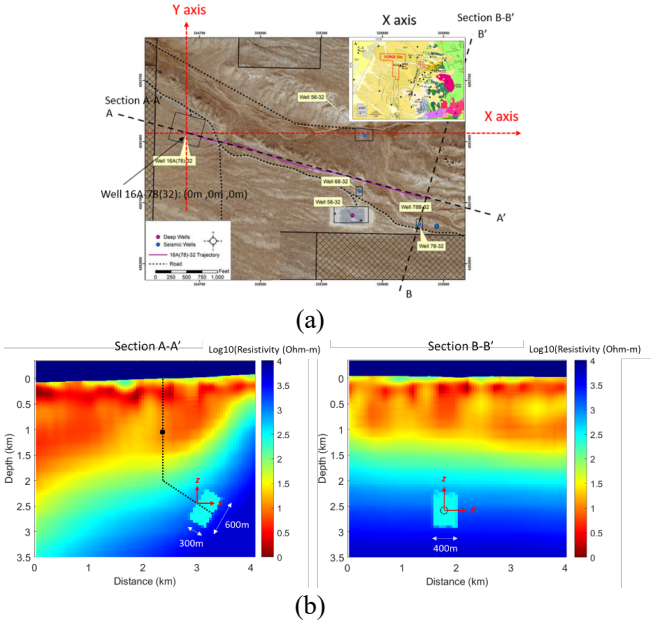

Figure 5. (a) The Utah FORGE map showing the injection well and other observation wells. The red broken lines indicate a coordinate system with the center set at the wellhead of the injection well. The trajectory of the deviated part of the injection well is indicated by the magenta line. (b) A-A'(left) and B-B'(right) cross-sections of the Utah FORGE MT model featuring an expected stimulated fracture zone and a local coordinate system (red) used for describing the orientation of the fracture system.

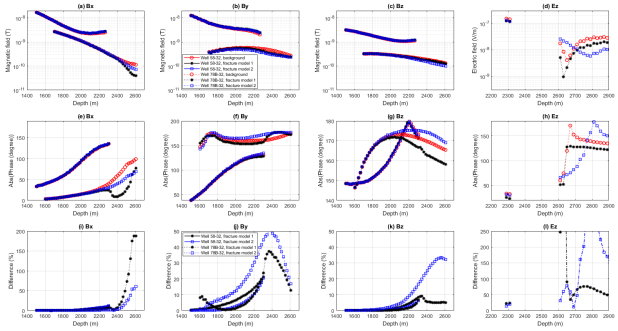

Figure 6. Comparison in EM measurements (the 1st row) at 50 Hz before and after stimulation, the phase (the 2nd row) and their relative amplitude differences (the 3rd row). The surface electrode is grounded at (-1.4km, 0km, 0km).

CONCLUSION

We have introduced a novel modeling workflow designed for the efficient simulation of casing source EM responses in a 3D complex geology model. This approach combines the strengths of both 3D cylindrical-mesh-based and 3D tetrahedral-mesh-based EM modeling codes. Through illustrative examples, we have demonstrated the effectiveness of our workflow in scenarios involving a vertical cased well, multiple vertical cased wells, and a single deviated cased well. While we acknowledge that our proposed workflow may not encompass all the details associated with casing EM modeling, we believe it can serve as a valuable first-order approximation for assessing casing source EM responses to realistic 3D geology model.

ACKNOWLEDGMENTS

This research received support from the Utah FORGE project and DOE's Core Carbon Storage and Monitoring Research program, sponsored by the U.S. Department of Energy under Contract No. DE-AC02-05CH11231.

REFERENCES

Alumbaugh, D., Um, E., Wilt, W., Nichols, E., and Osato, K. 2023. Deep Borehole EM Deployment for Fracture Mapping at the FORGE Geothermal Site. In Proceedings of the 48th Workshop on Geothermal Reservoir Engineering, Stanford, California.

Castillo-Reyes, O., Queralt, P., Marcuello, A., & Ledo, J. (2021). Land CSEM simulations and experimental test using metallic casing in a geothermal exploration context: Vallès basin (NE Spain) case study. IEEE Transactions on Geoscience and Remote Sensing, 60, 1-13.

Commer, M., Hoversten, G.M. and Um, E.S., 2015. Transient-electromagnetic finite-difference time-domain earth modeling over steel infrastructure. Geophysics, 80(2), E147-E162.

Daily, W., Ramirez, A., Newmark, R. and Masica, K., 2004. Low-cost reservoir tomographs of electrical resistivity. The Leading Edge, 23(5), 472-480.

Finnila, A., and Podgorney, R. 2020. Exploring hydraulic fracture stimulation patterns in the forge reservoir using multiple stochastic DFN realizations and variable stress conditions. In Proceedings of the 45th Workshop on Geothermal Reservoir Engineering.

Heagy, L.J. and Oldenburg, D.W., 2022. Electrical and electromagnetic responses over steel-cased wells. The Leading Edge, 41(2), 83-92.

Hu, Y., Yang, D., Li, Y., Wang, Z. and Lu, Y., 2021. 3-D numerical study on controlled source electromagnetic monitoring of hydraulic fracturing fluid with the effect of steel-cased wells. IEEE Transactions on Geoscience and Remote Sensing, 60, 1-10.

Lee, K.H., Kim, H.J. and Uchida, T., 2005. Electromagnetic fields in a steel-cased borehole. Geophysical prospecting, 53(1), 13-21.

Li, Y. and Yang, D., 2019. Fast electrical imaging of injected fluid in hydraulic fracturing using a practical interactive parameter estimation method. In SEG Technical Program Expanded Abstracts 2019, 1024-1028, Society of Exploration Geophysicists.

Marsala, A.F., Hibbs, A.D. and Morrison, H.F., 2014, October. Borehole casing sources for electromagnetic imaging of deep formations. In SPE Annual Technical Conference and Exhibition? (SPE-170845). SPE.

MacLennan, K., Nieuwenhuis, G., Ramadoss, V., Wilkinson, M., Anderson, P., and Richards, T., 2016, October. Using depth to surface resistivity for mapping CO2. In 2016 SEG International Exposition and Annual Meeting.

Puzyrev, V., Vilamajo, E., Queralt, P., Ledo, J. and Marcuello, A., 2017. Three-dimensional modeling of the casing effect in onshore controlled-source electromagnetic surveys. Surveys in Geophysics, 38, 527-545.

Schenkel, C.J. and Morrison, H.F., 1990, Effects of well casing on potential field measurements using downhole current sources, Geophysical Prospecting, 38(6), 663-686.

Sullivan, M., Rodosta, T., Mahajan, K. and Damiani, D., 2020. An overview of the Department of Energy's CarbonSAFE Initiative: Moving CCUS toward commercialization. AIChE Journal, 66(4), e16855.

Tang, W., Li, Y., Swidinsky, A., and Liu, J. 2015. Three-dimensional controlled-source electromagnetic modelling with a well casing as a grounded source: a hybrid method of moments and finite element scheme. Geophysical Prospecting, 63, 1491-1507.

Um, E.S., Kim, J., Wilt, M.J., Commer, M. and Kim, S.S., 2019. Finite-element analysis of top-casing electric source method for imaging hydraulically active fracture zones. Geophysics, 84(1), E23-E35.

Um, E.S., Kim, J. and Wilt, M., 2020. 3D borehole-to-surface and surface electromagnetic modeling and inversion in the presence of steel infrastructure. Geophysics, 85(5), E139-E152.

Wannamaker, P., Simmons, S., Miller, J., Hardwick, C., Erickson, B., Bowman, S., Kirby, S., Feigl, K., and Moore, J. 2020. Geophysical Activities over the Utah FORGE Site at the Outset of Project Phase 3. Proceedings, 45th Workshop on Geothermal Reservoir Engineering, Stanford University, Stanford, CA.

Weiss, C.J., Aldridge, D.F., Knox, H.A., Schramm, K.A. and Bartel, L.C., 2016. The direct-current response of electrically conducting fractures excited by a grounded current source. Geophysics, 81(3), E201-E210.

Weiss, C.J., 2017. Finite-element analysis for model parameters distributed on a hierarchy of geometric simplices. Geophysics, 82(4), E155-E167.

Wilt, M., Takasugi, S., Uchida, T., Kasameyer, P., Lee, K. and Lippmann, M. 1997. Fracture mapping in geothermal fields with long-offset induction logging. In Proceedings: Twenty-Second Workshop on Geothermal Reservoir Engineering, Stanford University, Stanford, California.

7th International Symposium on Three-Dimensional Electromagnetics
Vancouver, BC, Canada, November 13–15, 2023

On the Robustness, Efficiency and Scalability of an Iterative Framework in Combination With the Block-Based PREconditioner For Square Blocks PRESB Applied To Controlled-Source Electromagnetic Modelling

Michael Weiss[1], Thomas Kalscheuer[2] and Maya Neytcheva[2]
[1]Leibniz Institute for Applied Geophysics, Hanover, Germany
[2] Uppsala University, Uppsala, Sweden

Summary

We introduce an efficient and robust iterative framework based on the Block-Based PREconditioner for Square Blocks known as PRESB for 3D controlled-source electromagnetic problems in frequency domain. We study the robustness, efficiency and scalability of the iterative solver and compare it to other solution methods.

Keywords: iterative solution methods, preconditioning, numerical modelling, controlled-source electromagnetics

Introduction

Electromagnetic (EM) surveys may comprise numerous receivers and multiple sources in complex three-dimensional (3D) settings with topography and subsurface structures. Accurate numerical forward or inverse modelling of such large-scale studies accounting for their respective survey setup as well as reliefs requires large 3D meshes which may yield computational models of large proportion ranging from a couple to hundreds of millions degrees of freedom. Solving problems of these sizes is computationally challenging and expensive and consequently strategies reducing the computational burden are paramount. A key component of both the forward and inverse problem is the solution of the algebraic system of equations stemming from Maxwell's equations, that is solving a discrete system of the form $\mathbf{Ux} = \mathbf{b}$ where matrix $\mathbf{U}$ is sparse and non-singular and where $\mathbf{x}$ and $\mathbf{b}$ denote the solution and source vectors, respectively.

In general, two types of numerical solution methods are employed to obtain solutions of linear systems of equations, namely direct and iterative approaches with their respective advantages and disadvantages. Direct methods find broad application due to their generality, robustness and ease of use and despite their high memory requirements (proportional to $\mathcal{O}(N^2)$ in 3D with N denoting the number of degrees of freedom) for large problems. Iterative solution techniques on the other hand are considered very resource friendly, but may be afflicted by slow convergence or even divergence if applied without adequate and problem-specific preconditioning techniques as preconditioning greatly improves the robustness and efficiency of iterative methods.

The objective of this work is to present a developed and efficient iterative solution framework for controlled-source EM problems. The framework is shown to be robust to discretisation and material parameters. In addition, the framework is compared against other iterative and direct solution methods. Lastly, the scalability of the framework is investigated and studied.

Method

The algebraic linear system of equations governing the physics encountered in frequency-domain controlled-source EM problems based on a total field formulation is given by

$$(\mathbf{K} + i\mathbf{M}_\sigma - \mathbf{M}_\varepsilon)\,\mathbf{e} = \mathbf{b}, \tag{1}$$

where matrix $\mathbf{K}$ denotes the sparse symmetric positive semi-definite stiffness matrix, matrices $\mathbf{M}_\sigma$ and $\mathbf{M}_\varepsilon$ are the sparse symmetric positive definite mass matrices. The vectors $\mathbf{e}$ and $\mathbf{b}$ denote the solution vector and the right hand side vector.
This sparse symmetric complex-valued system can be cast into an equivalent real-valued two-by-two block system that reads as follows

$$\underbrace{\begin{bmatrix} \mathbf{M}_\sigma & -(\mathbf{K}-\mathbf{M}_\varepsilon) \\ \mathbf{K}-\mathbf{M}_\varepsilon & \mathbf{M}_\sigma \end{bmatrix}}_{\mathbf{C_{RI}}} \begin{bmatrix} \mathbf{e_R} \\ -\mathbf{e_I} \end{bmatrix} = \begin{bmatrix} \mathbf{b_I} \\ \mathbf{b_R} \end{bmatrix}, \tag{2}$$

and belongs to systems of the more general type of

form

$$\boldsymbol{\mathcal{A}} = \begin{bmatrix} \mathbf{A} & -b\,\mathbf{B_2} \\ a\,\mathbf{B_1} & \mathbf{A} \end{bmatrix}. \tag{3}$$

For systems of this type and if matrix $\mathbf{A}$ is symmetric positive definite and the non-zero scalars a and b are of the same sign, there exists an efficient preconditioner known as PRESB short for 'PREconditioner for Square Blocks' (see e.g. Axelsson et al., 2014) that is of form

$$\boldsymbol{\mathcal{P}}_{\text{PRESB}} = \begin{bmatrix} \mathbf{A} & -b\,\mathbf{B}_2 \\ a\,\mathbf{B_1} & \mathbf{A} + \sqrt{ab}(\mathbf{B_1} + \mathbf{B_2}) \end{bmatrix} \tag{4}$$

and for which it can be shown that all the eigenvalues of the preconditioned system $\boldsymbol{\mathcal{P}}^{-1}_{\text{PRESB}}\boldsymbol{\mathcal{A}}$ lie in the interval 0.5 and 1 (see e.g. Axelsson et al., 2016). The clustering of the eigenvalues translates to excellent convergence properties of the preconditioner. In addition, the preconditioner is robust with respect to mesh discretisation and material parameters. The preconditioner possesses the following block factorisation

$$\begin{bmatrix} \mathbf{A} & -\mathbf{B}^T \\ \mathbf{B} & \mathbf{A}+\mathbf{B}+\mathbf{B}^T \end{bmatrix} = \begin{bmatrix} \mathbf{I} & -\mathbf{I} \\ \mathbf{0} & \mathbf{I} \end{bmatrix} \begin{bmatrix} \mathbf{A}+\mathbf{B} & \mathbf{0} \\ \mathbf{0} & \mathbf{I} \end{bmatrix} \begin{bmatrix} \mathbf{I} & \mathbf{0} \\ \mathbf{B} & \mathbf{I} \end{bmatrix} \begin{bmatrix} \mathbf{I} & \mathbf{0} \\ \mathbf{0} & \mathbf{A}+\mathbf{B}^T \end{bmatrix} \begin{bmatrix} \mathbf{I} & \mathbf{I} \\ \mathbf{0} & \mathbf{I} \end{bmatrix}. \tag{5}$$

Applied to the two-by-two system (2), the computational cost of applying the PRESB preconditioner amounts to solving to linear systems with $\mathbf{M}_\sigma + (\mathbf{K} - \mathbf{M}_\varepsilon)$ and $\mathbf{M}_\sigma + (\mathbf{K} - \mathbf{M}_\varepsilon)^T$, one multiplication with the matrix $\mathbf{M}_\sigma$ and three vector additions. This is equivalent to solving a system of the form

$$\underbrace{\begin{bmatrix} \mathbf{M}_\sigma & -(\mathbf{K}-\mathbf{M}_\varepsilon) \\ \mathbf{K}-\mathbf{M}_\varepsilon & \mathbf{M}_\sigma + 2(\mathbf{K}-\mathbf{M}_\varepsilon) \end{bmatrix}}_{\mathbf{P}_{\text{PRESB}}} \begin{bmatrix} \mathbf{w_1} \\ \mathbf{w_2} \end{bmatrix} = \begin{bmatrix} \mathbf{f_1} \\ \mathbf{f_2} \end{bmatrix}, \tag{6}$$

which is summarised in Algorithm 1 as

Algorithm 1: Solving linear system with preconditioner $\mathbf{P}_{\text{PRESB}}$

1 Solve $(\mathbf{M}_\sigma + \mathbf{K} - \mathbf{M}_\varepsilon)\,\mathbf{g} = \mathbf{f_1} + \mathbf{f_2}$
2 Compute $\mathbf{M}_\sigma\mathbf{g}$ and $\mathbf{f_1} - \mathbf{M}_\sigma\mathbf{g}$
3 Solve $(\mathbf{M}_\sigma + \mathbf{K} - \mathbf{M}_\varepsilon)\,\mathbf{h} = \mathbf{f_1} - \mathbf{M}_\sigma\mathbf{g}$
4 Compute $\mathbf{w_1} = \mathbf{g} + \mathbf{h}$ and $\mathbf{w_2} = -\mathbf{h}$

The linear systems in the above procedure constitute discretised $\mathcal{H}_0(\text{curl}, \Omega)$ problems which can be solved fast and efficiently using the auxiliary-space technique (see e.g. Xu, 1996; Hiptmair & Xu, 2007; Kolev & Vassilevski, 2009). Here, the auxiliary-space Maxwell solver (AMS) implemented in hypre (Falgout & Yang, 2002) is used to precondition a generalised conjugate residual method (GCR; Eisenstat et al., 1983) to obtain solution to systems involving $(\mathbf{M}_\sigma + \mathbf{K} - \mathbf{M}_\varepsilon)$. Alternatively, the systems at hand can be solved using a direct solver such as MUMPS (Amestoy et al., 2000) for example.

The two-by-two system given in equation (2) is solved using a GCR method and preconditioned with PRESB and the iterative solver is described in Algorithm 2. The algorithm thus consists of an outer solver with a nested inner solver. Each outer iteration requires applying the preconditioner PRESB thus necessitating two inner solves as outlined in Algorithm 1.

Algorithm 2: PRESB-preconditioned GCR method

Input: $\mathbf{C_{RI}}, \mathbf{b_{R,I}}, \mathbf{M}_\sigma + \mathbf{K} - \mathbf{M}_\varepsilon, \mathbf{M}_\sigma$, initial guess $\mathbf{x}_0$, tol
Output: $\mathbf{e_{R,I}}$
Set $\mathbf{r}_0 = \mathbf{b} - \mathbf{C_{RI}}\mathbf{x}_0$
for $i = 0, \dots m$ **do**
  Solve $\mathbf{P}_{PRESB}\mathbf{p}_i = \mathbf{r_i}$ using Algorithm 1
  $\mathbf{q}_i = \mathbf{C_{RI}}\mathbf{p}_i$
  $\mathbf{q}_i = \mathbf{q}_i - \sum_{j=0}^{i-1} \mathbf{q}_j \frac{(\mathbf{q}_i, \mathbf{q}_j)}{(\mathbf{q}_j, \mathbf{q}_j)}$
  $\mathbf{p}_i = \mathbf{p}_i - \sum_{j=0}^{i-1} \mathbf{p}_j \frac{(\mathbf{q}_i, \mathbf{q}_j)}{(\mathbf{q}_j, \mathbf{q}_j)}$
  $\alpha_i = \frac{(\mathbf{r}_i, \mathbf{q}_i)}{(\mathbf{q}_i, \mathbf{q}_i)}$
  $\mathbf{x}_{i+1} = \mathbf{x}_i + \alpha_i \mathbf{p}_i$
  $\mathbf{r}_{i+1} = \mathbf{r}_i - \alpha_i \mathbf{q}_i$
  if $\frac{||\mathbf{r}_{i+1}||_2}{||\mathbf{r}_0||_2} < tol$ **then** $\mathbf{e_{R,I}} = \mathbf{x}_{i+1}$ & Stop
end

The iterative framework described has been implemented using distributed-memory parallelism and makes use of functionalities provided by the open-source libraries PETSc (Balay et al., 2022), hypre (Falgout et al., 2006) and MUMPS (Amestoy et al., 2000) as a standalone Fortran code (see Weiss et al., 2023). More recently, the iterative framework has been added to custEM (Rochlitz et al., 2019) and will be made available with the next version update.

Results

Robustness

The results presented in the following subsection summarise the findings in Weiss et al. (2023). For the reader's convenience, the essential information and observations are repeated here.

The robustness of the iterative framework is tested

using two problems as depicted in Figure 1. Table 1 indicates relevant information about the model and source for Problems 1 and 2.
All simulations presented are run using two MPI processes on a AMD Ryzen Thread-ripper 2950X 16-core processor with a clock frequency of 3.5 GHz and with 128 GB RAM. Moreover, each computation is stopped when the relative residuals of the outer and inner solver dips below 10^{-12} and 10^{-3}, respectively.

The iterative framework is tested for Problem 1 with respect to variable frequencies as well as problem size at the same time. Table 2 displays the outer iteration counts and simulation times for three problem sizes and for four frequencies spanning almost five orders of magnitude. It can readily been observed that the outer iteration count is very stable across the tested range of frequencies. In addition, the outer iteration count is independent of the problem size.

Problem 2 is used to asses the robustness of the iterative solver with respect to magnetic permeability and dielectric permittivity. Results of simulations for the chosen material properties (see Table 1) are given in Table 3 and verify that the iterative framework is robust with regard to variable material properties as indicated by the outer iteration counts.

Comparison and Scalability

The iterative solver is compared to other solution methods and tested with regard to scalability using the crooked loop example on a three-layer Earth from the custEM toolbox (Rochlitz et al., 2019). All simulations are run using polynomial of first order on the example's finest mesh yielding $13'447'978$ degrees of freedom for the two-by-two system. The iterative procedure is terminated when the relative residual of the outer algorithm falls below 10^{-8}. All computations times are obtain on a Dell PowerEdge R940 server with four Intel Xeon Gold 6154 processors clocked at 3 GHz and 48 LRDIMM 64 GB, DDR4-2666, Quad Ranks.

The preconditioner PRESB is compared to a highly efficient block diagonal preconditioner (see e.g. Chen et al., 2010; Grayver & Bürg, 2014). The numerical experiments for this comparison are run using 56 MPI processes. Figure 2 shows the convergence histories for simulations using the PRESB and block diagonal preconditioner, respectively, across four frequencies. In addition, the corresponding simulation times are annotated in the plots. It is evident that PRESB requires fewer iterations to reach the desired relative residual and thus saves some time compared to the block diagonal preconditioner.

The scalability, time and memory requirements for the direct solver MUMPS and the iterative framework are compared in Figure 3. The plot on the left displays the run times against the number of parallel processes used and indicates that the iterative framework reduces the simulation times by a factor of 2.9 to 3.8. On the right, the memory usage is tracked over the run time for both the direct solver (blue) and iterative algorithm (red). Peak memory consumption is annotated in the plot. Overall, the iterative framework requires approximately one order of magnitude less memory for this example with a system size of $13'447'978$ than the direct solver MUMPS.

All in all, the developed iterative framework proves highly efficient in terms of computational time and memory requirements in comparison to the direct solver MUMPS. Further, as indicated by the convergence histories and the simulations times in Figure 2, PRESB is slightly more efficient than the block diagonal preconditioner. As the implementation of both preconditioners is based on similar building blocks, changing to the preconditioner PRESB is straight forward and simple and thus suggested.

Figure 3 further reveals the considerable potential of the algorithm in terms of computational resources which may be harnessed in inverse modelling by incorporating the iterative solver as an underlying engine for it.

Conclusion

The numerical experiments attest to the robustness of the PRESB-preconditioned GCR method with regard to frequency, problem size, mesh discretisation and spatially variable material properties, that is electric conductivity, magnetic permeability and dielectric permittivity. Comparisons with other solvers and the scalability example demonstrate the potential of the iterative solver in terms of computational resources and as a possible future engine for inversions.

Acknowledgements

This work was partly funded by Uppsala's Center for Interdisciplinary Mathematics (CIM) and by the Germany Ministry for Education and Research (BMBF) as part of the DESMEX II project in the framework of the research and development program Fona-r4 under grant 033R130DN.

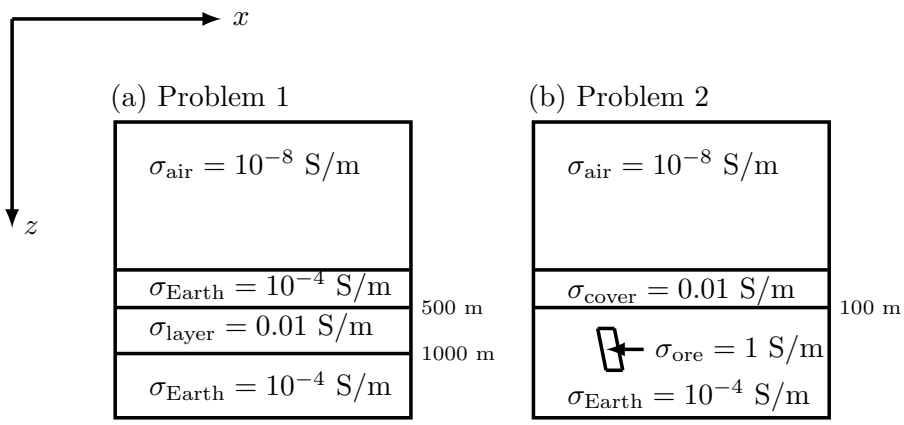

Figure 1: Schematic profile of Problems 1 and 2 (see Weiss et al., 2023).

Table 1: Model information for Problems 1 and 2

Model	Problem 1 - Layered Earth	Problem 2 - 3D model
Domain size [km^3]	$30 \times 30 \times 30$	$30 \times 36 \times 30$
Coordinates of 3D body	-	$(-4000, 2000, \pm 331), (-3000, 2000, \pm 331)$ $(-3000, 5000, \pm 331), (-2000, 5000, \pm 331)$
Source type	Grounded cable extending from $(-100, 0, 0)$ m to $(100, 0, 0)$ m	Grounded cable extending from $(-75, 0, 0)$ m to $(59, 0, 0)$ m
Source moment [Am]	100	100
Conductivities [S/m]	$\sigma_{\text{air}} = 10^{-8}$, $\sigma_{\text{Earth}} = 10^{-4}$, $\sigma_{\text{layer}} = 10^{-2}$	$\sigma_{\text{air}} = 10^{-8}$, $\sigma_{\text{Earth}} = 10^{-4}$, $\sigma_{\text{cover}} = 0.01$, $\sigma_{\text{ore}} = 1$
Relative permeabilities	$\mu_{\text{air}} = 1$, $\mu_{\text{Earth}} = 1$, $\mu_{\text{layer}} = 1$	$\mu_{\text{air}} = 1$, $\mu_{\text{Earth}} = 1$, $\mu_{\text{cover}} = 1$, $\mu_{\text{ore}} = 1$ or 10
Relative permittivities	$\varepsilon_{\text{air}} = 1$, $\varepsilon_{\text{Earth}} = 1$, $\varepsilon_{\text{layer}} = 1$	$\varepsilon_{\text{air}} = 1$, $\varepsilon_{\text{Earth}} = 5$, $\varepsilon_{\text{cover}} = 20$, $\varepsilon_{\text{ore}} = 1$
Approximation order	1st	1st
# elements	$54 \times 54 \times 54$	332'580
# degrees of freedom	980'100	2'033'986

Table 2: Problem 1: Robustness with respect to problem size and across frequency for the iterative solver shown by the outer iteration counts ($N_{\text{it}}^{\text{outer}}$) and solving times (time [s]) (see Weiss et al., 2023).

	frequency [Hz]							
	0.1		10		1000		8000	
Problem size	$N_{\text{it}}^{\text{outer}}$	time [s]	$N_{\text{it}}^{\text{outer}}$	time [s]	$N_{\text{it}}^{\text{outer}}$	time [s]	$N_{\text{it}}^{\text{outer}}$	time [s]
980'100	7	42.2	16	79.3	19	70.2	18	96.8
3'641'400	8	152.9	15	286.4	18	272.6	19	310.2
6'879'600	8	343.4	16	646.5	18	521.8	18	790.5

Table 3: Problem 2: Robustness with regard to spatially variable dielectric permittivity and for two different magnetic permeabilities for the ore body across frequencies for the iterative algorithm shown by the outer iteration counts (N_{it}^{outer}) and solution times (time [s]) (see Weiss et al., 2023).

relative dielectric permittivity of air, cover, host rock and ore body	$\varepsilon_r^{air}=1$, $\varepsilon_r^{cover}=20$, $\varepsilon_r^{Earth}=5$, $\varepsilon_r^{ore\ body}=1$			
relative magnetic permeability of ore body	$\mu_r=1$		$\mu_r=10$	
frequency [Hz]	N_{it}^{outer}	time [s]	N_{it}^{outer}	time [s]
0.1	9	590.4	11	691.6
10	16	282.3	16	279.8
100	23	278.5	24	285.1
8000	18	341.0	18	322.4

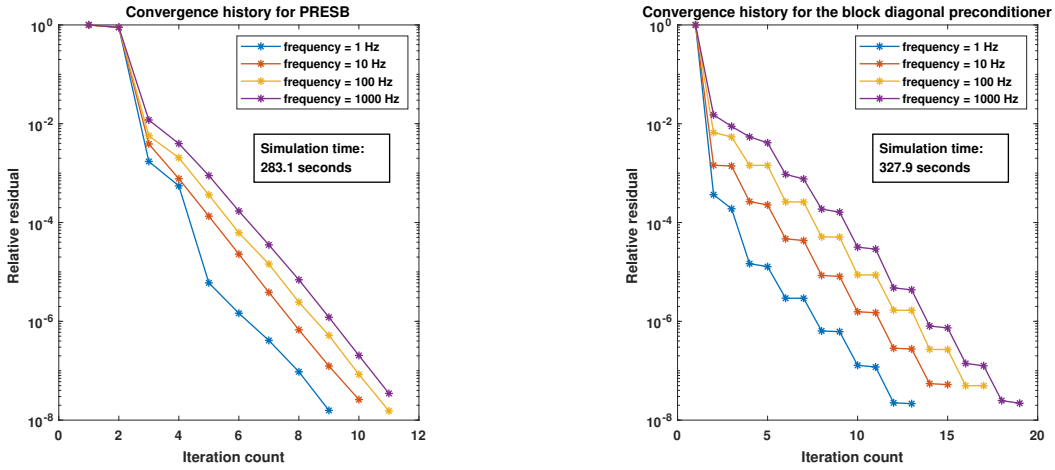

Figure 2: Comparison of the convergence histories for the crooked loop example run across four frequencies between PRESB and the block diagonal preconditioner. The subplots indicate the overall simulation time.

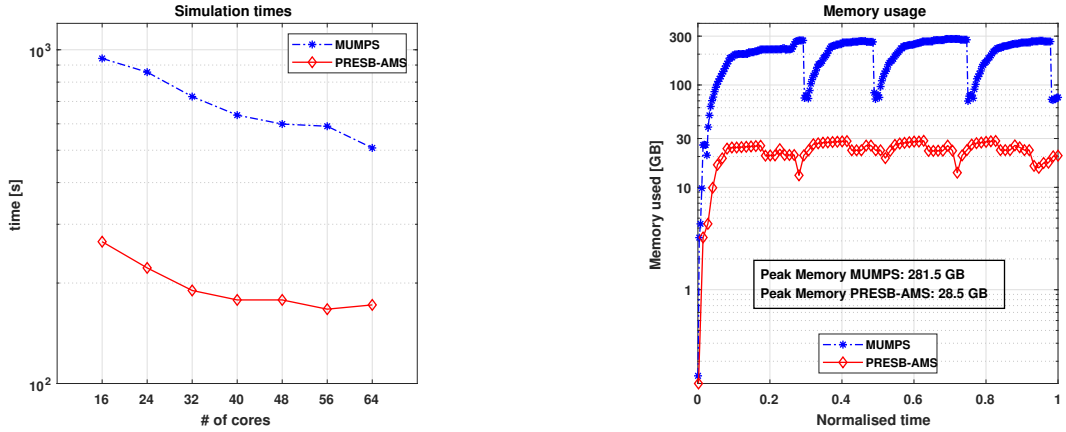

Figure 3: Scalabilities and computational requirements (time and memory) for the iterative framework denoted as PRESB-AMS and the direct solver MUMPS for the crooked loop example.

REFERENCES

Amestoy, P. R., Duff, I. S., & L'excellent, J.-Y. (2000). Multifrontal parallel distributed symmetric and unsymmetric solvers. *Computer Methods in Applied Mechanics and Engineering*, *184*(2-4), 501–520.

Axelsson, O., Farouq, S., & Neytcheva, M. (2016). Comparison of preconditioned Krylov subspace iteration methods for PDE-constrained optimization problems. *Numerical Algorithms*, *73*(3), 631–663.

Axelsson, O., Neytcheva, M., & Ahmad, B. (2014). A comparison of iterative methods to solve complex valued linear algebraic systems. *Numerical Algorithms*, *66*(4), 811–841.

Balay, S., Abhyankar, S., Adams, M. F., Benson, S., Brown, J., Brune, P., et al. (2022). *PETSc/TAO users manual* (Tech. Rep. No. ANL-21/39 - Revision 3.17). Argonne National Laboratory.

Chen, J., Chen, Z., Cui, T., & Zhang, L.-B. (2010). An adaptive finite element method for the eddy current model with circuit/field couplings. *SIAM Journal on Scientific Computing*, *32*(2), 1020–1042.

Eisenstat, S. C., Elman, H. C., & Schultz, M. H. (1983). Variational iterative methods for nonsymmetric systems of linear equations. *SIAM Journal on Numerical Analysis*, *20*(2), 345–357.

Falgout, R. D., Jones, J. E., & Yang, U. M. (2006). The design and implementation of hypre, a library of parallel high performance preconditioners. In *Numerical Solution of Partial Differential Equations on Parallel Computers* (pp. 267–294). Springer.

Falgout, R. D., & Yang, U. M. (2002). hypre: A library of high performance preconditioners. In *International Conference on Computational Science* (pp. 632–641).

Grayver, A. V., & Bürg, M. (2014). Robust and scalable 3-D geo-electromagnetic modelling approach using the finite element method. *Geophysical Journal International*, *198*(1), 110–125.

Hiptmair, R., & Xu, J. (2007). Nodal auxiliary space preconditioning in H (curl) and H (div) spaces. *SIAM Journal on Numerical Analysis*, *45*(6), 2483–2509.

Kolev, T. V., & Vassilevski, P. S. (2009). Parallel auxiliary space AMG for H (curl) problems. *Journal of Computational Mathematics*, 604–623.

Rochlitz, R., Skibbe, N., & Günther, T. (2019). custEM: Customizable finite-element simulation of complex controlled-source electromagnetic data. *Geophysics*, *84*(2), F17–F33.

Weiss, M., Neytcheva, M., & Kalscheuer, T. (2023). Iterative solution methods for 3D controlled-source electromagnetic forward modelling of geophysical exploration scenarios. *Computational Geosciences*, *27*, 81–102.

Xu, J. (1996). The auxiliary space method and optimal multigrid preconditioning techniques for unstructured grids. *Computing*, *56*(3), 215–235.

7th International Symposium on Three-Dimensional Electromagnetics
Vancouver, BC, Canada, November 13–15, 2023

Reparametrizing the Geophysical Inverse Problem using a Convolutional Neural Network

Anran Xu[1], Lindsey Heagy[1]
[1]Department of Earth, Ocean and Atmospheric Sciences, University of British Columbia

SUMMARY

The recent surge in artificial intelligence has garnered substantial attention among researchers, particularly in the context of incorporating machine learning algorithms into inversion procedures. In the realm of Computer Vision (CV), the Convolutional Neural Network (CNN) architecture has been identified as inherently enforcing prior knowledge, proving advantageous for addressing diverse CV inverse problems, including de-noising and inpainting. This intrinsic regularization effect has shown promise in enhancing models recovered through full waveform inversion of seismic, and it has the potential for application in other geophysical inverse problems. In this study, we examine the applicability to the inversion of DC resistivity data. The CNN maps an arbitrary vector to the model space (e.g., log-conductivity on the simulation mesh). The predicted subsurface model is fed into the SimPEG numerical simulation package to generate corresponding predicted measurements. Subsequently, the data misfit is computed by comparing these predicted measurements with the observed field measurements. This is combined with an L1 smallness term to form the objective function. The backpropagation algorithm is employed to update the trainable parameters of the CNN until convergence. Note that the CNN does not require training prior to the inversion, rather, the CNN weights are estimated in the inversion algorithm. Our preliminary work shows that we can recover models that are comparable to, and even superior to that obtained using a standard inversion. For example, we have found that relying on the implicit regularization of the CNN improves the recovery of the dip of a target when a standard L1 regularization is employed. This method is training-data-free, so it can be adapted to other EM inversion problems.

Keywords: Deep image prior (DIP), Convolutional Neural Network (CNN), Direct Current (DC) inversion

INTRODUCTION

The recent emergence of artificial intelligence has garnered significant attention from researchers, particularly regarding the integration of machine learning algorithms into the inversion algorithm. Researchers in Computer Vision (CV) have discovered that the Neural Network architecture inherently enforces a prior knowledge that is advantageous for addressing diverse CV inverse problems, including de-noising and inpainting (Hattori et al., 2021; Ulyanov et al., 2018). These works show that solving inverse problems in a self-supervised manner is feasible and sometimes has better performance than learning the prior in a supervised manner, which require a large training set, because of the inherent regularization effect in Convolutional Neural Networks (CNN) or Graph Neural Networks (GNN).

In this abstract, we focus on the Direct Current (DC) resistivity survey, which is used for a range of applications including mineral exploration, groundwater studies, and a variety of environmental and geotechnical applications. The goal of the inverse problem is to find a conductivity model of the subsurface that is consistent with the observed data and other prior information or assumptions. There are several avenues through which prior information and assumptions are included in the inversion: the choice reference model, norms on the components of the regularization, and the model parameterization (e.g., using log-conductivity or a parametric model). In this abstract, we explore the use of a CNN to parameterize the model. Our experiments thus far show that we can recover models that are comparable to a standard inversion, and that there may be some advantages in using the CNN. Using an example of a dipping structure, we find that relying on the implicit regularization of the CNN improves the recovery of the dip of a target as compared to standard approaches.

METHODS

In the DC resistivity survey, transmitters on the ground inject a steady state electrical current into the ground and the receivers on the ground observe the resulting distribution of potentials (voltages) on the surface (Fig. 1).

The conventional way of solving this inverse problem is by iteratively updating the conductivity values for each cell in the mesh which discretized the subsurface. At each iteration, we input the current conductivity model into a numerical simulation package (a PDE solver based on Maxwell's equations), whose output would be the predicted measurements. We define the objective function to be the summation of the data misfit term ϕ_d (i.e., the difference between predicted and field measurements) and the regularization term ϕ_m:

$$\min_{\mathrm{m}} \phi_d(m) + \beta\phi_m(m),$$

where m represents the conductivity model (see for example Oldenburg & Li, 2005). In our proposed method, the model, m, is parametrized by a convolutional neural network F_z, where z is the fixed input of the convolutional neural network (i.e., m = F_z(w)), where w is the vector of weights in the CNN. Another update we make is how we "cool" the influence of the regularization. Rather than only reducing the trade-off parameter multiplying the regularization, we simultaneously decrease the trade-off parameter multiplying the regularization and increase the contribution of the data misfit by the same amount. We have found that when using first-order optimization methods employed in deep learning that this leads to better convergence. Thus, the objective function in our proposed method is:

$$\min_{w} \ (1-\beta)\phi_d\big(F_z(w)\big) + \beta|F_z(w) - m_{ref}|^1.$$

Since the inverse problems in geophysics are typically ill-posed, the regularization plays a very important role in inversion.

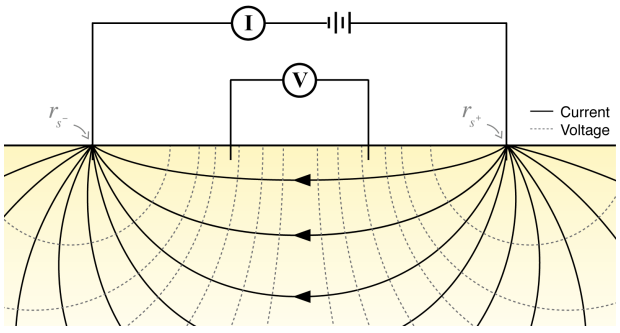

Figure 1: Transmitter and receiver in a DC resistivity survey (Cockett et al., 2016).

To demonstrate, we consider a model that consists of 2 layers with a dike in the second layer, as shown in Figure 2. We consider 3 different dip angles (first, second, and third rows) to test the robustness of the proposed model. We simulate a dipole-dipole survey with 348 data points. We perform several inversions with the conventional methods to serve as the benchmark. The second column used an approximate L0 norm on the smallness and an L1 norm on the smoothness; these inversions were performed without sensitivity weighting. The third column used an L0 norm on the smallness and an L1 norm on the smoothness, and these inversions were performed with sensitivity weightings. Our results using a CNN to parameterize the model are shown in the fourth column. Note that only a smallness term is used in the regularization, and an L1 norm is applied.

All models recover a conductive structure in approximately the correct location, but we see the influence of the first-order smoothness in the standard inversion results, which tends to align structures with the axes along which we are regularizing (horizontal and vertical). The use of the CNN and only the smallness term is better able to recover the dip of the target. Although no explicit smoothness term is used in the regularization, we hypothesize that the CNN provides implicit regularization that promotes recovery of a reasonable target.

DISCUSSION

In this study, we examine the applicability of the inherent regularization effect from the CNN structure to the inversion of DC resistivity data by utilizing trainable weights within the CNN to parameterize the conductivity model. Namely, the CNN maps an arbitrary vector to the mesh space. The predicted subsurface model is then fed into the numerical simulation package to generate corresponding predicted measurements. Subsequently, the objective function value is computed. Compared to the objective function in the conventional methods, the objective function in the proposed methods doesn't have the smoothness term and doesn't use sensitivity weighting. The backpropagation algorithm is employed to update the trainable parameters of the CNN until convergence. Note that the CNN does not require training prior to the inversion, rather, the CNN weights are estimated in the inversion algorithm. Our preliminary work shows that we can recover models that are comparable to, and even superior to that obtained using a standard inversion. For example, we have found that relying on the implicit regularization of the CNN improves the recovery of the dip of a target when a standard L1-smallness regularization is employed (Figure 2). In general, the proposed method can also eliminate the problem that structures are concentrated near the electrodes in the recovered model. This method is training-data-free, so it can be adapted to other EM inversion problems.

CONCLUSION

There are many choices of CNN architecture that can be employed and it's likely that the best choice of network will depend on the nature of the expected model, we conduct inversions for the above examples (3 examples in Figures 2) with the same CNN architecture to illustrate the robustness of the method. The next step of this project would be further exploring this implicit regularization effect by looking at the inversion results using different depths of the CNN architecture, different modes for the up-sampling layers, and different kernel sizes and stride values for the convolutional layers.

ACKNOWLEDGMENTS

We would like to thank Doug Oldenburg, Devin Cowan, Jorge Lopez-Alvis, Joseph Capriotti, John M. Weis, Johnathan C. Kuttai and Santiago Soler for their invaluable guidance and advice on SimPEG usage.

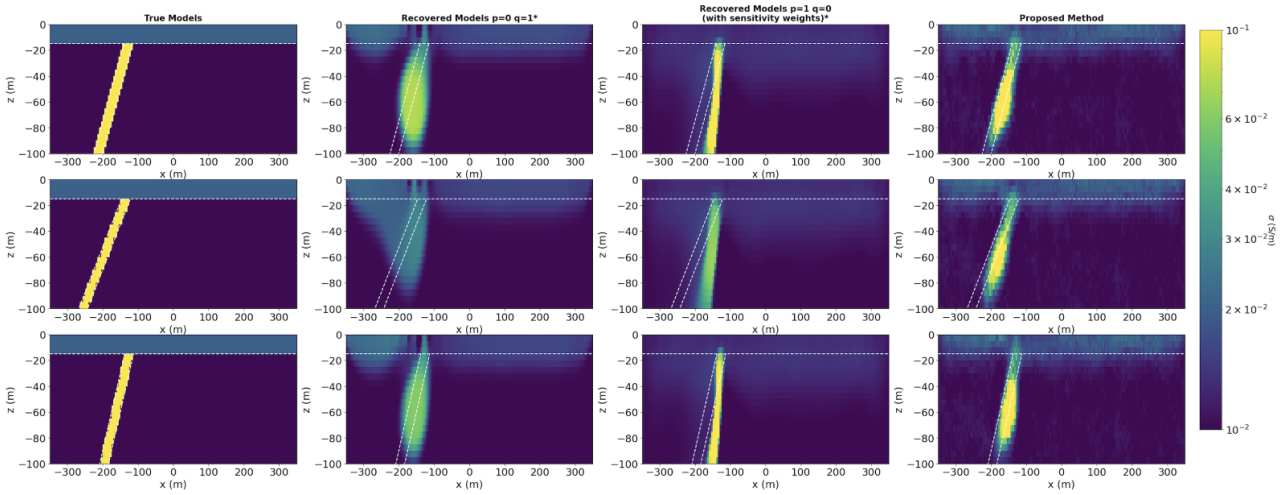

Figure 2: The comparation between the conventional methods (middle two columns) and proposed method (the right most column) in three dike models with the different dip angles. The subplots on the second/third column are from the standard sparse-norms inversions without/with sensitivity weights respectively. The p and q values shown indicate the choice of norm used for the smallness and smoothness terms respectively.

REFERENCES

Cockett, R., Kang, S., Heagy, L. J., Pidlisecky, A., & Oldenburg, D. W. (2015). SimPEG: An open source framework for simulation and gradient based parameter estimation in geophysical applications. Computers & Geosciences.

Ulyanov, D., Vedaldi, A., and Lempitsky, V., (2018), "Deep Image Prior," Proceedings of the IEEE Conference on Computer Vision and Pattern Recognition (CVPR), pp. 9446-9454.

Cockett, R., Heagy, L. J., and Oldenburg D. W., (2016). "Pixels and their neighbors: Finite volume." The Leading Edge, 35(8), 703–706.

Zhu, W., Darve, K., Biondi B., and Beroza, G., (2022), "Integrating deep neural networks with full-waveform inversion: Reparameterization, regularization, and uncertainty quantification," *GEOPHYSICS* 87: R93-R109.

Hattori, S., Yatagawa, T., Ohtake, Y., and Suzuki H., (2021), "Deep Mesh Prior: Unsupervised Mesh Restoration using Graph Convolutional Networks," Proceedings of the IEEE Conference on Computer Vision and Pattern Recognition (CVPR).

Negative transients in central-loop time-domain electromagnetic data: Induced polarization or 3D coupling effect?

Dikun Yang[1], Ming Cheng[1] and Qiang Luo[2]
[1] Southern University of Science and Technology (SUSTech)
[2] Guangdong Provincial Geophysical Prospecting Team

SUMMARY

Negative transient data in time-domain electromagnetic (TEM) are often explained by the induced polarization (IP) effect. However, a field example from a mineral exploration site in China proves that the 3D coupling effect, as a result of the strong literal variation in conductivity, can be a more appealing explanation. This article presents an interesting TEM dataset that confused geophysicists who were used to the conceptual model of 1D layered earth. Using the advanced fast 3D modeling tools accelerated by the survey decomposition method and decentralized massive parallel computing, we can quickly establish some representative block models that help us understand and verify the mechanism of negative transient TEM data. The forward modeling exercises also generates a good candidate of the initial model for the subsequent inversion process, as the regular uniform subsurface models may lead to a non-convergence due to local minima. The outcome of our research is a robust workflow for 3D inversion in practice: fast forward simulation of ballpark models to search for an initial model sufficiently close to the truth, then warm-start the 3D inversion to fine-tune the small-scale structures.

Keywords: time-domain electromagnetic, three-dimensional, inversion, negative transients, induced polarization

INTRODUCTION

The central-loop configuration of time-domain (transient) electromagnetic (TEM) places the receiver coil at the middle of the transmitter loop. Such a configuration, as well as the ones with a transmitter-receiver offset sufficiently small, has the advantage of a strong source-target-receiver coupling and the ability of being adopted for airborne and other mobile platforms (Maurya et al., 2023).

It also appears repeatedly in literatures that the central-loop configuration can be used to discriminate the induced polarization (IP) effect, which is indicative in mineralization, soil contamination and other applications. Theoretical studies have proven that only chargeable earth media characterized by the Cole-Cole model or alike can generate negative transient data for coincident loop systems (Weidelt, 1982). Recently, a number of works, particularly for the airborne TEM, have proposed different methods to extract valuable IP information from the negative data that were once discarded as uninterpretable data (e.g. Legault, 2015; Kang & Oldenburg, 2016; Maurya et al., 2022).

However, to use the inductive source central-loop TEM for IP, one has to assume that the source loop can be regarded as a magnetic dipole. For non-dipole loop sources, negative central-loop data may not necessarily be the IP effect. This article reports a real dataset with negative transients that were thought to be the IP effect but later numerically and geologically proven to be the 3D coupling effect.

In the following, we first describe the background of the site, the survey and the data; then some numerical tools were developed to enable people to efficiently explore the possibilities of 3D effects; eventually, we demonstrate how we used the tools to solve the puzzle, and to yield a conclusive model through a warm-started 3D inversion.

SURVEYS AND DATA

The field data were collected at a polymetallic mining site in Guangdong province, south China. The survey area is composed of two distinct geologic units, the Cambrian Gaotan Formation made of fine-grained quartz sandstone and the Cambrian Niujiaohe Formation composed of siltstone and metamorphic sandstone (Figure 1). Rock samples from the Gaotan Formation on the southeastern side of the area have measured resistivities from 8000 to 20000 Ω·m; the Niujiaohe Formation on the northwestern side is in the range from 46 to 200 Ω·m.

A survey line of receiver stations was planned from the distance 340 to 2160 m at a 10 m spacing. Six rectangular transmitter loops of 750 × 150 m were deployed to cover the entire line, so that the receiver stations are always in the central portion of the loop where the primary magnetic field is mostly vertical (Figure 1). At each station, the

dBz/dt data were measured at 28 time channels from 0.05262 to 24.291 ms with a step-off current waveform.

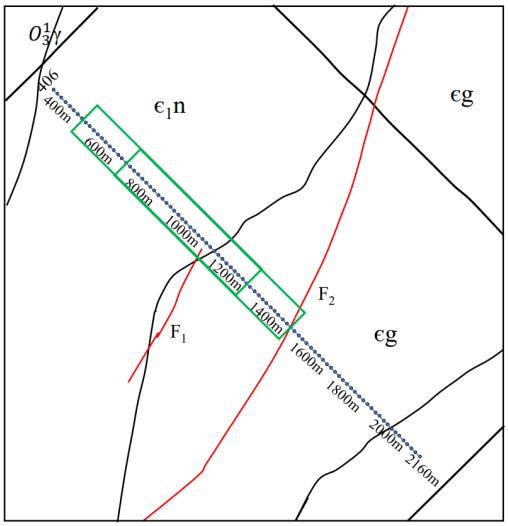

Figure 1: Geological map and the survey layout. The blue dots mark the receiver stations; two of the six rectangular transmitter loops are outlined by green.

The TEM decay patterns along the line is variable (Figure 2). Consistently normal and slow decays are observed at the stations smaller than 1000 m (Figure 3a); clear positive-negative sign flips are found at the stations around 1000 m (Figure 3b); the stations beyond 1100 m are characterized by rapid positive decays followed by noises (Figure 3c).

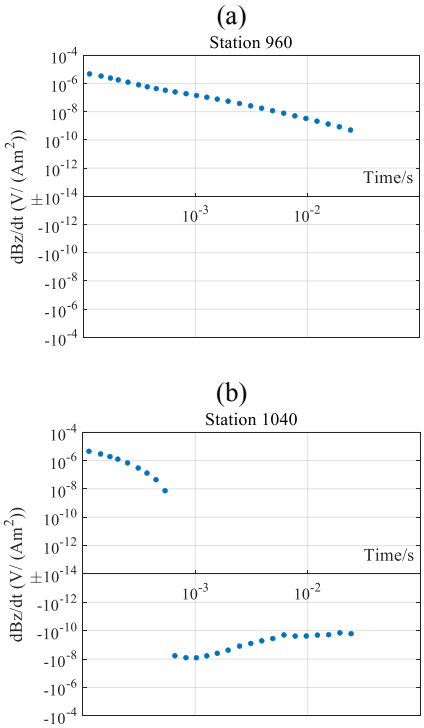

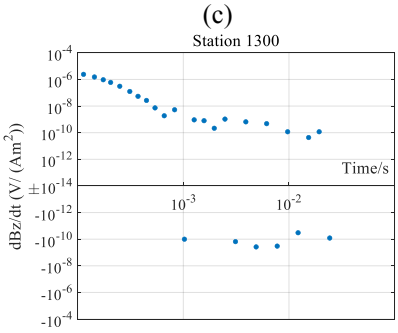

Figure 3: TEM decay data at select stations.

The 1D layered earth inversions were first performed (Figure 4). Some stations are missing on the cross section as the result of negative transient data and high noise. The negative transients around Station 1000 m are clear signals, and some practitioners proposed to interpret it using the Cole-Cole IP model. We did not think so. Most IP effects are found in a resistive background, where the induced currents can dissipate quickly, leaving alone the opposite discharging currents of the IP effect. It is unlikely IP-caused negative transients can be observed at the stations close to the conductive Niujiaohe Formation. Our hypothesis is that the rectangular source loop cannot be treated as a dipole source, and the 3D coupling between the large loop and the geologic structure is responsible for the sign flips in the central-loop data.

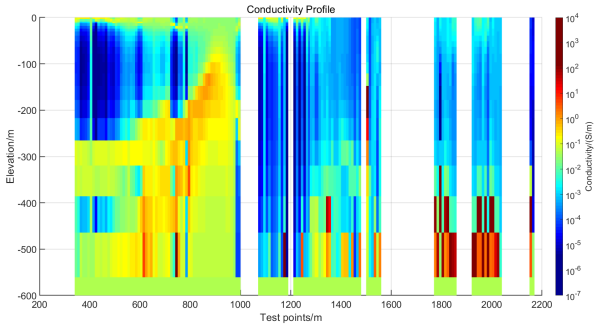

Figure 4: Stitched 1D inversion models.

SURVEY DECOMPOSITION METHOD

3D numerical simulation is necessary to verify our hypothesis. While rigorous 3D TEM modeling methods have been long established, practitioners often find it unpractical to use because of the long computing time compared with the 1D and plate modeling. In general, people manipulate models and expect to obtain the responses in seconds or minutes. To meet the need of timely trial-and-error forward modeling, we develop fast 3D modeling tools using the survey decomposition (SD) (Yang & Oldenburg, 2016).

In our implementation, the large source loop is treated as a combination of magnetic dipoles. Depending on the

time channel or the spatial scale of EM induction, the loop needs to be divided finely for the early times and coarsely for the late times. The resultant dipole source-receiver pairs are then efficiently modelled using local meshes customized for individual pairs (Figure 5). The time stepping for TEM is also decomposed to allow multiple time steps to be computed in parallel and at scale-adapted step sizes, so late times do not need to wait for the early times. Each decomposed subproblem is only for one datum and is solved on a local mesh only accommodating a dipole source and a receiver operating at a certain time channel.

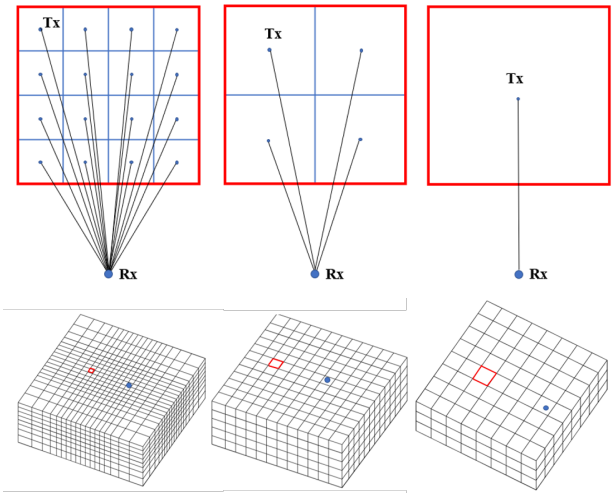

Figure 5: Decomposition of source loop and the local meshes for early (left), middle (middle), and late (right) time channels.

Our 3D TEM algorithm adopts the finite volume method on rectilinear meshes; the time stepping is based on the implicit backward Euler method; the linear system of equations is solved by the parallel direct solver MKL PARDISO; the code is written by C++. We present some metrics of an example TEM sounding (Table 1). The sounding consists of 25 time channels from 0.1 to 30 ms. The early times require finer decomposition of the loop and smaller time steps; for time channels later than 4.7 ms, the large loop can be effectively represented by a single magnetic dipole. The local meshes are relatively small at the order of dozens of thousands of cells. The computing time of each subproblem varies from 7 to 14 s. If the independent subproblems are solved on a cluster with sufficient nodes, the 3D modeling of this sounding can be finished in seconds.

The independency of subproblems after SD makes the method particularly suitable for massive parallelization. In another test with 2850 subproblems, SD shows a good linear scalability from 100 nodes (4000 cores) all the way up to 780 nodes (31200 cores) (Figure 6). Further speed-up can be expected on even larger clusters or cloud computing.

Table 1: Decomposed subproblems of one sounding.

Time Channels (s)	Time step (s)	Number of dipoles	Number of cells in local mesh	CPU time of a single subproblem(s)
1×10^{-4}	5.0×10^{-6}	16	28,800–29,760	7
1.208×10^{-4}	6.308×10^{-6}	16	28,800–29,760	7
1.499×10^{-4}	7.498×10^{-6}	16	28,800–30,720	7
2.005×10^{-4}	1.003×10^{-5}	9	29,760–31,620	8
2.499×10^{-4}	1.250×10^{-5}	9	29,760–31,620	8
3.001×10^{-4}	1.500×10^{-5}	9	30,720–32,640	8
3.813×10^{-4}	1.907×10^{-5}	9	30,720–32,674	8
4.805×10^{-4}	2.403×10^{-5}	4	32,640–34,782	9
7.108×10^{-4}	3.554×10^{-5}	4	33,660–35,836	9
9.475×10^{-4}	4.737×10^{-5}	4	34,680–35,836	9
1.204×10^{-3}	4.013×10^{-5}	4	35,700–36,890	9
1.699×10^{-3}	5.665×10^{-5}	4	36,720–37,800	10
2.149×10^{-3}	7.164×10^{-5}	4	36,750–37,800	10
2.599×10^{-3}	8.664×10^{-5}	4	36,750–37,800	10
3.498×10^{-3}	1.166×10^{-4}	4	36,750–37,944	10
4.749×10^{-3}	1.583×10^{-4}	1	39,060	11
5.498×10^{-3}	1.833×10^{-4}	1	40,320	11
5.999×10^{-3}	1.999×10^{-4}	1	40,460	11
8.249×10^{-3}	2.750×10^{-4}	1	41,616	11
1.075×10^{-3}	2.688×10^{-4}	1	44,064	12
1.325×10^{-2}	3.313×10^{-4}	1	45,928	12
1.600×10^{-2}	4.000×10^{-4}	1	46,656	13
2.175×10^{-2}	5.437×10^{-4}	1	47,952	13
2.550×10^{-2}	6.376×10^{-4}	1	49,248	14
3.000×10^{-2}	7.500×10^{-4}	1	51,840	14

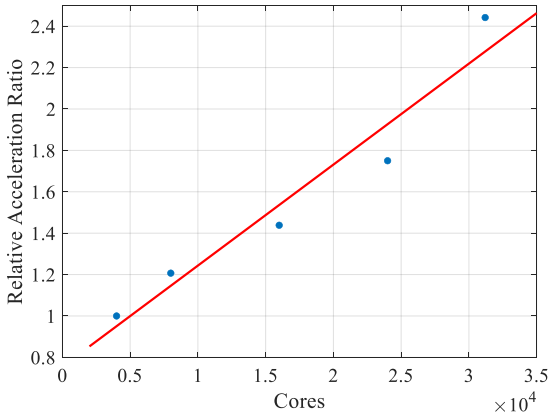

Figure 6: Acceleration in the environment of massive parallelization.

FORWARD SIMULATION

A number of block models are constructed to investigate the positive-negative transient data around Station 1000. Each forward modeling is decomposed to 1755 independent subproblems. The computing time of those subproblems on 50 cluster nodes is about 3.8 minutes, short enough for people to carry out trial-and-error simulations for hypothesis tests.

After some trials, we construct a contact model to reasonably reproduce the positive-negative transients observed in the field. The model consists of a resistive quarter-space of 10^{-4} S/m and a conductive quarter-space of 10^{-2} S/m; a very conductive block of 10^{2} S/m is embedded in the conductive side and is out-cropping. When the transmitter loop is placed across the contact

boundary (Figure 7a), the receivers off the conductor can observe sign-flipped transient data (Figure 7b).

We offer an intuitive explanation of such a phenomenon. At early times, the induced current is strong in both the conductive and the resistive sides, so the transients are positive. After a period of time, the induction on the resistive side disappears quickly, leaving only a horizontally circular eddy current on the conductive side. So, at late times, the receivers outside of the conductor measure the magnetic field generated by the slowly-decaying eddy current loop confined in the conductor.

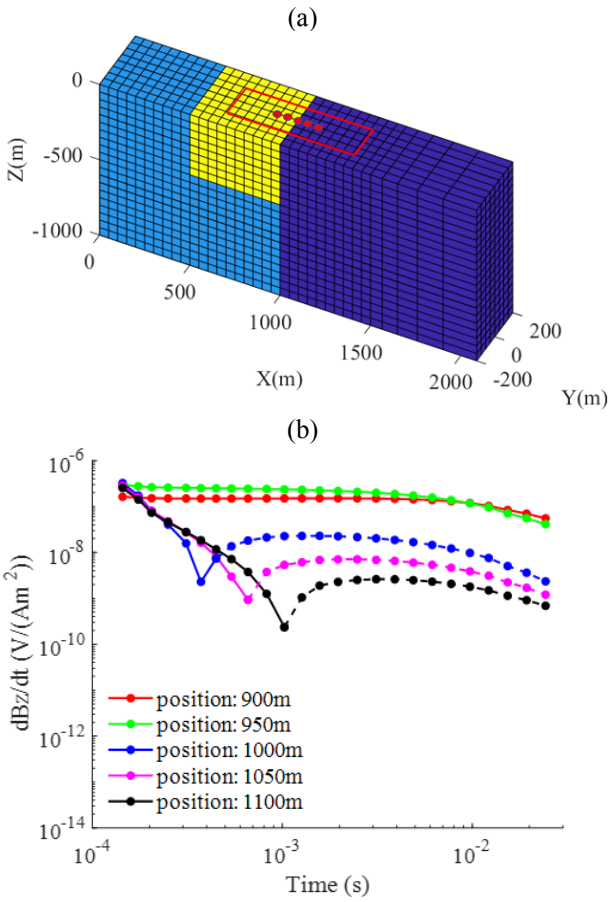

Figure 7: Forward simulation of conceptual models. (a) A contact and block model and the layout of source loop outlined by the red rectangle; (b) The simulated TEM data at the receiver locations marked by the red dots.

INVERSIONS

The TEM data from the transmitter loop that contains strong positive-negative transients (Figure 3b) are chosen for 3D inversion. The first attempt of 3D inversion is carried out with a starting model of a uniform subsurface. However, the inversion stalls in a local minimum after a few iterations with little improvement in the data misfit (Figure 8a). The recovered model does not represent anything geologically meaningful or tendency of moving towards reasonable models (Figure 8b). The reason is that it is impossible for the inversion to fit the negative data by knowingly generating strong lateral variations. Mathematically, the starting model is not sufficiently close to the true model, so the gradient-based model search may fail.

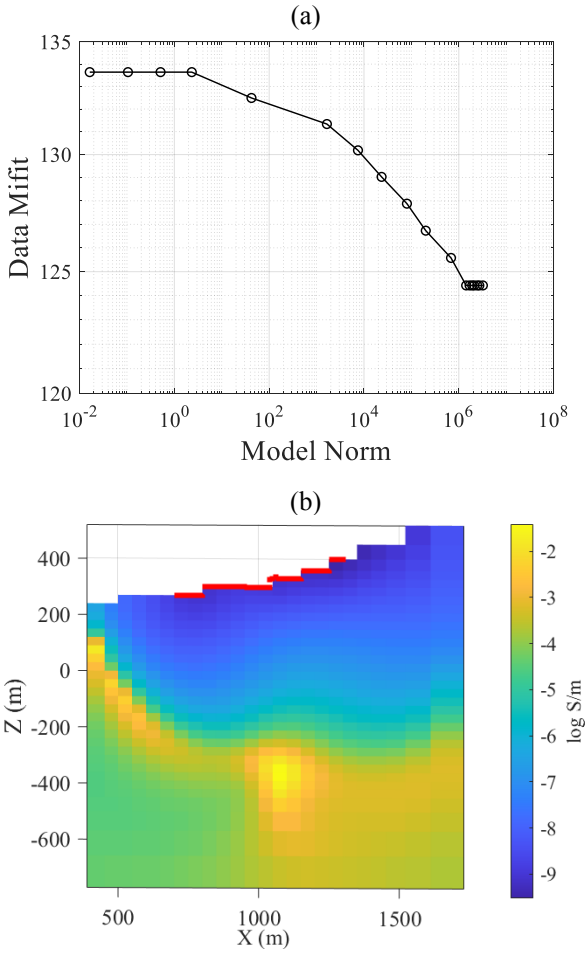

Figure 8: 3D inversion starting from a uniform subsurface. (a) Convergence curve of the data misfit; (b) Resultant conductivity model.

Next, the model from the forward simulation (Figure 7a) is used as the starting and reference model to "warm-start" the inversion. Although such a model contains some unrealistic conductivities and boundaries, it has the critical ability of generating positive-negative transients, a significant step in fitting the negative data. The subsequent inversion iterations can further polish the model in the L-2 smooth manner. The warm-start inversion is able to converge to a normalized misfit close to unity (Figure 9a). The positive-negative transient data are adequately fit (Figure 9b). The final inversion model resembles the ballpark structure in the starting model, but some small-scale features are fine-tuned by the inversion (Figure 9c). The final model confirms the contact between

the conductive Niujiaohe Formation and the resistive Gaotan Formation. The credibility of the model is also supported by an independently processed CSAMT 2D inversion model along the same survey line (Figure 9d).

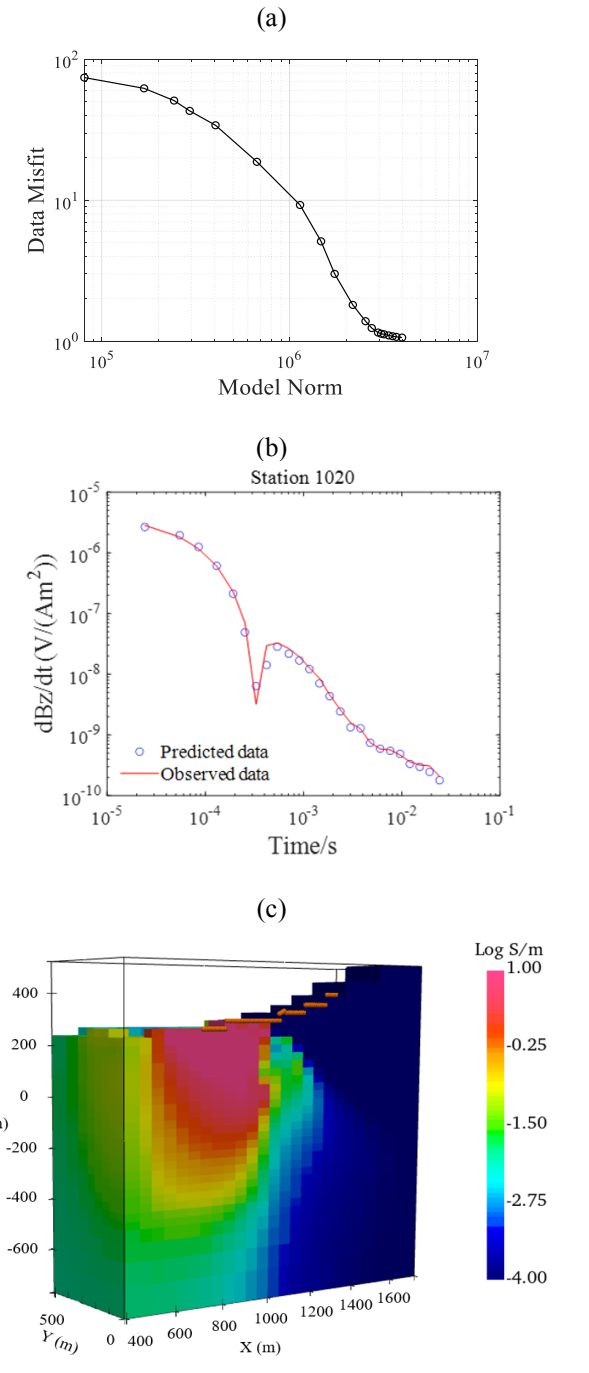

Figure 9: 3D warm-start inversion. (a) Convergence of the data misfit; (b) Fitting negative transient data; (c) Recovered 3D model; (d) CSAMT inversion result.

CONCLUSION

We presented an educational and inspiring case study that highlights the importance of 3D EM inversion and interpretation. The following can be learned.

Negative transient data in central-loop TEM are not necessarily the IP effect; the 3D coupling effect can also generate negative data if a large source loop encloses conductive and resistive terrains, and the in-loop receivers are off the conductive terrain.

The fast forward modeling powered by the survey decomposition is highly parallelizable and can respond to hypothetical model tests in seconds or minutes; the fast modeling tool is the key to quickly understand the measured data in practice.

We recommend to use the representative ballpark models from the forward exercise to warm-start the 3D inversion for a stable convergence and robust recovery of model.

ACKNOWLEDGEMENT

This work was funded by the Southern Marine Science and Engineering Guangdong Laboratory (Zhuhai) under the grant No. SML2021SP303.

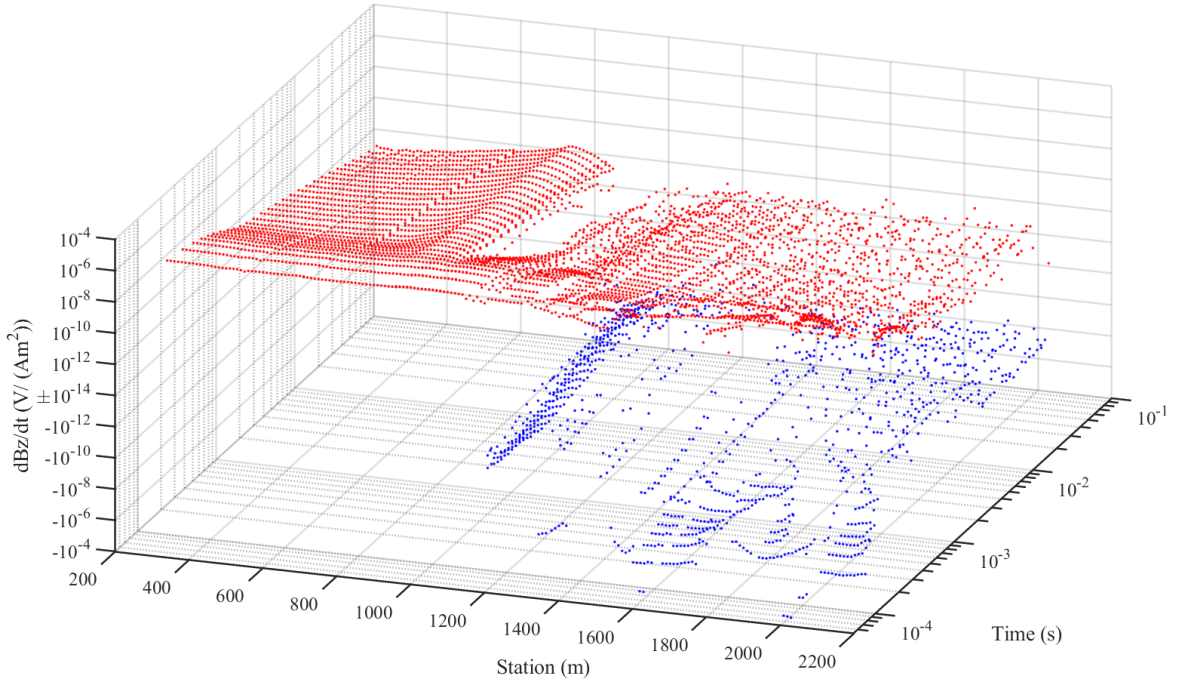

Figure 2: TEM data along the survey line. The red and blue dots indicate the positive and negative data respectively.

REFERENCES

Legault, J. M. (2015). Airborne electromagnetic systems–state of the art and future directions. *CSEG Recorder*, 40(6), 38-49.

Maurya, P. K., Foged, N., Madsen, L. M., & Christiansen, A. V. (2023). Comparison of towed electromagnetic with airborne electromagnetic and electrical resistivity tomography in a hydrogeophysical context. *Geophysical Journal International*, 235(1), 817-830.

Maurya, P. K., Grombacher, D., Lind, J., Lane, J. W., & Auken, E. (2022). Inversion of induced polarization-affected towed-transient electromagnetic data in a lateritic regolith geology: A case study from western Tanzania. Geophysics, 87(4), B247-B254.

Kang, S., & Oldenburg, D. W. (2016). On recovering distributed IP information from inductive source time domain electromagnetic data. *Geophysical Journal International*, 207(1), 174-196.

Weidelt, P. (1982). Response characteristics of coincident loop transient electromagnetic systems. *Geophysics*, 47(9), 1325-1330.

Yang, D., & Oldenburg, D. W. (2016). Survey decomposition: A scalable framework for 3D controlled-source electromagnetic inversion. *Geophysics*, 81(2), E69-E87.